

# Integrated Sensor Orientation on Micro Aerial Vehicles

THÈSE N° 7530 (2017)

PRÉSENTÉE LE 27 FÉVRIER 2017

À LA FACULTÉ DE L'ENVIRONNEMENT NATUREL, ARCHITECTURAL ET CONSTRUIT

LABORATOIRE DE TOPOMÉTRIE

PROGRAMME DOCTORAL EN GÉNIE CIVIL ET ENVIRONNEMENT

ÉCOLE POLYTECHNIQUE FÉDÉRALE DE LAUSANNE

POUR L'OBTENTION DU GRADE DE DOCTEUR ÈS SCIENCES

PAR

**Martin REHAK**

acceptée sur proposition du jury:

Prof. F. Golay, président du jury

Dr J. Skaloud, directeur de thèse

Dr C. Strecha, rapporteur

Dr M. Cramer, rapporteur

Prof. O. Kölbl, rapporteur



ÉCOLE POLYTECHNIQUE  
FÉDÉRALE DE LAUSANNE

Suisse  
2017



# Acknowledgements

This thesis would not appear in its present form without the assistance and support of many people. I would like to express my gratitude, recognition, and appreciation to everybody who made this thesis possible:

- First and foremost, my supervisor Dr. Jan Skaloud, for encouraging me to start a thesis, his continuous support, encouragements, and positive guidance throughout all stages of my PhD studies.
- Prof. Bertrand Merminod for giving me the opportunity to work in a research unit full of experts and highly motivated people.
- All the past and present colleagues and friends at the TOPO lab.
- To my family for their continuous support, and last, but definitely not least, to my wife Michaela, for her unconditional love, support, and for being so close despite being so far.

*Lausanne, 15th December 2016*

M. R.



# Abstract

Mapping with Micro Aerial Vehicles (MAVs whose weight does not exceed 5 kg) is gaining importance in applications, such as corridor mapping, road and pipeline inspections, or mapping of large areas with homogeneous surface structure, e.g. forest or agricultural fields. When cm-level accuracy is required, the classical approach of sensor orientation does not deliver satisfactory results unless a large number of ground control points (GCPs) is regularly distributed in the mapped area. This may not be a feasible method either due to the associated costs or terrain inaccessibility.

This thesis addresses such issues by presenting a development of MAV platforms with navigation and imaging sensors that are able to perform integrated sensor orientation (ISO). This method combines image measurements with GNSS or GNSS/IMU (Global Navigation Satellite System/Inertial Measurement Unit) observations. This innovative approach allows mapping with cm-level accuracy without the support of GCPs, even in geometrically challenging scenarios, such as corridors. The presented solution also helps in situations where automatic image observations cannot be generated, e.g. over water, sand, or other surfaces with low variations of texture.

The application of ISO to MAV photogrammetry is a novel solution and its implementation brings new engineering and research challenges due to a limited payload capacity and quality of employed sensors on-board. These challenges are addressed using traditional as well as novel methods of treating observations within the developed processing software. The capability of the constructed MAV platforms and processing tools is tested in real mapping scenarios. It is empirically confirmed that accurate aerial control combined with a state-of-the-art calibration and processing can deliver cm-level ground accuracy, even in the most demanding projects.

This thesis also presents an innovative way of mission planning in challenging environments. Indeed, a thorough pre-flight analysis is important not only for obtaining satisfactory mapping quality, but photogrammetric missions must be carried out in compliance with state regulations.

**Key words:** UAV, MAV, Integrated Sensor Orientation, Bundle adjustment



# Résumé

Les micro-véhicules aériens (Micro Aerial Vehicles : MAVs dont le poids n'excède pas 5 kg) sont de plus en plus utilisés en cartographie, notamment pour la cartographie de canyons (naturels ou urbains), l'inspection d'infrastructure linéaire (oléoducs, routes, lignes haute tension...) ou la cartographie de larges zones ayant une surface homogène, comme par exemple les forêts ou les exploitations agricoles. Lorsqu'une précision centimétrique est requise, l'approche classique d'orientation de capteurs ne donne pas de bons résultats, excepté s'il y a un grand nombre de point de calages au sol (ground control points : GCPs) répartis uniformément sur la surface cartographiée. Cependant, la mise en place de ces GCPs est coûteuse, voire impossible si le terrain est difficile d'accès.

Cette thèse aborde ces problématiques en présentant le développement de plateformes de type MAV sur lesquelles sont embarqués capteurs de navigation et appareils photographiques. L'ensemble de ces capteurs permet de calculer à tout moment la position et l'orientation du MAV. Cette méthode, appelée integrated sensor orientation (ISO) combine des mesures effectuées sur les images prise par l'appareil photographique, des méthodes de positionnement par satellites (Global Navigation Satellite System : GNSS) et optionnellement des mesures effectuées par une centrale inertielle (Inertial Measurement Unit : IMU). Cette approche innovante permet de cartographier avec une précision centimétrique sans utiliser de GCPs même dans des scénarios géométriquement difficiles tels que les canyons. De plus, la solution présentée apporte une plus-value lorsqu'il n'est pas possible d'effectuer automatiquement des mesures sur les photographies comme par exemple sur l'eau, le sable ou d'autres surfaces présentant de faibles variations de texture.

L'application de l'ISO à la photogrammétrie aéroportée par MAV est une solution originale et sa mise en œuvre entraîne de nouveaux défis en matière d'ingénierie et de recherche en raison de contrainte de charge utile, et donc de qualité des capteurs utilisés à bord. Ces défis sont abordés à l'aide de méthodes traditionnelles puis avec de nouvelles méthodes dans le logiciel de traitement développé lors de la thèse. La capacité des plateformes MAV et des outils de traitement développés est testée dans des scénarios de cartographie réels. Il est confirmé empiriquement qu'un contrôle aérien précis, combiné à un étalonnage des capteurs et un traitement de données adéquat permet d'atteindre la précision centimétrique voulue pour les points au sol.

Cette thèse présente également des méthodes novatrices de planification de missions dans des environnements difficiles. En effet, une analyse approfondie avant d'effectuer le vol est importante non seulement pour obtenir une qualité de cartographie satisfaisante, mais aussi

## **Acknowledgements**

---

pour satisfaire la réglementation.

**Mots clefs :** UAV, MAV, Integrated Sensor Orientation, Bundle adjustment



# Contents

<b>Acknowledgements</b>	<b>i</b>
<b>Abstract (English/Français)</b>	<b>iii</b>
<b>List of figures</b>	<b>xiii</b>
<b>List of tables</b>	<b>xix</b>
<b>Conventions and Notation</b>	<b>xxiii</b>
<b>Notations and Abbreviations</b>	<b>xxiii</b>
<b>1 Introduction</b>	<b>1</b>
1.1 Context . . . . .	1
1.2 Research Objectives . . . . .	2
1.3 Methodology . . . . .	3
1.4 External Contributions . . . . .	3
1.5 Thesis Outline . . . . .	4
<b>2 UAV Photogrammetry</b>	<b>7</b>
2.1 Definition and Context of UAV Photogrammetry . . . . .	7
2.2 Work-flow and Products . . . . .	9
2.2.1 Photogrammetric Work-flow . . . . .	9
2.2.2 Mapping Products . . . . .	10
2.2.3 Data Processing Tools . . . . .	11
2.3 Regulations of UAV Platforms . . . . .	11
2.4 Platforms and Categories . . . . .	12
2.4.1 Fixed-wing Platforms . . . . .	14
2.4.2 Multirotor Platforms and Helicopters . . . . .	14
2.4.3 Airships and Other Platforms . . . . .	15
2.5 Optical Sensors . . . . .	16
2.5.1 Passive Sensors . . . . .	17
2.5.2 Active Sensors . . . . .	19
2.6 Orientation Methods . . . . .	20
2.6.1 Coordinate frames . . . . .	21

## Contents

---

2.6.2	Indirect Orientation . . . . .	24
2.6.3	Direct Orientation . . . . .	24
2.6.4	Integrated Orientation . . . . .	26
2.7	Evolution of Orientation Methods on UAVs . . . . .	28
2.7.1	Indirect SO on MAVs . . . . .	28
2.7.2	DiSO and ISO on MAVs . . . . .	29
2.8	Basic Geometry and Accuracy Relations . . . . .	30
2.8.1	Image Measurement . . . . .	31
2.8.2	Influence of Image Measurements and Scene Geometry . . . . .	33
2.8.3	Ground Control Points . . . . .	34
2.8.4	The influence of Geometry . . . . .	36
2.8.5	The Influence of Aerial Position and Attitude . . . . .	38
<b>3</b>	<b>Mission Planning and Flight Management</b>	<b>41</b>
3.1	Requirements and Relations . . . . .	41
3.2	Overview of Mission Planners . . . . .	42
3.3	Mission Planning Work-flow and Considerations . . . . .	42
3.3.1	Photo Overlap . . . . .	43
3.3.2	Trajectory Design . . . . .	45
3.3.3	Technical Aspects of Platform and Camera . . . . .	46
3.4	Planning in a Complex Terrain . . . . .	48
3.4.1	Developed Mission Planner Tool . . . . .	49
3.4.2	Custom Base Maps and Digital Models . . . . .	50
3.4.3	Accounting for Terrain Variations . . . . .	51
3.4.4	Alternative Flight Patterns . . . . .	51
3.4.5	Overlap and GSD Assessment . . . . .	52
3.4.6	GNSS Satellite Visibility . . . . .	54
3.4.7	Additional Features . . . . .	55
3.5	Real-time Monitoring and Flight Management . . . . .	56
<b>4</b>	<b>Measurements, Models and Estimation Methods</b>	<b>59</b>
4.1	Introduction . . . . .	59
4.2	Image Observations . . . . .	60
4.3	Additional Parameters of Interior Orientation . . . . .	62
4.4	Aerial Observations . . . . .	63
4.5	Absolute Aerial Position and Attitude Control . . . . .	65
4.6	Relative Aerial Position and Attitude Control . . . . .	65
4.7	Absolute Spatio-temporal Control . . . . .	66
4.8	Relative Spatio-temporal Control . . . . .	67
4.9	Stochastic Models of Aerial Control . . . . .	67
4.10	Bundle Adjustment . . . . .	69
4.10.1	Functional Model . . . . .	70
4.10.2	Stochastic Model . . . . .	71

4.11 Program and Data Structure . . . . .	73
4.11.1 Data Preparation and Formatting . . . . .	73
4.11.2 Bundle Adjustment . . . . .	74
4.11.3 Graphical Output and Reporting . . . . .	74
<b>5 Developed MAV Platforms and Sensor Equipment</b>	<b>77</b>
5.1 General Challenges . . . . .	77
5.2 Platform Development . . . . .	78
5.2.1 TOPO Copter . . . . .	78
5.2.2 TOPO Plane . . . . .	80
5.2.3 Sensor Payload . . . . .	81
5.3 Optical Sensors . . . . .	82
5.4 GNSS Positioning . . . . .	83
5.4.1 Multi-frequency and Multi-constellation Receiver . . . . .	84
5.4.2 Single-frequency, Low-cost Receiver . . . . .	84
5.4.3 GNSS Antennae . . . . .	85
5.5 Inertial Measurement Unit . . . . .	86
5.5.1 IMU technology . . . . .	87
5.5.2 Employed IMU on the MAV platforms . . . . .	88
5.6 Sensor Payload . . . . .	88
5.6.1 TOPO Copter . . . . .	89
5.6.2 TOPO Plane . . . . .	89
5.6.3 Communication Links . . . . .	91
5.6.4 Communication security . . . . .	91
5.6.5 Electromagnetic Interference . . . . .	92
<b>6 System and Sensor Calibration</b>	<b>95</b>
6.1 Testing fields and data acquisition campaigns . . . . .	95
6.1.1 Close-range Calibration Field . . . . .	95
6.1.2 Open Space Testing Field . . . . .	96
6.1.3 Acquired Data Sets . . . . .	96
6.2 System Calibration of Spatial Offsets . . . . .	97
6.2.1 TOPO Copter . . . . .	99
6.2.2 TOPO Plane . . . . .	99
6.2.3 Antenna L1 Phase Centre Calibration . . . . .	101
6.3 System Calibration of Angular Misalignment . . . . .	102
6.3.1 Concept . . . . .	102
6.3.2 Initial Alignment . . . . .	103
6.4 The problem of the IMU and Camera Synchronisation . . . . .	103
6.4.1 IMU Synchronisation . . . . .	104
6.4.2 Camera Synchronisation . . . . .	105
6.5 Sensor Calibration . . . . .	109
6.5.1 Camera Calibration . . . . .	109

## Contents

---

6.5.2	Inertial Sensor Calibration . . . . .	114
<b>7</b>	<b>Evaluation and Performance Assessment</b>	<b>119</b>
7.1	Introduction . . . . .	119
7.2	Data Pre-processing . . . . .	120
7.2.1	Image Conversion . . . . .	121
7.2.2	Image Observations . . . . .	121
7.2.3	GNSS/IMU Processing and Trajectory Interpolation . . . . .	122
7.3	Aerial Position Control . . . . .	123
7.3.1	Absolute Relative Aerial Position Control in the GNSS Perturbed Environment . . . . .	123
7.3.2	Aerial Position Control With a Low-cost GNSS Receiver . . . . .	129
7.4	Aerial Position and Attitude Control . . . . .	134
7.4.1	Aerial Control in Corridor Mapping . . . . .	134
7.4.2	Sensor Orientation Without Automatic Tie-points . . . . .	139
7.4.3	Redundancy in EO observations . . . . .	144
7.5	Spatio-temporal Aerial Control . . . . .	146
7.5.1	Processing Strategy . . . . .	146
7.5.2	Testing Methods . . . . .	146
7.5.3	Processing Steps . . . . .	148
7.5.4	Residual Analysis . . . . .	149
7.5.5	Convergence and Stability . . . . .	151
7.5.6	On the Origin of the Camera Delay . . . . .	151
7.5.7	Impact on Mapping Accuracy . . . . .	153
7.5.8	Summary . . . . .	154
7.6	Stability of Camera IO parameters . . . . .	154
<b>8</b>	<b>Conclusion and Perspectives</b>	<b>159</b>
8.1	Summary of Contributions . . . . .	159
8.1.1	Theoretical/Conceptual Contributions . . . . .	159
8.1.2	Engineering Contributions . . . . .	160
8.2	Conclusions . . . . .	161
8.3	Perspectives . . . . .	162
<b>A</b>	<b>Overview of Photogrammetric Platforms, Sensors, and Mission Planners</b>	<b>165</b>
<b>B</b>	<b>TOPOBUN Bundle Adjustment</b>	<b>169</b>
<b>C</b>	<b>System and Sensor Calibration</b>	<b>175</b>
C.1	Lever-Arm Calibration . . . . .	175
C.2	Camera Calibration . . . . .	176
	<b>Bibliography</b>	<b>195</b>

**Curriculum Vitae**

**196**



# List of Figures

1.1	Challenging mapping scenarios: (A) Water coast lines and sand banks, (B) Dense vegetation, (C) Pipeline and product-line inspection, (D) Road corridor mapping.	2
1.2	Methodology cycle of the presented development.	4
2.1	Multiple types of remote sensing platforms. UAV technology complements existing techniques, fitting between large area imagery from satellites and high altitude platforms and manned aircraft and smaller coverage, but highly accurate terrestrial approaches.	8
2.2	Four scenarios to fly a drone in France, modified after (DIY Drones [2014]).	13
2.3	Fixed-wing MAVs with GNSS RTK capability.	14
2.4	Multicopter MAVs dedicated to mapping and inspection tasks.	15
2.5	Less conventional mapping platforms.	16
2.6	Fixed-wing UAV with VTOL capabilities Songbird (Aerolution GmbH [2016]). Depending on the payload, this UAV fits into MAV or Mini UAV categories.	16
2.7	Frame RGB cameras (not to scale).	18
2.8	Frame multi- and hyper- spectral cameras (not to scale).	18
2.9	Headwall Nano-Hyperspec camera (Headwall [2016]).	20
2.10	Velodyne VLP-16 LiDAR sensor (Velodyne LiDAR [2016]).	20
2.11	Sensor orientation methods.	21
2.12	Image coordinate system, camera frame and main elements of IO parameters.	22
2.13	The principle of direct georeferencing.	26
2.14	Pinhole camera model and GSD calculation.	34
2.15	Normal case of stereo photogrammetry.	35
2.16	General case of stereo and multi-stereo photogrammetry with simulated data. Error ellipsoids represent the estimated precision of object points (not to scale).	35
2.17	Effect of GCPs distribution on scene geometry; a) no GCPs or badly distributed, b) not optimal distributed GCPs, c) optimally distributed GCPs.	36
2.18	3D precision of scene points of a strip with four GCPs as a function of a distribution of GCPs for a single strip corridor. Fixing both ends significantly improves the theoretical precision.	37
2.19	Estimated precision of object coordinates of tie-points represented by error ellipsoids.	37
2.20	Problematic geometry of a single corridor strip.	38

## List of Figures

---

2.21	3D precision of scene points of a block with GCPs distributed in the four corners and along the border. . . . .	38
2.22	Projection of roll and pitch errors on the ground from different flying heights. .	39
3.1	Schematics of forward and side overlap. . . . .	44
3.2	Classical vs. modern block setup. The shades of grey represent the number of overlapping images. . . . .	45
3.3	Classical flight pattern of an aerial mission from two distinct flight height levels.	46
3.4	Flight pattern for close-range mapping and 3D modeling. Three distinct flight levels are depicted, but their number is optional depending on the size and shape of the mapped object. . . . .	46
3.5	Graphic environment for UAV mission planning. The central 3D map is surrounded by control panels. . . . .	50
3.6	Flight configurations; A) simple flight in one level, B) two flight levels, C) progressive changing of flight altitude. . . . .	51
3.7	Classical, overshoot and smoothed turning curves. The red trajectory is based on practical tests and represents dynamics of a fixed-wing drone. . . . .	52
3.8	Alternative flying pattern. . . . .	52
3.9	Polygon projection to the camera frame. . . . .	54
3.10	Overlap evaluation. Green colour represents areas with high overlap, red and blue with low overlap (Pascale [2016]). . . . .	54
3.11	Evaluation of GSD. The darker the blue colour, the lower expected GSD (Pascale [2016]). . . . .	54
3.12	Visibility of GNSS satellites for certain points represented by imaginary rays between sampled trajectory and satellites. . . . .	55
3.13	Minimum number of GNSS satellites as a function of survey time for a specific trajectory. . . . .	55
3.14	Post-mission analysis; blue path: the executed flight, white path: the planned path. . . . .	56
4.1	Integrated sensor orientation schema, i.e. general adjustment using satellite, inertial, and photo observations. . . . .	60
4.2	Image and object coordinate systems of an aerial photograph. . . . .	62
4.3	Two types of wrong time synchronisation: Case a) depicts time delay (positive) between the observed and estimated EO parameters. Case b) depicts negative delay that is caused by registering the time mark ahead in time. . . . .	66
4.4	Bundle block scene with images, tie-points, GCPs and GNSS/IMU trajectory that results in absolute or relative camera EO parameters, velocity and angular rate observations. . . . .	70
4.5	TopoBun data flow chart. . . . .	73
4.6	3D view on a corridor scene with error ellipsoids of tie-points and cameras. . .	75
5.1	Multicopter system. . . . .	79



5.2	Schematic sketch of the stabilised sensor mount for two distinct tilting angles. The relative position and orientation between the sensors do not change when tilting the mount. . . . .	79
5.3	Schematic sketch of the coaxial and flat multirotor configurations. . . . .	80
5.4	Fixed-wing platform. . . . .	81
5.5	Sony NEX 5N with 16 mm Sony lens (Sony [2016]). Image courtesy of B & H Foto & Electronics Corp. [2016]. . . . .	83
5.6	Javad TR-G3T receiver (Javad GNSS Inc. [2016]) . . . . .	84
5.7	U-Blox NEO-8T GNSS receiver with a serial data logger, GNSS signal splitter (GPS Source [2016]), and L1/L2 GNSS antenna Maxtena (Maxtena [2016]). During the presented experiment, a second receiver Javad TR-G3T was connected via the splitter to provide with a reference trajectory. . . . .	86
5.8	Antcom L1/L2 GPS+Glonass antenna (left image) (Antcom Corp. [2016]) and Maxtena L1/L2 GPS+Glonass (right image) (Maxtena [2016]). . . . .	87
5.9	Gecko4Nav R-IMU and Sony NEX 5N RGB camera mounted on a stabilised mount. . . . .	90
5.10	Camera sensor head of the fixed-wing platform. . . . .	90
6.1	Close-range calibration field. . . . .	96
6.2	An example of ARTag fiducial marker. . . . .	96
6.3	Open space calibration field. . . . .	97
6.4	Schematic sketch of the sensor offsets between the camera projection centre, the IMU-sensor frame and the ARP. . . . .	99
6.5	Schematic sketch (top view) of the sensor offsets calibration procedure. Offsets measured from three stations. . . . .	100
6.6	Antenna's L1 phase centre calibration; both antennae placed on known ARPs. . . . .	102
6.7	Time-alignment of NavChip IMUs (Intersense [2015]) sensed specific force to the reference (iMAR-FSAS) (Mabillard [2013]). . . . .	104
6.8	Determination of a camera lag using LED bar-graphs. . . . .	106
6.9	Influence of synchronisation error $\Delta t = 1, 2.5$ and $5$ ms on velocity and resulting 2D position error. . . . .	107
6.10	Influence of synchronisation error $\Delta t = 1$ and $5$ ms on angular rates ( $\omega$ or $\varphi$ ) and resulting 2D position error for three different flying heights. . . . .	109
6.11	Siemens star calibration target. . . . .	112
6.12	A detail of the Siemens star target where the loss in contrast equals to 50 %. . . . .	112
6.13	An example of the Gaussian point spread function for different colour channels. Image courtesy of IFP, University of Stuttgart. . . . .	112
6.14	A detail of the calibration target. . . . .	112
6.15	Camera calibration flight over a dedicated field. The yellow line symbolises the flown trajectory, the red arrows symbolise the camera orientation during the image acquisition. . . . .	113
6.16	Distribution of image residuals. The red lines represent 1 pixel size i.e. $\sim 4.8 \mu m$ . . . . .	115

## List of Figures

---

6.17	Image residuals (blue dots) with respect to the radial distance. The green line represents a trend in residuals. . . . .	115
6.18	Typical IMU errors: a bias, a scale factor, time-correlated noise. Modified after NovAtel [2014]. . . . .	116
6.19	Example data set before (blue) and after (green) calibration of an IMU showing the differences in the acceleration norm at different attitudes. The reference gravity value $g$ is shown in a purple colour (Clausen et al. [2016]). . . . .	118
7.1	Processing scheme; raw data inputs are in yellow, blue are the input/output products, green are the processing steps, and grey is the BA. . . . .	120
7.2	Automatic and manual image conversion from raw to JPEG format; a) automatic conversion using the senseFly eMotion2, b) manual correction using a photo editor. The image was taken with the Canon PowerShot S110 camera having 12.1 Mpix resolution (Canon Inc. [2016]). . . . .	121
7.3	Observability of tie-points for the datasets FW1 and FW2. The two areas were clipped in order to cover the same region. . . . .	123
7.4	Placement of 3 GCPs and 22 ChPs. . . . .	125
7.5	Estimated vertical and horizontal accuracy, and position DOP values for the 68 images. . . . .	127
7.6	Differences in absolute observations between reference EO parameters and those determined from a perturbed GNSS signal. . . . .	127
7.7	Differences in relative observations between reference EO parameters and those determined from a perturbed GNSS signal. . . . .	127
7.8	Accuracy at ChPs from the cases A-D. . . . .	129
7.9	Differences in absolute camera positions between the Javad and the U-Blox GNSS receivers. . . . .	130
7.10	Differences in the relative camera positions between the Javad and the U-Blox GNSS receivers. . . . .	130
7.11	3D view on the scene with camera stations, GCPs and a point cloud of tie-points from the Pix4D Mapper. . . . .	130
7.12	A scheme of a strip separation of the FW1 flight. Green triangles represent the GCPs. . . . .	134
7.13	The propagation of roll and pitch errors on the ground from two different flying heights in contrast with the estimated accuracy of measured angles. . . . .	136
7.14	Residuals at ChPs. ISO configuration with absolute aerial position control (I), and with position and attitude control (II). The base orthophoto was processed in the Pix4D Mapper. . . . .	137
7.15	DSM differences with respect to the reference for different types of absolute orientation; <b>A)</b> 9 GCPs, <b>B)</b> 4 GCPs, <b>C)</b> accurate GNSS/IMU-derived positions. . . . .	138
7.16	Estimated precision of object coordinates of tie-points for different types of absolute orientation. <b>A)</b> 9 GCPs, <b>B)</b> 4 GCPs, <b>C)</b> accurate GNSS/IMU-derived positions and attitude. . . . .	139

---

7.17 Flown trajectory, ground control, and check points on a base orthophoto map from the Pix4D Mapper. . . . .	141
7.18 Distribution of GCPs, ChPs, and tie-points in Fast AT and ISO. . . . .	141
7.19 Absolute attitude residuals; influence of an IMU residual boresight on attitude accuracy. . . . .	142
7.20 Relative attitude residuals. . . . .	142
7.21 Estimated 3D precision of object coordinates of tie-points represented by error ellipsoids (scaled 70 times). The ISO project with absolute position, absolute attitude, and 5 GCPs. . . . .	143
7.22 A scheme of the calibration block FW1 and its division. . . . .	147
7.23 Modified processing scheme in Fig. 7.1: raw data inputs are in yellow, blue are the input/output products, green are the processing steps, and the BA is in grey. Red arrows symbolise iterative processes. . . . .	148
7.24 Block B: Aerial 2D camera position residuals; low weights on aerial position observations = indirect SO (all GCPs, all IO parameters self-calibrated). The trend in residuals corresponds to $\Delta t = -9.2$ ms. . . . .	149
7.25 Block B: Residuals in the horizontal camera positions and a fitted slope in comparison to the slope of the time delay of $\Delta t = -6.2$ ms estimated in the BA using absolute spatio-temporal position and attitude observations. . . . .	150
7.26 Block B: Residuals in horizontal camera positions and fitted slope in comparison to the slope of the residual time delay of $\Delta t = -0.3$ ms estimated in the BA using absolute spatio-temporal position and attitude observations. . . . .	151
7.27 Added vs. estimated delay after correcting the original time events for $\Delta t = -6.2$ ms. . . . .	152
7.28 Simplified schematics of the possible source of a synchronisation error. Time T1 is an interval between the mid-exposure and shutter opening to which the EO parameters are related. Time T2 is a delay between the flash pulse and shutter initial opening. Interval T3 is the half of the max. synchronisation shutter speed, i.e. $\geq 1/320s$ , for Sony NEX 5R. The sum of T2 and T3 is the time needed for the flash electronics to prepare for flashing and for reaching the maximal flash intensity. . . . .	152
7.29 Correlations between EO and IO parameters for randomly selected images. . .	156
C.1 The lever-arm calibration setup. The fuselage without wings and with the camera and antenna pointing towards the calibration field. . . . .	175
C.2 Distribution of image observations in the image plane. . . . .	176
C.3 Image residuals in the camera sensor plane. . . . .	177



# List of Tables

1	Reference frames and coordinate systems. Further details are in Sec. 2.6 . . . .	xxiv
2.1	UAV classification, adopted after Blyenburgh [2008] . . . . .	13
2.2	Overview of reference frames (adopted after Skaloud and Legat [2010], Schaer [2009]). . . . .	22
4.1	Main sensor orientation approaches. . . . .	64
5.1	Advantages and disadvantages of the selected coaxial configuration. . . . .	80
5.2	Main features of the employed GNSS receivers. . . . .	85
5.3	Sensor accuracy and price for low-cost MEMS, tactical, and navigation grade IMUs. . . . .	88
5.4	Stochastic characteristics of the inertial sensors (Intersense [2015]). . . . .	88
5.5	Summary of imaging and navigation components weight. . . . .	91
5.6	Communication links of the developed MAVs. . . . .	92
6.1	Summary of acquired data. Acronyms in the data sets CR_ stand for close-range, FW_ for fixed-wing. . . . .	98
6.2	Measured vs. estimated lever-arm $\mathbf{a}_{CAM-ARP}^c$ . . . . .	99
6.3	Ground calibrated vs. BA-estimated lever-arm between the camera perspective centre and the antenna ARP. . . . .	101
6.4	Camera-lag statistics in a manual exposure mode. . . . .	105
6.5	Angular rates observed during a real mapping flight. . . . .	108
6.6	Results of the static resolution test indicated in an image and object space. . . .	112
6.7	RMS of image observation residuals and camera IO parameters from self-calibration.	114
6.8	Significant correlations of a randomly selected image. . . . .	114
6.9	Calibrated accelerometer biases of the R-IMU Clausen et al. [2016]. . . . .	118
7.1	Network characteristics and accuracy of the measured tie-points and GNSS aerial positions. . . . .	124
7.2	Case A: Summary of indirect SO (AT + 3 close GCPs) at 22 checkpoints. . . . .	125
7.3	Case B: Summary of ISO projects without bias. . . . .	126
7.4	Case C: Summary of ISO on projects with GNSS positioning bias. . . . .	128
7.5	Case D: Summary of ISO (3 close GCPs + 61 relative GNSS + GNSS bias) at 22 checkpoints. . . . .	128

## List of Tables

---

7.6	Mapping accuracy at 23 ChP, with an absolute aerial position control, without GCPs, and with absolute aerial positions. The acronym TPB states for the TopoBun. The average GSD of these ISO projects is 4 cm. . . . .	132
7.7	Significant correlations of a randomly selected image. . . . .	132
7.8	Mapping accuracy at 22 ChPs, with 1 or 4 GCPs, and with relative aerial position control. . . . .	133
7.9	RMS of image obs. residuals with the camera IO parameters and boresight from self-calibration. . . . .	135
7.10	Quality of the GNSS/IMU data and estimated precision of the object and control points. . . . .	135
7.11	Residuals at 9 check points, no GCPs used in the adjustment. . . . .	136
7.12	Test configurations and their properties . . . . .	142
7.13	Accuracy assessment at independent check points; 5 GCPs and 15 ChPs, the test parameters correspond to those in Tab. 7.12. In DiSO, no GCPs were used. . . .	143
7.14	Testing configurations with redundant EO parameters; $\mathbf{Position}_n/\mathbf{Attitude}_n$ where $n$ is a particular set of EO parameters (1-4); "a" and "r" stand for absolute and relative observations, respectively. . . . .	145
7.15	Results of BA with redundant EO parameters. In ISO and Fast AT, the same 5 GCPs as depicted in Fig. 7.17 were used. In DiSO, no GCPs were used. Accuracy evaluated at 15 ChPs. One pixel = 45 mm. . . . .	145
7.16	Data set FW1 division into two blocks and their properties. . . . .	147
7.17	Pertinent results from the self-calibrating BA. . . . .	147
7.18	Estimated synchronisation errors using different observations. . . . .	150
7.19	Evaluation Block (E); estimated accuracy of aerial positions and ground accuracy measured at 9 independent check points in the case of block configuration and 7 check points of single strip corridor, respectively. The parameter $\mathbf{O}$ states for original, $\mathbf{C}$ states for calibrated events, i.e. the time events corrected for $\Delta t = -6.2$ ms. The average GSD of this project is 4.5 cm. . . . .	153
7.20	Comparison of IO parameters and their precision. The data set CR2 did not use the same camera body. . . . .	156
A.1	Main MAVs (<5 kg) currently available on the market that are dedicated to photogrammetry. . . . .	166
A.2	Frequently used RGB and multi/hyperspectral/thermal cameras on MAVs. . . .	167
A.3	Main mission planners dedicated to MAVs; A value "-" means no functionality or very low, "+" means low, "++" means medium, "+++" means high. This categorisation is based on the author's personal opinion and does not completely reflect the true functionality as some of the mission planners were not available for testing. . . . .	168
B.1	Structures of the design matrix $\mathbf{A}$ and the vector of observations $\mathbf{L}$ . In addition to the depicted observations, the following parameters can be used as weighted observations: camera IO, a boresight, a lever-arm and $\Delta t$ . . . . .	173

C.1 Parameters and their correlation for a random image from the dataset. . . . . 176





# Notations and Abbreviations

## Conventions

- A superscript in a vector indicates a particular frame in which the vector is represented.
- Rotation matrices between coordinate systems have a subscript (original frame) and superscript (target frame) indicating the two coordinate systems (e.g.  $\mathbf{R}_b^l$  indicates the rotation matrix from the  $b$ -frame to the  $l$ -frame).
- The elementary rotation matrices are defined as

$$\mathbf{R}_1(\alpha_1) = \begin{bmatrix} 1 & 0 & 0 \\ 0 & \cos(\alpha_1) & \sin(\alpha_1) \\ 0 & -\sin(\alpha_1) & \cos(\alpha_1) \end{bmatrix}$$

$$\mathbf{R}_2(\alpha_2) = \begin{bmatrix} \cos(\alpha_2) & 0 & -\sin(\alpha_2) \\ 0 & 1 & 0 \\ \sin(\alpha_2) & 0 & \cos(\alpha_2) \end{bmatrix}$$

$$\mathbf{R}_3(\alpha_3) = \begin{bmatrix} \cos(\alpha_3) & \sin(\alpha_3) & 0 \\ -\sin(\alpha_3) & \cos(\alpha_3) & 0 \\ 0 & 0 & 1 \end{bmatrix}$$

Definition of standard deviation (STD)

$$\sigma = \pm \sqrt{\frac{\sum_{i=1}^n (x_i - \bar{x})^2}{n}}$$

Definition of Root Mean Square difference (RMS)

$$RMS = \pm \sqrt{\frac{\sum_{i=1}^n x_i^2}{n}}$$

## Notations and Abbreviations

---

ID	Frame Name
c	Camera frame
b	Body frame
e	ECEF Earth-centered Earth-fixed frame
l	Local level frame
m	Mapping frame

Table 1 – Reference frames and coordinate systems. Further details are in Sec. 2.6

## Acronyms

AAT	Automatic Aerial Triangulation
AES	Advanced Encryption Standard
AOI	Area of Interest
ARP	Antenna Reference Point
AT	Aerial Triangulation
BA	Bundle Adjustment
CCD	Charge-coupled device
ChP	Check Point
CMOS	Complementary metal–oxide–semiconductor
CSV	Comma-Separated Value
DiSO	Direct Sensor Orientation
DOP	Dilution of Precision
DTM	Digital Terrain Model
DSM	Digital Surface Model
DSLR	Digital-Single-Lens Reflex
EO	Exterior Orientation
EMI	Electromagnetic Interference
FPGA	Field-Programmable Gate Arrays
FWHM	Full Width at Half Maximum
GCP	Ground Control Point
GIS	Geographical Information System
GMWM	Generalised Method of Wavelet Moments
GNSS	Global Navigation Satellite System
GPS	Global Positioning System
GUI	Graphical User Interface

ID	Identification
IMU	Inertial Measurement Unit
IO	Interior Orientation
ISO	Integrated Sensor Orientation
JPEG	Joint Photographic Experts Group
LiDAR	Light Detection and Ranging
MAV	Micro Aerial Vehicle
MEMS	Micro-Electro-Mechanical Systems
MTF	Modulation Transfer Function
PPS	Pulse-per-Second
PSF	Point Spread Function
RGB	Red, Green, Blue
RMS	Root Mean Square
RTK	Real-Time Kinematics
R-IMU	Redundant IMU
RP	Resolving Power
RPV	Remotely Piloted Vehicle
ROA	Remotely Operated Aircraft
SDK	Software Development Kit
SO	Sensor Orientation
UAS	Unmanned Aerial System
UAV	Unmanned Aerial Vehicle
UVS	Unmanned Vehicle System
VTOL	Vertical Take-Off and Landing
WMS	Web Map Service



# 1 Introduction

## 1.1 Context

Unmanned Aerial Vehicles (UAV) are gaining importance in the mapping and monitoring tasks of our environment. This technology was formerly exclusively employed by military, but it is nowadays spreading into the civilian sector as it allows acquiring information conveniently over places that are not attainable by other means. Its development creates new possibilities in various scientific fields, such as photogrammetry.

The UAV method of acquisition combines benefits of a close-range and aerial photogrammetry. As a result, higher resolution and mapping precision can be obtained over larger and possibly less accessible areas, e.g. mountains.

Although these systems allow a new way of data collection in the field of geomatics, they inherit an old, i.e. indirect approach of sensor/image orientation. Indeed, most of the commercially available UAVs carry simple cameras not primarily designed for photogrammetric purpose and GNSS/IMU instruments that do not allow direct sensor orientation (DiSO) with cm-level and arc-minute accuracy in position and attitude, respectively. Hence, missions with the need of accurate mapping require image acquisition in a block structure with large forward and side overlaps, the existence of possibly many ground control points, as well as contrast in the surface texture. Fig. 1.1 illustrates some examples of demanding mapping situations. The cases A and B present situations in which the automatic tie-point detection might not deliver reliable results or might not work at all. In contrast, scenarios C and D present situations with challenging geometric configurations, e.g. single strip corridors. Although single-strip operations are theoretically possible, the requirement on the number and distribution of GCPs makes them impractical. Overall, the need for ground operations limits the mapping productivity of UAVs.

It is known that a precise aerial control offers an improvement in the final mapping accuracy when employing ISO. Such mode of operation limits the number and distribution of GCPs, which in turn saves time and cost in their signalisation and surveying. Moreover, first responders and emergency personnel appreciate the possibility of making instant up-to-date georeferenced imagery. Thus, without the requirement of ground control, integrated

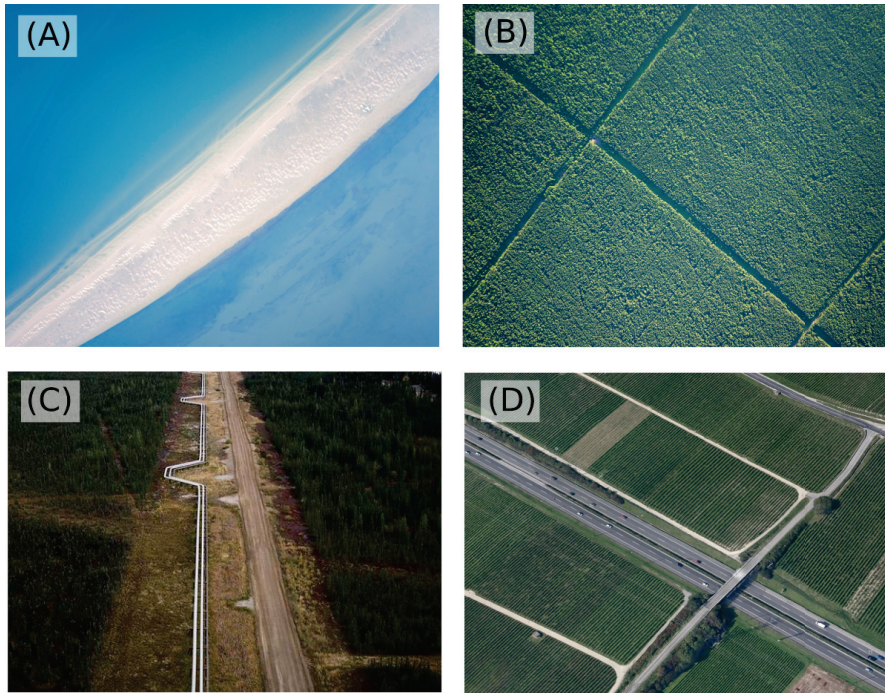


Figure 1.1 – Challenging mapping scenarios: (A) Water coast lines and sand banks, (B) Dense vegetation, (C) Pipeline and product-line inspection, (D) Road corridor mapping.

GNSS/IMU technology can offer significant advantages.

On the one hand, the integration of accurate navigation instruments into conventional unmanned systems helps to increase accuracy and to solve challenging mapping tasks. On the other hand, accurate aerial control requires thorough sensor integration and calibration. This is not a trivial task and together with a rather high initial cost of the equipment constitute the main reasons why the number of such equipped UAVs is rather low. Furthermore, the hardware integration of additional sensors to MAVs is even more challenging due to stronger payload constraints.

Apart from the hardware integration and data collection, another crucial task becomes data processing. Some of the challenging procedures related to the ISO and DiSO are, e.g. bore-sight, lever-arm calibration, or sensor time synchronisation. In ISO, these parameters can be self-calibrated or the need of their determination can be mitigated in the presence of new types of aerial observations, such as relative or spatio-temporal aerial control.

## 1.2 Research Objectives

The primary goal of this research is to design and construct MAV systems purposed for precise and efficient mapping that integrate imaging components with advanced navigation sensors and to develop as well as test suitable processing methods. The concept of ISO on MAVs was new when this thesis started. Up to then, no commercial or research MAV platforms had deliv-

ered comparable results in certain mapping scenarios, e.g. with high requirements on aerial position and attitude accuracy. Although certain concepts of aerial control are known from manned platforms, their employment on UAVs and MAVs, in particular, presents considerable challenges that have not yet been addressed in detail.

The main objectives of this work are summarised into the following points:

1. **Elaboration of concepts and methodologies needed for performing accurate mapping from MAVs.** This embraces the study and implementation of new methods of sensor orientation in the context of MAV mapping. Further objective is to create an adjustment tool that allows testing of different sensor orientation methods.
2. **Construction of MAV platforms integration and calibration of the necessary hardware to perform ISO.** This requires calibrating sensor and system parameters. The particular challenges are posed by the space and payload limitations, as well as GNSS signal perturbation due to the MAV electronics.
3. **Presentation of a thorough analysis of MAVs systems performance in real mapping scenarios.** The objective is to establish a processing chain for accurate MAV mapping and to demonstrate the performance and usefulness of the developed platforms and concepts. Special attention is paid to the evaluation of benefits of using relative and spatio-temporal observation models and mapping of corridors, as well as scenarios without automated tie-points. Lastly, a direct georeferencing method is tested.

### 1.3 Methodology

The concept of accurate aerial control on MAVs is very demanding on hardware and software components and their integration. Due to the interdisciplinary nature of this research, the hardware construction is combined with software development. Regular field tests provide direct feedback about platform's and algorithm's performance. Furthermore, new modifications, e.g. sensor adjustment, are carried out together with an incorporation of new concepts of sensor orientation, and the process is repeated. This cycle is depicted in Fig. 1.2. In the designed methodology each level depends on the results of the previous one, while simultaneously allows feedback on the previous level. A mission planning followed by a field test can be an example. The development of a mission planner was modified according to the results from a real flight. The presented steps roughly correspond to the actual thesis outline.

### 1.4 External Contributions

The development of fully functional MAVs with advanced sensors on-board is characterised by a high complexity both on the scientific and engineering levels. To achieve the aforementioned objectives within the given extent of a PhD thesis, several members of the Geodetic Engineering

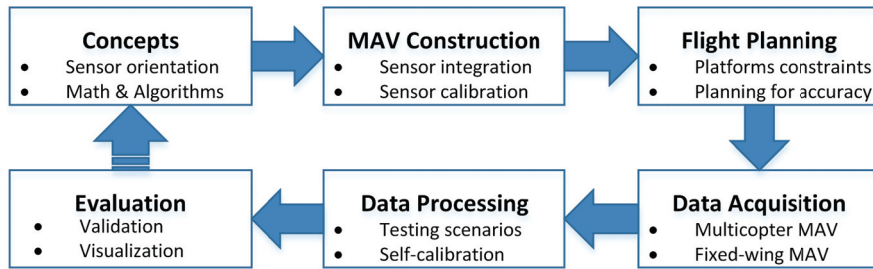


Figure 1.2 – Methodology cycle of the presented development.

Laboratory (TOPO-EPFL) kindly offered their valuable advice. The most important external contributions are:

- The TOPO Mission Planner tool: Chap. 3. The development of the described mission planner was initiated by the author and then developed, under his co-supervision, by Florian Gandor and Roberta Pascale during their master projects (Gandor [2015], Pascale [2016]). The development was published in an international conference paper written by the author (Gandor et al. [2015b]) and a local journal paper written by Florian Gandor (Gandor et al. [2015a]).
- IMU system calibration: Calibration of deterministic and stochastic errors was initially performed by Romain Mabillard in his master project that was co-supervised by the author (Mabillard [2013]). Calibration of the Redundant IMU (R-IMU) was performed by Philipp Clausen (Clausen et al. [2016]). Both works benefit from the long-term development of sophisticated stochastic tool GMWM (Generalised Method of Wavelet Moments) (Guerrier et al. [2015]).
- GNSS/IMU trajectory estimation and transformation was performed under close supervision of the thesis director.
- Plug-in for 3D visualisation of adjustment scene was done by Emmanuel Cledat.

Wherever further external sources have been used for the development, their contribution is clearly referenced and emphasised.

## 1.5 Thesis Outline

The thesis is structured into 8 chapters and can be roughly divided into 4 major blocks.

- **Review of UAV photogrammetry technology and mission planning:** The chapter 2 delivers background material related to the UAV legislation, UAV platforms and optical sensors. The main concepts of sensor orientation are introduced together with a literature review in the context of accurate sensor orientation of MAVs. Furthermore, basic



principles of pre-flight accuracy assessment are outlined.

The chapter 3 deals with basic concepts of aerial mission planning. Close attention is given to the aspects of mission planning in complicated terrain and calculation of predicted satellite visibility.

- **Development of Bundle Block Adjustment:** The chapter 4 is devoted to the concepts of aerial observations and their mathematical models. Methods of absolute, relative, and spatio-temporal observation are introduced together with details on a stochastic modelling. The chapter also presents developed software for a bundle adjustment (BA).
- **Hardware development and calibration:** The chapter 5 discusses the construction of two MAV platforms and integration of mapping and navigation sensors. Furthermore, it introduces main technological concepts behind the navigation and inertial sensor technology.

The chapter 6 focuses on the problematic aspects of sensor and system calibration. Theoretical concepts are followed by practical examples with the previously mentioned MAV systems.

- **Performance analysis and conclusions:** The backbone of the evaluation in the chapter 7 is four journal and conference articles dealing with practical evaluation of the hardware and software development. The presented tests are focused on a close-range application as well as on mapping of larger areas. The issue of corridor mapping is addressed by a comparison of a classical indirect sensor orientation method a method with accurate aerial control. Absolute spatio-temporal aerial control is tested and time synchronisation delay of a camera and GNSS/IMU is estimated.

The chapter 8 presents a summary of the main contributions of this thesis, conclusions, and perspectives for future work. This is followed by bibliography and appendices.



## 2 UAV Photogrammetry

*The term UAV photogrammetry describes a photogrammetric measurement platform which operates remotely controlled, semi-autonomously, or autonomously without a pilot sitting in the vehicle. The history and categorisation of UAVs in photogrammetry have been described in details in several publications, see e.g. Eisenbeiß [2009], Colomina and Molina [2014] and will not be presented in a great detail here. Nonetheless, a brief review on the recent advances and current trends will be given in this chapter to emphasise the rapid development that we have recently witnessed.*

### 2.1 Definition and Context of UAV Photogrammetry

The Unmanned Aerial Vehicle can be defined as a vehicle without a pilot that is physically aboard (Unmanned Aerial Vehicle Systems Association [2016]). Unmanned Aerial Systems (UAS), on the other hand, encapsulate the aircraft or the UAV, the ground control station/controller, and the system of communications connecting the two. These designations are used to define the flying object employed for recreational and professional applications. Even if these terms seem to have clear definition, the aviation agencies of many countries have decided to go for different terms than today's UAV/UAS. Here are the two most frequent designations that were adopted by the major professional actors in the UAV domain.

- **Drone:** The term drone refers mainly to an unmanned aircraft used in a military context. Nevertheless it is used to designate any type of aerial unmanned vehicle in the common language. This term is used as an official name for UAVs, among others, in French-speaking countries. Being at the forefront in the creation and implementation of regulations for the use of commercial UAVs, the French Directorate for Civil Aviation (DGAC [2016]) refers to UAVs as drones. The same applies to the Swiss Federal Office of Civil Aviation (FOCA [2017]).
- **RPAS:** The International Civil Aviation Organisation (ICAO [2016]) employs the acronym RPAS (Remotely Piloted Aircraft System). This term does not evoke military applications

## Chapter 2. UAV Photogrammetry

---

while comprising both aircraft and other ground and communication components. It is used in legislation of many countries, e.g. in the European Aviation Safety Agency (EASA [2016]).

Apart from these terms, several more or less frequent abbreviations can be found in literature, e.g. Remotely Piloted Vehicle (RPV), Remotely Operated Aircraft (ROA) or Unmanned Vehicle Systems (UVS).

In the past, the development of UAVs was primarily motivated by military goals and applications but their use for civilian purpose has extremely increased over the last few years. Among all the civilian applications, photogrammetry is one of the most relevant. The potential of UAVs for geomatic tasks is obvious in terms of cost, handiness, and flexibility. The typical UAV fills a gap between aerial mapping of large areas and classical local terrestrial surveying (Eisenbeiß [2009]). Fig. 2.1 depicts the position of UAV photogrammetry among other remote sensing technologies.

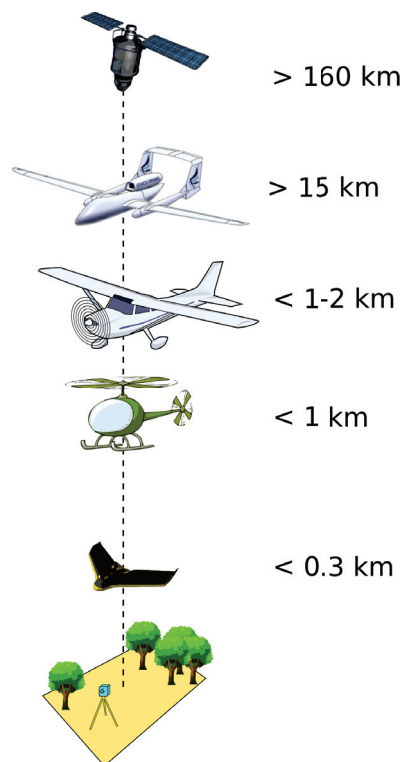


Figure 2.1 – Multiple types of remote sensing platforms. UAV technology complements existing techniques, fitting between large area imagery from satellites and high altitude platforms and manned aircraft and smaller coverage, but highly accurate terrestrial approaches.

Nowadays, UAVs have become a well established tool in photogrammetry and remote sensing. This is not surprising, as employing UAVs for aerial surveying is very cost-effective in comparison to hiring an aircraft with photogrammetry equipment. Thanks to their affordability they

have become a standard survey equipment of many organisations and individuals worldwide. Compared to other unmanned platforms, a photogrammetric platform is different due to its sensor equipment on-board. The platform is equipped with a photogrammetric measurement system, such as a small or medium size camera, thermal or infrared camera systems, airborne LiDAR (Light Detection and Ranging) system, or a combination thereof (Eisenbeiß [2009]). A brief review on the current sensor technology is given in Sec. 2.5

## 2.2 Work-flow and Products

### 2.2.1 Photogrammetric Work-flow

The work-flow for UAV mapping is similar to the work-flow of man-based aerial mapping systems. However, some elements are different or new. The following steps are chronologically ordered as the UAV photogrammetry project advances. Mission planning is further detailed in Chap. 3.

#### 1. Preparation and Terrain Recognition

- (a) Project feasibility analysis: a study of legislative restrictions and obtaining necessary permissions and exceptions.
- (b) Project parameter analysis: type of outputs, ground sampling distance (GSD) and the requirements on accuracy.
- (c) Terrain reconnaissance and a study of base maps and other geospatial data.
- (d) Consideration on the type of control, distribution and placement of GCPs and their stabilisation, signalisation, and survey.
- (e) Consideration of the type of the UAV platform, optical sensors and their preparation.

#### 2. Mission Planning

- (a) Determination of mission parameters: flight altitude, overlap, separation of lines.
- (b) Calculation of trajectory points.
- (c) Consideration of take-off and landing spots.
- (d) Selection of the best survey time as a function of satellite visibility.

#### 3. Field Work

- (a) Establishment and measurement of GCPs.
- (b) Flight execution and data collection.
- (c) Quality check: Upon landing, quick data verification, e.g. sufficiency of overlap, exposure of imagery, GNSS signal quality.

### 4. Data Processing and Products Generation

- (a) GNSS/IMU data processing.
- (b) Image exposure correction, generating image observations.
- (c) BA, dense matching, mesh generation, orthorectification.
- (d) Data export and visualisation.

#### 2.2.2 Mapping Products

Through the use of UAV photogrammetry, there are many products which can be extracted from the aerial data. These products include:

- Photos and video footage for periodic inspection and monitoring purposes,
- digital terrain/surface model (DTM/DSM),
- orthophotos,
- 3D models of objects, e.g. buildings,
- volumetric surveys,
- contour maps and planimetric features (roads, footprint of structures etc.).

Data collected from UAV platforms is characteristic for its high spatial resolution. Furthermore, the progress in fast and automatic processing enables collecting data with a high temporal resolution.

After image stitching and BA, the process of dense matching is used to densify the sparse point cloud generated from image tie-points. The resulting point cloud can be coloured and directly used for visualisation purposes or merged with a point cloud generated by other means, e.g. from a terrestrial LiDAR system. Standard methods such as triangulation and decimation are used to generate a DTM in a format of regular quadrangular network (GRID) or triangular irregular network (TIN). From the DTM, 3D models of buildings, roads etc. can be extracted. The DTM can be used, e.g. in calculation of mounds and excavations of earthworks by comparison of two digital terrain models. But more importantly, the DTM is necessary for creating orthophoto maps. Orthorectification is the process of removing the effects of an image perspective (tilt) and relief (terrain) effects for the purpose of creating a distortion free or georeferenced image. The resultant orthorectified image has a constant scale where the features are represented in their true positions. This allows for the accurate direct measurement of distances, angles, and areas (OSSIM [2016]).

The orthophotos and the DTM can be then analysed in the Geographic Information Systems (GIS) for various calculations of distance, volume, terrain slope, aspect analysis etc.

### 2.2.3 Data Processing Tools

Hardware development goes always hand in hand with software processing. Commercial UAV and MAV systems rely on the ability of post-processing tools to be able to process imagery from non-metric cameras with varying scale and often without a priori knowledge about camera positions and orientation. In addition, users operating UAVs for mapping purposes do not often possess necessary knowledge about photogrammetric data processing. All these attributes call upon sophisticated software that would have the ability to self-calibrate sensor and system parameters, have self-diagnostic tools, and robust processing work-flow.

Apart from professional photogrammetry tools, such as IMAGINE Photogrammetry (Hexagon Geospatial [2016]) or Inpho (Trimble [2016]), that are often inaccessible to many users due to their price and complexity, the current state-of-the-art UAV-dedicated mapping tools offer robust and effective processing even of large datasets. These tools allow users without a comprehensive knowledge of photogrammetry to turn imagery into 3D models, orthophotos, and other products mentioned earlier. The currently popular commercial software is, e.g. Agisoft PhotoScan (Agisoft [2014]), Pix4D Mapper (Pix4D SA [2016]), DroneDeploy [2016] or Drone Mapper [2016], to name a few. Furthermore, there are also tools on the market that were originally dedicated to aerial photogrammetry from manned platforms and satellites and now apply their existing work-flow to UAVs. Up-to-date systems are developed by, e.g. Icaros [2016], SimActive [2016], or Esri [2016].

The open-source community frequently relies on structure-from-motion (SFM) algorithms, such as Bundler (Snavely et al. [2008]) or a complete solution provided by e.g. MicMac (IGN France [2016]).

A frequent attribute of the UAV-oriented processing softwares is the lack of incorporation of system calibration parameters (lever-arm, boresight) as well as additional aerial position and attitude observations.

## 2.3 Regulations of UAV Platforms

As the UAV technology becomes more advanced, more approachable, and more affordable, the civil aviation institutions of many countries are working on defining proper rules and regulations to increase safety of UAV operations and to include them into the common airspace. The goal is to have a regulatory system that is as uniform as possible across countries. Nevertheless, each country adopts its own regulations and procedures of granting permissions for UAV operators. The common restrictions are as follows:

- Maximal take-off weight including additional equipment on-board,
- maximal flight height above ground level (AGL),
- flight in line of sight without artificial vision enhancements (binoculars, first person view (FPV)),
- use for hobby, research, or commercial purposes,

## Chapter 2. UAV Photogrammetry

---

- day-time operations,
- no-fly zones and restricted areas.

No-fly zones are typically created and enforced by the governing body and can include:

- **Controlled airspace** - aerodromes and airports
- **Military objects** - aerodromes, buildings, and camps,
- **Restricted areas** - prisons and power plants,
- **Prohibited areas** - government buildings,
- **Others** - national parks and urban areas in certain countries.

For instance, Switzerland constitutes a unique ecosystem of drone manufactures and users enabled by a favourable situation of the current legislation: Small UAVs under 30 kg can be operated below 150 m flying height (300 m outside controlled zones) within a line-of-sight and without need for individual permission to fly. This applies to all types of use including commercial, hobby, or research. Moreover, platforms with a take-off weight below 500 g are defined as toys and are allowed to be flown anywhere without any restriction (FOCA [2017]). On the contrary, the FAA (Federal Aviation Administration [2016]) issues certificates for UAS commercial and research operators. A person operating a small UAS must either hold a remote pilot airman certificate with a small UAS rating or be under the direct supervision of a person who does hold a remote pilot certificate (remote pilot in command). Other restrictions comply with the general operation rules including, e.g. flying in visual line of sight, maximal take-off weight of 25 kg, or daylight-only operations.

A third example concerns France. French DGAC established a thorough set of rules for drones operations (DGAC [2016]). Every operator must possess a certification to fly an UAV and must be registered together with the platform, provided it is certified to operate in one of the four scenarios illustrated in Fig. 2.2. Additionally, there are several categories of UAVs dividing the platforms by weight and type of work they are used for.

### 2.4 Platforms and Categories

This section reviews some of the existing commercial UAV platforms used for photogrammetry. In general, UAVs can be classified by many parameters but often it is its weight, Tab. 2.1. Weight is often the determining parameter when it comes to regulations by aviation agencies and is usually limited to 25 or 30 kg for a ready-to-fly system. The UAVs used for civilian mapping purposes usually fall into the Micro and Mini categories.

According to the platform construction, platforms can be divided into lighter-than-air and heavier-than-air or rotary-wing and fixed-wing. The majority of systems has some kind of











	Max. take-off weight	Max. altitude	Max. horizontal distance	Urban areas	Visual line of sight
<b>S1</b>	25 kg	↑ 150 m	← 100 m →		
<b>S2</b>	25 kg	↑ 50 m	← 1000 m →		
<b>S3</b>	4 kg	↑ 150 m	← 100 m →		
<b>S4</b>	2 kg	↑ 150 m	unlimited		

Figure 2.2 – Four scenarios to fly a drone in France, modified after (DIY Drones [2014]).

	Mass [kg]	Range [km]	Flight Alt. [m]	Endurance [h]
Micro	<5	<10	250	1
Mini	<20/25	<10	500	<2
Close-range	25-150	10-30	3000	2-4
Short-range	50-250	30-70	3000	3-6
Medium-range	150-500	70-200	5000	6-10

Table 2.1 – UAV classification, adopted after Blyenburgh [2008]

a propulsion system but there are also certain systems that are non-powered, e.g. kites or balloons. A detailed overview of current mapping platforms of the MAV category is in Appendix A in Tab. A.1. In the following sections, only the civilian MAVs deployed for remote sensing applications will be discussed.

UAV platforms come in many shapes and sizes. Each of these have their own unique advantages and disadvantages. In general, when selecting a drone for mapping purposes, the following criteria have to be considered:

- **Endurance:** Mapping of small areas and close-range photogrammetry or aerial mapping of large areas. How long and how far it can fly.
- **Payload capacity:** Take-off weight vs. useful payload capacity. How much weight it can carry. Weight limits given by national regulations and laws.
- **Type of equipment:** Vibration or EMI<sup>1</sup> sensitive equipment and types of photogrammetric sensors on-board.
- **Take-off and landing:** Consideration of available free space for a safe take-off and landing of a fixed-wing drone.

<sup>1</sup>Electromagnetic Interference, further discussed in Chap. 5.

- **Cost:** What the initial and service costs are and the overall profitability given the platform's lifespan.
- **Easiness of use:** How easy a mission planning and flying are, and whether the flying in manual mode is necessary or not.

### 2.4.1 Fixed-wing Platforms

Fixed-wing aircrafts are characterised by a simple structure and efficient aerodynamics. These attributes in turn provide the advantage of long-flight durations compared to the other platforms. Another advantage is the capability of gliding with no power. In case of an engine failure or battery depletion, the drone is still controllable automatically or manually and can land safely. However, limitations to fixed-wing platforms are imposed by the take-off and landing procedures. The take-off can be carried out either from hand (usually the case for platforms with a total weight below 3 kg), from a launcher (catapult), or using a runway. Furthermore, also the landing requires relatively large and obstacle-free space. The most common ways of landing are a belly or parachute landing.

Two examples are given for this category of MAVs in Fig. 2.3. These platforms represent the very few MAVs equipped with a RTK (Real Time Kinematic) GNSS receiver. The Mavinci Sirius Pro depicted in Fig. 2.3a employs the very same foam structure as one of the MAV presented in this research. More details are provided in Chap. 5.

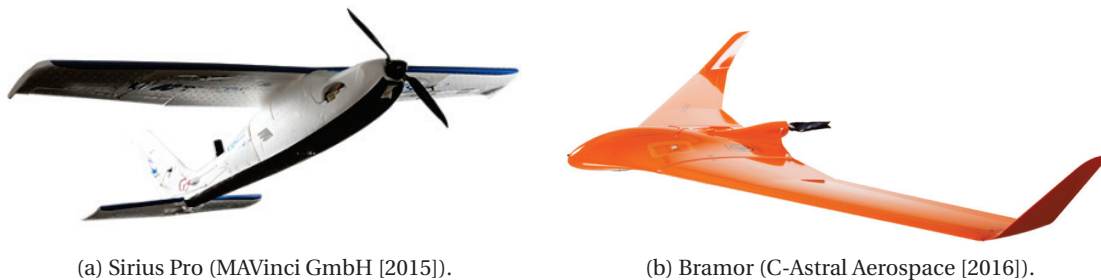


Figure 2.3 – Fixed-wing MAVs with GNSS RTK capability.

### 2.4.2 Multirotor Platforms and Helicopters

Rotary-wing aircrafts involve greater mechanical complexity, which translates generally into lower speed and shorter flight range. A rotary-wing aircraft can be a single-rotor helicopter or multirotory platforms sometimes called multicopter or as an acronym of the number of rotors employed: quadcopter (4 rotors), hexacopter (6 rotors) etc. Their advantages are their ability for Vertical Take-off and Landing (VTOL) and their capacity to hover and perform agile manoeuvring. This makes rotary-wing UAVs well suited to applications like

facility inspections, close-range photogrammetry, or 3D modelling which require manoeuvring around tight spaces and the ability to maintain visual on a single target for extended periods. Rotary-wings also facilitate greater flexibility with the payloads that they can deploy. The downside of multirotors is their limited endurance and speed, making them unsuitable for a large-scale aerial mapping, long-distance inspection of objects, such as pipelines, or roads and power lines monitoring.

Unlike the multirotor platforms, single-rotor helicopters have the benefit of much greater efficiency. Furthermore, they can be powered by a gas engine to achieve longer endurance. Nevertheless, the downsides are their mechanical complexity, cost, vibration, and also the potential danger posed by their large spinning blades.

Price-wise, multirotors are more affordable than any other platforms and user-friendly when it comes to the easiness of handling. In this respect, they are less demanding than, e.g. fixed-wing platforms despite their higher mechanical complexity.

From the stability point of view, rotary drones do not have the naturally built-in aerodynamic stability of their fixed-wing counterparts. To ensure a stable flight, they require a highly advanced autopilot to continually compensate attitude variations by changing rotation speed of the propellers. These changes are very sudden and require a highly optimised speed controller, motor and propeller setup. Fig. 2.4 provides an example of two multirotor MAVs deployed for inspection and close-range mapping tasks.

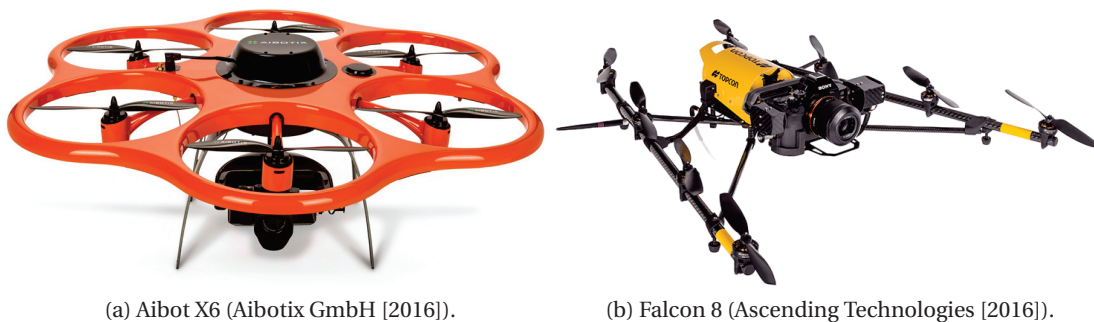


Figure 2.4 – Multirotor MAVs dedicated to mapping and inspection tasks.

### 2.4.3 Airships and Other Platforms

Airships or blimps come in various sizes, ranging from miniature systems that can be equipped with a small camera to large systems with laser scanners and medium-format cameras. Platforms lighter than air are inflated with helium rather than hydrogen due to its flammability. Platforms can be radio-controlled, autonomous or tethered. Operations with the latter do not require any specific authorisation because of the physical connection to the ground. The advantage of these platforms lies in their stability, long endurance, and safety. On the other hand, they are sensitive to wind and their cost and operation expenses are high, Fig. 2.5a.

Kites might not be as versatile as other platforms but they are very inexpensive and easy to

## Chapter 2. UAV Photogrammetry

---

use. They can be deployed for small photogrammetry tasks including 3D modelling of, e.g. archaeological sites or facades documentation or as a complementary source of images to ground imagery, Fig. 2.5b.

A relatively new category is comprised by platforms with vertical take-off and landing capabilities and yet capable of an efficient long-range flight in transition to a fixed-wing mode. These platforms benefit from both VTOL and fixed-wing concepts at the cost of being mechanically complex, Fig. 2.6.



(a) Airship with a remote sensing payload.



(b) A kite with a camera gimbal. (FiducialMark [2016]).

Figure 2.5 – Less conventional mapping platforms.



Figure 2.6 – Fixed-wing UAV with VTOL capabilities Songbird (Aerolution GmbH [2016]). Depending on the payload, this UAV fits into MAV or Mini UAV categories.

## 2.5 Optical Sensors

The primary function of an aerial platform is to collect high quality remote sensing data in order to obtain detailed mapping products. Achieving the maximal level of detail requires using high quality camera sensors and optics that are available on the consumer market. In general, optical sensors are divided into passive and active systems. Passive sensors are, e.g. digital cameras whereas active sensors are represented by laser scanners (LiDAR) or radars. The following section reviews some of the basic active and passive sensor characteristics. The physical characteristics of the presented sensors (plus others used in the context of MAV

remote sensing) are provided in Appendix A in Tab. A.2.

### 2.5.1 Passive Sensors

Passive optical sensors detect natural energy (radiation) that is emitted or reflected by the object or scene observed. Reflected sunlight is the source of radiation measured by passive optical sensors (NASA Earth data [2016]). Sensors in this category can be further divided by the physical construction of the sensor to frame vs. linear sensors or by frequency of electromagnetic spectrum they sense. Most passive systems used in MAVs operate in the visible, infrared, or thermal infrared spectra.

A camera sensing in visible spectrum is sensitive between 350 nm to 720 nm and is capable of detecting the red, green and blue (RGB) channels of visible light. Visible imagery is ideal for a wide range of applications including, e.g. surveying, archaeology, construction, or mining. Multispectral and hyperspectral sensors are capable of sensing in many (up to hundreds) narrow spectral bands ranging from 350 nm to 2500 nm. They can therefore capture much more information that is invisible to human eye or to a RGB sensor. The data can be then interpreted in so-called false colours to provide information about the condition of vegetation, mineral composition of archaeological sites, or expected crop yields.

#### Frame Sensors

Nowadays, there are many sensors on the market to choose from that are suitable for the use in MAVs, varying in size, weight, optical quality, and cost. However, these cameras are usually not designed for photogrammetric tasks and therefore, there is a fundamental need for their modification and calibration, Fig. 2.7a. Nevertheless, with the recent popularity of UAVs for mapping applications, dedicated mapping sensors appear in the research communities (Martin et al. [2014], Kraft et al. [2016]) and on the market (senseFly [2015a], Phase One [2016]). An example is given in Fig. 2.7b.

Multispectral and hyperspectral frame cameras used on MAVs work on two basic principles. The number of spectral bands is determined either by dedicated spectral filters inside the camera for each pixel, i.e. spectral sensitivity is changing progressively in the sensor, or the camera is composed of several independent sensors for each spectral band. Two examples are given in Fig. 2.8.

From the geometrical and scene reconstruction point of view, frame cameras have a big advantage of producing 2D images. This means that image matching techniques can be used for detecting corresponding points between images allowing for 3D scene reconstruction without the support of a GNSS/IMU system.

There are two types of sensors in these cameras: CCD (Charge-coupled device) and CMOS (Complementary metal-oxide-semiconductor). CCD sensor captures light on the instant and then converts this signal from analogue to digital (A/D) and is further processed. CCD is a mature technology that is nowadays used mainly in special cameras, e.g for near infrared



(a) Fuji X-M1 camera employed on Mavinci Sirius Pro (Fujifilm Corporation [2017]).



(b) senseFly SODA (Sensor Optimized for Drone Applications) RGB camera employed on eBee Plus (senseFly [2015a]).

Figure 2.7 – Frame RGB cameras (not to scale).



(a) Parrot Sequoia multispectral camera with four narrow-band cameras and one high-resolution RGB sensor (Parrot [2016]).



(b) Gamaya hyperspectral snapshot camera with up to 40 spectral bands (Gamaya SA [2017]).

Figure 2.8 – Frame multi- and hyper- spectral cameras (not to scale).

imaging or film cameras. On the contrary, the CMOS sensor has A/D converters for each sensor row. This allows sensing in higher frequencies.

The light can be captured line after line (rolling shutter) or at once (global shutter). The advantage of CMOS over CCD is its lower consumption, lower fabrication cost, and better efficiency. A majority of mass-market cameras is equipped with CMOS sensors. Nevertheless, large-frame mapping cameras employ such sensor technology too (Leica Geosystems [2017]). As for the shutter technology, the global shutter allows exposing the sensor at once. The advantages are obvious in terms of image geometry due to the object or camera movement during exposure. Mechanical global shutters are "central shutters" that are located inside the lens. Central shutters are found in consumer cameras with non-removable lenses or professional medium-format cameras. Electronic global shutters are often employed in industrial cameras. The global shutter can operate with both sensor technologies, but a majority of CMOS based cameras employs the rolling shutter.

The rolling shutter is where a line or a group of lines are recorded sequentially, vertically, or horizontally. In other words, not all parts of the image of a scene are recorded at exactly the same moment (MVP [2009]). The rolling shutter can be either mechanical or electronic. Shutter technology should be considered in photogrammetry as it affects mapping accuracy if the mathematical camera model does not account for the change in position and attitude during the exposure time (Vautherin et al. [2016]).

### Linear Sensors

A linear sensor is composed of a single-sensor array. Sensors of this type are called "push-broom" and require motion to occur for 2D image construction, i.e. either the sensor flies above the field of view or the field of view moves beneath the sensor. Their advantage lies often in a higher resolution compared to frame sensors, but the main drawback is the need for a relative orientation between consecutive lines.

Unlike the frame imagery, stitching of captured lines need to be done with the support of GNSS/IMU sensors. The possibility of using correspondences between the lines is limited only to side overlapping areas. Therefore, ISO and DiSO are the main sensor orientation methods in the linear sensor imagery.

The use of linear sensor cameras is more frequent in the context of hyperspectral imagery. A dedicated diffraction prism splits light into individual spectral bands and a 2D image sensor captures each spectral band with a different sensor row. The resulting image has 1D spatial resolution and n-spectral bands. After orthorectification, these lines constitute the hyperspectral data cube. An example of the smallest pushbroom hyperspectral camera is in Fig. 2.9. This camera is designed for UAV carriers. It captures 670 spectral bands and its weight of 500 g (without a lens) makes it suitable even for MAV applications.

### 2.5.2 Active Sensors

Active sensors provide their own source of energy to illuminate the objects they observe. An active sensor emits radiation in the direction of the target to be investigated. The sensor then detects and measures the radiation that is reflected or backscattered from the target (NASA Earth data [2016]). Although active sensors are not photogrammetric sensors, they are part of remote sensing instruments and as such are often deployed on UAVs. Optical range sensors, such as pulsed (Time-of-Flight), phase-shift, or triangulation-based directly measure and record ranges and register them with internal sensor parameters on a reference time scale. These sensors are, e.g. LiDAR or SAR (Synthetic Aperture Radar) (Remondino [2011]). LiDAR systems bring many advantages to some types of mapping projects, such as those concerned with forestry or mining. They can operate in environment with lower visibility and can penetrate certain surfaces, e.g. snow, vegetation thanks to the multi-echo signals that broaden the acquired information.

Unlike airborne photogrammetry, where the georeferencing of the data (images) can be established a posteriori by the means of GCPs, active sensors mostly depend on direct georeferenc-

ing for sensor orientation and coordinate computation. The need for accurate GNSS/IMU sensors therefore limits their deployment on the MAVs that are equipped with low accuracy MEMS (Micro-Electro-Mechanical System) inertial sensors. An example of LiDAR sensor is given in Fig. 2.10. Such sensor is often used for obstacle avoidance and close-range UAV mapping.



Figure 2.9 – Headwall Nano-Hyperspec camera (Headwall [2016]).



Figure 2.10 – Velodyne VLP-16 LiDAR sensor (Velodyne LiDAR [2016]).

## 2.6 Orientation Methods

The task of sensor orientation is the determination of parameters of the exterior orientation (EO) of a sensor at the time of recording and the restitution of the scene from the image data. The determination of EO parameters is a fundamental condition for the use of any kind of imagery in a photogrammetric way. These parameters define the position and orientation (also called attitude) of an image space coordinate system in the ground space coordinate system. The six EO parameters are:

- $X_0, Y_0, Z_0$ : object coordinates of the centre of projection.
- $\omega, \varphi, \kappa$ : image rotation in the object coordinate system.

The EO parameters may either be deduced indirectly from the known GCPs, mechanically (historical method - stereocomparator), by measuring them directly with navigation sensors – GNSS/IMU, or in combination of thereof (Skaloud and Legat [2008]). The need for GCPs, tie-point matching, or AT is significantly reduced with ISO and DiSO (Reese and Heipke [2006]). A schematic Fig. 2.11 depicts the principle of the three main sensor orientation methods. The concurrent determination of exterior and interior orientation (IO) parameters is also



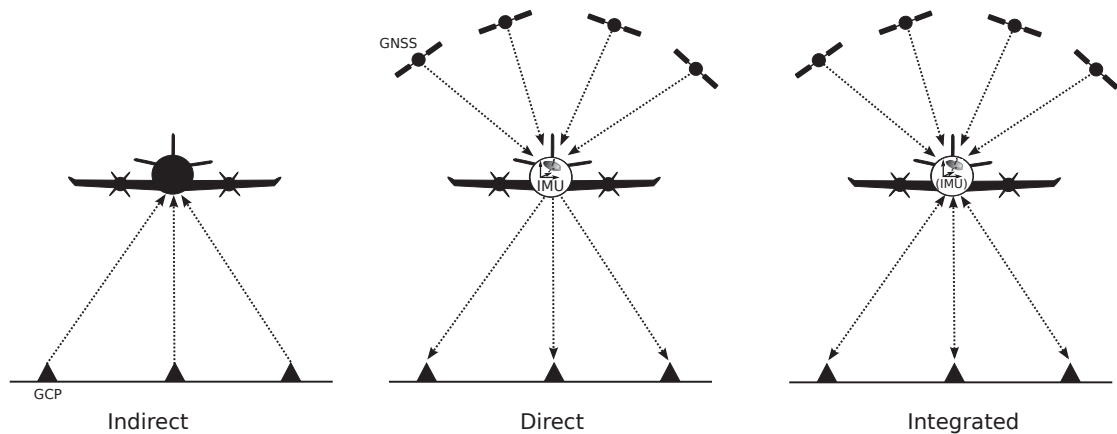


Figure 2.11 – Sensor orientation methods.

referred to as an orientation/calibration problem. The IO parameters define the internal geometry of a camera. The most important elements of IO include the following:

- Principal distance  $c$ ,
- coordinates of principal point  $x_0, y_0$ ,
- additional parameters of geometric distortion, i.e. symmetric radial distortions and asymmetric distortions caused by lens decentering as discussed in Sec. 4.3.

The list of elements varies with different types of cameras, e.g. airborne metric digital/film cameras vs. consumer grade cameras. Among other parameters could be, e.g. axis scale, sensor non-flatness, sensor dimensions, fiducial marks, spherical aberration, or astigmatism.

### 2.6.1 Coordinate frames

As georeferencing of airborne imagery involves GNSS and inertial measurements, computing platforms trajectory and/or sensor exterior orientation require the use of a global reference frame and a series of intermediate frames. An overview of the principal frames involved in navigation and photogrammetry, respectively, is provided in Tab. 2.2.

#### Image coordinate system ( $c'$ )

A 2D instrumental frame of the camera sensor is defined by the principal axis of the sensor. Image coordinates are used to describe positions on the sensor plane. Image coordinate units are given in millimetres or microns.

## Chapter 2. UAV Photogrammetry

ID	Frame Name	Description
c'	Image coordinate system	Two-dimensional coordinate system occurring on the image plane, defined by the principal axes of the sensor.
c	Camera frame	Identical to image coordinate system with a third axis ( $z$ ).
b	Body frame	Instrumental frame materialised by the triad of accelerometers in an IMU.
e	ECEF	Earth-centred Earth-fixed frame. The origin is the geocenter of Earth, the X-axis points towards the Greenwich meridian and the Z-axis is the mean direction of Earth rotation axis. The Y-axis is completed by the right-handed Cartesian system.
l	Local level frame	With coordinate sequence East-North-Up (ENU) and North-East-Down (NED), respectively. This frame is tangent to the global earth ellipsoid.
m	Mapping frame	A global terrestrial reference frame together with horizontal map-projected coordinates Easting, Northing, and vertical ellipsoidal or gravimetric heights $h$ .

Table 2.2 – Overview of reference frames (adopted after Skaloud and Legat [2010], Schaer [2009]).

### Camera Frame (c)

An image space system that is identical with an image-coordinate system with a third axis ( $z$ ), which is the camera axis. The origin of the camera frame is defined at the perspective centre. Its  $x$ -axis and  $y$ -axis are parallel to the  $x$ -axis and  $y$ -axis of the image coordinate system. Camera frame is often used for specifying the system spatial offset (lever-arm) and is depicted in Fig. 2.12.

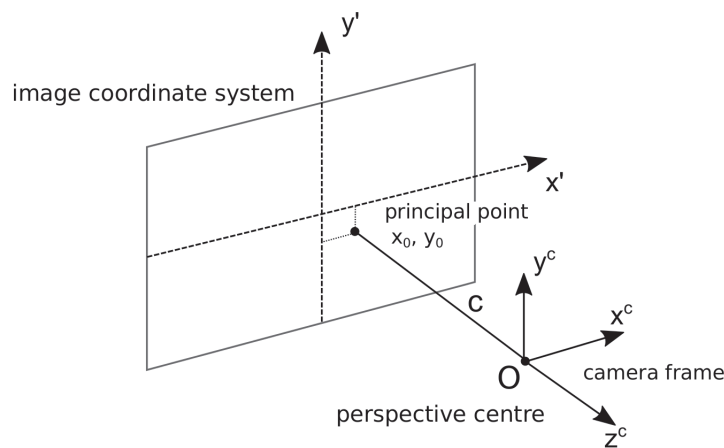


Figure 2.12 – Image coordinate system, camera frame and main elements of IO parameters.

### Body Frame (b)

The body-frame is represented by the axes of an IMU. The origin of the  $b$ -frame is physically located in the navigation centre of the IMU. The axes are materialised by the triad of accelerometers. This system is idealised in the sense that the navigation sensors are not perfectly aligned

in space and are not truly orthogonal. Normally, the  $b$ -frame axis approximately coincides with the principal axis of rotation of the carrier or can be rotated to them by a cardinal rotation. According to the general conventions, the axis and the rotations describing the 3D attitude are defined as follows: The  $x^b$ -axis is pointing forward along the fuselage, the  $y^b$ -axis points to the right and the  $z^b$ -axis points down. The associated parametrisation of attitude rotation by Euler angles is roll( $r$ ), pitch( $p$ ), and yaw( $y$ ). Respecting the aerospace attitude definitions (north-east-down), the corresponding rotation matrix from  $l$ -frame to the  $b$ -frame takes the following form:

$$\mathbf{R}_{l_{NED}^b}^b = \mathbf{R}_x(r)\mathbf{R}_y(p)\mathbf{R}_z(y) \quad (2.1)$$

where  $\mathbf{R}_x(r)$ ,  $\mathbf{R}_y(p)$  and  $\mathbf{R}_z(y)$  are defined as:

$$\begin{aligned} \mathbf{R}_x(r) &= \begin{pmatrix} 1 & 0 & 0 \\ 0 & \cos(r) & \sin(r) \\ 0 & -\sin(r) & \cos(r) \end{pmatrix} \\ \mathbf{R}_y(p) &= \begin{pmatrix} \cos(p) & 0 & -\sin(p) \\ 0 & 1 & 0 \\ \sin(p) & 0 & \cos(p) \end{pmatrix} \\ \mathbf{R}_z(y) &= \begin{pmatrix} \cos(y) & \sin(y) & 0 \\ -\sin(y) & \cos(y) & 0 \\ 0 & 0 & 1 \end{pmatrix} \end{aligned} \quad (2.2)$$

### ECEF Frame (e)

This frame rotates along with Earth. It is used for referencing the satellite orbits of GNSS systems. The outcome trajectory computation is primarily provided in this frame. A geocentric ellipsoid is normally attached to the ECEF frame which together with some other geophysical parameters define the world datum, such as WGS84. Coordinates in this frame can be either expressed as geocentric coordinates ( $x^e, y^e, z^e$ ), or as geographical coordinates: latitude  $\varphi$ , longitude  $\lambda$ , and ellipsoidal height  $h$ .

### Local Level Frame (l)

A local level frame represents the vehicle's position, attitude, and velocity when on or near the surface of Earth. A right-handed frame is referred to as ENU since its axes are aligned with the east, north, and up directions. A second right-handed system where the axes point to the north, east, and down direction is known as NED. The orientation of the l-frame with respect to the e-frame is changing with the position of the platform.

### Mapping Frame (m)

The basic implementation of such mapping frame is a local Cartesian tangent plane. The origin is defined as arbitrary position  $(\varphi_0, \lambda_0)$  on the ellipsoid. In this case the mapping frame substitutes the local level frame at a fixed point. In photogrammetry, the mapping frame usually takes form of a national coordinate system with a specific datum and projection.

### 2.6.2 Indirect Orientation

Nowadays, the most common orientation of the MAV imagery is done indirectly under a joint use of known GCPs and their corresponding image coordinates with many tie-points. GCPs are points on the mapped surface that can be identified in the imagery with known coordinates in object space/mapping frame. The coordinates of these points are derived by classical surveying methods, such as tachymetry, RTK GNSS survey, or from LiDAR point cloud. They can be signalled by artificial targets or by natural elements in the scene with, e.g. intersecting lines. Their size should be such that the measured point/centre of the target can be identified with a sub-pixel accuracy in the collected imagery.

Neighbourhood images are connected using advanced digital matching methods with hundreds of tie-points. For a block of images a sufficient forward and side overlap is essential (usually min. 60% and 30%). The object point coordinates, EO, IO, and additional parameters for each image in the image block can be estimated within a least-square adjustment known as bundle block adjustment. This approach is called aerial triangulation (AT) or automatic aerial triangulation (AAT). Thanks to computer vision techniques, a great number of tie-points can be detected in overlapping imagery. This allows re-estimating additional parameters, for instance the IO parameters, which are very often unstable in time (e.g. an influence of vibrations) on consumer grade cameras.

The observed exterior parameters from an autopilot are very inaccurate and enter only during the image pre-selection and/or serve as an initial approximation in the BA to ensure convergence. A problem occurs when sufficient number of the GCPs is not feasible or these are badly distributed. Furthermore, projects with demanding or homogeneous terrain surface are also not in favour of using indirect SO. The ability of resolving the EO parameters indirectly is therefore limited in such scenarios.

### 2.6.3 Direct Orientation

Direct georeferencing, also called direct sensor orientation, is able to directly relate the data collected by a remote sensing system to Earth by accurately measuring the geographic position and orientation of the sensor with navigation sensors (Mostafa et al. [2001]). By merging the GNSS and inertial navigation technologies, accurate position and orientation of the airborne imaging sensor can be determined directly with respect to Earth. The accuracy of such products depends not only on observation quality, but also on the initialisation, the trajectory profile e.g. dynamics, as well as on the system and sensor calibration.

The problem of determining exterior orientation parameters by direct observation of the camera position and attitude has been extensively researched in the past, e.g. in Colomina [1999], Skaloud [1999], Mostafa et al. [2001]. In principle, the following conditions must be met for the correct integration of position and attitude sensors (Skaloud [1999]):

1. The position and orientation offsets between a GNSS antenna, an IMU, and a sensor, i.e. a camera, as well as a laser scanner etc., must be determined.
2. These offsets must remain constant during each mission.
3. The time stamping of all observations must be achieved with sufficient accuracy.

To carry out these conditions, special attention has to be paid to the implementation of each system component and their mutual interconnection. Only a precise integration of all components ensures valuable results. The formulation of direct georeferencing can be expressed mathematically by the following Eq. 2.3 and is depicted in Fig. 2.13 (Schwarz et al. [1993]).

$$\mathbf{r}_i^m = \mathbf{r}_{GNSS/IMU}^m(t) + \mathbf{R}_b^m(t) \cdot [s_i \cdot \mathbf{R}_c^b \cdot \mathbf{r}_i^c(t) + \mathbf{a}^b] \quad (2.3)$$

where

$\mathbf{r}_i^m$	is the coordinate vector of point (i) in the mapping frame,
$\mathbf{r}_{GNSS/IMU}^m(t)$	is the vector containing the coordinates of the IMU centre in the m-frame, determined by the GNSS/IMU integration for a specific time epoch (t),
$\mathbf{R}_m^b$	is the attitude between the navigation sensor b-frame and the m-frame,
$s_i$	is the scale factor between the image and m-frame for a specific point (i),
$\mathbf{R}_c^b$	is the differential rotation (boresight) between the c-frame and b-frame,
$\mathbf{r}_i^c(t)$	is the coordinate vector of the point (i) in the c-frame (i.e., image coordinate),
$\mathbf{a}^b$	is the spatial offset (lever-arm) between IMU centre and camera perspective centre.

Although direct georeferencing in manned missions may seem to be a needed or an ideal approach to SO under many scenarios, e.g. corridor mapping, the main limiting factors can be overall summarised as a project size and required accuracy. For example, a very small project could actually be more expensive to perform using the direct georeferencing approach. There

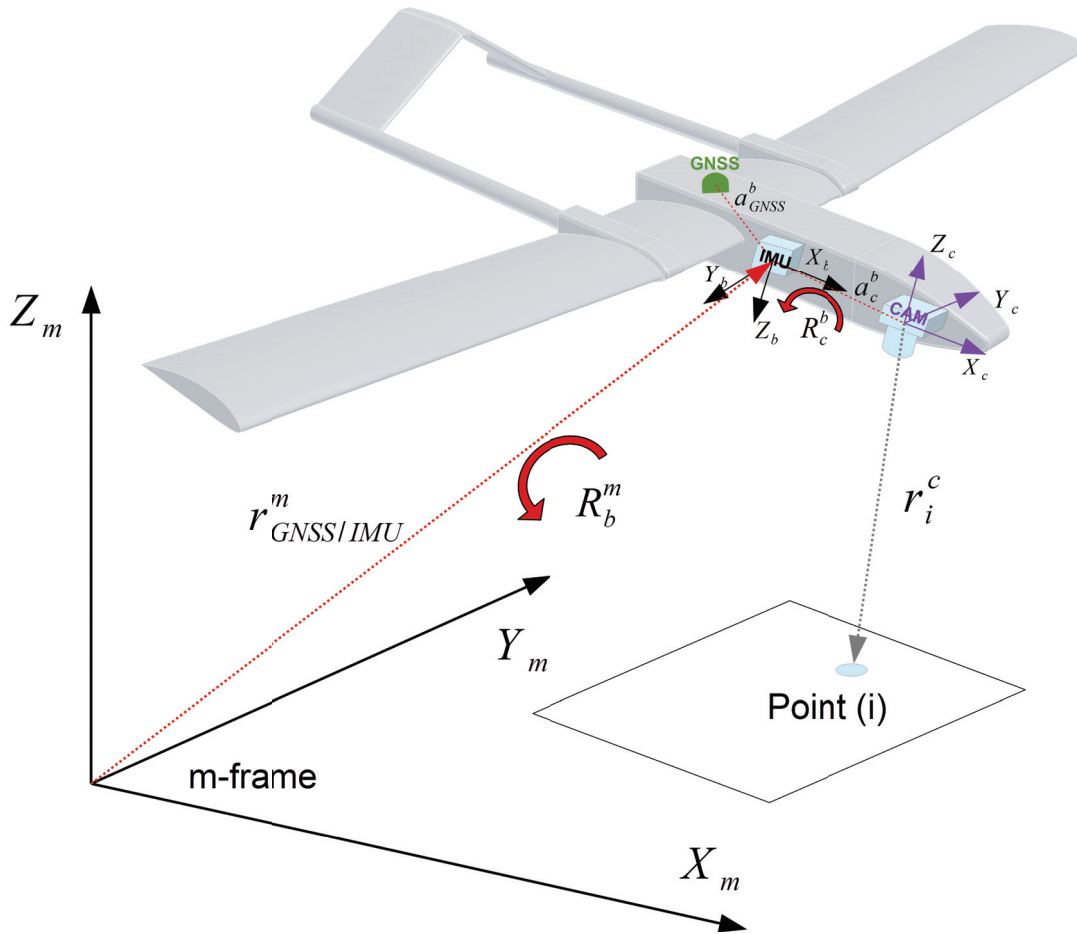


Figure 2.13 – The principle of direct georeferencing.

are certain fixed costs, including equipment as well as elaborate processing and calibration steps.

Nevertheless, the main limiting factor for MAVs remain the achievable accuracy with low-weight and low-cost IMUs, rather than the project size. In conclusion, the use of direct georeferencing in a mapping project can lead to substantial savings in both cost and time. The savings result from the elimination of aerotriangulation for the project, as well as the substantial elimination of GCPs within the project area.

#### 2.6.4 Integrated Orientation

Integrated sensor orientation, sometimes called assisted AT, benefits from aerial, image, and possible ground data. It is a robust and efficient method under proper conditions of sufficient image overlap. GNSS/IMU output for camera exposures serves as additional observations as well as initial values for BA in the AT. The measured control points serve as an optional control of the overall project quality and are also used to correct the systematic errors. Furthermore,

only a limited number of tie points in the overlapping area is needed (Ip et al. [2007]). Although the accuracy of directly measured EO parameters by MAVs may not be always high enough to perform DiSO, these observations can still considerably contribute either as initial parameters for BA, or in the tie-point matching process by reducing the computational time and number of errors. By using sufficiently accurate aerial positions as additional observations, the need for GCPs can be eliminated if a geometrically stable block of tie-points can be formed (Cramer [2001], Heipke et al. [2002], Jacobsen [2004]). Furthermore, by using an IMU, the orientation of the images can be determined directly. Therefore, good aerial control via the GNSS/IMU system can overcome the need for GCPs in all situations (Colomina [1999]).

ISO benefits from the high robustness when additional parameters (e.g. antenna offset, interior camera parameters or boresight matrix) can be self-calibrated under certain observability conditions, whereas when performing DiSO, a proper calibration of the system and sensors has to be done beforehand. The evolution of sensor quality has made ISO an important alternative to conventional AT since the end of the 1990's (Jacobsen [2004]). There are several different possibilities of combining indirect and direct georeferencing, namely:

- GNSS/IMU results are used as additional observations within BA (most common),
- use AT data as additional updates of the Kalman filter (Skaloud and Schaer [2003]),
- use of raw inertial and image observations within a common adjustment of a dynamic network (Colomina and Blázquez [2005], Rouzaud and Skaloud [2011]).

### Mapping in National Projection Systems

Although the mathematical model of DiSO is made in a Cartesian frame, it is common to use a conformal mapping projection for the object space coordinate system to reduce the computation cost of generating output maps (Legat [2006]). A simple transformation of EO parameters to a national system may introduce errors for several reasons. Firstly, due to the curvature of Earth, secondly, due to the different scales in plane and height, and thirdly, due to the variations of the scale in plane, i.e. big differences in terrain relief (Ressl [2002]).

This problem is often not correctly addressed even in manned mapping systems. Similarly to DiSO, ISO projects are also influenced by the use of projection systems. However, the employment of sufficient number of GCPs and additional parameters for modelling of systematic errors ensures certain mitigation so the aforementioned problems remain unnoticed.

Several solutions have been proposed to address this issue or substantially mitigate its influence on mapping accuracy. The most accurate method is by formulating the collinearity condition in projection or by reconstructing the geometry in a local-level, Cartesian coordinate system defined at the centre of the scene, and subsequently, by transforming the object space coordinate system to a projected mapping frame using geodetic methods. The other possibility is a transformation of “virtual” GCPs obtained from partial scene restitution in a Cartesian frame and last, a transformation of the EO parameters prior to the restitution with certain corrections (Legat [2006], Skaloud and Legat [2008]).

These effects are usually ignored in UAV photogrammetry for obvious reasons:

- The mapped areas are rather small in size, e.g.  $< 1 \text{ km}^2$ ,
- the terrain variations are usually not so significant over small areas,
- the accuracy of directly measured EO parameters is often low,
- DiSO as a mode of operation is not common with UAVs,
- absolute altitude is low, i.e.  $< 2000 \text{ m}$ .

### 2.7 Evolution of Orientation Methods on UAVs

UAV photogrammetry is not a new method although the usage was limited to hobby projects taking aerial photographs from kites, balloons and primitive remote-controlled toys until the mid 2000's when dedicated UAV platforms appeared on the market (Eisenbeiß [2009]). Nowadays, there are dozens of various platforms available with specific attributes making the mapping task unprecedentedly easy and affordable. Despite the significant evolution from amateurs hobby platforms to professional working tools, the prevailing concept of sensor orientation has not changed. The latter is based on indirect SO, as it used to be in the early days of photogrammetry. The following section reviews the evolution of orientation concepts in the context of UAV photogrammetry.

#### 2.7.1 Indirect SO on MAVs

The majority of today's MAV platforms is equipped only with a single frequency GNSS receiver without the precise phase observations and a low-cost MEMS IMU. Depending on the geometry of satellites, this enables position determination at a level of several meters provided that the conditions are optimal. That is indeed insufficient for many applications. Furthermore, the attribution of the image-acquisition time in a global (i.e. UTC and/or GNSS time scale) is imprecise ( $\sigma_t > 0.001 - 0.01 \text{ s}$ ) and the quality of the employed inertial sensor (often part of a low-cost autopilot unit) is not sufficient for accurate attitude determination (i.e.  $\sigma_{rpy} \gg 0.01 - 0.1 \text{ deg}$ ). Although in principle every autonomous MAV system is equipped with all the necessary sensors to perform an automated waypoint flight, such as a GNSS receiver and an IMU, these are insufficiently accurate for ISO or DiSO in most of the remote sensing or surveying applications (Yoo and Ahn [2003]).

In general, the problem of current MAV systems is the lack of precise time, position, velocity, and mainly attitude control (tPVA) which improves the consistency of the geometrical quality. The indirect approach faces up to problems mainly under two situations: a single strip corridor or an area with homogeneous surface. Although single strip configurations are theoretically possible, the requirement for the number and distribution of GCPs makes them



impractical. Overall, these requirements limit firstly the mapping productivity of MAVs, e.g. due to the establishment of a large number of GCPs, and secondly, due to the high dependency on automatic image observations.

### 2.7.2 DiSO and ISO on MAVs

Despite the market dominance of indirect SO in mapping applications, ISO and DiSO techniques appear in research communities. The first attempts to perform ISO and DiSO with UAVs are dated almost ten years ago (Eugster and Nebiker [2008]). This study describes direct georeferencing of a mini UAV in an application context. The authors conclude that the overall accuracy in the object space of 6 to 15 m for flying heights of up to 300 m is achievable and sufficient for many applications with the advantage of providing real-time georeferencing.

A complete DiSO work-flow is presented in Perry [2009]. A customised UAV is equipped with off-the-shelf components and calibrated for system and sensor parameters. The presented development is focused on the ISO, and the accuracy of the employed mapping system is assessed by comparing an orthomosaic georeferenced by GCPs with an orthomosaic georeferenced by GNSS/IMU observations. The achieved accuracy lies in the level of several meters. A study Rieke et al. [2011] presents an implementation of a RTK-enabled GNSS positioning system on the Microdrones md4-200 UAV. The initial study describes the hardware implementation of this positioning method. Its work-flow with the case study are presented. The precision of 90 cm (without a RTK service) measured at a fixed control point in non-flying mode is described. Similarly, also Bäumker and Przybilla [2011] investigate the accuracy of the aerial position data of Mikrokopter system with the conclusion that navigation components of the autopilot unit meet the precision of C/A-Code GPS accuracy. A follow-up of the latter study is presented in Bäumker et al. [2013], where the authors present the first results from an upgraded GNSS/IMU system with RTK capability.

A study by Pfeifer et al. [2012] shows the capability of inbuilt navigation components of the Mikrokopter quadrocopter. The investigated work-flow describes the camera modification, camera lag estimation and GNSS/IMU combination resulting in direct position and attitude estimation. The evaluation is done by comparing the measured values with the EO parameters obtained from a custom BA software. The differences between estimated and measured 3D position and attitude have a mean value of 1.8 m and 1.92 deg in roll/pitch and 18 deg in yaw, respectively. Images were taken in a position hold mode and thus, the correctness of the camera lag estimation and time synchronisation cannot be confirmed. The planar calibration field comprised 24 points and the camera was restricted only to nadir viewing. Hence the BA does not assure uncorrelated IO/EO parameters.

In addition to classical GNSS/IMU method, an alternative way of determining sensor positions using tracking devices is studied in Bláha et al. [2011]. This article concentrates on the position estimation by tracking a multicopter with a total station and compares this reference with the solution from the autopilot's GNSS receiver. This tachymetry solution is precise in terms of positioning, but is very limited in range. Another limit is the speed of the tracking device

which makes this method applicable only to VTOL systems.

Recent (after 2014) progress in the field of miniaturisation and price drop of GNSS receivers and antennae allowed creation of the first commercial platforms with embedded systems offering at least accurate aerial position control. With contemporary cutting edge technologies presented by, e.g. senseFly and Mavinci in the case of fixed-wing platforms and Aibotix in multicopters (senseFly [2015a], MAVinci GmbH [2015], Aibotix GmbH [2016]), the users can benefit from geodetic grade GNSS RTK receivers closely integrated into the platform's processing work-flow as presented, e.g. in the following studies: Gerke and Przybilla [2016] and Survey Group [2015]. Although such systems allow accurate aerial position control, they are often limited to RTK positioning solution. Furthermore, the quality of the employed inertial sensors, often part of low-cost autopilot units, is not sufficient for attitude determination better than  $0.5 - 1^\circ$ .

Recently, improvements in miniaturisation and mass-production have enabled the use of high quality MEMS IMUs and multi-frequency GNSS receivers in a combination. Such systems offer GNSS/IMU integrated solution in a small package, often bundled with processing software (Mian et al. [2015]).

Despite the fact that the majority of the presented systems deliver reasonable accuracy, moving from post-processing to real-time mapping adds significant challenges. A study by Eling et al. [2013] discusses the development of a custom VTOL platform with stereo-vision cameras and a GNSS/IMU sensor board running tightly coupled filtering that provides accurate real-time position and attitude solutions. In several follow-up studies the authors continue with the development and present cm-level accuracy in ISO configuration (Eling et al. [2014], Eling et al. [2015]). These are, however, performed under ideal conditions, i.e. strong block configurations with high redundancy in image observations and under small flight dynamics.

Despite the amount of published studies dealing with georeferencing and direct georeferencing in particular, to the best of the author's knowledge, none of them actually performs direct georeferencing with the absence of automatic tie-points. By the same token, most of the studies do not assess the contribution and accuracy of the measured attitude on mapping accuracy. Besides, VTOL platforms are preferred as carriers. In this regard, the precision of time synchronisation is less demanding.

### 2.8 Basic Geometry and Accuracy Relations

The following section provides basic relations to offer some insight into the theoretical quality of UAV mapping in relation to simple geometry. Similarly to geodetic surveying, the accuracy delivered by photogrammetry depends on the accuracy of the individual measures and their geometrical relations. When starting a mapping project, the considerations are: what accuracy (absolute/relative) for which GSD is desirable, and the choice of equipment and effort (technical + labour) required to achieve it. In general, stepping up from meter- to decimetre-level accuracy requires less effort than going from decimetre- to centimetre- level or even

below. Mapping accuracy is influenced by the following aspects:

- Quality of automatic image observations
  - sensor and lens types and quality
  - light/exposure conditions, image sharpness etc.
  - surface texture
  - distribution of tie-points points
- Type of control
  - number and distribution of GCPs together with their observability
  - availability and accuracy of aerial control
- Geometry of a scene
- Elimination of systematic errors
  - sensor models and calibration
  - system models and calibration
  - synchronization quality
- Processing and realistic stochastic modelling

### 2.8.1 Image Measurement

Image observations constitute a crucial prerequisite for photogrammetric photo reconstruction. In the classical setup, the number of tie-points was intentionally kept as small as tolerable, since selecting and measuring tie-points manually is very time-consuming and costly. With the computer vision techniques, obtaining hundreds and thousands of tie-points, no real additional effort is required, as the images are in direct access and the speed of measuring allows to acquire as many points as necessary, enabling to exploit the resulting redundancy for increasing accuracy and stability (Förstner [1995]).

Image matching is an automatic establishment of correspondences (identification and measurement) between two or more images, using natural points or targets. Image matching is a key component of many tasks in photogrammetry, and image analysis (Grün [2012]). It was first introduced in the early 1950s and has been an issue of research ever since. Fast progress was further supplemented by increasing computational resources making the task of detection very fast (<1 h) even for large datasets (>1000 images). These techniques also boosted the rapid utilisation of UAVs in photogrammetry (Remondino [2016]). The huge network redundancy due to a large number of observations allowed users to employ sensors not originally designed for mapping with all their imperfections and drawbacks.

The identification of homologous points, i. e. image points (locatable image feature) referring

to the same object point in the images now becomes the critical step. There are several criteria for selecting these points in images (Förstner [1995]):

1. Points should lie in as many overlapping images as possible,
2. points should cover the images as uniformly as possible,
3. points should be distinct for supporting efficient matching,
4. points should possibly be suited for multi-image matching,
5. the position of the points should be accurate enough for the adjustment process.

### Image Features Detection, Description and Matching

Feature detection, description, and matching are essential components of various computer vision applications. Hence, they have received a considerable attention in the last decades. Several feature detectors and descriptors have been proposed in the literature with a variety of definitions for what kind of points in an image are potentially interesting.

- **Feature detection:** Feature (keypoint) detection is a low-level image processing operation. It is usually performed as the first operation on an image and examines every pixel to see if there is a feature present at that pixel. The types of features are global (valid for the entire image, e.g. colour or shape) and local: points, corners, blobs, or ridges. Once features have been detected, a local image patch around the feature can be extracted. This extraction may involve quite a considerable amount of image processing. The result is known as a feature descriptor or feature vector.
- **Feature description:** It characterises the extracted features with some properties (scale, rotation, etc.) independently from any geometric transformation applied to the image. The characterisation is done with a variable number of elements computed with e.g. histogram of gradient location and orientation (Lowe [1999]), moment invariant (Gool et al. [1996]) or linear filter (Schaffalitzky and Zisserman [2002]). Some methods perform both detection and description, e.g. SIFT (Lowe [1999, 2004]), binary BRISK (Leutenegger et al. [2011]), SURF (Bay et al. [2006]), LDAHash (Strecha et al. [2012]), to name a few (Remondino [2016]).
- **Feature matching:** Once the descriptors are computed, they can be compared to find a relationship between images for performing matching/recognition tasks. The aim is to find the best correspondence between images by comparing the descriptors between keypoints (Hassaballah et al. [2016]).

### Challenges in Automatic Tie-point Generation

The current trend in UAV photogrammetry and computer vision is to extract a large number of tie-points and automatically orient the images. UAV data is characteristic by high scale variations, occlusion in vertical and horizontal view combinations, and sometimes even by illumination changes. These are particularly important in a close-range aerial mapping. Furthermore, the collected imagery is often processed without a priori information about positions and orientations. This mainly influences the matching speed.

In addition, UAV imagery frequently suffers from strong texture homogeneity (repetitive patterns of e.g. vegetation) or a complete lack of texture (water). In these cases, the methods of keypoint detection and description fail to deliver consistent and reliable tie-points.

#### 2.8.2 Influence of Image Measurements and Scene Geometry

One of the determining factors of expected accuracy is a photo scale. This scale is a ratio or a proportion between a distance on aerial images and a actual distance on the ground or land surface as expressed in Eq. 2.4. It is the same ratio as the distance between the object/ground to the camera perspective centre and the image principal point to the perspective centre.

$$s_p = \frac{c}{h} \quad (2.4)$$

where  $s_p$  is the photo scale,  $c$  is the principal distance and  $h$  is the flight height above mean ground level. Given the scale and sensor's physical dimensions, the ground sampling distance (GSD) can be calculated from Eq. 2.5 as depicted in Fig. 2.14. The GSD represents the distance between pixel centres measured on the ground. The GSD on a vertical aerial photography image is consistent for every pixel considering flat terrain and the pinhole camera model. The GSD can be expressed as follows:

$$GSD = \frac{p}{s_p} \quad (2.5)$$

where  $p$  is the sensor's pixel size, which is square for most digital frame cameras. The uncertainty in image measurement translates into an uncertainty in the direction of the ray that is projected through the perspective centre into the scene. Providing that the expected image measurement accuracy is  $\sigma_{x'}$ , the photo scale can be used to convert this accuracy into ground accuracy  $\sigma_{X,Y}$  in X and Y axis, respectively.

$$\sigma_{X,Y} = \frac{\sigma_{x'}}{s_p} \quad (2.6)$$

To predict depth accuracy, a simple case of stereo photogrammetry with two images is considered, Fig. 2.15.

$$\sigma_Z = \frac{\sigma_{x'}}{s_p} \cdot \frac{h}{b} \quad (2.7)$$

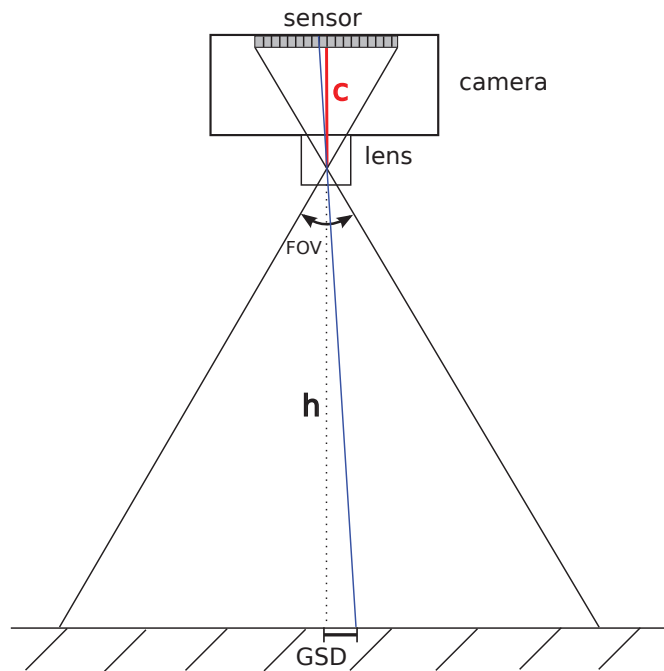


Figure 2.14 – Pinhole camera model and GSD calculation.

where  $b$  is the separation between two cameras (base). In addition, data collected with UAVs is typical for its high redundancy. Generated tie-points are often visible in multiple images (even  $>20$ ) and thus, the normal stereo pair becomes too pessimistic for 3D point accuracy estimation. In this case, the multi-stereo view provides a better way of accuracy estimation. This situation is illustrated in Fig. 2.16 on simulated data. The left scene shows a general stereo photogrammetry case where the object points are determined with poor precision due to errors in image observations. By adding a third image and creating a multi-stereo view as depicted in the right scene, it becomes apparent that the object points are estimated with a higher precision.

### 2.8.3 Ground Control Points

Distribution of GCPs in the mapping area plays a major role in a successful terrain reconstruction. Ideally, GCPs are placed evenly in the area of interest in a regular grid. Such distribution mitigates the influence of random errors in image observations as depicted in Fig. 2.17. The vertical accuracy is more affected in aerial photogrammetry. If no GCPs are used or placed in the boundaries of the mapped area, the resulting model will be tilted due to the accumulation of random errors. On the other hand, when the GCPs are well distributed, the final plane will be a better approximation of the optimal one. The horizontal accuracy of 3D object points is less affected due to overlapping imagery. In addition to classical GCPs, the geometry can be constrained by vertical or horizontal line features (Gerke [2011]). Nevertheless, placement of a large number of GCPs is time and labour intensive effort which may be difficult to realise

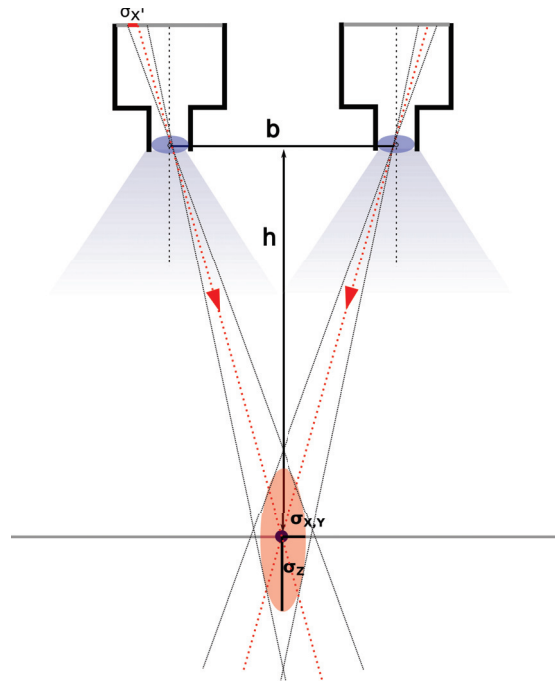


Figure 2.15 – Normal case of stereo photogrammetry.

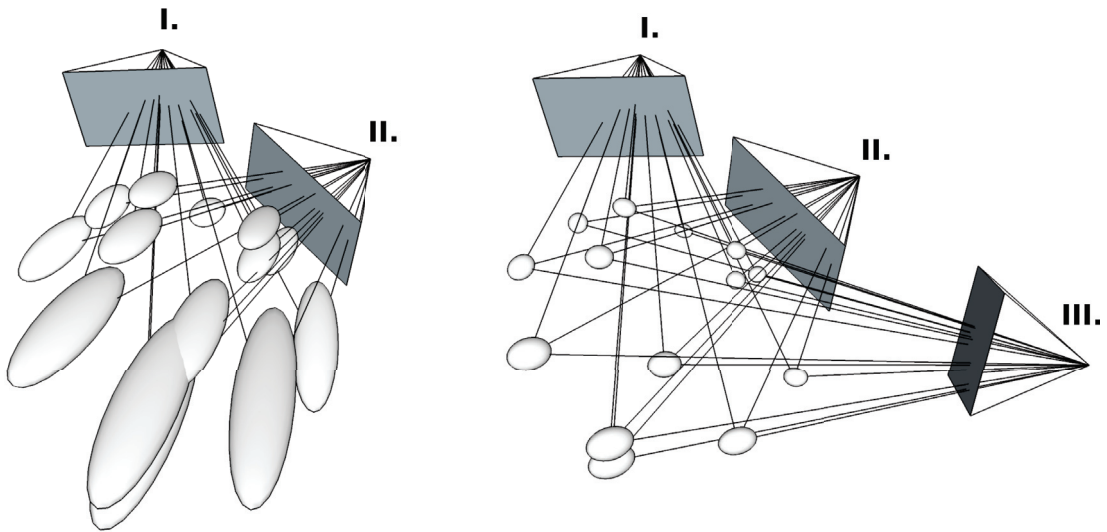


Figure 2.16 – General case of stereo and multi-stereo photogrammetry with simulated data. Error ellipsoids represent the estimated precision of object points (not to scale).

in certain places, e.g. dangerous or inaccessible areas. Regarding the amount of GCPs, the number of points is important only until a certain threshold. Then, the influence on accuracy is rather small as demonstrated in e.g. Gerke and Przybilla [2016] for a MAV mapping project. This issue is further exploited in Chap. 7. Examples of projects with rather poor GCP distribution are compared with ideal cases and with projects with accurate aerial control.

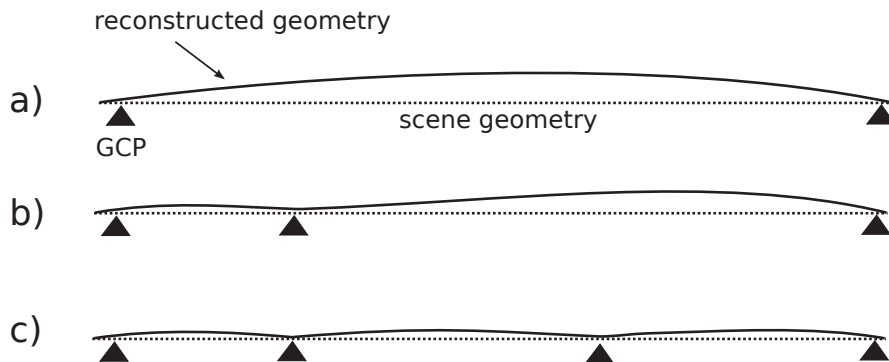


Figure 2.17 – Effect of GCPs distribution on scene geometry; a) no GCPs or badly distributed, b) not optimal distributed GCPs, c) optimally distributed GCPs.

The common practice of distributing GCPs in a mapped area is establishing far more points than necessary. Their placement is often irregular with hollow areas. The solution to this problem would offer a pre-flight simulation of achievable precision, e.g. BA with synthetic data for the given area.

Regarding the accuracy of GCP measurements, it should be performed with higher accuracy than what is expected from photogrammetry projects. For example, the typical desired accuracy of UAV mapping projects is around 1-1.5 pixels in horizontal and 2 pixels in vertical plane, respectively. Thus, the coordinates of GCPs should be measured with  $1\sigma = 2 - 3$  cm. This corresponds to the popular GNSS RTK method.

#### 2.8.4 The influence of Geometry

Mapping quality is interpreted as the precision of the estimated parameters and ground accuracy assessed at independent check points (ChP). For indirect SO, the precision deteriorates with the distance from the control points and particularly in a strip/corridor configurations as depicted in Fig. 2.18. The strips tend to bend due to the accumulation of random effects at the boundaries between images. This effect can be mitigated by, e.g. a closing loop, adding GCPs or providing external aerial control from GNSS or GNSS/IMU. A real world example of the 3D ground precision is shown in Fig. 2.19. The upper image shows an unfavourable placement of GCPs into its right corner. This results in high uncertainty of object coordinates determination that is represented by large error ellipses. On the contrary, the bottom image shows a significant improvement when one of the GCPs is moved to the corridor's left corner. The corridor configuration is schematically depicted in Fig. 2.20 together with requirements on image orientation. Even when considering a favourable image texture that allows automated measurement of a large number of tie-points, the absolute image orientation is in the case of indirect sensor orientation (A) stabilised by a large number of GCPs, while in the case of ISO (B) by on-board observations of EO. In other words, in the absence of accurate aerial position and attitude control, the lack of significant lateral overlap in single or double strip operations requires that absolute orientations of images are passed from the ground up. Technically, for



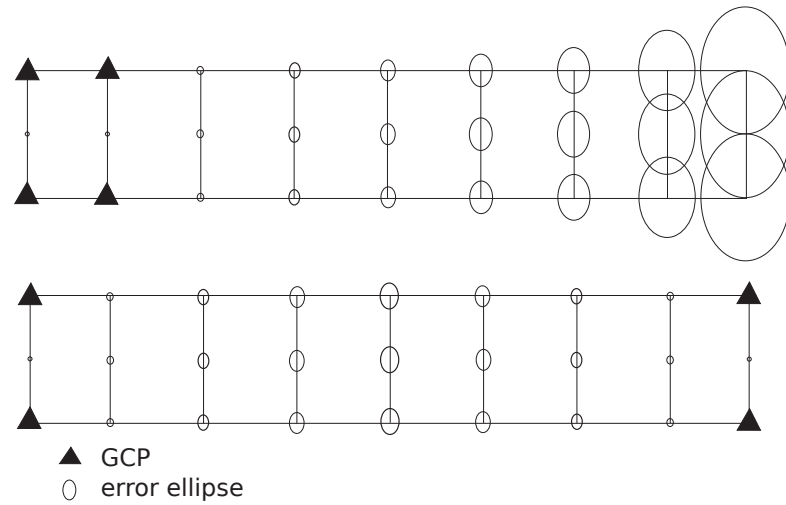


Figure 2.18 – 3D precision of scene points of a strip with four GCPs as a function of a distribution of GCPs for a single strip corridor. Fixing both ends significantly improves the theoretical precision.

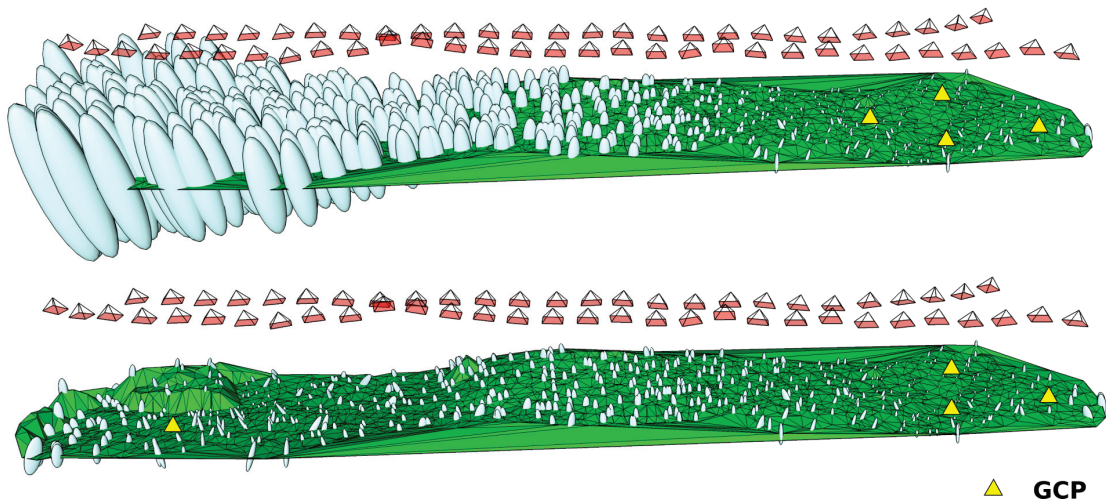


Figure 2.19 – Estimated precision of object coordinates of tie-points represented by error ellipsoids.

today’s MAVs, there are only two ways to deal with such a problem: either a sufficient number of GCPs along and on both sides of the corridor is established or a block-structure flying path is performed. Despite the obvious impracticalities of such solutions, several rather long corridor mapping projects have been presented using indirect sensor orientation approach (Delair-Tech [2014], senseFly [2015b]).

The situation is different in blocks where images are not arranged in a linear pattern but cover a larger region. Here, the inner geometry does not show effects of instability except at the border where the images are connected to the others by one side. The inhomogeneity at the border

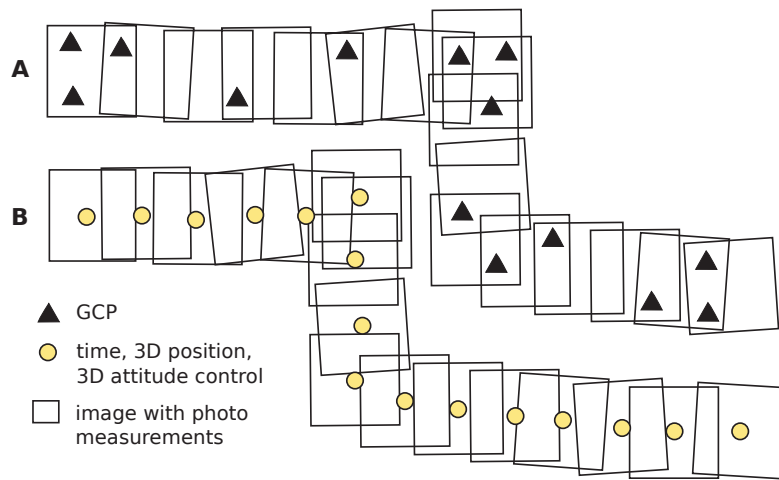


Figure 2.20 – Problematic geometry of a single corridor strip.

can be eliminated by a dense control point chain along the border as depicted in Fig. 2.21 (Ackermann [1966], Förstner and Wrobel [2016]). This is, however, very impractical process and the common solution to this problem is either inclusion of additional aerial control, or a few strips are added to the block, i.e. the mapped area becomes larger than originally desired in order to account for the deformation at the border. Such enlargement, however, increases the volume of collected imagery and slows down the processing.

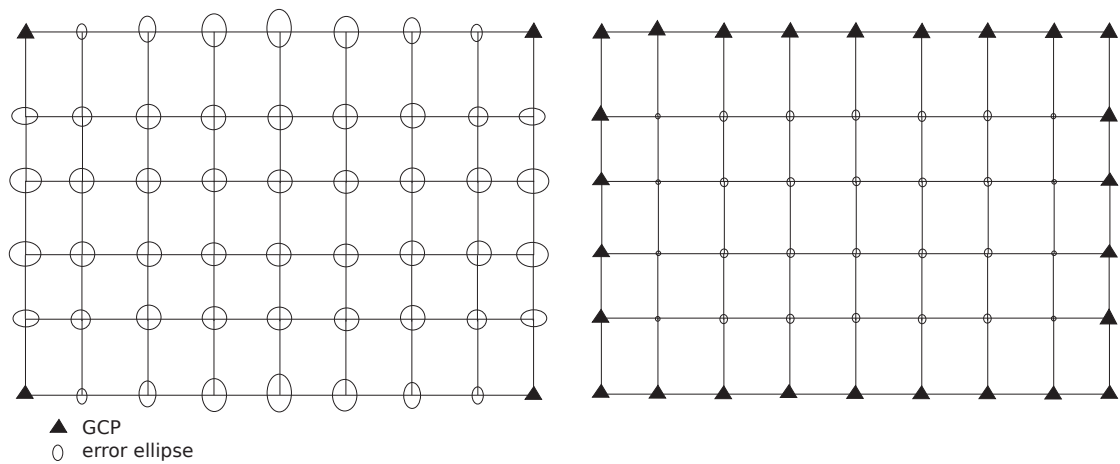


Figure 2.21 – 3D precision of scene points of a block with GCPs distributed in the four corners and along the border.

### 2.8.5 The Influence of Aerial Position and Attitude

Accurate aerial control is required in application with low quality image observations or weak scene geometry. Although the overall accuracy on the ground is dependent on many aspects,

the acceptable attitude error is proportional to the GSD and inversely proportional to the flying height above ground as shown in Fig. 2.22. The requirement on aerial position control is directly related to GSD. The state-of-the-art of kinematic carrier-phase differential positioning is situated at 2 cm – 5 cm noise level. Hence, if  $\sigma_{GCP} < 1$  cm and demands on accuracy lie at the same level, such setup requires GCPs. Apart from the type and quality of aerial control, the results are also influenced by the imaging sensor quality and image resolution (Nassar and El-Sheimy [2005]).

It will be demonstrated later that despite relatively lower accuracy of the MEMS IMUs employed on MAVs, e.g. in the range of  $1\sigma_{\omega,\varphi} = 0.04 - 0.1$  deg, the attitude observations still contribute positively to the ground accuracy.

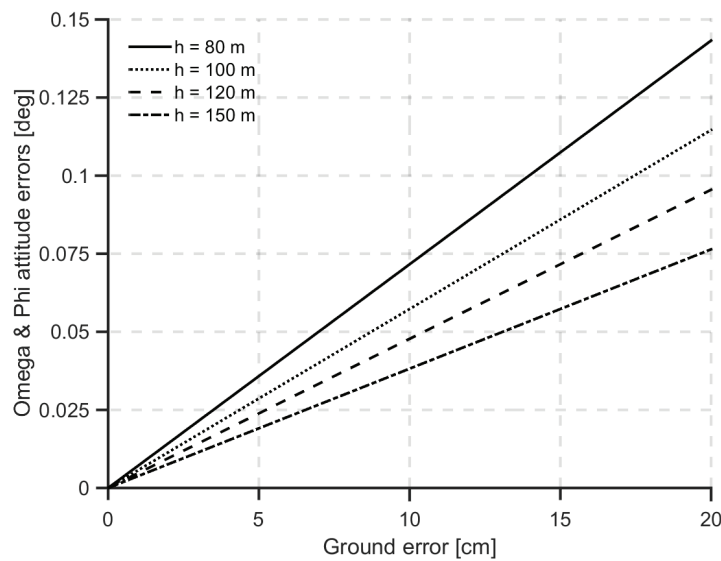


Figure 2.22 – Projection of roll and pitch errors on the ground from different flying heights.

**Summary**

In this chapter, the general problematic of UAV photogrammetry was introduced. This included terminology and an insight into the current legislation trends. Then, a brief summary was given on the categorisation of MAV platforms and optical sensors. One of the main contributions of this chapter was an overview of the principal sensor orientation methods followed by a literature review. The last part was devoted to the general aspects influencing mapping accuracy. These prerequisites are essential for a thorough mission planning.



## 3 Mission Planning and Flight Management

*Mission planning and flight management are the key elements in the UAV work-flow. This chapter presents requirements on UAV mission planning, reviews some of the existing tools, and summarises the main features of the developed flight planning software that is dedicated to a high-precision photogrammetric mapping.*

### 3.1 Requirements and Relations

An indisputable task of every UAV mission is planning. Mission planning can be defined as the planning process of locations to fly and the vehicles actions to do, e.g. taking pictures, typically over a certain period of time. The mission (flight and data acquisition) is commonly planned with a dedicated software. Mission planning is a prerequisite for obtaining satisfactory results while assuming compliance with specific legislation restrictions. The current generation of a flight plan is controlled by an automated process that considers spatial relations and proposes a trajectory (often in a form of a list of waypoints).

Photogrammetric mission planning additionally considers mapping requirements, such as the area of interest, required GSD, overlap ratios, and platform and imaging sensor characteristics against a priori information about the mapping site. The functionality of planning is often connected to the mission control, but can also be separated. Hence, the mission planners can be connected in real-time to UAV platforms or serve only for a complementary offline planning. The planning part for UAVs is somewhat similar to that of manned airborne vehicles which has been thoroughly developed over decades as mapping evolved from analogue to digital, e.g. see Leica Mission Pro (Leica Geosystems [2016]), IGIplan (IGI mbH [2017]) for planes or Schaer et al. [2007] for close-range helicopter mapping.

### 3.2 Overview of Mission Planners

The market nowadays offers hundreds of different platforms that are all coupled with various mission planners. These planners can be divided into four main categories. The first category comprises proprietary planners purposed for a specific platform. These are for example eMotion3 (senseFly [2015a]) or MAVinci Desktop (MAVinci GmbH [2015]), both dedicated to fixed-wing platforms. Examples of multicopters are Mikrokoetter Tool (HiSystems GmbH [2016]), mdCockpit (Microdrones GmbH [2016]), or DJI Ground Station (DJI Innovations [2016]). The proprietary mission planners feature a tight integration of platform's characteristics into the planning, and therefore do not allow to change vital properties related to the flight dynamics. These mission planners are usually very easy to use as many parameters are defined implicitly, which decreases software complexity. Furthermore, a real-time monitoring or a pre-flight mission simulation are integrated into a common software package.

The second category includes open-source mission planners. These are often highly customisable tools and based on do-it-yourself projects, such as ArduPilot (ArduPilot Dev Team [2016]). The open-source mission planners contain a variety of functions making them very universal, however, not very suitable for certain tasks. One of such tasks is a photogrammetric mission planning in challenging terrain. The most popular open-source project Mission Planner (ArduPilot Dev Team and Osborne [2016]) lacks advanced mapping features, such as visual 3D planning (the ability to view the trajectory in 3D), or splitting long flights into separate missions. The lack of visual 3D planning decreases the capability of detecting altitude boundaries and may lead to critical situations especially in highly structured terrain. Other mission planner fitting into this category is QGroundControl (QGC Dev Team [2016]) that includes mission control for all kind of autonomous unmanned systems. Its high versatility is in contrast with a user-friendliness. In this respect, less experienced users may find mission planning too difficult or less intuitive contrary to that of the proprietary systems.

Universal mission planners fall into the third category. They are not dedicated to a specific platform. One of them is Universal Ground Control Station (Engineering [2016]) that can control a variety of platforms in real-time. It basically benefits from both the latter categories despite being relatively easy to use.

Last but not least, free mobile applications from providers of image processing software, such as Pix4D or DroneDeploy, allow mission planning and execution for common MAV platforms, e.g. DJI Phantom (DJI Innovations [2016]). Furthermore, the obtained imagery can be directly uploaded either to a working station or cloud processing service. One of their major advantages is that they readily enable using drones for mapping that are not originally designed for this task. An extended overview about the current mission planners is provided in Appendix A in Tab. A.3.

### 3.3 Mission Planning Work-flow and Considerations

A mission plan must consider the physical capabilities of the UAV and its sensor package against the quality of information required at each mapping location. A planning algorithm

### 3.3. Mission Planning Work-flow and Considerations

---

should provide optimal, yet flyable trajectory in relations to the mapping needs. The essential steps of every photogrammetric mission planning for UAVs are:

1. Defining a region of interest.
2. Verifying possible obstacles and restricted zones.
3. Considering platform's constrains, e.g. endurance, payload capacity, min/max speed.
4. Considering the terrain morphology.
5. Setting the photogrammetric parameters, such as overlap, resolution, or camera parameters.
6. Identifying the take-off and landing positions.
7. Generating the mission plan.
8. Considering areas with limited or perturbed GNSS and control signals and changing the mission accordingly.
9. Verifying maximal distance between ground station and the UAV for continuous line-of-sight.
10. Manual modifying, rotating the automatically generated waypoint mission.

The GSD, overlap ratios, and imaging sensor geometry are the main parameters determining the mission characteristics. Following the calculation of the photo scale and GSD from the Sec. 2.8, the area covered by an image on the ground can be calculated by dividing the camera sensor size by the photo scale.

#### 3.3.1 Photo Overlap

Overlap ratios represent the amount by which one photograph includes the area covered by another photograph. Assuming vertical aerial photographs, coverage of an area is normally designed as a series of overlapping flight strips. Two types of overlap are addressed:

- **Forward overlap** sometimes also called endlap, is the common image area on consecutive photographs along a flight strip. When mapping with MAVs, the forward overlap usually ranges between 60 to 80%. The size of overlapping area is dependent on many aspects, e.g. the quality of imaging and navigation instruments, morphology of the mapped terrain or the demanded mapping products.
- **Side overlap**: sometimes called sidelap, comprises the overlapping areas of photographs between adjacent flight lines. The side overlap usually ranges between 40 to 60% of the photo width.

### Chapter 3. Mission Planning and Flight Management

---

Forward and side overlap can be calculated from a simple relation between sensor's physical parameters, the photo scale, and desired overlap in percentage, Eq. 3.1. Fig. 3.1 portrays the two overlapping scenarios.

$$d = \frac{w}{s_p} \cdot \frac{100 - o}{100} \quad (3.1)$$

where

- $d$  is the distance between exposure stations/adjacent lines in meters,  
 $s_p$  is the photo scale,  
 $w$  is the width or length of the camera sensor in meters,  
 $o$  is the desired forward or side overlap in percentage.

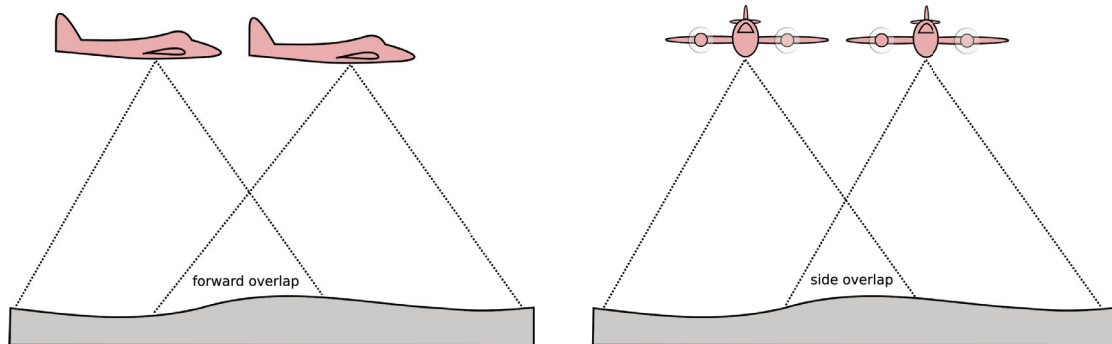


Figure 3.1 – Schematics of forward and side overlap.

One particular thing about MAVs is the amount of overlap in mapping missions. While the classical design of block structures would consider only the minimum necessary overlap, e.g. 60% forward and 20% side overlap, common practise of mapping with MAVs requires as much overlap as possible, e.g. 80% forward and 60% side overlap, respectively. This situation is depicted in Fig. 3.2. Such network strengthening is due to the requirements on high observability of tie-points. The need for high redundancy is due to the following reasons:

- Consumer grade cameras require frequent self-calibration,
- IO parameters may vary per image,
- low accuracy of aerial control compensated by high observability of GCPs,
- high variations in attitude and speed may result in missing data in certain areas.



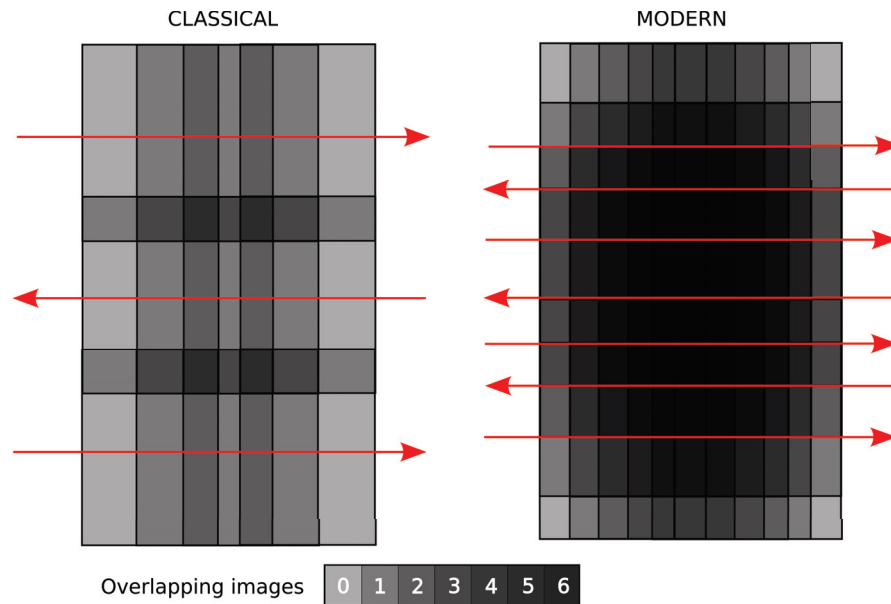


Figure 3.2 – Classical vs. modern block setup. The shades of grey represent the number of overlapping images.

#### 3.3.2 Trajectory Design

UAV mapping missions are usually flown in a specific pattern of parallel lines, commonly described as transects, which are connected to a series of waypoints. Such flight is depicted in Fig. 3.3. A transect flight pattern is a method of ensuring that the UAV captures an adequate quantity of images that overlap to the degree required for the processing software to create a high-quality and accurate map (Kakaes et al. [2015]).

The common feature of mission planners is flying two different overlapping patterns over the same area to enhance the block structure. This is, however, frequently executed at the same flight level rather than at different heights. This method collects a larger quantity of data and helps to resolve elevation variation problems as discussed later in Sec. 3.4.3. Two basic approaches are considered when planning a trajectory (Gandor [2015]).

- **Bottom-up approach:** This approach takes as an input the parameters determining the end-product characteristics, i.e the GSD and overlap. The program automatically computes the flight parameters for a given camera. This approach is used in, e.g. eMotion3 (senseFly [2015a]) in order to make the planning as simple as possible for users without appropriate knowledge about other parameters.
- **Top-down approach:** User can specify the flight height, line separation and overlap, and the program calculates the resulting GSD. This approach is more common and usually combines also the first approach so the users have full control over the parameters like in Mission Planner (ArduPilot Dev Team and Osborne [2016]).

In close-range applications, the UAVs (usually VTOL) follow a multiple-level flight pattern in order to collect high convergent imagery as illustrated in Fig. 3.4. In practice, aerial imagery is often combined with ground imagery or LiDAR data to better reconstruct challenging scene elements and to deliver a high quality texture.

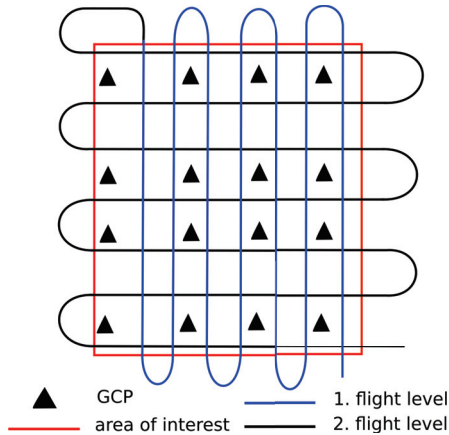


Figure 3.3 – Classical flight pattern of an aerial mission from two distinct flight height levels.

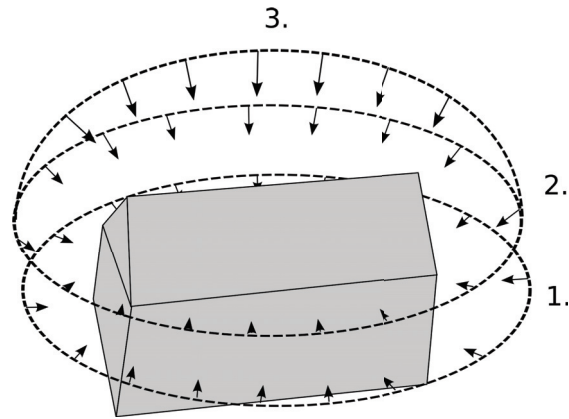


Figure 3.4 – Flight pattern for close-range mapping and 3D modeling. Three distinct flight levels are depicted, but their number is optional depending on the size and shape of the mapped object.

### 3.3.3 Technical Aspects of Platform and Camera

A correctly planned mission shall account for the platform's and sensor's operation limits. This means that the mission should not be designed in such a way that it is not in compliance with the platform's minimal turning radius, autonomy, or speed. Except for rotary-wing UAVs, which are holonomic vehicles <sup>1</sup>, the fixed-wing UAVs have a constrained trajectory. One of the notable constraints lying in the device's attributes is the distance needed to complete a U-turn. This turning radius is important as it affects the minimum distance between the lines.

#### Image Frequency

An important aspect is the camera's capability of taking images fast enough so it assures constant forward overlap. This problem might occur when the platform's ground speed is too high with respect to the overlap. The distance between two consecutive images can be calculated from Eq. 3.1. Considering ground speed  $v(t)$  in time  $(t)$ , time interval between consecutive images will be:

$$dt = \frac{d}{v(t)} \tag{3.2}$$

<sup>1</sup>a vehicle can move freely in every direction

Two options are viable without sacrificing the amount of overlap. First, the height above ground must be increased or the ground speed must be decreased. As the latter might not be always feasible due to the platform's dynamics, the solution is to fly only in the direction against the wind or perpendicularly to the wind to decrease ground speed. This solution is at the expense of a higher price of longer flights.

#### Image Blur

Image blur significantly decreases information in the imagery and the ability of computer vision algorithms to find correspondences (Sieberth et al. [2013, 2015]). When accounting for platforms ground speed, one of the considerations should be the movement of the sensor during the exposure time. As a rule of thumb, this movement should not be bigger than a half of the pixel. Generally, the image blur has the following origins:

- **Forward movement** (velocity): issue with fast flying platforms, i.e. fixed-wing UAVs. The problem of the head and tail wind may cause big variations in ground speed. The theoretical blur  $b(t)$  in pixels caused by forward velocity is:

$$b(t) = \frac{v(t) \cdot \epsilon \cdot c}{h \cdot p} \quad (3.3)$$

where  $v(t)$  is the ground velocity in m/s,  $\epsilon$  is the exposure time in seconds,  $c$  is the principal distance,  $h$  is the flight height above mean ground level and  $p$  is the pixel size.

- **Angular movement** (angular rate): problematic mainly on VTOL platforms due to the fast attitude compensations of the autopilot. These angular dynamics are of two types: low frequency caused by platforms acceleration and rotation as an effect of wind, sudden input of an operator etc., and high frequency vibrations generated by the propulsion system. Examples of angular rates exhibited on a fixed-wing platform are presented in Sec. 6.4.2. The theoretical blur in pixels caused by the angular rate  $\omega(t)$  in rad/s can be calculated using the following equation:

$$b(t) = \frac{c \cdot \omega(t) \cdot \epsilon}{p} \quad (3.4)$$

- **Camera properties:** There are several parameters that further influence the image sharpness. These are related to the camera settings or its physical construction. For example, a wrong camera focus, too shallow depth of field, or moving internal lens or camera elements, may all result in blurred imagery.

#### Camera Setting and Triggering

Camera setting is a crucial step in achieving quality imagery. Cameras employed on MAVs do not often allow manual setting of exposure parameters. These are: shutter speed, aperture,

and the level of sensor sensitivity. To get the image properly exposed, so that it is not too bright or too dark, these three parameters need to play together.

As a rule of thumb in aerial mapping, the shutter speed should be fixed to a rather fast speed, i.e. 1/500-1/1250 s to prevent direction blur due to the camera's forward movement and angular changes.

The aperture can be set automatically, i.e. the camera is set to shutter priority mode or can be set manually if the light conditions are constant during a mapping mission. Apart from the amount of light coming to the sensor, the aperture also influences the depth of field (more important for close-range applications than aerial mapping). Therefore, rather narrow aperture should be considered, e.g. f-stop > 5.6. Moreover, camera lenses tend to have higher sharpness for narrower apertures, but this is particular to each of the lens. The sensor sensitivity should be set at a rather low value, depending on the camera's noise level characteristics for a particular sensor size. High sensitivity settings generally introduce noise into the images and drastically reduce the quality of the results (PhotographyLife [2016]).

Furthermore, camera must be manually focused to infinity to prevent the lens elements from moving between the images. As for the data format of the captured imagery, raw format stores data with a higher dynamic range allowing to correct exposure in the post-processing. However, raw files have significantly bigger size than their compressed counterparts and require higher volumes of data to be stored by the camera. As a result, the shutter frequency may be negatively influenced by slow media storage devices.

Regarding the methods of a camera triggering, the following options are often adopted by the UAV operators:

- **Interval triggering:** Camera is triggered automatically by the autopilot or by its internal function in a specific interval. This method is popular on small VTOL platforms that are commonly not designed for mapping purposes. The interval triggering usually results in excess imagery and diverse overlap in case the flying speed varies.
- **Distance triggering:** Distance between consecutive images is calculated according to Eq. 3.1 and the autopilot issues triggering signals when this distance is reached. The advantage of this method lies in maintaining a constant overlap even with a variable platform's speed.

### 3.4 Planning in a Complex Terrain

Flying in challenging areas, such as hilly or mountainous areas, requires the mission planner to extend planning functionality beyond the common features, such as 2D zone definition and waypoint layout based on GSD and overlap criteria. By combining real 3D terrain awareness into mission planning with some advanced functions, the planning tool facilitates the process of mission preparation. Despite the globally available terrain model, the user should be able to use custom digital elevation models (surface included) of high resolution to improve the planning of photo positions with respect to the area of coverage, overlap, and resolution. The

risk of having uncovered areas is then significantly reduced. Furthermore, the reception of signal for satellite positioning should be evaluated for a specific time and area in order to determine the best time to perform the survey.

The following part of this chapter focuses on advanced mission planning features that were implemented into TOPO Mission Planner. Such functionality is usually not included in the tools available on the market.

#### 3.4.1 Developed Mission Planner Tool

TOPO Mission Planner is an open-source flight planning tool that is dedicated to a high-precision photogrammetric mapping. The tool was programmed using the open-source Java SDK (Software Development Kit) World Wind developed at NASA (NASA [2016]). The latter contains main geospatial components, e.g. high-performance 3D virtual globe, basic digital elevation model and includes a variety of demos and examples for fast implementation of custom functions. Apart from the standard planning functions presented above, a main focus was given to additional features dealing with safety and accuracy. The main functions available are:

- A survey area can be drawn and flight path is generated automatically depending on the a priori requirements, e.g. overlap, GSD, or height. Physical constraints of the platform are considered in the trajectory generation.
- The user can either define the camera and UAV device or choose from some predefined systems. The latter are stored in CSV (Comma-Separated Values) files and therefore can be easily modified or extended. Camera parameters of FOV and its direction and inclination can be modified directly in the panels or uploaded from the CSV file.
- Digital elevation models can be imported in order to work with user-provided high-precision elevation information. These elevation models enable analysis of the terrain and create inclined trajectory that respects the end-product requirements.
- Automatic camera tilting option for platforms with variable-pitch sensor mount, typically for VTOL UAVs.
- GNSS satellites availability along the trajectory can be checked in order to predict the best survey time. The number of satellites as well as expected DOP (Dilution of Precision) values are calculated for certain mission points.
- Some safety features are available, such as checking the visual line of sight, geo-fence, or restricted areas.
- GIS functions for terrain slope and aspect analysis can be used for creating new layers in the 3D environment.



resolution increases the chance of better control over this parameter throughout the mission. Additionally, the mission planning tool allows performing terrain analysis, e.g. slope and aspect, and visualises its outcomes. This is particularly useful in mountainous areas when assessing light conditions, e.g. places in shadow.

#### 3.4.3 Accounting for Terrain Variations

Guaranteeing certain ground resolution is an important requirement to fulfil when designing a flight pattern. This can be particularly problematic in hilly or mountainous terrain. The implemented function for multi-level flight pattern assures unified resolution over the whole mapping area. The situation is depicted in Fig. 3.6. The height is calculated relatively to the terrain or to the home position altitude. In the case of the single flight level, the GSD of the mapping product is not uniform and causes strong correlation between the camera IO and EO parameters.

Next, the base flight height level is accompanied by a second flight level that is placed above the first level. The separation between them is calculated in relation to the desired GSD, so the average predicted resolution is maintained for the whole area. Furthermore, flying at two separate heights improves the geometry of the subsequent 3D scene reconstruction (Pothou et al. [2004]). Additionally, the second level can be oriented perpendicularly to the first one. Such configuration helps with sensor and system self-calibration and mitigates unmodeled systematic errors.

If the employed UAV platform has the capability of changing the altitude progressively, such as a multirotor UAV, method C in Fig. 3.6, or a combination of B and C, bring a major advantage. This pattern is desired mainly in close-range 3D modelling and documentation.

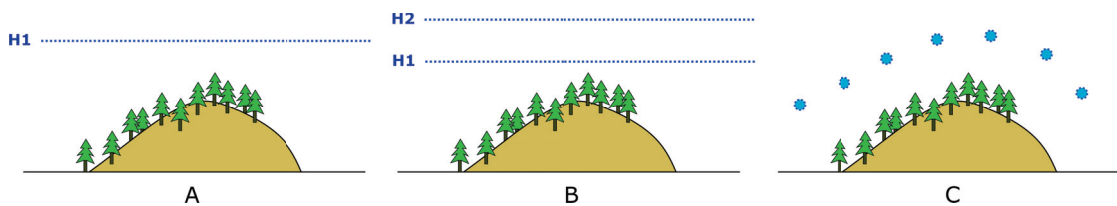


Figure 3.6 – Flight configurations; A) simple flight in one level, B) two flight levels, C) progressive changing of flight altitude.

#### 3.4.4 Alternative Flight Patterns

One of the major constraints residing in the platform's attributes is its turning radius. This is particularly important for fixed-wing UAVs. The turning radius is vital as it affects the dynamic layout of waypoints. A special guidance option was created to handle the turning radius for fixed-wing platforms even if the consecutive flight lines are very close. The user has an option of choosing between classical and smoothed curves. The latter adds a few waypoints at the

end of each line to respect the turning radius and better guide the plane to the subsequent line. Fig. 3.7 depicts these two turning options. Usually, this problem is handled by adding so-called overshooting area, i.e. a trajectory extension in one or more sides of the flight plan. This option was also implemented in the presented tool. Both options improve the alignment of the platform to the desired trajectory and minimise attitude variations over the mapped area. Apart from the plan itself, the trajectory is mainly influenced by the UAV performance, in-built control-loop tuning, and wind. The last trajectory design is called an alternative flying pattern and is depicted in Fig. 3.8. In such a mission design, the UAV skips every second line in order to have wider line separation for safe turning. This function is implemented in many mission planners, e.g. in eMotion3 (senseFly [2015a]). A certain drawback of this method is the time delay between the neighbouring lines are mapped. This can result in changes in shadows or surface texture.

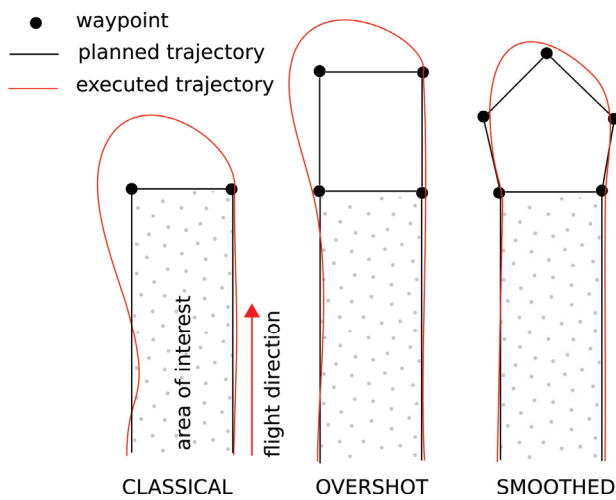


Figure 3.7 – Classical, overshoot and smoothed turning curves. The red trajectory is based on practical tests and represents dynamics of a fixed-wing drone.

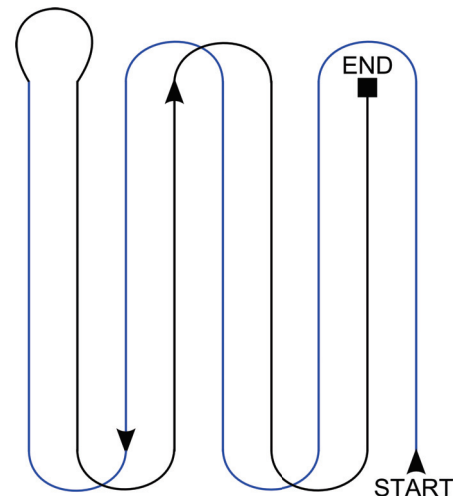


Figure 3.8 – Alternative flying pattern.

### 3.4.5 Overlap and GSD Assessment

To achieve the requested image overlap, spacing between consecutive images and the trajectory's flight lines is regulated by the basic planning functions. The closer the images/flight lines are, the higher the overlapping ratio is. Additionally, the targeted GSD value, calculated using Eq. 2.5, represents an ideal GSD and is hardly achievable in the real world situations. The calculation implicitly assumes flat terrain and also that images are perfectly at nadir so each picture is attributed a single value of GSD.

In reality, position and attitude of the collected imagery varies significantly (without an active sensor stabilisation system) and so does the terrain, particularly in hilly or mountainous areas. A method that calculates and displays the overlap and expected GSD, respectively, was



developed. The analysis can be carried out on both synthetic and real data. For further details about implementation and testing see Pascale [2016]. The assessment is done as follows:

#### Overlap Prediction

1. In order to sample the terrain, WGS84 coordinates of the area of interest (AOI) are first converted into ENU system.
2. The AOI is divided into small sectors. Their number is optional and they constitute a regular 3D grid.
3. For each cell, a centroid <sup>4</sup> is calculated.
4. A counter is associated to each cell to store the number of images from which it is visible.
5. For each trigger point in the list:
  - (a) The centroid is projected into the camera frame of the considered trigger position.
  - (b) If the projected centroid falls into the boundaries of the camera sensor, its counter is incremented.
6. The overlap is visualised based on the appearances of individual centroids in images. Fig. 3.10 shows the layer over the AOI.

#### Theoretical GSD

Similarly to the overlap assessment, a prediction of the resulting GSD can be carried out in the following steps:

1. The same centroids are used as in the overlap assessment.
2. Every four centroids constitute a small polygon whose area is calculated.
3. Centroids are projected to the camera frame and the area of the projected polygon is calculated. This situation is illustrated in Fig. 3.9.
4. The GSD is evaluated as the ratio between these two areas:

$$GSD = \frac{A_{ENU}[m^2]}{A_{cam}[pixel^2]} \quad (3.5)$$

where  $A_{ENU}$  is the area covered by the polygon on the ground and  $A_{cam}$  is the area projected into the camera frame (Pascale [2016]).

5. The GSD is visualised as a new layer rendered on the terrain surface as illustrated in Fig. 3.11.

---

<sup>4</sup>the centre of mass of a geometric object of uniform density

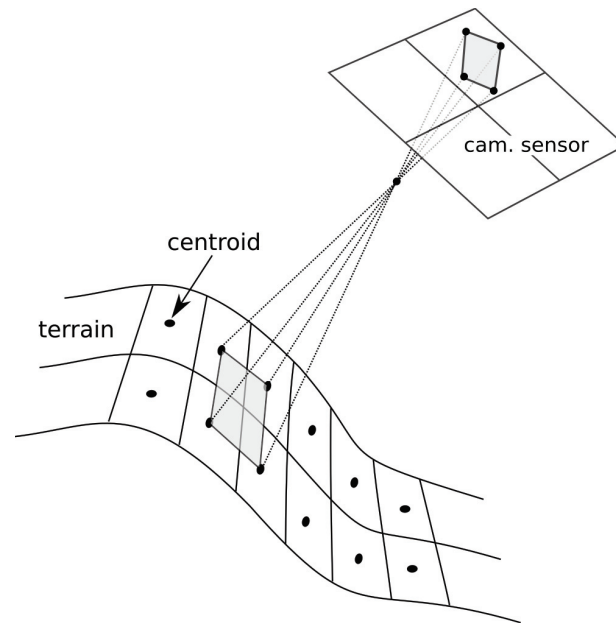


Figure 3.9 – Polygon projection to the camera frame.

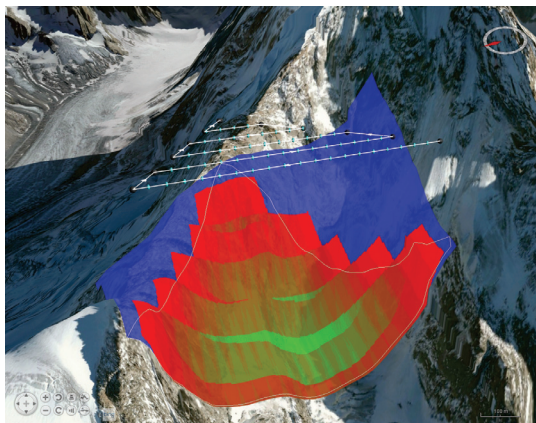


Figure 3.10 – Overlap evaluation. Green colour represents areas with high overlap, red and blue with low overlap (Pascale [2016]).

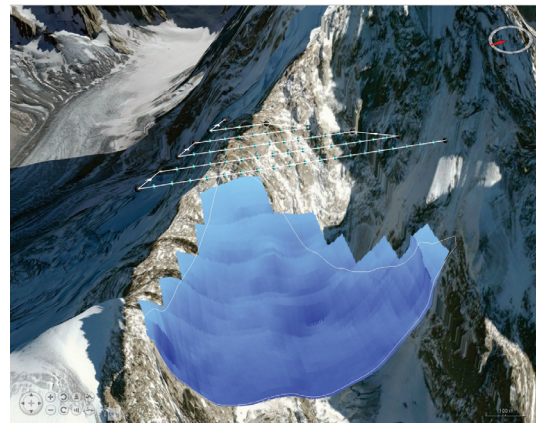


Figure 3.11 – Evaluation of GSD. The darker the blue colour, the lower expected GSD (Pascale [2016]).

### 3.4.6 GNSS Satellite Visibility

Good reception of GNSS signal during the whole mission is a critical factor that affects the navigation of an UAV as well as the accuracy of the final mapping product in cases of ISO or DiSO. When a platform performs an autonomous waypoint to waypoint flight, navigation mainly relies on regular GNSS position fixes, and therefore a good reception of GNSS signals is essential for safety. Furthermore, UAV mapping missions are usually executed at low altitudes and often on demanding topography where partial GNSS satellite masking by the relief is very frequent. In addition, the satellite constellation changes constantly throughout the day and it

is therefore important to plan a mission with the highest GNSS satellite observability. In order to predict the best survey time and to overcome the possible unexpected GNSS outage caused by a signal obstruction, the geometry of the satellite constellation along the planned path is assessed within the planner itself with respect to the elevation model. First, satellite's orbits are computed from an almanac using Keplerian orbit elements. These elements describe the motion of a satellite orbiting around the Earth. Then, rays between the mission points and satellites positions are tested for intersection with the terrain. The criteria for these evaluations (e.g. trajectory sampling, time-span, elevation mask etc.) can be modified. Finally, an algorithm deduces GNSS constellation characteristics (such as DOP values, min. number of visible satellites) for the mission. Fig. 3.12 shows the imaginary rays between satellites and significant points in the mission for a specific time interval and Fig. 3.13 depicts the number of visible satellites for a specific time interval. Occlusions caused by the platform's tilting in turns present the only limitation in the prediction of satellite's availability. These effects can be mitigated by constraining the platform's maximum bank angle or by employing a GNSS antenna with a wider radiation pattern resulting in a higher gain for signals coming in at low elevation angles.



Figure 3.12 – Visibility of GNSS satellites for certain points represented by imaginary rays between sampled trajectory and satellites.

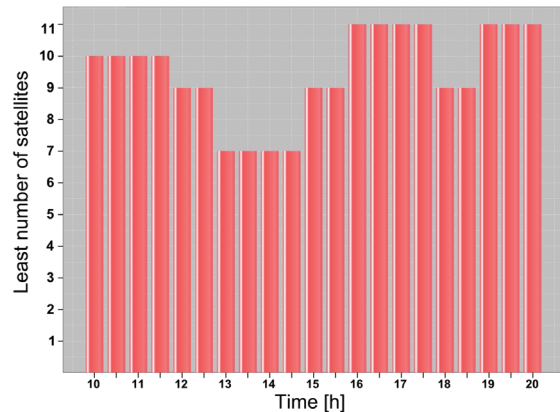


Figure 3.13 – Minimum number of GNSS satellites as a function of survey time for a specific trajectory.

#### 3.4.7 Additional Features

An important point that shall be taken into account in planning a mission is safety, as discussed in Sec. 2.3. Therefore, constant direct line-of-sight should be kept between an operator and an UAV. The TOPO Mission Planner has a functionality for checking direct visibility.

The line of sight between the operator and the drone is computed similarly to the approach evaluating GNSS signal reception. An algorithm samples the UAV's trajectory and tests the intersection with the terrain at discrete intervals. Two positions concerning the observer and the moving drone are needed to compute the vector between them. The norm of the vector

## Chapter 3. Mission Planning and Flight Management

---

divided by the interval distance gives the number of points to be tested. The elevation of the points along the vector is tested against the elevation of the terrain at the same coordinates. If the terrain is higher, the visibility is declared as masked for this portion of trajectory. In addition, maximal distance of the UAV to the operator's position is computed. The mission planner contains functions for reading and interpreting the autopilot's files with the stored path. The actual flight trajectory can be then loaded and compared to the original plan. The projection centres of the images can be displayed in 3D on a map and provide an overview of coverage. The Fig. 3.14 illustrates a planned versus executed multilevel flight.



Figure 3.14 – Post-mission analysis; blue path: the executed flight, white path: the planned path.

### 3.5 Real-time Monitoring and Flight Management

Flight and mission management systems are usually an integrated part of commercial UAS. These tools often combine mission planning, real-time monitoring, and offline management functionality. The real-time monitoring consists of several components:

- Monitoring of a mission progress,
- payload configuration and triggering,
- sensor configuration and settings of an autopilot,
- mission commands, e.g. mission selection, autopilot mode, type of landing etc.

These components are embedded in commercial mission planning tools which were presented in Sec. 3.2. The introduced TOPO mission planner is in its current configuration only able to

plan and store missions but not command or execute tasks in real-time. This will be a subject of later development.

Although mission planning and real-time monitoring cover important parts of UAV work-flow, general mission management and equipment inventory are of a great importance too. Indeed, maintaining history about flights, operators, and equipment ensures safer flights and helps with delivering stable results over time.

Commercially available universal management tools are often developed as mobile applications allowing users simple and fast logging of events, missions, and platforms. Furthermore, these tools are scalable from single UAV operations to large business production (DroneAnalytics [2016], Skyward [2016], UniFly [2016]). The key properties of a veritable management tool are the following:

- **Inventory and Maintenance**

- platform's name and characteristics (type of airframe, weight etc.)
- batteries (type, capacity, charging history, age etc.)
- equipment (cameras and other sensors)
- log book of flights and jobs

- **Fleet Management**

- pilots
- history of projects
- customers

- **Missions and Projects**

- mission planning
- weather monitoring, forecast
- storing of planned and executed missions

- **Real-time monitoring**

- online monitoring of other drones flying in the same area
- database of restricted areas

- **Reporting**

- reporting flight accidents
- generating compliance reports for aviation institutions
- generating of operation and inventory reports
- flight log analysis

#### Summary

This chapter was devoted to a photogrammetric mission planning. The first section reviewed the state-of-the-art mission planners dedicated to UAVs. A particular focus was given to their categorisation, advantages, and disadvantages. In the next part, the basics of a mission planning work-flow were presented with fundamental mathematical relations. The aspects of mapping in challenging areas were addressed in the context of the development of a custom TOPO Mission Planner. Among the presented features, the most important ones are the prediction of GNSS satellite availability, assessment of overlap and GSD, and adjustment of flight trajectory according to the platform's dynamics. The chapter was concluded with the subject of real-time monitoring and flight management. These two elements are indispensable in a thorough mission preparation and execution.

## 4 Measurements, Models and Estimation Methods

*This chapter addresses the issue of aerial control in the context of photogrammetric BA. Mathematical models of absolute, relative, and spatio-temporal observations are introduced with a particular focus on their stochastic modelling. A method of BA is presented and implemented into a custom processing tool.*

### 4.1 Introduction

TopoBun is an estimation tool that treats image, ground, and aerial observations within a common BA. It was developed in Matlab (The MathWorks Inc. [2016]) and aimed at testing a variety of new observation models on data collected with MAVs that are not part of commercially available software. Custom implementation allows full control of observation stochastic modelling that is particularly important when using accurate control. The schema of a general concept of BA in ISO is depicted in Fig. 4.1. TopoBun allows using the following observations:

- Image measurements of tie-, ground control, and check points,
- object coordinates of GCPs,
- absolute and relative position, and attitude of EO parameters from GNSS/IMU,
- velocity and angular rates from GNSS/IMU,
- one or multiple camera IO parameters, i.e. coordinates of the principal point, principal distance, and additional parameters related to optical distortions.

Based on the latter observations, the following parameters can be estimated:

- Camera(s) exterior orientation parameters,
- object coordinates of tie-, ground control and check points,

- camera(s) IO parameters,
- boresight and lever-arm parameters,
- constant synchronisation delay between camera time-stamps and GNSS time.

The following sections provide a detailed overview about the implemented observation models, BA, and the TopoBun software. The structure of this chapter follows the schema in Fig. 4.1 .

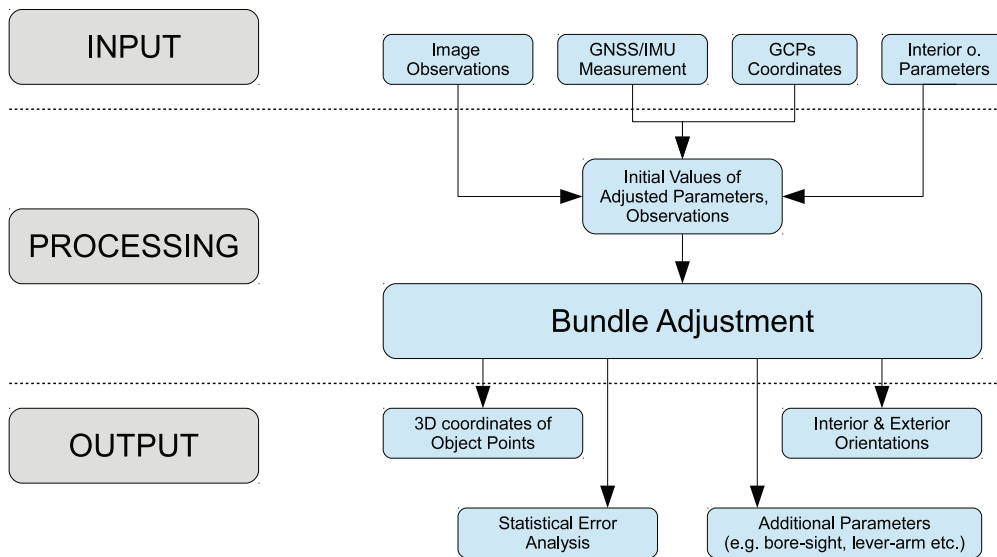


Figure 4.1 – Integrated sensor orientation schema, i.e. general adjustment using satellite, inertial, and photo observations.

## 4.2 Image Observations

The relation between an image and an object is derived from a physical assumption that the perspective centre, the object, and its image are collinear, Fig. 4.2. This relation gives the following functional collinearity model in Eq. 4.1. Partial derivatives of the collinearity model are detailed in Appendix B.

$$x + v_x = x_0 - c \cdot \frac{r_{11}(X - X_0) + r_{21}(Y - Y_0) + r_{31}(Z - Z_0)}{r_{13}(X - X_0) + r_{23}(Y - Y_0) + r_{33}(Z - Z_0)} + \Delta x \tag{4.1}$$

$$y + v_y = y_0 - c \cdot \frac{r_{12}(X - X_0) + r_{22}(Y - Y_0) + r_{32}(Z - Z_0)}{r_{13}(X - X_0) + r_{23}(Y - Y_0) + r_{33}(Z - Z_0)} + \Delta y$$



where

- $x, y$  are the image coordinates,
- $\nu_x, \nu_y$  are the image observation residuals,
- $X, Y, Z$  are the object point coordinates,
- $X_0, Y_0, Z_0$  are the coordinates of the centre of projection,
- $c$  is the principal distance,
- $x_0, y_0$  are the photo-coordinates of the principal point that is the projection of the perspective centre to the image plane,
- $r_{11} - r_{33}$  are the elements of the rotation matrix  $\mathbf{R}_c^m$  that describes the rotation from the camera coordinate system to the object space coordinate system parametrised by Euler angles in the sequence  $\omega\varphi\kappa$ .

$$\mathbf{R}_c^m = \mathbf{R}_x(\omega)\mathbf{R}_y(\varphi)\mathbf{R}_z(\kappa)$$

$$\mathbf{R}_x(\omega) = \begin{pmatrix} 1 & 0 & 0 \\ 0 & \cos(\omega) & -\sin(\omega) \\ 0 & \sin(\omega) & \cos(\omega) \end{pmatrix}$$

$$\mathbf{R}_y(\varphi) = \begin{pmatrix} \cos(\varphi) & 0 & \sin(\varphi) \\ 0 & 1 & 0 \\ -\sin(\varphi) & 0 & \cos(\varphi) \end{pmatrix} \quad (4.2)$$

$$\mathbf{R}_z(\kappa) = \begin{pmatrix} \cos(\kappa) & -\sin(\kappa) & 0 \\ \sin(\kappa) & \cos(\kappa) & 0 \\ 0 & 0 & 1 \end{pmatrix}$$

- $\Delta x, \Delta y$  are the additional parameters describing optical distortions.

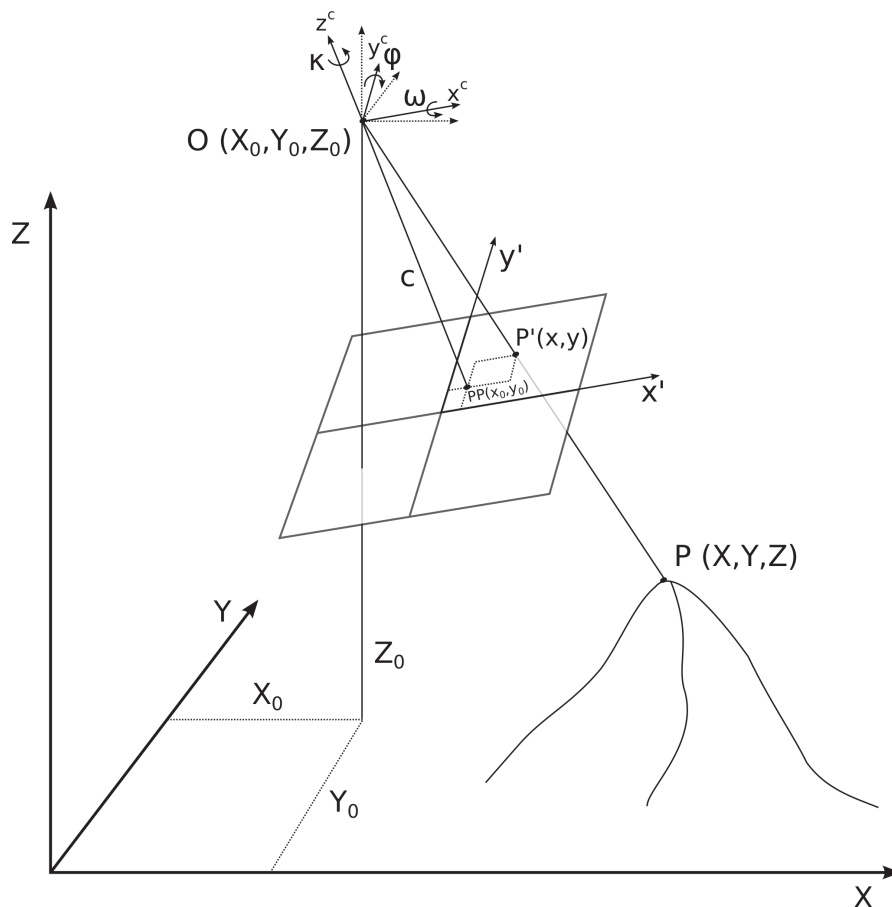


Figure 4.2 – Image and object coordinate systems of an aerial photograph.

### 4.3 Additional Parameters of Interior Orientation

Interior orientation parameters are properties of the optical and physical configuration of a camera lens and a sensor. The IO parameters of a camera provide a corrective model to adjust for deviations in the internal camera geometry from an ideal collinearity model. Regardless of the model used, the sum effect of the IO parameters is to produce a corrected image coordinate for the use in collinearity equations in Eq. 4.1 (Fraser [1997]). Hence, the set of additional parameters may be used to account, e.g. for lens distortion (radial and tangential), image plane distortions (in-plane and out-of-plane), and other sensor biases (e.g. origin).

Several sets of additional parameters have been presented in literature, such as mathematical polynomials of Ebner function (Ebner [1996]) or Grün function (Grün [1986]). These have been often applied to aerial photogrammetry. A combined physically-oriented distortion model that is widely accepted for digital cameras was presented by Brown (Brown [1971]) and has been traditionally used in close-range photogrammetry.

The choice of an additional set of parameters depends on several aspects. One of them is the knowledge of exterior orientation parameters. If these parameters are provided by a

GNSS/IMU system with sufficient accuracy, the Ebner function needs to be extended from 12 to 18 parameters to constitute "EO constrained" self-calibration function as discussed in (Blázquez and Colomina [2010]). On the contrary, the Brown model is often used in UAV aerial photogrammetry due to the mapping scale that is similar to close-range photogrammetry and lack of accurate EO parameters. The UAV-dedicated processing software tools usually adopt the Brown model (Pix4D SA [2016], Agisoft [2014], Drone Mapper [2016]).

The size of a particular calibration set may be even larger and depends on the system and type of calibration (Grün [1982]). However, the use of inappropriate additional parameters (e.g. parameters have no foundations based on observable physical phenomena) can often lead to over-parametrisation resulting in weakening the solution for the coordinates of the target points (Fraser [1982]). An overview of the existing calibration methods and models is presented, e.g. in Abraham and Hau [1997], Fraser [1997], Clarke and Fryer [1998], Remondino and Fraser [2006].

The model implemented in the presented TopoBun adjustment is the Brown and comprises three radial lens distortion terms,  $K_1$ ,  $K_2$  and  $K_3$ , and two tangential distortion terms  $P_1$  and  $P_2$ . The model can be extended by two further parameters to account for affinity and shear within the image plane, but such terms are rarely, if ever, significant in modern digital cameras (Remondino and Fraser [2006]). The number of additional parameters is optional in the implemented adjustment, e.g. the estimation can be done only for  $K_1$  and  $K_2$ . The methodology and practical calibration of the employed camera is detailed in Sec. 6.5.1. The corrections are calculated as:

$$\begin{aligned} \Delta x &= \bar{x} \cdot (K_1 r^2 + K_2 r^4 + K_3 r^6) + P_2 (r^2 + 2\bar{x}^2) + 2P_1 \bar{x} \bar{y} \\ \Delta y &= \bar{y} \cdot (K_1 r^2 + K_2 r^4 + K_3 r^6) + P_1 (r^2 + 2\bar{y}^2) + 2P_2 \bar{x} \bar{y} \end{aligned} \quad (4.3)$$

where  $\bar{x}$  and  $\bar{y}$  are the reduced image coordinates:

$$\begin{aligned} \bar{x} &= (x - x_0) \\ \bar{y} &= (y - y_0) \end{aligned} \quad (4.4)$$

The square of radial distance  $r^2$  is calculated as:

$$r^2 = \bar{x}^2 + \bar{y}^2 \quad (4.5)$$

## 4.4 Aerial Observations

The benefits of aerial control for larger platforms were extensively studied in the past (Schwarz et al. [1993], Skaloud et al. [1996]). A comprehensive summary and evolution of SO approaches was presented for instance in Colomina [1999, 2007] or see Legat et al. [2006], Skaloud [2006] for the challenges in DiSO.

The effort of introducing an absolute position and attitude aerial control on MAVs is relatively recent as presented in Sec. 2.7. Such approaches allow us to significantly reduce, or even

completely eliminate the requirement on GCPs. That brings not only significant savings in the mapping operations, but also extends their applicability over inaccessible areas or regions with poor image texture. Each orientation method represents a certain trade-off between operational efficiency and resulting accuracy. The most important aspect is the control of the resulting quality that is related to geometrical redundancy and mitigation or detection of systematic effects. In this respect, relative aerial position and attitude observations between successive images allow to address some issues or inconveniences in aerial control (e.g. boresight) while reducing the effect of the other problems (e.g. GNSS bias). What is even more interesting is the fact that in the case of ISO, the replacement of absolute position and/or attitude observations with the relative ones, leads to similar mapping accuracy. This was demonstrated in Blázquez and Colomina [2012b] in the case of mapping with precise GNSS/IMU sensors on a conventional aircraft and in Skaloud et al. [2014] on a MAV.

In the mapping scenarios where automatic tie-point detection is either not possible or difficult due to problems with terrain texture, rapid processing is needed, small or sparse overlap between images exists or an elevation model is at disposition, the quasi direct orientation proposed in Blázquez and Colomina [2012a] offers an interesting alternative.

So called Fast AT is BA with either absolute or relative aerial control and a very few image observations. Indeed, these image observations are reduced to ground control and check points. As will be demonstrated, the Fast AT is a very relevant concept for MAVs in the situations where the terrain texture is limited, and/or the automatically generated tie-points are of poor and inconsistent quality, or their distribution is not regular. Moreover, it is also substantially faster since the automatic tie-point detection can be skipped. Tab. 4.1 overviews the most pertinent methods of sensor orientation used in photogrammetry ordered according to the availability/type of aerial control observations.

In addition, the classical models of absolute and relative aerial position and attitude control can be extended to spatio-temporal aerial control. Such modelling is possible through the inclusion of additional information on velocity and angular rate observations into the adjustment. This moves the optimisation problem from 3D to 4D. This extension allows, under certain conditions, to determine a constant synchronisation delay within the BA as investigated in Blázquez [2008] in the case of mapping with a manned aircraft. This is indeed an interesting option for MAVs that very often employ consumer market cameras without necessary adaptation for the precise recovery of mid-exposure time.

Method	Tie-points	GCPs	Aerial position obs.	Aerial attitude obs.	Camera self-calibration	Boresight	Lever-arm
Indirect SO	thousands	$\geq 3$	-	-	possible	-	-
ISO (position control)	thousands	optional	absolute	-	possible	-	needed/calibrated
		$\geq 3$	relative	-			needed
ISO (full aerial control)	thousands	optional	absolute	absolute	possible	needed/calibrated not needed	needed/calibrated
		$\geq 3$	relative	relative			needed
Fast AT	-	$\geq 1$	absolute	absolute	limited	needed not needed	needed
		$\geq 3$	relative	relative			needed
DiSO	-	-	absolute	absolute	-	needed	needed

Table 4.1 – Main sensor orientation approaches.

## 4.5 Absolute Aerial Position and Attitude Control

For aerial as well as for terrestrial images, the observations and conditions of exterior orientation can be introduced into the adjustment. In certain cases, the number of geodetic measurements, e.g. GCPs, can thus be reduced considerably or may even be completely eliminated in some configurations. The observation equation that models the relation between the imaging sensor and IMU body frame, for which absolute position is derived, takes the form:

$$\mathbf{X}^m + \mathbf{v}_X^m = \mathbf{X}_0^m + \mathbf{R}_c^m(\Gamma) \cdot \mathbf{A}^c + \mathbf{S}^m \quad (4.6)$$

where

$\mathbf{X}^m$	is the GNSS/IMU-derived position for one epoch in a Cartesian mapping frame $m$ ,
$\mathbf{v}_X^m$	is the vector of aerial position residuals,
$\mathbf{X}_0^m$	is the vector of a camera projection centre,
$\mathbf{R}_c^m(\Gamma)$	is the nine-elements rotation matrix from camera $c$ to $m$ frame parametrised by the traditional Euler angles $\Gamma = (\omega, \varphi, \kappa)$ ,
$\mathbf{A}^c$	is the camera-GNSS antenna lever-arm,
$\mathbf{S}^m$	is the possible positioning bias in the GNSS-derived positions.

Note, that time is a parameter for all components in Eq. 4.6 with the exception of  $\mathbf{A}^c$ . The absolute attitude observations can be expressed by the following equation:

$$\mathbf{R}_b^m(\chi + \mathbf{v}_\chi) = \mathbf{R}_c^m(\Gamma) \cdot \mathbf{R}_b^c(\Upsilon) \quad (4.7)$$

where  $\mathbf{R}_b^m$  is the GNSS/IMU-derived attitude parametrised by Euler angles  $\chi = (r, p, y)$ ,  $\mathbf{v}_\chi$  is the vector of attitude residuals, and  $\mathbf{R}_b^c(\Upsilon)$  is the IMU-camera boresight.

## 4.6 Relative Aerial Position and Attitude Control

Relative observations relate the position and attitude parameters of two consecutive epochs (Li and Stueckmann-Petring [1992], Blázquez and Colomina [2012a]). Differencing two sensor positions from Eq. 4.6 results in an observation equation for coordinate differences:

$$\Delta \mathbf{X}^m(t_{ij}) + \mathbf{v}_{\Delta X}^m = \mathbf{X}_0^m(t_j) - \mathbf{X}_0^m(t_i) + (\mathbf{R}_c^m(\Gamma_{t_j}) - \mathbf{R}_c^m(\Gamma_{t_i})) \cdot \mathbf{A}^c \quad (4.8)$$

where  $t_i$  and  $t_j$  distinguish the two epochs. In comparison to Eq. 4.6, the term  $\mathbf{S}^m$  is cancelled for certain  $(t_j - t_i) < \Delta t$ , but the noise is increased by  $\sqrt{2}$  and must be still considered in the stochastic model. The application of differencing makes use of the fact that certain effects of the neighbouring GNSS positions within strips or blocks occur systematically. The attitude-

relative observations can be expressed as follows:

$$\Delta \mathbf{R}_b^m(\chi_{t_{ij}} + \mathbf{v}_{\Delta\chi}) = \mathbf{R}_c^m(\Gamma_{t_j}) \cdot \mathbf{R}_m^c(\Gamma_{t_i}) \quad (4.9)$$

Note, that the boresight parameter vanished in Eq. 4.9 compared to Eq. 4.7. Hence, this method represents an attractive alternative in the context of MAVs for three reasons. Firstly, an angular misalignment, so called boresight, between a camera and an IMU does not have to be determined. Secondly, the effect of the IMU initial alignment is mitigated, and lastly, the effect of possible systematic errors in satellite positioning is mitigated. Since the observations are relative position vectors between images, the differencing operation removes the time-dependent biases. These could be considered constant between two subsequent exposures. This opens up the possibility of constraining the relative baselines within flight lines where the time period between successive exposures is short (typically  $dt < 5-10$  s) while the satellite-receiver geometry does not vary significantly. In other words, if present, the position bias (e.g. incorrect ambiguities) gets eliminated by the process of differencing without the need of additional modelling which may not correspond to reality (e.g. a drift is not linear within a flight-line).

### 4.7 Absolute Spatio-temporal Control

There is a possibility of determining whether a constant synchronisation error  $\Delta t$  is present in the data or not. This analysis can be done via an extension of the classical models of absolute and relative aerial position and attitude control to spatio-temporal aerial control. A potential error  $\Delta t$  can be positive or negative. This is illustrated in Fig. 4.3. Ideally, the imaging sensor issues a synchronisation signal at the moment of sensor full opening (in global shutter technology), or in the middle of exposure (in rolling shutter technology). However, the imaging sensor might issue a synchronisation signal at a different moment. Therefore, an error can be positive or negative or, in other words, the time marks can be delayed or ahead in time. The problem of the origin of  $\Delta t$  is discussed in detail in Sec. 6.4.2 with a practical example in Sec. 7.5.

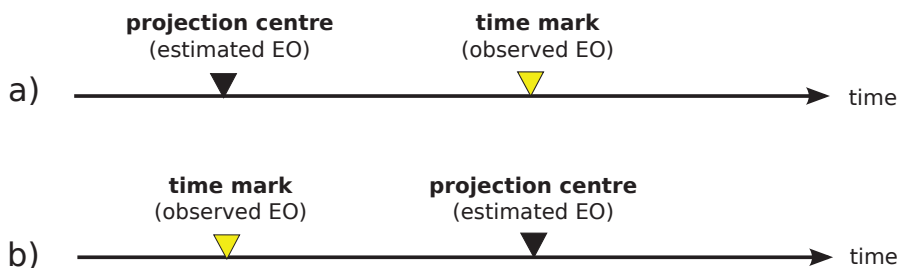


Figure 4.3 – Two types of wrong time synchronisation: Case a) depicts time delay (positive) between the observed and estimated EO parameters. Case b) depicts negative delay that is caused by registering the time mark ahead in time.

Absolute aerial observation that relates the  $\Delta t$  synchronisation parameter to the position and velocity  $\mathbf{V}^m$  with its residuals  $\mathbf{v}_V^m$  is:

$$\mathbf{X}^m + \mathbf{v}_X^m = \mathbf{X}_0^m + \mathbf{R}_c^m(\Gamma) \cdot \mathbf{A}^c + \mathbf{S}^m - (\mathbf{V}^m + \mathbf{v}_V^m) \cdot \Delta t \quad (4.10)$$

In the observations, the error caused by  $\Delta t$  can be both added or subtracted from the position observation as long as it is consistent with the correction definition applied to the original time marks. For example, if the estimated  $\Delta t$  has a negative sign, the time marks are registered ahead in time and must be corrected by adding this  $\Delta t$  to the original time marks. Absolute spatio-temporal attitude observations can be expressed by the following equation:

$$\mathbf{R}_b^m(\chi + \mathbf{v}_\chi) = \mathbf{R}_c^m(\Gamma) \cdot \mathbf{R}_b^c(\Upsilon) + \dot{\mathbf{R}}_b^m \cdot \Delta t \quad (4.11)$$

In short, the rate change of angular matrix  $\dot{\mathbf{R}}_b^m$  can be approximated as follows:

$$\dot{\mathbf{R}}_b^m = \mathbf{R}_b^m(\chi + \mathbf{v}_\chi) \cdot \boldsymbol{\Omega}_{mb}^b \quad (4.12)$$

where  $\boldsymbol{\Omega}_{mb}^b$  is the skew-symmetric matrix of transformed and calibrated angular velocities  $\boldsymbol{\omega}_{mb}^b$  sensed by the IMU after transformation to a mapping frame, and  $\mathbf{v}_{\omega_{x,y,z}}$  are the angular velocity residuals. During the calibration process, the angular rates are corrected for deterministic and stochastic errors as discussed in detailed in Sec. 6.5.2.

$$\boldsymbol{\Omega}_{mb}^b(\boldsymbol{\omega}_{x,y,z} + \mathbf{v}_{\omega_{x,y,z}}) = \begin{pmatrix} 0 & -\omega_z & \omega_y \\ \omega_z & 0 & -\omega_x \\ -\omega_y & \omega_x & 0 \end{pmatrix} \quad (4.13)$$

## 4.8 Relative Spatio-temporal Control

For the sake of completeness, relative spatio-temporal models are defined here, albeit these were not implemented and tested in the scope of this research. A relative aerial observation relates  $\Delta t$  synchronisation parameter to the relative position and velocity.  $t_i$  and  $t_j$  distinguish the two epochs.

$$\Delta \mathbf{X}^m(t_{ij}) + \mathbf{v}_{\Delta X}^m = \mathbf{X}_0^m(t_j) - \mathbf{X}_0^m(t_i) + (\mathbf{R}_c^m(\Gamma_{t_j}) - \mathbf{R}_c^m(\Gamma_{t_i})) \cdot \mathbf{A}^c - (\Delta \mathbf{V}^m(t_{ij}) + \Delta \mathbf{v}_V^m(t_{ij})) \cdot \Delta t \quad (4.14)$$

Relative temporal attitude observations can be expressed by the following equation:

$$\Delta \mathbf{R}_b^m(\chi_{t_{ij}} + \mathbf{v}_{\Delta \chi}) = (\mathbf{R}_c^m(\Gamma_{t_j}) + \dot{\mathbf{R}}_b^m(t_j) \cdot \Delta t) \cdot (\mathbf{R}_m^c(\Gamma_{t_i}) + \dot{\mathbf{R}}_m^b(t_i) \cdot \Delta t) \quad (4.15)$$

## 4.9 Stochastic Models of Aerial Control

Proper observation weighting is very important in BA. The variances in absolute position and attitude observations are usually derived from the corresponding diagonal elements

of a covariance matrix from a Kalman filter/smoother. Despite IMU error modelling and IMU calibration, the GNSS/IMU-derived observations remain time-correlated. Absolute positions might be affected by wrongly estimated ambiguities or multipath effects, while IMU observations suffer from remaining unmodelled systematic errors as well as from residual effects due to the initialisation. A typical approach for handling these drawbacks is to introduce an additional shift and/or drift parameters. In the case of relative position control, the relation of variance propagation can be used if we assume elimination of a constant GNSS shift/bias between the subsequent observations within a strip and during a flight due to differencing. In Eq. 4.16,  $\sigma_{X(t_{ij})}$  parameter represents a standard deviation of a relative position on one axis calculated according to Eq. 4.8 from two consecutive epochs  $\sigma_{X(t_i)}$  and  $\sigma_{X(t_j)}$ .

$$\sigma_{X(t_{ij})} = \sqrt{\sigma_{X(t_i)}^2 + \sigma_{X(t_j)}^2} \quad (4.16)$$

The stochastic models of aerial attitude control are not straightforward. Given the quality and error characteristics of MEMS-based on IMUs, the on-line calibration process does not completely eliminate all the systematic errors due to the observability issues. Hence, time-correlation prevails. This may lead to unrealistic (i.e. low) covariance matrices for the attitude estimates and hence incorrect stochastic modelling in the BA (Martínez et al. [2007]). However, over a short time interval within a flight time (i.e. limited acceleration and orientation changes), the accuracy of relative attitude aerial observations can be predicted by applying stochastic models for gyroscopes. In many cases this can be approximated as a superposition of a random walk (i.e. integrated white noise)  $\omega_{RW}$  and uncalibrated part of gyro drift  $\omega_b$ .

$$\sigma_{\omega}^2 = \sigma_{\varphi}^2 = \sigma_{\kappa}^2 = (\omega_{RW} \text{ deg/s} \cdot \sqrt{\Delta t})^2 + (\omega_b \text{ deg/s} \cdot \Delta t)^2 \quad (4.17)$$

From our empirical experience, standard deviations of a relative kappa angle shall differ from those of omega and phi. It is usually sufficient to multiply  $\omega_b$  by a constant  $k = 1.5$ . Again, the approximation of Eq. 4.17 holds only within a short time interval  $\Delta t$  between two consecutive images within the same flight line. In our evaluation, the maximal  $\Delta t$  was set to 10 seconds. This constraint eliminates the observations between the separate flight lines of the trajectory. The variances of velocity observations are usually derived from the corresponding diagonal elements of a covariance matrix by the Kalman filter/smoother. Angular rates are observed by an IMU and corrected for Earth's rotation and deterministic stochastic errors. Angular rate covariances can be derived from the signal error characteristics of an inertial sensor. Namely from the remaining uncompensated errors (after calibration) of a gyroscope. The value  $\sigma_{\omega_{xzy}}$  is stated in Eq. 4.18, where the  $\sigma_{WN}$  is white noise,  $\sigma_{\Delta t}$  is correlated noise,  $\sigma_{RC}$  is a random constant and  $\sigma_{S_G}$  is a residual scale-factor.

$$\sigma_{\omega_{xzy}}^2 = \sigma_{WN}^2 + \sigma_{\Delta t}^2 + \sigma_{RC}^2 + \sigma_{S_G}^2 \quad (4.18)$$



## 4.10 Bundle Adjustment

Bundle adjustment is a unified method aimed to simultaneously estimate the internal and external camera parameters and 3D coordinates of the scene points in a statistically optimal manner using least square technique with all available observations (Förstner and Wrobel [2016]). In the presented development, a non-linear triangulation problem is reduced to an optimisation problem which is solved using a generalised Gauss-Newton process taking into account functional and stochastic models of each observation. The least squares method tries to find the vector of the adjusted parameters  $\hat{\mathbf{x}}$  to minimise the quadratic error of the parameters in fitting the observation models. It is extended by linearisation of the model to optimally solve for non-linear systems, Eq. 4.19 where  $\Sigma$  is the covariance matrix of the parameters and  $\mathbf{v}_-$  is the vector of a subset of all observation residuals listed below.

$$\mathbf{v}_-^T \Sigma^{-1} \mathbf{v}_- \rightarrow \min \quad (4.19)$$

$\mathbf{v}_{x,y}$	Image observations,
$\mathbf{v}_X$	absolute aerial positions,
$\mathbf{v}_\chi$	absolute aerial attitude,
$\mathbf{v}_{GCP}$	object coordinates of GCPs,
$\mathbf{v}_{IO}$	IO parameters,
$\mathbf{v}_{\Delta X}$	relative aerial positions,
$\mathbf{v}_{\Delta \chi}$	relative aerial attitude,
$\mathbf{v}_V$	velocities,
$\mathbf{v}_\omega$	angular rates,
$\mathbf{v}_S$	system parameters.

Collinearity and other equations presented in the previous sections are non-linear, hence a non-linear least square method must be employed. This method needs sufficiently close initial values to find the values of the parameters satisfying minimisation criterion in a global sense. Fig. 4.4 illustrates elements of a bundle block adjustment.

The solution of the BA is given by iteration, solving for the update vector in Eq. 4.21 and updating the initial approximations at each step. This is an implemented weighted Gauss-Newton method for the solution of non-linear systems. It should be noted that the weakness of the Gauss-Newton method lies in the possibility that the solution will not converge to a global minimum or will not converge at all because a particular update vector "overshoots". If this occurs, it is possible to employ a damping factor to normal equations. This technique is widely implemented as the Levenberg-Marquardt algorithm. For further details see, e.g. Teunissen [2000] with a practical application to the BA presented in Triggs et al. [2000] and Jacobsen [2002a].

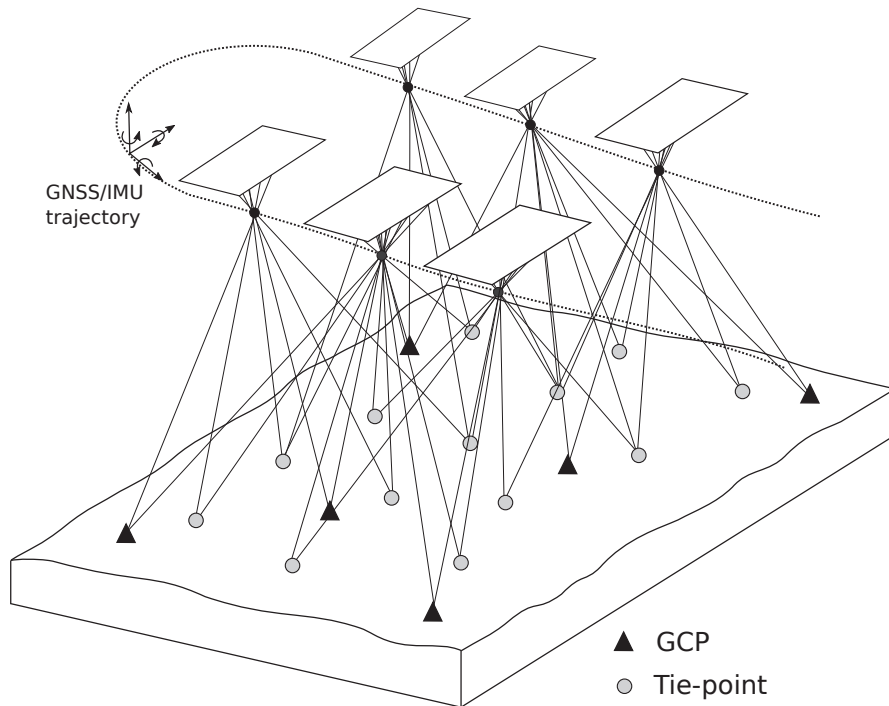


Figure 4.4 – Bundle block scene with images, tie-points, GCPs and GNSS/IMU trajectory that results in absolute or relative camera EO parameters, velocity and angular rate observations.

#### 4.10.1 Functional Model

Mathematical models given above are non-linear, therefore, they must be linearised with respect to their corresponding parameters. Combining all the observation equations, a functional model according to the adjustment of observation equations is given by:

$$\mathbf{l} + \mathbf{v} = \mathbf{A} \delta \hat{\mathbf{x}} \quad (4.20)$$

where

- $\mathbf{l}$  is the vector of discrepancies ("observed" minus "computed" observations),
- $\mathbf{v}$  is the vector of residuals,
- $\mathbf{A}$  is the Jacobian matrix consisting of differential quotients which describe the functional relation between parameters,
- $\delta \hat{\mathbf{x}}$  is the vector of corrections.

The solution of all observation equations for one set of values for unknown parameters is obtained by solving normal equations:

$$(\mathbf{A}^T \mathbf{P} \mathbf{A}) \delta \hat{\mathbf{x}} = \mathbf{A}^T \mathbf{P} \mathbf{l} \quad (4.21)$$

where  $\mathbf{P}$  is the weight matrix. The Eq. 4.21 can be also expressed as:

$$\mathbf{N} \delta \hat{\mathbf{x}} = \mathbf{n} \quad (4.22)$$

where

$\mathbf{N}$  is the normal equation matrix:  $\mathbf{N} = \mathbf{A}^T \mathbf{P} \mathbf{A}$ ,

$\mathbf{n}$  is the right side of the normal equation:  $\mathbf{n} = \mathbf{A}^T \mathbf{P} \mathbf{l}$ .

The vector of unknowns  $\hat{\mathbf{x}}$  is calculated by adding the vector of corrections  $\delta \hat{\mathbf{x}}$  to the vector of initial values  $\mathbf{x}^0$ .

$$\hat{\mathbf{x}} = \mathbf{x}^0 + \delta \hat{\mathbf{x}} \quad (4.23)$$

The adjustment is solved iteratively where the corrected values from Eq. 4.23 in iteration  $k$  are used as new starting values in the next iteration  $k+1$ . This process is repeated, e.g. until the maximal correction  $|\delta \hat{\mathbf{x}}|$  from Eq. 4.21 is smaller than the convergence criteria.

#### 4.10.2 Stochastic Model

For the adjustment of observation equations, a normal distribution with known variances is assumed. Gauss-Markov adjustment model does not consider gross errors and considers that the introduced standard deviations are correct. As the reality differs from ideal cases, gross errors may appear. Therefore, an implementation of some outliers detection techniques is essential for assuring algorithm convergence. The following equation describes an implemented stochastic model:

$$\mathbf{Q}_{ll} = \frac{1}{s_0^2} \mathbf{K}_{ll} = \mathbf{P}^{-1} \quad (4.24)$$

where

$\mathbf{P} = \mathbf{Q}_{ll}^{-1}$  is the weight matrix where only the diagonal elements are set with non-zero elements, assuming stochastically independent observations,

$s_0$  is the a priori standard deviation of unit weight before the adjustment,

$\mathbf{K}_{ll}$  is the covariance matrix with standard deviations of observations.

After the least square solution is converged, the vector of residuals is computed from the following equation:

$$\mathbf{v} = \mathbf{A} \delta \hat{\mathbf{x}} - \mathbf{l} \quad (4.25)$$

## Chapter 4. Measurements, Models and Estimation Methods

---

An empirical standard deviation of the unit's weight (a posteriori)  $\hat{\sigma}_0$  is calculated as follows:

$$\hat{\sigma}_0^2 = \frac{\mathbf{v}^T \mathbf{P} \mathbf{v}}{r} \quad (4.26)$$

The redundancy  $r$  is a difference between the number of observations and unknowns. Next, the weight coefficient matrix of the adjusted observations  $\mathbf{Q}_{\hat{i}\hat{i}}$  is calculated:

$$\mathbf{Q}_{\hat{i}\hat{i}} = \mathbf{A} \mathbf{N}^{-1} \mathbf{A}^T \quad (4.27)$$

Standard deviations of the adjusted unknowns is calculated as:

$$\sigma_x = \hat{\sigma}_0 \text{diag}(\sqrt{\mathbf{Q}_{\hat{x}\hat{x}}}) \quad (4.28)$$

where

$$\mathbf{Q}_{\hat{x}\hat{x}} = \mathbf{N}^{-1} \quad (4.29)$$

The weight coefficient matrix  $\mathbf{Q}_{vv}$  of the residuals is:

$$\mathbf{Q}_{vv} = \mathbf{Q}_{ll} - \mathbf{Q}_{\hat{i}\hat{i}} \quad (4.30)$$

Diagonal elements of the matrix  $\mathbf{Q}_{vv}$  from Eq. 4.30 are important for reliability, the search for "gross" errors according to the method of Baarda (Baarda [1968]), and for variance-component estimation with a practical implementation demonstrated, e.g. in Kruck [2001], Jacobsen [2002a] or Triggs et al. [2000]. A standard deviation of a residual is calculated from the following equation:

$$\sigma_v = \hat{\sigma}_0 \sqrt{\mathbf{Q}_{vv}} \quad (4.31)$$

A residuum according to Baarda  $w_i$  is derived from:

$$w_i = \frac{v_i}{\sigma_{v_i}} \quad (4.32)$$

where  $v_i$  is a residual and  $\sigma_{v_i}$  is the estimated standard deviation of a residual. Assuming that residuals  $v$  have Gaussian distribution  $N(0, 1)$ , the measurement  $i$  is rejected when:

$$|w_i| > c \quad (4.33)$$

The confidence level of  $\alpha = 99.7\%$  corresponds to a critical test value  $c = 3$ ,  $\alpha = 99.9\%$  results in  $c = 3.3$ . If the observation is rejected, it is removed in the next adjustment cycle, and the remaining observations are adjusted again. This procedure is carried out until no more outliers are detected. It has to be noted that this statistical test assumes that only one blunder is present in the system, the one with the highest value  $w_i$ . However in practice, in configurations with a higher redundancy and better reliability, several errors can be detected at the same time as

discussed, e.g. in Kersten et al. [1992] and practically implemented, e.g. in Kruck [2001].

## 4.11 Program and Data Structure

This section provides a brief introduction to the developed BA tool TopoBun. The implementation is done in Matlab and uses an input compatible with the state-of-the-art adjustment tools Bingo (Kruck [2001]) and Fembun (Lichti and Chapman [1997]).

The program structure is depicted in Fig. 4.5. The scheme already assumes processed GNSS/IMU trajectory and its products (positions, attitude, velocities, angular rates) and image observations. A detailed processing work-flow of images and GNSS/IMU data is described in Sec. 7.2. The data processing can be split into three phases: data preparation and

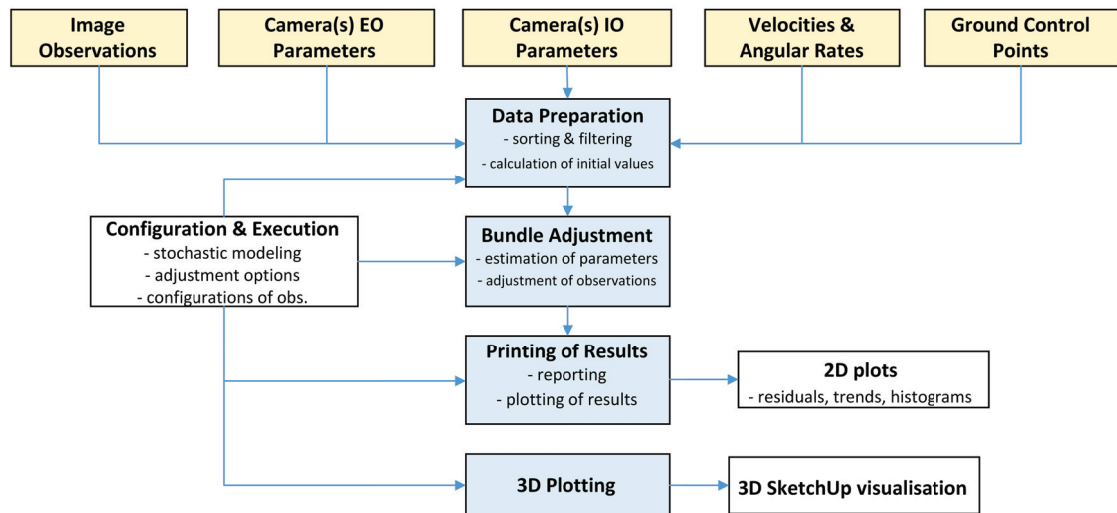


Figure 4.5 – TopoBun data flow chart.

formatting, BA, and reporting. These modules are executed from a command script. This script configures the way the observations are treated in the BA, configures stochastic models (e.g. of gyroscopes for relative attitude observations) and sets a priori adjustment parameters, e.g. the number of iterations, convergence criteria, etc. Each of the blue modules can be run independently, i.e. after the *Data Preparation*, the *Bundle Adjustment* can run several times with different configuration without the need of running the entire processing work-flow. The following section discusses some of the modules.

### 4.11.1 Data Preparation and Formatting

In initialisation, the observations of image point coordinates, GCPs, and exterior orientation elements are read from files, filtered, checked, transformed into internal format, and stored in data structures. Regarding the basic filtering of image observations, the following adequacy is

verified:

- The number of observations in each image is sufficient: each image has at least three tie-points.
- The completeness of observations: observations are complete and have a correct format.
- Observability: each point is visible on at least 2 images.

Tie-points which failed the quality control are deleted. Similar filtering is done for camera EO parameters. Several formats are supported, both in degrees or gons. The next step is the calculation of approximate object coordinates of tie-points. With the problem of intersection, EO parameters of images and camera IO parameters are used to determine the coordinates of tie-points in the object frame. This employs the principle of stereovision and combines all observations in a linear least-square manner that has a direct analogue to the DLT (Direct Linear Transformation) method. The method was implemented according to an algorithm published in Hartley and Zisserman [2003]. The latter implementation assumes that the camera IO and EO parameters are provided with a reasonable accuracy, e.g. camera IO parameters from the optical sensor manufacturer and sensor EO parameters from GNSS/IMU integration.

It has to be noted that image observations derived by the state-of-the-art computer vision algorithms are filtered for gross errors. This is, for instance, the case for the employed approaches using the Pix4D Mapper. The procedure of obtaining image observations from images is described in Sec. 7.2.

### 4.11.2 Bundle Adjustment

The BA itself is developed according to the described theoretical and functional stochastic model from Sec. 4.10. Regarding the issues of computational speed and memory needs, the program takes advantage of internal functions of Matlab by working with sparse matrices. Indeed, multiplication and inversion of matrices are operations with high computing effort. In adjustment computations, however, many matrix elements are zero. Therefore, the implementation is such that only the non-zero coefficients are stored in a vector by rows and corresponding column numbers. The design of normal matrix is detailed in Appendix B with partial derivatives of observations presented earlier in this chapter.

The outlier detection is implemented in two steps. First, "gross" errors in image observations are detected during the initial calculation of approximate values of the object point coordinates. Then, data snooping according to Baarda (Baarda [1968]) is performed.

### 4.11.3 Graphical Output and Reporting

A scene can be displayed in 3D environment of SketchUp (Trimble Inc. [2016]). The process parameters calculated in the BA are sent to a function converting all entities to SketchUp

primitives in Ruby scripting language. These Ruby scripts are then loaded to SketchUp and displayed. The advantage of this approach is the capability of SketchUp to display large quantities of features and fluent navigation in a 3D environment. An example is shown in Fig. 4.6. On the contrary, Matlab plots are used for visualising in 2D. More examples of some possible plots are given during the presentation of results from real projects in Chap. 7.

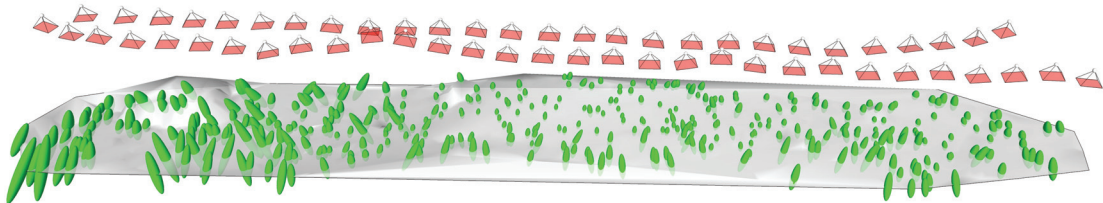


Figure 4.6 – 3D view on a corridor scene with error ellipsoids of tie-points and cameras.

#### Summary

This chapter introduced the mathematical model of collinearity that was extended by additional parameters of lens distortion. Furthermore, observation models of absolute, relative, and spatio-temporal aerial control were described. A significant part of this chapter was devoted to a stochastic modelling. Indeed, a proper observation weighting is essential in aerial control and as such, it must be realistic and must properly model sensor errors. The next part discussed the concept of BA. Functional and stochastic models of Gauss-Newton adjustment were presented with an example of an outlier detection according to Baarda. One of the main contributions to the overall scope of the thesis was the development of the BA tool TopoBun.





# 5 Developed MAV Platforms and Sensor Equipment

*This chapter discloses the overall concept and challenges in implementation of navigation and imaging sensors into custom developed MAV platforms. Although the nature of this development is rather practical, its significance for mapping accuracy is at least as important as that of software development. Nonetheless, the goal of this chapter is not to provide an exhaustive study of hardware components, but rather to demonstrate their importance in the design of MAVs for accurate mapping.*

## 5.1 General Challenges

Accurate georeferencing of airborne data is an exercise in systems integration and data processing. In general, the UAV platform market is getting more favourable every year in terms of price and performance. Manufactures produce sophisticated platforms, autopilots, and camera gimbals. Nevertheless, the design is often closed and does not allow access or control of vital sensor components. Moreover, the platforms cannot be easily extended with additional sensors for a precise sensor orientation or for improving their capacity in autonomous navigation in case of a signal interference or denial of GNSS service.

The current availability and affordability of inertial and GNSS technology in principle allows to create a relatively small and integrated system from of-the-shelf components. Although its implementation is non-trivial, its correct functionality is a prerequisite for ISO and DiSO from MAVs. The presented MAV platforms offer such capacity while having comparable flight characteristics to the state-of-the-art commercial MAV systems.

Physical and operational limitations imposed by UAVs and MAVs, in particular, constrain the navigation and remote sensing payload in several aspects. Constraints in the sensor's size and weight limit the ease of integration. Furthermore, they proportionally limit the sensor's quality and accuracy. Indeed, a correlation between size and quality/accuracy is known for IMU sensors (Titterton and Weston [1997]). Hence, the selection of sensors is a matter of compromise guided by strict design limitations. Note that some of the commercial GNSS/IMU systems became available only after the presented MAVs were constructed.

Although the general concept of processing of gathered GNSS/IMU data is similar to that of

## Chapter 5. Developed MAV Platforms and Sensor Equipment

---

manned platforms, there are important variations in the system and sensor calibration as well as in the GNSS/IMU integration. The difficulty of constructing a MAV capable of direct georeferencing with cm-level accuracy can be explained by the following points:

- The hardware integration of sensors is not trivial.
- The implementation and synthesis of a consumer grade camera with a GNSS/IMU is not straightforward and proper calibration is necessary.
- Contrary to the indirect orientation approach, the complexity of DiSO and ISO oblige to perform carrier-phase differential GNSS processing, either real-time or post-processing. The latter implies the use of a base station receiver or availability of a national correction service.
- The IMU systems with sufficient performance, e.g. tactical or navigational grade are not small enough to be mounted on MAVs and low-cost MEMS-based IMUs still do not provide sufficient precision of attitude.
- Price of the geodetic-grade GNSS technology and size/weight/price of the multi-frequency antennae is still considerable with relation to the other drone components.

### 5.2 Platform Development

This section presents custom development of a multirotor and a fixed-wing MAVs.

#### 5.2.1 TOPO Copter

The hardware development was initiated by a construction of a multirotor system. The overall weight was constrained by 5 kg to remain within the MAV category. The custom design allows mounting the necessary devices needed to perform modern photogrammetry with aerial GNSS/IMU observations. The platform is equipped with eight brushless motors to support the needed payload and to increase the redundancy in case of engine failure. The MAV accommodates an open-source autopilot with appropriate sensors to perform stabilised and autonomous flights. The autopilot is based on a do-it-yourself project intensively developed during past years by the community of engineers and amateurs called Pixhawk (Meier et al. [2012]). This autopilot unit includes MEMS gyroscopes and accelerometers, a 3-axis magnetic sensor, a barometric pressure sensor, and a single frequency low-cost GPS receiver. The cooperation of these navigation components allows horizontally and vertically stabilised positioning of the system as well as position hold, return to the launch site, or mission flights according to pre-planned trajectories.

The frame consists of carbon tubes and glass fibre base plates. The MAV is depicted in Fig. 5.1. Special attention is given to a camera mount. This very light servo-powered gyro-stabilised camera holder keeps the equipment in level (or in selected inclination) during the flight. Such

mechanisation ensures stable system calibration parameters, i.e. spatial and angular offsets and at the same time it dampens the vibrations from the engines. The sensor mount can be tilted remotely to a desired angle along its horizontal axis. Fig. 5.2 shows a schematic location of the navigation components on the sensor mount.

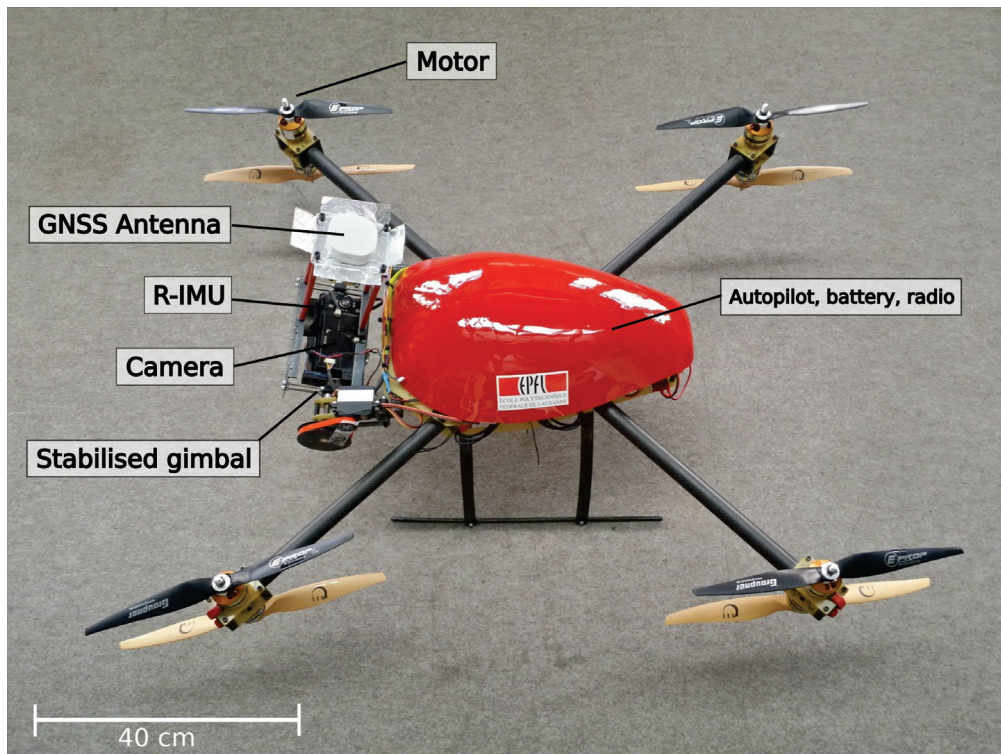


Figure 5.1 – Multirotor system.

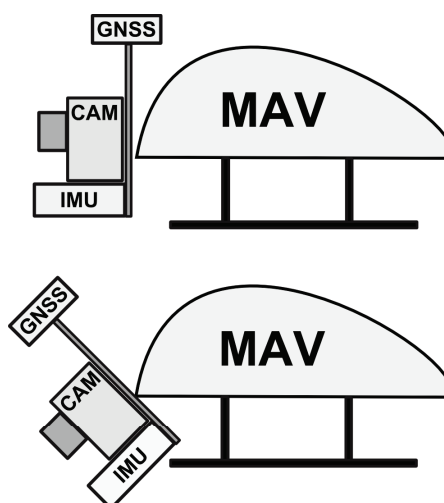


Figure 5.2 – Schematic sketch of the stabilised sensor mount for two distinct tilting angles. The relative position and orientation between the sensors do not change when tilting the mount.

## Chapter 5. Developed MAV Platforms and Sensor Equipment

The system is powered by high capacity LiPO (Lithium-Polymer) batteries. Depending on the application and especially on the payload (1 kg – 1.5 kg), the flight times vary from 10 to 15 minutes. The system with all the equipment and additional sensors weighs 4.8 kg.

To enhance the safety either for people and public infrastructure on the ground, or also for the MAV itself, the multirotor is optionally equipped with a parachute to face emergency situations. The parachute is currently deployed manually by the operator. As a consequence of this additional payload of 240 grams, the flight times lower to approximately 8 minutes. Its functionality was tested during several field tests and the minimal flying altitude for a correct deployment was empirically estimated to be about 40 m.

The selected coaxial concept, i.e. two engines on each arm of the multirotor, has its specific advantages and disadvantages compared to a classical flat configuration. Fig. 5.3 and Tab. 5.1 show the basic characteristics of this configuration. In manual mode the MAV multirotor can be operated by one pilot or as a cooperation between two operators: one pilot and a second person responsible for the image acquisition. The system structure is universal as it can be (relatively easily) modified into a version with motors with higher power to increase the overall payload capacity.

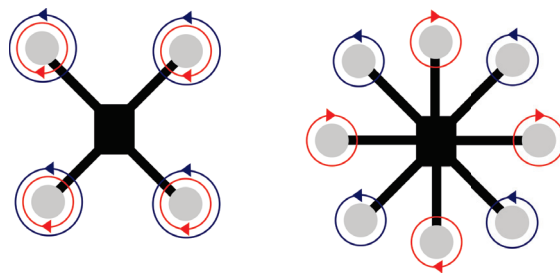


Figure 5.3 – Schematic sketch of the coaxial and flat multirotor configurations.

Advantages	Disadvantages
Higher redundancy Improved compactness More agile Wider field of view for the camera Better response to wind gusts Better orientation for the pilot	Efficiency loss 15%-30%

Table 5.1 – Advantages and disadvantages of the selected coaxial configuration.

### 5.2.2 TOPO Plane

In order to fully examine the potential of an advanced sensor integration in mapping with MAVs, the flight should be performed under different scenarios (e.g. speed). The VTOL drone is limited by its operational radius, flying speed, and height, as well as endurance. For this reason, a complementary fixed-wing platform was developed. The design specifications were

established by experience gained during the VTOL construction.

The plane is based on a popular hobby platform that was heavily modified in order to accommodate all the navigation and imaging sensors. Its structure is made of expanded polypropylene foam. The plane is easy to assemble and repair with ordinary hobby-grade tools. It is very stable in flight and offers (after modification) a large internal compartment for the photogrammetric payload. It has a wingspan of 1630 mm and length of 1170 mm. The maximal payload capacity is around 800 g. The operational weight varies between 2200-2800 g, Fig. 5.4. Despite the weight, the flexible nature of the construction material makes the platform resistant to damage. The cost of the system components is significantly lower with respect to the size and endurance of comparable platforms such as the Sirius Pro (MAVinci GmbH [2015]). Endurance with 600 g payload is approximately 40 minutes. The plane is controlled by the Pixhawk autopilot.

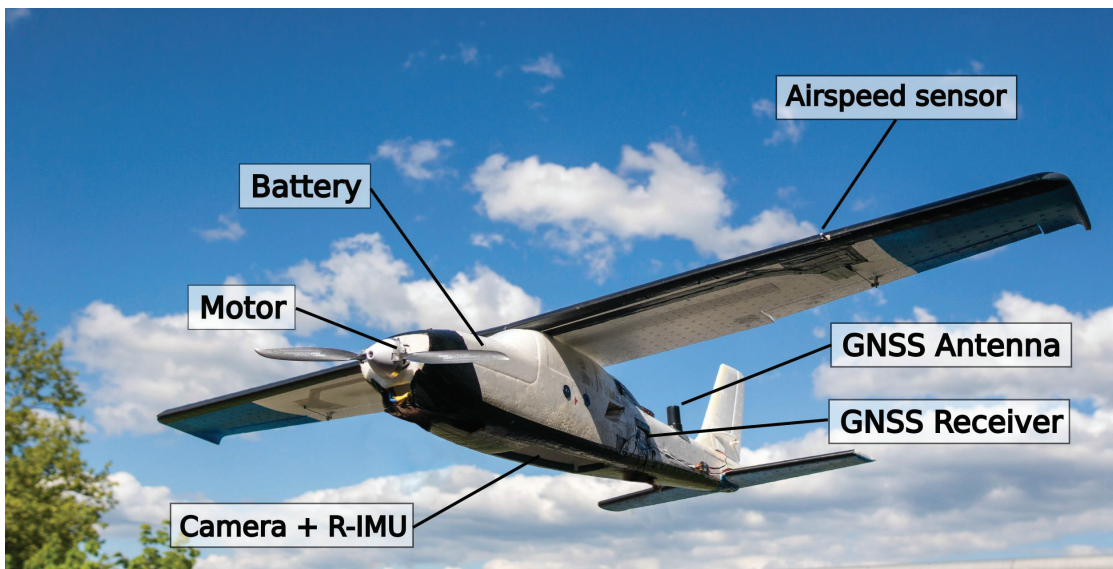


Figure 5.4 – Fixed-wing platform.

### 5.2.3 Sensor Payload

Imaging and navigation components are of great importance to the mapping accuracy of ISO and DiSO. The imaging sensor usually comprises one or more cameras or another type of optical device as discussed in Sec. 2.5. The two main components of the navigation system are the IMU and GNSS sensors, which are software-integrated using a state estimation filter/smoothing. After such integration, a set of EO parameters is calculated for distinct camera events. Additional sensors, such as magnetometers and air pressure sensors can be used to augment the performance of trajectory determination.

Size, weight, and cost restrictions seriously limit the selection of the navigation sensors. In general, the selection for MAVs is limited to the two lowest accuracy classes of these devices; a MEMS-based IMU and a code-solution single-frequency GNSS receiver. As a

result, the accuracy is too low for the EO parameters to be used for direct georeferencing. Nevertheless, the recent progress in miniaturisation has brought new and affordable multi-frequency GNSS receivers. Therefore, the problem of precise positing on MAVs is solved. From the attitude accuracy point of view, the small yet affordable MEMS IMUs do not often provide sufficient accuracy for performing DiSO. However, as it will be demonstrated later, they can still significantly contribute in certain mapping scenarios. Furthermore, an employment of a R-IMU increases the potential of MEMS technology in attitude determination on MAVs (Clausen et al. [2016]).

The following section describes in detail the imaging and navigation sensors used on the developed platforms. The sensors were identical on both platforms with a small difference in the camera body.

### 5.3 Optical Sensors

The primary imaging sensor on the multicopter MAV is the Sony NEX 5N, while the fixed wing is equipped with the newer model Sony NEX 5R. Apart from some settings options, the cameras share the same body and APS-C (Advanced Photo System type-C) sensor, the size of which is  $25.1 \times 16.7$  mm. The only considerable difference between them is in resolution that is 14 Mpix and 16 Mpix, respectively (Sony [2016]).

Overall, the quality of this mirror-less camera is comparable with an entry-level DSLR (digital single-lens reflex) camera despite being considerably smaller (only  $111 \times 59 \times 39$  mm) and lighter (210 g without lens). These properties make it highly suitable for MAV platforms. An important aspect is the lack of an image/sensor stabilisation system. This helps to keep the IO parameters more stable over time and throughout a flight.

The cameras were modified for better performance and integration into the MAV systems. The on-board video-processing segment procures a digital to analogue conversion, video streaming together with on-screen-display information of the current camera state, as well as the telemetry data from the autopilot. A servo signal emitter of the autopilot triggers the camera shutter, and a hotshoe adapter captures the camera's flash signal that is time-stamped by a GNSS receiver. These modifications together with the external power supply convert this low-cost camera to a photogrammetric tool. The problem of time synchronisation with GNSS/IMU system is addressed in Sec. 6.4 and practically verified in Sec. 7.5.

The lens selection was restricted by stringent weight and size limits given by the MAVs maximal payload capacity and dimensions of their internal compartments.

The cameras are equipped with a 16 mm fixed focal <sup>1</sup> and f/2.8 Sony lens which size is  $6.2 \times 2.2$  cm and weight 70 g. When manual focus is chosen, the lens offers a sufficient stability of the IO parameters throughout a mission. The stability is owing to a missing optical stabilisation system and solid construction quality. Although this lens suffers from high distortion due to its wide field of view, it appears to be a good complement to Sony camera. The camera-lens

---

<sup>1</sup>16 mm focal length on a APS-C sensor (1.5 crop factor) lens which is the equivalent to 24 mm on a full-frame sensor.

system is depicted in Fig. 5.5. The results from lens calibration are summarised in Sec. 6.5.1.



Figure 5.5 – Sony NEX 5N with 16 mm Sony lens (Sony [2016]). Image courtesy of B & H Foto & Electronics Corp. [2016].

## 5.4 GNSS Positioning

GNSS is a component essential for positioning on which the overall position, velocity, and indirectly also attitude accuracy delivered by GNSS/IMU, depend. GNSS provides both the position and velocity updates which are used to correct for the imperfections of inertial sensors. This is particularly effective due to the complimentary characteristics of the two systems. GNSS receivers can be classified according to the number of tracked signals (ESA Navipedia [2014]). Multi-frequency GNSS receivers provide observations under higher dynamics than single-frequency receivers, they have advanced multipath filters and generally provide highly accurate results. Single-frequency receivers have more favourable pricing, reduced size, and lower power consumption. There are two categories of single-frequency receivers: geodetic and low-cost, as they significantly vary in price as well as performance, e.g. in signal tracking. The main challenge in carrier-phase differential processing is to correctly resolve ambiguities. Mass-market receivers typically use narrow-band single frequency front-ends that are more prone to noise and multipath. They are also less capable of signal tracking under strong acceleration or vibrations. Furthermore, these modules have much less processor and memory resources to call upon. Besides, single-frequency observations inherently limit measurement redundancy compared to dual or even triple-frequency counterparts, making the task of ambiguity fixing and cycle-slip detection difficult. Two operation modes are distinguished when resolving the phase ambiguities.

- **Float:** Ambiguities are fixed to float numbers. The RTK/post-processing float mode will typically provide dm-level accuracy.
- **Fixed:** Ambiguities are fixed to integer values. The RTK/post-processing fixed mode will provide the highest level of positioning accuracy, but can exhibit position jumps when transitioning from a float to a fixed solution or reliability issues when operating

## Chapter 5. Developed MAV Platforms and Sensor Equipment

---

in degraded signal environments that lead to wrong ambiguity fixes (ESA Navipedia [2014]).

Regarding the use, single-frequency GNSS receivers are typically employed in automotive industry and consumer electronics. Their use in surveying is possible, but often limited to static or low-dynamic applications, e.g. glacier movement or deformation monitoring (Benoit et al. [2015]). They have been tested on MAVs in several cases, e.g. in Stempfhuber and Buchholz [2011] or Mongredien et al. [2016]. However, their use for the purpose of accurate aerial positioning of aerial imagery in cm-level has not yet been assessed under real mapping conditions and particularly not on fixed-wing platforms.

### 5.4.1 Multi-frequency and Multi-constellation Receiver

The GNSS receiver employed on-board is a geodetic-grade GPS/Glonass/Galileo multi-frequency receiver by Javad TR-G3T (Javad GNSS Inc. [2016]), Fig. 5.6. This receiver was the first on the market to offer a high update rate (up to 20 Hz), multiple constellation and frequencies, had several communication and synchronisation ports, and a small size. The receiver has RTK capability and 10 Hz sampling frequency. A similar setup is used as a base station for carrier-phase differential processing. A similar receiver is used as a base station for differential processing.

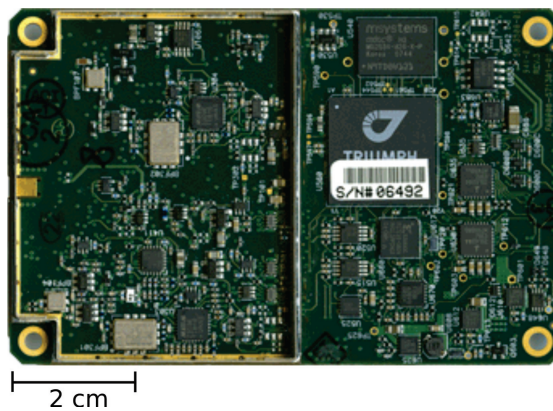


Figure 5.6 – Javad TR-G3T receiver (Javad GNSS Inc. [2016])

### 5.4.2 Single-frequency, Low-cost Receiver

Additionally, a single-frequency and low-cost GNSS receiver U-Blox NEO-8T (U-Blox [2016]) was tested on a fixed-wing platform during a real mapping project. The performance assessment is presented in Sec. 7.3.2. The receiver is depicted in Fig. 5.7. The employment of a single-frequency, low-cost GNSS receiver on MAV platforms is challenging for several reasons:

- The quality of receiver's front-end,



- computational resources for signal sampling tracking,
- limited acceleration under which the signal tracking works,
- less channels for signal tracking,
- single-frequency and thus worse capability of resolving ambiguities,
- limited support for synchronisation - input and output timing,
- usually no internal memory,
- lower sampling frequency, i.e. 1-10 Hz.

The advantages over geodetic-grade receivers are the price, power consumption, and weight. Tab. 5.2 summarises the main characteristics of the two employed GNSS receivers <sup>2</sup>. The receiver is customised for storing raw observation on a memory card.

Parameter	Javad TR-G3T	U-Blox NEO-8T
Size [mm]	88x57x12	40x18x10
Weight [g]	47	13
Tracking frequencies	GPS L1/L2/L2C/L5, GLONASS L1/L2, Galileo E1/E5A, SBAS	GPS L1, GLONASS L1, BeiDou B1, SBAS
Tracking channels	36 per frequency	72
Rate [Hz]	10	5
Built-in RTK	YES	NO
Synchronisation	PPS + Event	PPS
Price (USD)	10 000	75

Table 5.2 – Main features of the employed GNSS receivers.

### 5.4.3 GNSS Antennae

An antenna is an important part of the GNSS receiver system. It receives and translates GNSS signal from an electromagnetic wave into a signal that contains the amplitude and phase information of the GNSS signal. In general, an antenna's characteristics and performance set the boundaries of how well the GNSS receiver system will perform in standard conditions as well as in challenging scenarios, e.g. in the effects of multipath (Moernaut and Orban [2009], Bartone [2013]).

Antennae requirements can vary in the following attributes: gain vs. azimuth and elevation, multipath and interference rejection, stability of the electrical phase centre, size, shape, or environmental constraints (Kunysz [1998], ESA Navipedia [2016]). It is therefore crucial to find a good compromise between the above mentioned attributes that would meet the general

<sup>2</sup>Parameters of Javad TR-G3T can be modified and purchased upon request, the Tab. 5.2 describes the currently available features. The U-Blox receiver is mounted on a breakout board (CSG Shop [2016]).

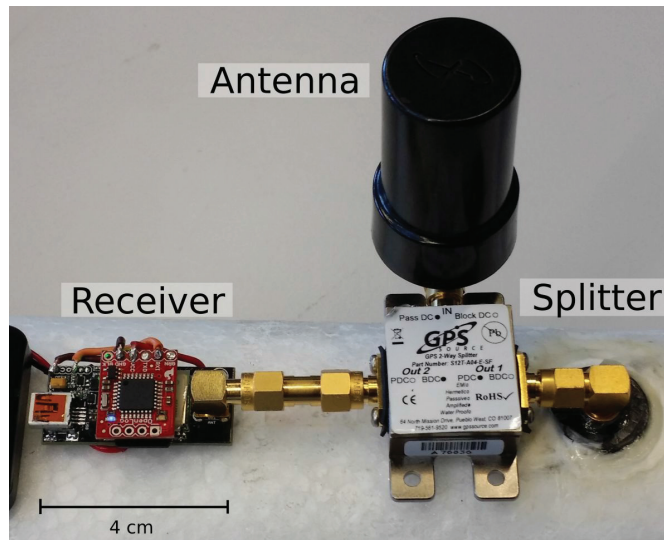


Figure 5.7 – U-Blox NEO-8T GNSS receiver with a serial data logger, GNSS signal splitter (GPS Source [2016]), and L1/L2 GNSS antenna Maxtena (Maxtena [2016]). During the presented experiment, a second receiver Javad TR-G3T was connected via the splitter to provide with a reference trajectory.

requirements of the MAV's GNSS system. Furthermore, the placement of a GNSS antenna and connection to the GNSS receiver are particularly important. Indeed, wrong placement or power losses due to inappropriate antennae and cabling deteriorate the quality of the resulting observations, and hence positioning.

Several types of antennae can be distinguished according to their construction. In general, patch and helix antennae are frequently employed on UAVs and mobile devices (ESA Navipedia [2016]). The latter are able to acquire GNSS signals in wider angle which is of a great importance in mitigating the influence of platforms bank-angles in turns. The two employed antennae are depicted in Fig. 5.8.

The multirotor system was equipped with an antenna by Antcom (Antcom Corp. [2016]) and the fixed-wing with the first generation of Maxtena (Maxtena [2016]). Although they are both capable of receiving L1 and L2 GNSS signals, they significantly vary in size and weight. Similarly to the correlation between small and big IMUs, also antennae have certain correlation in size and performance, as the physical size is limited by the wavelength of the signal (Tallysman Wireless [2014]). Hence, the multirotor features larger and heavier as well as more sensitive antenna, while the fixed-wing a small, and compact, yet sufficiently sensitive antenna for aerial mapping.

### 5.5 Inertial Measurement Unit

An inertial measurement unit observes specific forces using one or more accelerometers and detects changes in rotation using one multi-axis or more gyroscopes. In addition, it may also

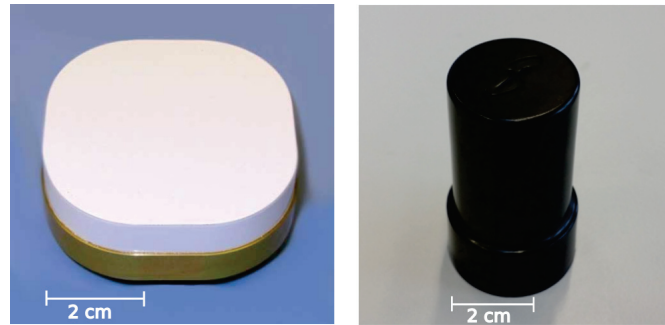


Figure 5.8 – Antcom L1/L2 GPS+Glonass antenna (left image) (Antcom Corp. [2016]) and Maxtena L1/L2 GPS+Glonass (right image) (Maxtena [2016]).

include a triaxial magnetometer, mostly to limit orientation drift and to assist in initialisation. In the context of ISO and DiSO, the primary role of an IMU is in the determination of attitude and the improvement of the position and velocities in higher frequencies of the motion. The gyroscopes generally represent the most expensive part of an IMU and their performance is limiting the navigation performance (Titterton and Weston [1997]).

### 5.5.1 IMU technology

Gyroscopes can be divided into several categories based on the technology they use. In the MEMS category, vibratory gyroscopes make use of the principle that a vibrating object tends to keep moving in the same plane despite rotation of the base. The angular rates are sensed either from a single rotating accelerometer or a pair of accelerometers to which a high frequency acceleration has been applied. A majority of today's MEMS devices is based on this concept (Skaloud and Legat [2010]).

Accelerometers measure specific forces. Two major groups of accelerometers can be distinguished in MEMS category based on the working principle. These are vibratory accelerometers and electrostatic levitation (Titterton and Weston [1997], Skaloud and Legat [2010]).

Performance-wise, IMUs are classified into three groups with accuracy specifications in Tab. 5.3.

- **Navigation grade:** Navigation-grade instruments accumulate a position error of about 1 nautical mile<sup>3</sup> per hour (nmi/h) in a pure inertial navigation mode without the GNSS updates.
- **Tactical grade:** Instruments in this category may accumulate as much as 10 to 20 nmi/h. These instruments are often used in the context of GNSS/IMU navigation for airborne mapping.
- **MEMS:** Compact, low-cost, and low-power devices that used to be solely employed in

<sup>3</sup>1 nmi = 1.85 km

## Chapter 5. Developed MAV Platforms and Sensor Equipment

consumer electronic devices can nowadays achieve accuracy close to Tactical grade IMUs for a lower price. The low-cost MEMS sensors are used on a majority of UAVs for navigation purposes as a part of the autopilot system. On the contrary, high-end MEMS can be employed for the sensor attitude determination (Applanix Corporation [2015], SBG Systems [2016]).

Grade	low-cost MEMS	high-end MEMS	Tactical	Navigation
Gyro drift [deg/hr]	>100	0-100	0.1-10	0.005-0.01
Accelerometer bias [ $m/s^2$ ]	0.05-0.5	$5 \cdot 10^{-3}$	$5 \cdot 10^{-3}$	$2 - 5 \cdot 10^{-3}$
Price (Euro)	<50	500-20 000	>40 000	>100 000

Table 5.3 – Sensor accuracy and price for low-cost MEMS, tactical, and navigation grade IMUs.

### 5.5.2 Employed IMU on the MAV platforms

Within the scope of the presented research, an in-house developed board called Gecko4Nav (Kluter [2013]) was employed. This board comprises up to four MEMS IMU chips, all precisely synchronised to the GNSS time-reference. The details about synchronisation are provided in Sec. 6.4. Gecko4Nav contains two main components. The FPGA (Field-Programmable Gate Array) board handling the synchronisation, data flow, and storage is connected to a custom sensor board, equipped with various types of sensors. The main components are the NavChips IMUs (each with a triad of gyroscopes, accelerometers and magnetometers) that can be software-combined to a R-IMU. The performance characteristics for each sensor type provided by the manufacturers are shown in Tab. 5.4. The acquisition and control of the measurements are performed by an on-board firmware which also governs the IMU sampling frequency. That can be selected by the user in the range from 250 to 500 Hz. In the scope of this research, two sensor boards were employed. One was equipped with two IMUs, while in the later projects a different board with four IMUs was used.

Sensor performance parameters	Gyroscopes	Accelerometers
In-run bias stability	$10^\circ/hr$	$0.05\ mg$
Scale factor	0.1 %	0.06 %
Angle random walk	$18^\circ/\sqrt{hr}$	$0.03\ m/s/\sqrt{h}$
Noise density	$0.003^\circ/s/\sqrt{hr}$	$50\ \mu g/\sqrt{Hz}$

Table 5.4 – Stochastic characteristics of the inertial sensors (Intersense [2015]).

## 5.6 Sensor Payload

A proper physical integration of navigation components is important for several reasons. First and foremost, the components have to be rigidly attached to each other, e.g. a camera with an IMU and antenna, to constitute a stable relation that is necessary for preserving boresight and

lever-arm parameters. Second, the sensors have to be mounted inside the platform in such a way that the vibrations from a propulsion system are not transferred to the sensors, or are sufficiently dampened. Third, a user must be able to access the sensors to get the data or to setup their parameters.

A poor sensor mount can significantly affect the data quality, e.g. due to the vibrations, and can worsen the quality of a determined trajectory or even make the data processing impossible. The requirements on sensor integration are motivated by the following objectives:

- Weight limit,
- modular design,
- stability and rigidity of the spatial offsets,
- vibration dampening,
- accessibility and necessary communication interfaces,
- single battery system.

Addressing the first objective, the maximal weight of the sensor equipment considerably affects other requirements, i.e. on modularity and necessary interfaces. For example, a higher payload capacity would allow for a more sophisticated dampening and attitude compensation systems, but the weight limits do not allow it. Concerning the problems of spatial offsets, to rigidly mount a consumer grade camera with an IMU is a challenging task. A consumer market camera is usually equipped only with one mounting hole for tripod stabilisation that makes its integration to a stable mount rather demanding.

### 5.6.1 TOPO Copter

The sensor mount attached to the multicopter was fabricated from carbon material and both the camera and IMU were rigidly mounted to it. The vibrations were dampened by using rubber spacers between the mount and body of the multicopter. The camera was screwed to the mount plate and secured with hot glue as depicted in Fig. 5.9. The sensor mount is stabilised in one axis (pitch) and can be remotely tilted to a desired angle as schematically shown in Fig. 5.2 while preserving a relative position and orientation between the sensors.

### 5.6.2 TOPO Plane

A second realisation of a sensor head was dedicated to a fixed-wing platform. Due to the physical limitations of the airplane's internal compartment, the camera is oriented sideways. This configuration considerably influences mission planning due to a narrower swathe in side direction. Then the forward swathe is higher and the camera thus triggers in a lower

**Chapter 5. Developed MAV Platforms and Sensor Equipment**

frequency. The mount is made out of two carbon plates and the sensors are squeezed in between, Fig. 5.10. As for vibration dampening, the material the fixed-wing is made of, naturally dampens vibrations generated from the engine. An overview about weight of all the individual components mounted on MAV platforms is listed in Tab. 5.5.

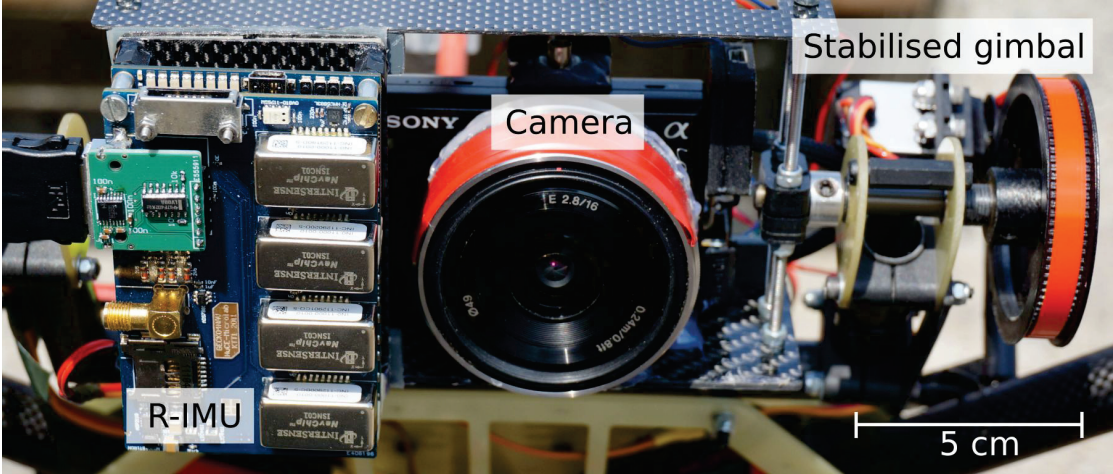


Figure 5.9 – Gecko4Nav R-IMU and Sony NEX 5N RGB camera mounted on a stabilised mount.

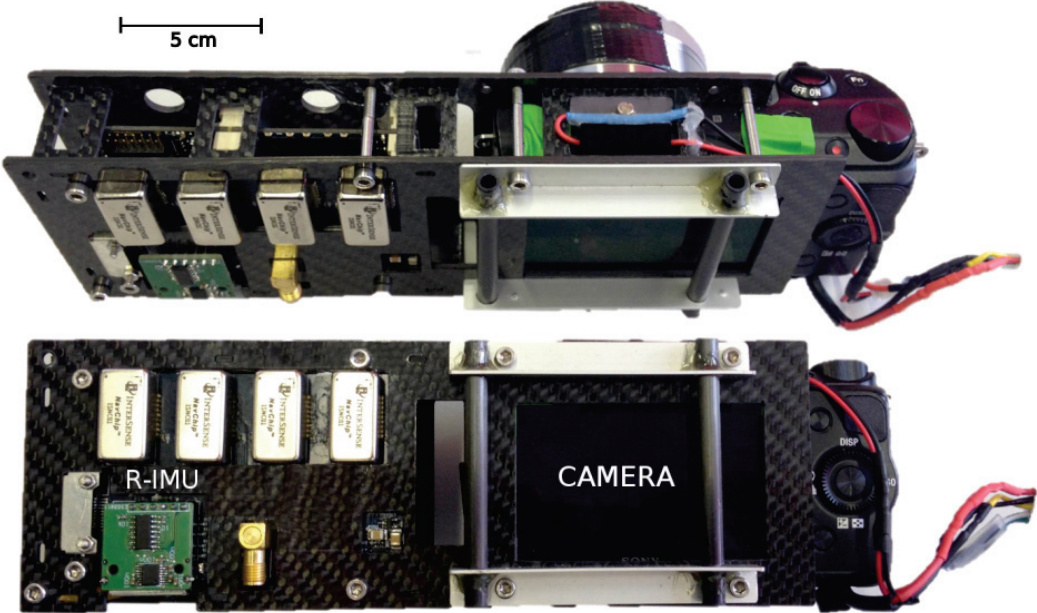


Figure 5.10 – Camera sensor head of the fixed-wing platform.

Sensor	Weight [g]
Sony NEX 5N (R) + 16 mm lens	280
Javad TR-G3T receiver	47
U-Blox Neo 8T receiver	13
Maxtenna antenna	17
Antcom antenna	102
GNSS splitter	23
RTK modem	24
R-IMU with 4 Navchips	82

Table 5.5 – Summary of imaging and navigation components weight.

### 5.6.3 Communication Links

Communication between an UAV and its pilot is essential for the accomplishment of mission tasks. Generally, requirements on communication links are defined by the platform, mission objectives and the flight environment. Regarding the communication links, every UAV is equipped with at least one communication link for basic manual or semi-automatic control. This communication link serves for connecting the ground transmitter with the drone and is usually on 2.4 GHz frequency. However, this is the same frequency in which wireless computer networks work and therefore, in certain urban regions a strong band saturation might occur resulting in a limited range, or a complete loss of signal.

UAVs capable of fully autonomous flights require a two-way communication link with the ground control station for managing the flight parameters and for receiving mission updates. Depending on the region, the communication link often works on the 433 MHz or 915 MHz frequencies. In addition, UAVs employed for inspection tasks are either equipped with a live video preview or they transmit the collected imagery in real-time to the ground. The most common frequencies used for video transmission are: 900 MHz, 1.2 GHz, 2.4 GHz, and 5.8 GHz. Here again, the choice depends on the state regulations and on the possible interference with the other transmitting devices on-board.

Last but not least, the RTK correction can be either embedded in a two-way communication link with the GCS, or can be transmitted independently via a separate, e.g. 866 MHz link. This connection provides data transmission for low data rates over long ranges (< 10 km) and with a small power consumption. This band is harmonised throughout the EU and in certain sub-bands there are limits on the transmitting volume of the data (GS1 [2016]). An overview of employed communication links on the presented MAVs is given in Tab. 5.6.

### 5.6.4 Communication security

Concerning safe UAV operations, two of the most important subjects of any UAV communication systems are data-link protection and data security (Butcher et al. [2014]).

Communication security is a widely discussed topic in many fields of human activities. How-

## Chapter 5. Developed MAV Platforms and Sensor Equipment

	Manual flight control	Autopilot's telemetry	RTK corrections	Live-video
<b>Frequency</b>	2.4 GHz	433 MHz	866 MHz	5.8 GHz
<b>Data-rate</b>	low <30 Kb/s	low <100 Kb/s	low <30 Kb/s	high <2 Mb/s
<b>Coverage</b>	1 km	3 km	3 km	0.2-1.5 km
<b>Direction</b>	two-way	two-way	up	down
<b>Security</b>	frequency hopping	network id	AES Encryption	none
<b>Advant.</b>	-small antennas -long range	-long range -low power consumption	-long range	-small antennas -high throughput
<b>Disadv.</b>	- prone to saturation	-low throughput	-legal limits on throughput	-range affected by obstacles -high power consumption

Table 5.6 – Communication links of the developed MAVs.

ever, the problem of communication security revolving around drones is not addressed properly, and as a result, commercially available drones are very prone to hijacking and other sorts of attacks (Makezine [2016], Rodday [2016]). An attacker can, e.g. alter waypoints, change data in the autopilot, or set a different coming home position while blocking the operator from controlling the drone.

The communication devices employed on the presented MAVs are standard versions of commercially available systems. Manual control working on 2.4 GHz is equipped with a frequency hopping technology. This is a method of transmitting radio signals by rapidly switching a carrier among many frequency channels, using a pseudo-random sequence known to both the transmitter and receiver. This method significantly reduces the chance of interference and interception, but does not provide any significant increase in security.

Alternatively, the autopilot's telemetry uses only a few ID bits that separate the communication links, e.g. the transmitter and receiver pair share the same network ID. This method does not prevent active attempts aiming to hack the system, but prevents from accidental conflicts when several platforms operate in a close radius. Nonetheless, telemetry modems can be upgraded with a customised firmware that procures encryption.

The RTK data link uses an advanced AES (Advanced Encryption Standard) technology, preventing from intentional attempts to access the data stream. Finally, common devices performing analogue video streaming do not provide any mean of secure transmission.

### 5.6.5 Electromagnetic Interference

The issue of the UAV interfering with its own on-board systems is a common aspect of sensor integration. The problem of interference associated with MAVs electronics, e.g. motors, speed controllers, or photogrammetric payload, is that these components may interfere with the communication systems. This is mainly because of insufficient shielding of EMI emitting devices and harmonic frequencies generated by the equipment that is originally not designed to generate radio signals.

Such signal deterioration limits the ability of the GNSS receiver to acquire fixed position and negatively influences the range of communication links. A solution to this problem is a proper shielding as well as maximal possible separation between the source of EMI and sensitive



devices. Due to weight and space limitations on MAVs, this is not a trivial task.

### **Summary**

This chapter was devoted to the custom development of two MAV platforms and installation of camera and GNSS/IMU instruments on-board. Both platforms feature good endurance and excellent flight capabilities while being equipped with an open-source autopilot and state-of-the-art navigation sensors. General issues related to the accurate positioning and orientation determination on MAVs were addressed together with the enabling technologies behind. The final part of this chapter identified a frequently ignored issue of safe communication and data links. The outcomes from this realisation have a critical influence on further aspects of mapping. After this important development, the system and sensors are ready for calibration.



## 6 System and Sensor Calibration

*This chapter discusses sensor and system calibration of the photogrammetric and navigation payload on MAVs. First, calibration fields and acquired data sets are introduced. Then, sensor and system calibration procedures are presented along with empirical examples on the developed platforms.*

### 6.1 Testing fields and data acquisition campaigns

#### 6.1.1 Close-range Calibration Field

A dedicated calibration field was constructed for camera/lens calibration and for system calibration. This field is further suitable for multicopter operations. The calibration field is depicted in Fig. 6.1. Its size is approximately 30 m x 20 m with height differences of up to 2 m. A set of 90 digitally coded targets was placed in a regular grid across the field. The placement of 25 targets was stabilised by surveying nails and their 3D positions were determined by tachymetric measurements and complemented with accurate levelling. These points serve as ground control/check points and are determined with accuracy  $\sigma_{X,Y} < 0.5$  cm and  $\sigma_Z < 1$  cm. In such a setup a high redundancy and an excellent distribution of measurements across the image plane can be obtained. The estimation of the signalised target centres in the image space is achieved by adopting the methodology commonly used by the research community concerned with computer vision. Specifically, the open-source software library ARToolkitPlus (Wagner and Schmalstieg [2007]) is used to perform automatic target recognition. The ARTag marker set is employed due to its near-zero false positive identification rate as well as good accuracy potential for determining the target centres, which is reported to be 1/10 of a pixel (Fiala [2010]). A detail on one of the markers is in Fig. 6.2. The open-source C++ library was inbuilt into a custom script allowing both real-time as well as post-processed target detection and image centre observation on a batch of images.

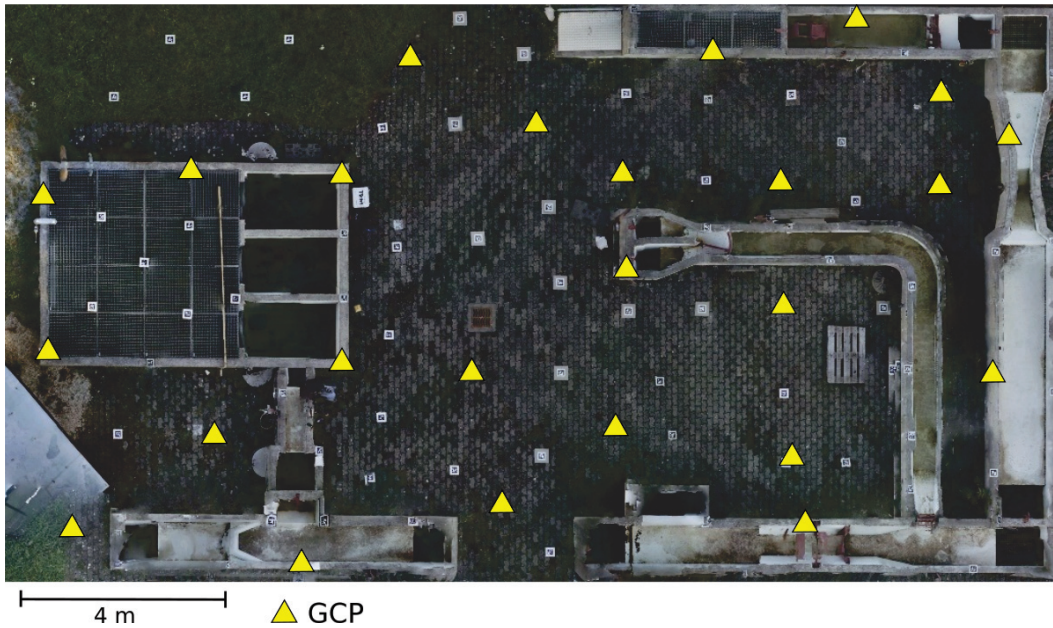


Figure 6.1 – Close-range calibration field.

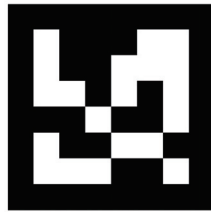


Figure 6.2 – An example of ARTag fiducial marker.

### 6.1.2 Open Space Testing Field

In order to test fixed-wing platforms that have higher endurance and operational radius than multirotors, a dedicated control field was established. The field has the size of approximately 1 x 1.2 km and is located in a rural area west from Lausanne. The chosen terrain has height differences up to 30 m and includes a variety of surfaces, such as crop fields, roads, and a forest. There are 25 dedicated markers regularly placed across the field mainly along the road network as depicted in Fig. 6.3. The markers are permanently stabilised by surveying nails on tarmac, signalled by white colour circles (15 cm in diameter) and accurately surveyed to the accuracy of  $\sigma_{X,Y} \sim 2$  cm and  $\sigma_Z \sim 2.5$  cm.

### 6.1.3 Acquired Data Sets

Tab. 6.1 summarises the main data sets used for a variety of tests and evaluations. The flights were conducted with the both MAV platforms under different weather conditions and time periods of the year. As a result, there are variances in flying speed and in the number and

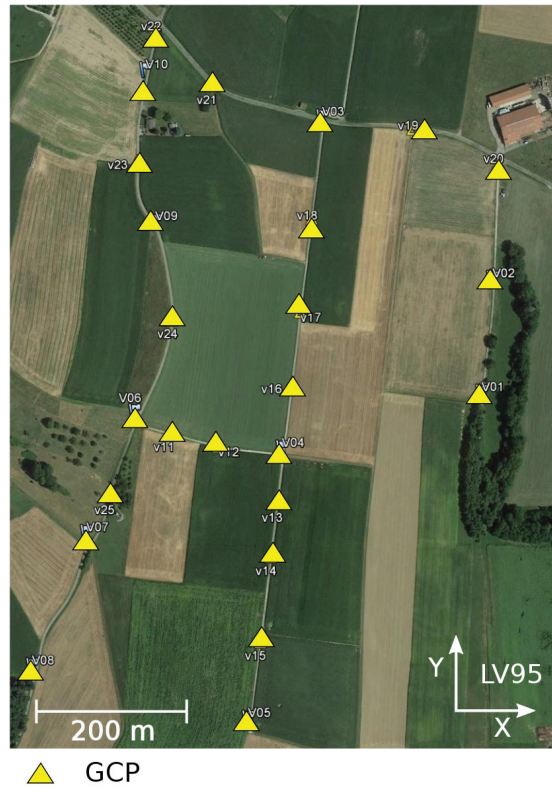


Figure 6.3 – Open space calibration field.

quality of the automatically detected image measurements due to the changes in a surface texture. Furthermore, as every test was carried out for a slightly different purpose, there are some variations in hardware configurations. Last but not least, only the most relevant data sets are presented in the scope of this thesis. Many other flights were conducted for testing purposes of, e.g. platform's flight capabilities and endurance, RTK connections, data quality, camera triggering, or camera calibration. In general, the close-range field was flown with the multirotor MAV and the flights were carried out for testing and calibration purposes. The open space testing field was used for testing and evaluation purposes by the both platforms.

## 6.2 System Calibration of Spatial Offsets

In a photogrammetric system with GNSS/IMU instruments, two lever-arms have to be determined. Depending on the installation, the eccentricity can be significant, e.g. > 10 cm. Hence, an accurate determination of the lever-arms is important for the overall system accuracy. Firstly, the eccentricity between the centre of the IMU and the camera perspective centre  $\mathbf{a}_{CAM-IMU}^c$  has to be estimated in the camera frame. The displacement is difficult to measure as the perspective centre is not known or not directly accessible. This is the case for large systems as well as those using consumer grade cameras on unmanned aerial platforms. Secondly, the lever-arm between an antenna reference point (ARP) and an IMU navigation

Data set	CR1	CR2	FW1	FW2	FWubx
Date	2013	2015	2014	2015	2016
Platform	Multicopter		Fixed-wing		
Camera	Sony NEX 5N		Sony NEX 5R		
GNSS	Javad OEM TR-G3T				+ Ublox
IMU	-		2 x Navchips	4 x Navchips	-
Freq. GNSS/IMU [Hz]	10/-	10/-	10/500	10/250	5/-
Flight level [m]	5-10	3-10	120/150	140/170	130/160
Flight speed [m/s]	0-5	0-5	11-24	11-22	12-20
Area covered [ha]	0.1	0.1	112	56	98
Mean GSD [cm]	0.4	0.4	3.8	4.5	4
Overlap [%]	70/90	90/90	80/60	80/60	80/50
No. of images	68	102	467	207	326
No. of tie-points	50	2 035	11 912	4 926	6 982
No. of GCP/ChP	22	19	25	20	23
No. of image obs.	4 105	75 880	188 054	107 100	146 694

Table 6.1 – Summary of acquired data. Acronyms in the data sets CR\_ stand for close-range, FW\_ for fixed-wing.

centre  $\mathbf{a}_{IMU-ARP}^b$  needs to be determined in the IMU b-frame. The offset  $\mathbf{a}_{CAM-ARP}^c$  in the camera frame can be expressed as in Eq. 6.1. The practical determination on the developed platform is detailed in Sec. 6.2.2.

$$\mathbf{a}_{CAM-ARP}^c = \mathbf{R}_b^c \cdot \mathbf{a}_{IMU-ARP}^b + \mathbf{a}_{CAM-IMU}^c \quad (6.1)$$

A common problem with measuring the lever-arms is that the GNSS antenna and the ARP are located on a fuselage while the camera and IMU are placed inside as schematically illustrated in Fig. 6.4. Moreover, the centre of the camera sensor is not usually shown on the camera body. Therefore, an indirect estimation, such as "pseudo" measurement technique has to be used (Ellum and El-Sheimy [2002]). The corresponding offsets are determined by building differences in the positions of the ARP which is determined by the GNSS or tachymetry, and the camera perspective centre from BA. These differences need to be expressed in the camera frame, which orientation is determined concurrently with the camera perspective centre.

The lever-arm may be also estimated as an additional parameter when using accurate observations of the aerial position within BA or within the Kalman Filter for the case of an antenna-IMU offset. However, accuracy of such estimation is somewhat limited because the spatial offset is correlated with the camera IO parameters, synchronisation error as well as with a GNSS bias. When the project geometry lacks strong overlap, various ground speed and/or height changes, these parameters cannot be estimated with a sufficient precision.

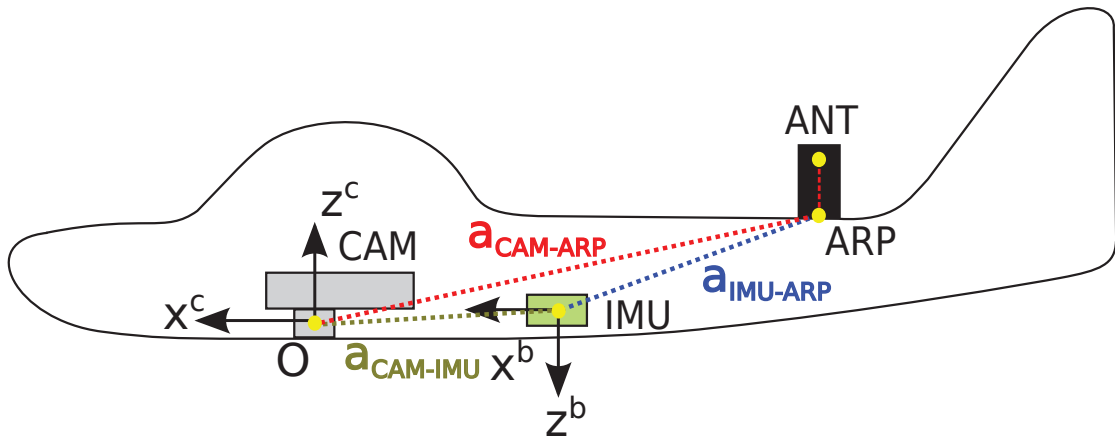


Figure 6.4 – Schematic sketch of the sensor offsets between the camera projection centre, the IMU-sensor frame and the ARP.

### 6.2.1 TOPO Copter

In the case of the multirotor system, the sensor's physical mount allowed the lever-arm between the ARP and camera to be measured by a calliper and this result was compared with the estimation indirectly via the BA. The respective correspondences are shown in Tab. 6.2. The good agreement between the measured and the estimated values is due to a favourable converging geometry over the calibration field that allows decorrelation of the estimated parameters.

Lever-arm	Measured with a calliper   $\sigma$ [cm]	Estimated in BA   $\sigma$ [cm]
$\mathbf{a}_{CAM-ARP}^c(x)$	5.5   0.5	5.6   1.5
$\mathbf{a}_{CAM-ARP}^c(y)$	17.5   0.5	17.6   2.5
$\mathbf{a}_{CAM-ARP}^c(z)$	1   0.5	0.1   1.4

Table 6.2 – Measured vs. estimated lever-arm  $\mathbf{a}_{CAM-ARP}^c$ .

### 6.2.2 TOPO Plane

In order to measure the lever-arm on a fixed-wing platform, the pseudo measurement technique was used over a close-range calibration field in a static scenario. The GCPs were located in vertical and horizontal planes of a 3D calibration field. The fuselage of the plane was mounted on a tripod in a horizontal position with the camera pointing towards the calibration field as schematically shown in Fig. 6.5. Then, the position of the ARP was measured by a theodolite from two stations. The theodolite was beforehand oriented to the local coordinate system. An image of the target field was taken by the camera and the process repeated on the second and third camera stations. An additional set of 10 images was taken between stations 1 and 3 in order to establish a high number of tie-points and to better determine the EO parameters of the camera at these stations.

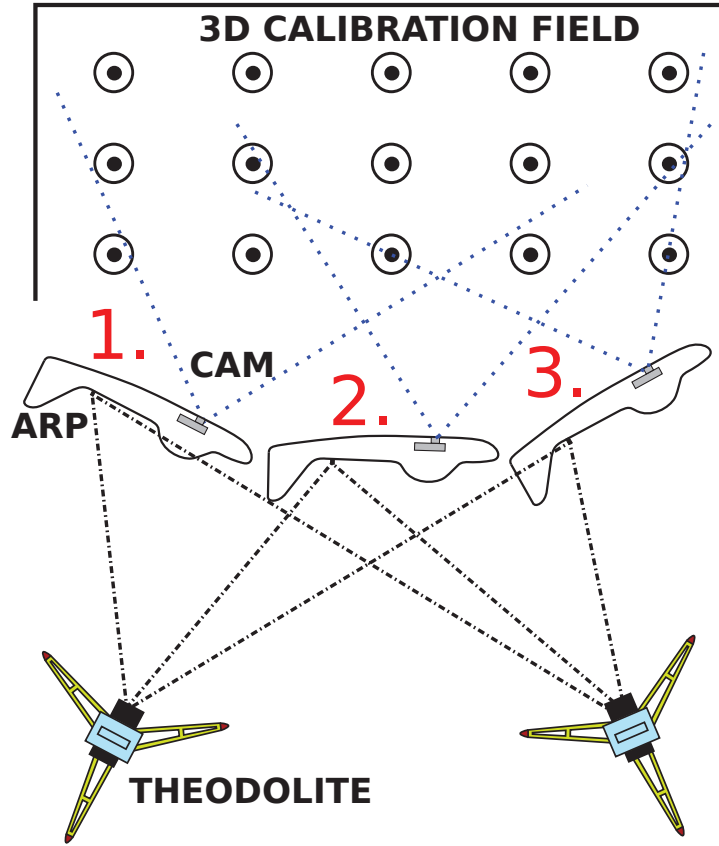


Figure 6.5 – Schematic sketch (top view) of the sensor offsets calibration procedure. Offsets measured from three stations.

The processing was done in the Pix4D Mapper. The resulting camera EO parameters were further processed to express the spatial offsets  $\mathbf{a}_{CAM-ARP}^c$  between the camera perspective centre and ARP in the camera frame according to Eq. 6.2. The  $\mathbf{R}_m^c$  is the rotation matrix from mapping to the camera frame and the  $\mathbf{a}_{CAM-ARP}^m$  is the lever-arm in the mapping frame.

$$\mathbf{a}_{CAM-ARP}^c = \mathbf{R}_m^c(\omega\phi\kappa) \cdot \mathbf{a}_{CAM-ARP}^m \quad (6.2)$$

where  $R_m^c(\omega\phi\kappa)$  is the transposed rotation matrix from Eq. 4.2 and

$$\mathbf{a}_{CAM-ARP}^m = \begin{pmatrix} X_{ARP}^m - X_{CAM}^m \\ Y_{ARP}^m - Y_{CAM}^m \\ Z_{ARP}^m - Z_{CAM}^m \end{pmatrix} \quad (6.3)$$

As the employed R-IMU contains four independent sensors, the corresponding spatial offsets have to be determined for each of them. The short lever-arm  $\mathbf{a}_{CAM-IMU}^c$  between the camera and each particular IMU inside the R-IMU was measured by a calliper. As previously stated,



the second lever-arm between the ARP and the IMU, i.e.  $\mathbf{a}_{IMU-ARP}^b$  was calculated as:

$$\mathbf{a}_{IMU-ARP}^b = \mathbf{R}_c^b \cdot (\mathbf{a}_{CAM-ARP}^c - \mathbf{a}_{CAM-IMU}^c) \quad (6.4)$$

The final 3D offset  $\mathbf{a}_{CAM-ARP}^c$  is stated in Tab. 6.3 together with an offset estimated in-flight, which is detailed in Sec. 7.3.2. The relatively high difference between the measured and estimated values is caused by a high correlation of the lever-arm with the camera IO parameters during an in-flight self-calibration as well as by an unfavourable photogrammetric block geometry, i.e. low flight height separation. Furthermore, a constant time delay in a sensor synchronisation has similar impact on the accuracy of the sensor position as that of a lever-arm when considering constant flight speed. An image from the ground calibration procedure is in Appendix C.1.

Lever-arm	Ground calibration   $\sigma$ [cm]	Estimated in BA   $\sigma$ [cm]
$\mathbf{a}_{CAM-ARP}^c(x)$	-46.8   1	-56.3   0.4
$\mathbf{a}_{CAM-ARP}^c(y)$	0.5   1	3.4   0.5
$\mathbf{a}_{CAM-ARP}^c(z)$	9.5   1.5	4.4   1.9

Table 6.3 – Ground calibrated vs. BA-estimated lever-arm between the camera perspective centre and the antenna ARP.

### 6.2.3 Antenna L1 Phase Centre Calibration

The knowledge of the point of reception of the GNSS carrier phase signals is essential for an accurate positioning. The goal of the calibration is to determine corresponding offsets to L1 and L2 phase centres from the physical point on the antenna to which the antenna calibration values are referenced, i.e. the ARP. The point of signal reception is, however, not a directly measurable location. The calibration parameters are usually provided by the antenna's manufacturer, but this was not the case for the antenna employed on the TOPO plane. Therefore, a calibration procedure had to be carried out. The calculated offset was further used as a part of the estimated lever-arm  $\mathbf{a}_{CAM-ANT}^c$ . The following steps were taken during the calibration.

1. The reference (with known parameters) and calibrated (with unknown parameters) antennae were placed on known positions. The situation is schematically depicted in Fig. 6.6.
2. Static data was recorded over a 5 h long period.
3. A carrier-phase differentially post-processed position of the calibrated antenna was compared to its ARP. The resulting difference corresponded to the ARP of the L1 phase offset.

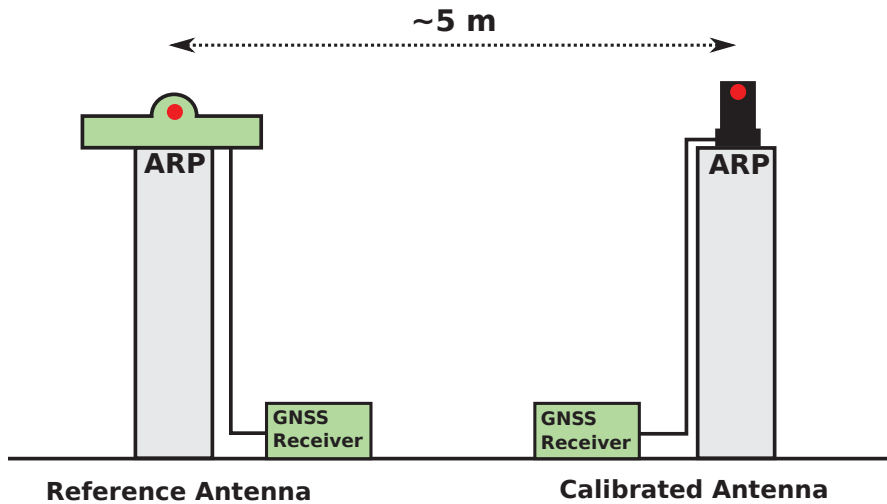


Figure 6.6 – Antenna's L1 phase centre calibration; both antennae placed on known ARPs.

### 6.3 System Calibration of Angular Misalignment

#### 6.3.1 Concept

Considering the physical mounting of the IMU and the camera, a perfect alignment of these two systems is not possible. Similarly to the positional offset, an angular offset  $\mathbf{R}_c^b$  of the camera with respect to the IMU has to be determined. While the spatial offsets between the different sensors can be measured with classical methods (by a calliper or by photogrammetry means) with millimetre accuracy, analytical methods are almost certainly required to obtain misalignment angles (also called boresight) correction for consumer grade cameras (Cramer and Stallmann [2002]).

A key assumption is that the boresight angles remain constant as long as the IMU remains rigidly mounted to the camera. This criterion is difficult to meet with standard off-the-shelf components not originally designed to be used for mapping. The camera sensor usually lacks proper mounting holes. However, with a carefully designed mount, such problem can be eliminated, as shown in Fig. 5.10.

There are several techniques of boresight calibration for imaging sensors presented in, e.g. Skaloud et al. [1996], Kruck [2001], Cramer and Stallmann [2002] or Mostafa [2002]. The  $\mathbf{R}_b^c$  can be determined indirectly by comparing GNSS/IMU-derived attitude of images  $\mathbf{R}_b^m$  and attitude  $\mathbf{R}_c^m$  calculated from photogrammetric triangulation using BA. The more direct method estimates  $\mathbf{R}_b^c$  within a self-calibrating BA by introducing additional parameters to absolute attitude observations as in Eq. 4.7. The first method does not require BA modification and may also consider the remaining temporal correlations within the navigation system, which leads to a realistic estimation of the variances (Skaloud and Schaer [2003]). In the presented study, the boresight  $\mathbf{R}_b^c$  was calculated using the self-calibration technique.

### 6.3.2 Initial Alignment

On the contrary to the position, attitude determination by the GNSS/IMU largely depends on the IMU quality. Generally, better accuracy can be expected in a roll and pitch angles (as compared to yaw) due to their correlation with the gravitational acceleration (Skaloud [1999]). The quality of the IMU alignment also has a significant impact on the residual orientation errors. Practically, the uncertainties in the initialisation are modelled as state parameters which values the GNSS/IMU filter/smoothing keeps on refining throughout the flight.

The inertial navigation system is a dead-reckoning system, and as such, it needs the initial attitude  $\mathbf{R}_b^l$  to be either known or determined. Typically, the initial alignment can be achieved through two consecutive stages: coarse alignment and fine alignment. The coarse alignment is a procedure used to estimate attitude parameters approximately. When the IMU is not moving with respect to the Earth's surface, the inertial sensors observe natural quantities, such as local gravity (roll and pitch determination via accelerometer levelling), Earth's rotation, or a local magnetic field (yaw determination via gyro-compassing). With tactical and navigation grade IMU systems, the initial azimuth is determined during a procedure called gyro-compassing. The essential condition for this initial alignment is to have a gyroscope precise enough to sense the Earth's rotation ( $15^\circ/\text{hour}$ ), in other words, to have a gyroscope drift and noise-level lower than the Earth's rotation rate. If a gyroscope does not have such capabilities, the initial alignment of a yaw angle has to be carried out in different manners as is the case for most MEMS sensors.

For the MEMS IMU that are employed as a part of an autopilot system and not used for mapping tasks, the quality of the initial alignment is not crucial since the autopilot needs only roll and pitch angles to stabilise the platform. The problem of a yaw determination is partially solved by adding a magnetometer as a part of the navigation system. This very sensitive device can measure the Earth's magnetic field and when its reading is combined with the reading from accelerometers, the azimuth can be determined. The problem occurs when using the magnetometer on a platform with highly integrated electronic components in a very limited space. The main problems aroused by the EMI are the influence on magnetometer and also on the GNSS signal. The magnetic reading is corrupted by the components, such as motors which create their own magnetic field that perturbs the sensor reading. Its shape and amplitude vary depending on the amount of current drawn.

The problem of the initial alignment on a fixed-wing platform was partially solved by placing the platform on the ground and keeping it static (no current to motor) for some time and using magnetometer observations to determine the azimuth with a few degrees certitude. Then, the alignment was refined in a flight with the Kalman filter/smoothing.

## 6.4 The problem of the IMU and Camera Synchronisation

The task of synchronisation is fundamentally common in electronic systems, and as such, it is assessed in almost any navigation or communication field. To benefit from on-board position and attitude determination in mapping, the camera events need to be registered

to the same (global) time frame as satellite and inertial data. The necessity of such precise time synchronisation of measurements from multiple sensors is widely recognised (Toth et al. [2008]). Synchronisation errors are common in navigation systems and they can either originate in hardware or software components. The presence of these errors deteriorates the accuracy of the derived sensor exterior orientation parameters (Schwarz et al. [1993]). In certain configurations, i.e. block structures, the synchronisation errors can be mitigated and their influence absorbed by GNSS shift and drift parameters (Jacobsen and Schmitz [1996], Cramer [2003]). However, in DiSO, their impact on the mapping accuracy is direct and significant (Jacobsen [2002b], Skaloud [2006]).

### 6.4.1 IMU Synchronisation

The custom Gecko4Nav board accommodates up to four NavChip IMUs on the same platform. A sampling of all the inertial observations at the same time is a prerequisite for exploiting the benefits of the redundancy and performance alleviation. The Gecko4Nav features a synchronisation module, which uses the pulse-per-second (PPS) signal issued by the GNSS receiver to adjust dynamically its crystal clock oscillator. This method ensures the continuity of the measurement procedure even if the PPS signal is lost.

Synchronisation was tested by placing the Gecko4Nav with the R-IMU on the top of a tactical grade inertial unit whose synchronisation is known to be correct (Skaloud and Schaer [2010]). This IMU served as a reference, although only approximate alignment with respect to the MEMS IMUs was determined. The whole system was shaken along each axis, and the dynamic responses were compared in time. As shown in Fig. 6.7, the four MEMS IMUs are synchronised well, both relative to each other and to the reference. Note that the depicted signal does not account for residual misalignment between the sensors, which results in slight variations between the IMUs in the projection of the input signal.

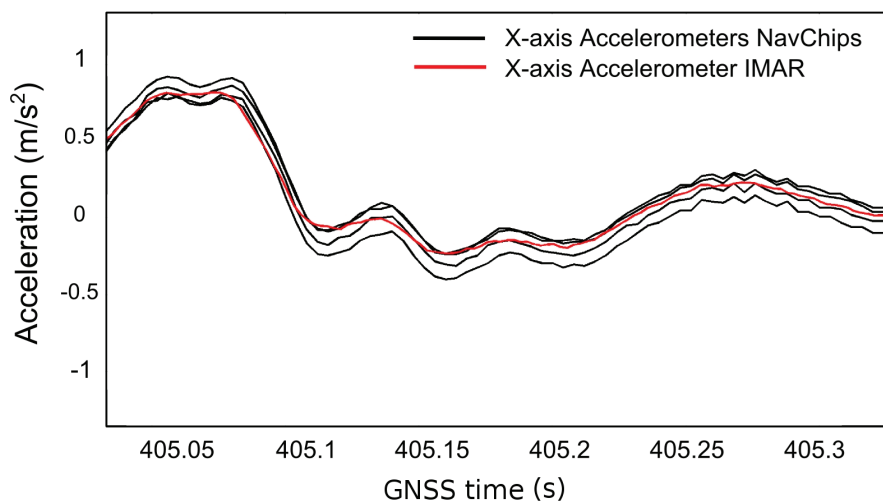


Figure 6.7 – Time-alignment of NavChip IMUs (Intersense [2015]) sensed specific force to the reference (iMAR-FSAS) (Mabillard [2013]).

### 6.4.2 Camera Synchronisation

Mapping with MAVs is somewhat similar to a close-range photogrammetry with the use of non-metric cameras for the purposes of multisensory systems (Perry and Childs [2009]). For this reason, it is necessary to precisely establish the time registration of imagery with other navigation components, such as GNSS/IMU or with other cameras constituting a camera array (Ding et al. [2008]).

#### Methods of a Camera Synchronisation

With MAVs, the first common method of image synchronisation with the exterior orientation parameters is through a correlation between the image acquisition time stored in image meta-data file and the GNSS log or other trajectory files. This method is sufficient for the indirect approach to the sensor orientation where the sensor positions and orientations enter only during the image pre-selection, and/or as an initial approximation for the BA. In order to use the EO parameters as weighted observations, as required in ISO and DiSO, a considerably more accurate method of synchronisation has to be employed.

The second method is based on time-stamping of a trigger pulse that is sent by the autopilot to an imaging device. In this case, the precise time stamping is affected by the camera's internal electronics. A camera delay, or so-called shutter lag, is a feature which affects all the consumer grade cameras and has a significant influence on the precision of synchronisation. When the shutter button is actuated locally or remotely via a triggering signal, the camera may seem to take a photo instantly. However, there is a certain delay before a photo is actually taken (Jon et al. [2013]). There are several ways of reducing this delay, e.g by using manual rather than automatic camera settings, or by making a hardware modification by implementing an electronic trigger instead of infra-red remote trigger. Employing manual settings makes the residual delay not only smaller but also more stable, which is an important prerequisite for its elimination. This method is sometimes sufficient for slow flying platforms, such as multirotors, but not sufficiently precise for fixed-wing platforms. Despite its limitations, this method is widely used among UAV users as it is relatively easy to implement, and results can be obtained with much higher geotagging accuracy than the previously mentioned approach. Several options are viable in terms of modification of a triggering system or signalisation

Number of samples:	88
Maximum delay:	0.486 s
Minimal delay:	0.406 s
Average delay:	0.433 s
$\sigma$	0.013 s

Table 6.4 – Camera-lag statistics in a manual exposure mode.

of a shutter opening to minimise the effect of camera internal electronics on the quality of time registration. The commonly employed method on off-the-shelf cameras is based on the

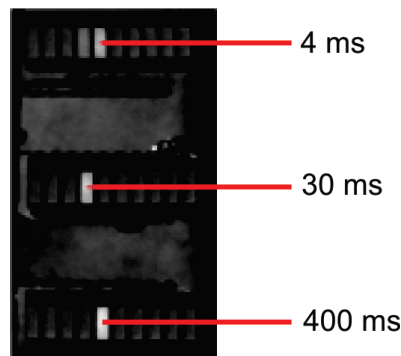


Figure 6.8 – Determination of a camera lag using LED bar-graphs.

processing of a camera flash signal. Such signal is sent by the camera at a certain instance of exposure and can be time-tagged in further processing.

Using this feature, also frequently called the marker input of the GNSS receivers, is a well-established form of synchronising imaging sensors to the GNSS time base. This method usually requires only minor hardware and software modifications of the existing components. However, as the flash pulse is unlikely to be sent at the exact moment of the mid-exposure, a residual error can persist. Contrary to the trigger time stamping, this approach provides time registration that is considerably more precise. Indeed, using flash in photography requires good synchronisation, and such a capability can be readily integrated into the camera's electronics.

Probably the most precise method of synchronisation of a mechanical shutter is performed by recording the signals of shutter curtains directly from the camera circuitry. Such signals correspond to the real exposure in terms of milliseconds while being independent of the camera settings. A considerable drawback of this method is accessing such signals that may require a non-trivial hardware adaptation. A complete elimination is surprisingly not possible even with such a modification due to physical limits of a mechanical construction of the shutter (Eling et al. [2015]). Nevertheless, such delay, if detectable, is small and stable in time. The global shutter technology may overcome the issues of the mechanical construction of the rolling shutter, but does not solve the problem of synchronisation with a flash pulse.

The need for such modifications can be possibly eliminated by employing industrial cameras equipped with a synchronisation port and the global shutter technology. However, these cameras are significantly more expensive and generally provide a considerably smaller resolution for the same size and weight than mass-market cameras. Furthermore, their implementation into a MAV system often requires a tight integration with the autopilot as well as an additional computer to govern the camera and to store the acquired imagery.

### The Influence of a Synchronisation Error on Mapping Accuracy

A constant synchronisation error  $\Delta t$  causes a 3D error in sensor EO parameters as a function of the dynamics. The resulting error  $\Delta_{xy} = \Delta t \cdot v(t)$  is independent of the flying height, but its

## 6.4. The problem of the IMU and Camera Synchronisation

influence on the mapping accuracy depends on the flight configurations. Fig. 6.9 shows the influence of synchronisation errors on position for typical flying speeds. The typical flying speed  $v(t)$  of today's fixed-wing MAVs is between 10 and 20 m/s. A synchronisation error of, e.g. 1 ms propagates into a position error between 1 and 2 cm. Although this might seem negligible, in the case of 5 ms delay, the error is 5 and 10 cm, respectively.

For MAVs operating close to the ground ( $< 100$  m), the most influenced parameters are those concerning position. The height component of EO parameters is somewhat less influenced by potential  $\Delta t$  as the vertical speed is very low in a data acquisition phase of a flight, e.g. in the range of 0.5-1 m/s.

Considering carrier-phase differential noise around 2 cm, the time-stamping shall be performed better than 2.5 ms for ground velocities  $< 10$  m/s and 1 ms for velocities 10-30 m/s. Note that for fixed-wing MAVs operating at nominal speed of 10-15 m/s, a tail wind of 10 m/s pushes the aircraft to a ground speed of 25 m/s. Regarding the accuracy of a directly

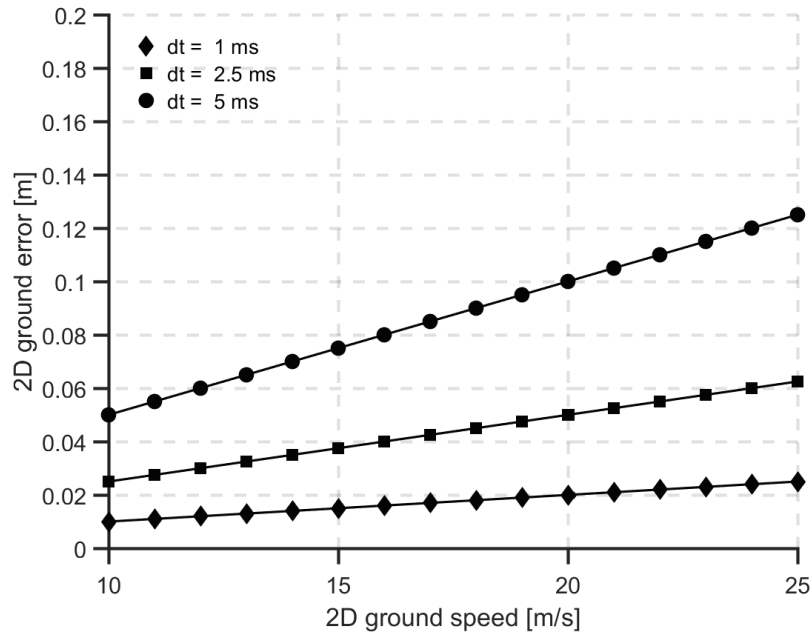


Figure 6.9 – Influence of synchronisation error  $\Delta t = 1, 2.5$  and 5 ms on velocity and resulting 2D position error.

measured attitude, angular errors induced by synchronisation depend on angular rates as well as on the altitude above ground level. Angular rates can be observed by gyroscopes inside an IMU. Some UAVs are equipped, similarly to manned aircrafts, with a stabilisation mount that compensates sudden attitude variations. In such a case, the camera attitude changes during  $\Delta t$  are likely negligible. In the case of fixed-wing MAVs whose weight does not exceed 5 kg, the weight and size limitations do not allow such stabilisation systems to be carried on-board. The majority of MEMS IMUs employed on MAVs for the purpose of a flight stabilisation has insufficient accuracy to act as useful attitude measurements for an image orientation. However,

state-of-the-art MEMS IMUs can deliver sufficiently precise observations with the support of ISO and DiSO on MAVs (Eling et al. [2015], Mian et al. [2015], Rehak and Skaloud [2015]). In addition, an employment of a R-IMU can further mitigate the attitude noise-level (Clausen et al. [2016]).

To demonstrate the influence of synchronisation errors on the attitude determination, angular rate observations were extracted from a test flight for every image and statistically evaluated, Tab. 6.5. As expected from a fixed-wing MAV flight, the most dynamic is in roll (omega angle) axis. If synchronisation error of  $\Delta t = 1 - 2$  ms is present in the system, it translates into the mean angular error of  $\Delta_\omega \approx 0.01^\circ$ . However, in the case of maximal angular rate, the error is considerably larger  $\Delta_\omega \approx 0.058^\circ$ . Such values start to be significant for many accurate GNSS/IMU systems available on the market (Applanix Corporation [2015], SBG Systems [2016]).

	$\omega$ [deg/s]	$\varphi$ [deg/s]	$\kappa$ [deg/s]
Mean	7.9	2.2	2.9
Median	5.9	1.6	2.4
Max	57.6	7.9	13.7

Table 6.5 – Angular rates observed during a real mapping flight.

The influence of attitude errors caused by a synchronisation error on the ground accuracy is depicted in Fig. 6.10 for three different height levels. It can be seen that an error in attitude increases its influence on horizontal ground accuracy with increased height and angular rate. Assuming nadir viewing imagery, the influence on the vertical component is negligible in the central part of the imagery and increases with radial distance.

### The Camera Synchronisation Error Observability

Synchronisation errors can be often absorbed by other parameters during camera or system self-calibration. For instance, modelling the errors in aerial positions by an additional shift and drift parameters for each strip allows absorbing the synchronisation errors within BA (under small variations of ground velocity within each strip). Also, it is known that errors in the camera principal point ( $x_0, y_0$ ) result in a ground shift, whose size is proportional to the flying height. Depending on the camera orientation with respect to a MAV's fuselage, the correlated coordinate to  $\Delta t$  is either  $x_0$  or  $y_0$ . However, unlike the synchronisation error, a shift in the ground coordinates caused by errors in the principal point coordinates depends on the flying height/scale rather than on the flying speed. Therefore, decorrelation of the principal point coordinates from the synchronisation error requires various flight levels.

Uncertainty in the lever-arm offset has a similar impact on the ground accuracy as the synchronisation error. This lever-arm error is, similarly to that of  $\Delta t$ , height independent and its influence on the exterior orientation accuracy is independent of the flying speed. The lever-arm can be determined in a laboratory calibration, or during a dedicated calibration flight, and is often stable enough even on MAVs. Therefore, if known, it should not be estimated



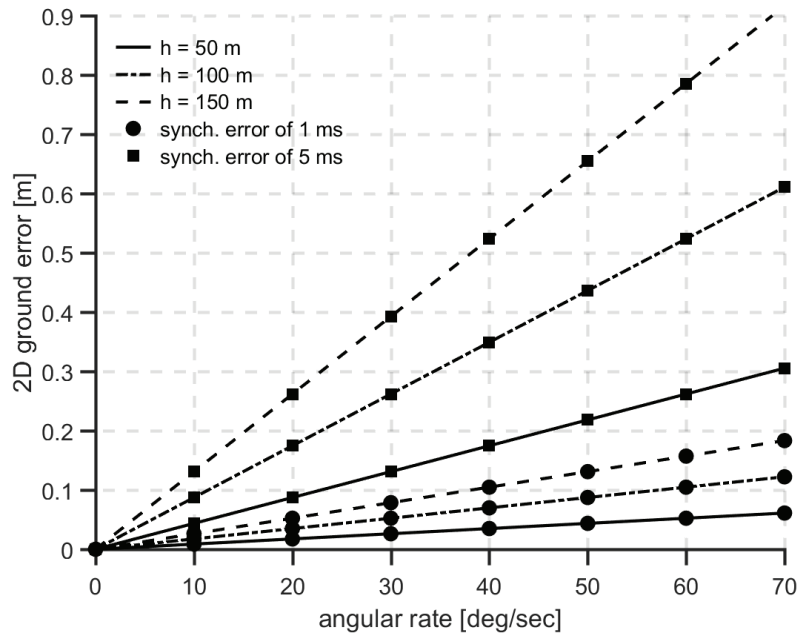


Figure 6.10 – Influence of synchronisation error  $\Delta t = 1$  and 5 ms on angular rates ( $\omega$  or  $\varphi$ ) and resulting 2D position error for three different flying heights.

within BA together with  $\Delta t$  if the latter needs to be calibrated. A strong prerequisite for such decorrelation is a sufficiently varying ground speed during the flight. It should be noted that the lever-arm parameters might be also correlated with the principal point coordinates. In conclusion, a prerequisite for a reliable  $\Delta t$  calibration is a strong block configuration with aerial and ground control with variances in the flying speed. Additionally, high forward and side overlaps as well as cross strips, assure strong redundancy in image observations. Last but not least, variations in height level as well as certain obliquity help with decorrelating the IO and EO parameters, particularly the camera principal distance with Z coordinates. Nevertheless, the possibility of fixing the camera's IO parameters can be a big advantage.

## 6.5 Sensor Calibration

### 6.5.1 Camera Calibration

Camera calibration is a process whereby the geometric aspects and relations of an individual camera are determined (Jones [1982]). These geometric aspects are called IO parameters. A camera calibration procedure presented within the scope of this thesis is focused primarily on measuring the main elements, i.e. principal distance, principal point coordinates, and additional parameters of the lens distortion.

### Requirements

The quality of camera calibration depends on several aspects, and the calibration process must meet certain criteria to be effective. Firstly, at least three pictures of a calibration field must be taken. Secondly, the interior geometry of the camera and the points to be measured must remain stable during the calibration (Clarke and Fryer [1998]). This is difficult to fulfil on consumer grade cameras that are equipped with zoom lenses.

Such instability can be mitigated, for example by using prime lenses, by disabling sensor or lens stabilisation, or by physically fixing lens internal moving elements. In the context of this work, the camera constant and principal point coordinates were considered stable during the mission due to the fact that neither the camera nor the lens have stabilisation elements and the prime lens has solid build quality. The additional parameters of lens distortion were considered stable even across different projects. The issue of IO stability is further discussed in Sec. 7.6

Next requirement specifies the needs of the photogrammetric network (calibration field). Typically, the camera calibration is performed in a laboratory and prior to mounting the camera in the MAV, by imaging a 3D field of targets in a strong geometric configuration. The strong geometric configuration has the following attributes:

- The existence of a dense target field with height variances,
- images are taken from different locations,
- images are taken with varying angles  $\omega$  and  $\varphi$  from moderate to high convergence and sufficient variations in  $\kappa$  angle,
- images are taken from different distances to the calibration field.

These network design conditions are more easily achieved with the camera decoupled from the MAV platform. In order to eliminate the need for dismounting the camera for regular calibrations, a preferable alternative is to calibrate it once installed on the platform. However, an airborne calibration still must incorporate the desired network geometry features as listed above and theoretically evaluated in Lichti et al. [2008].

Fourth and the last requirement is on a sufficient number of well-distributed points across all images. As soon as these conditions are properly met, good calibration results can be obtained.

### Optical Resolution of the Imaging Sensor

Optical resolution of an imaging system is defined as its ability to resolve a detail in an object. A typical approach to determine the optical resolution is the analysis of dedicated resolution patterns, e.g. the USAF 1951 resolution target or the Siemens star.

Several methods of resolution analysis can be employed. The simplest one is based on a visual evaluation of the smallest separation distance for which the optical system can distinguish lines. However, the visual evaluation may lead to different results depending on the person performing the test.

More sophisticated methods have been developed to better indicate the overall sharpness and quality of an image. These are, e.g. the PSF (Point Spread Function) or the MTF (Modulated Transfer Function) (Kölbl [2005]).

As a resolution unit, in the case of film-based optical systems, lines or line pairs per millimetre (L/mm, LP/mm) are used, while in the case of digital cameras, the units can be lines per pixel or line pairs per pixel (L/pix, LP/pix) (Cramer and Leinss [2014]). In the case of a PSF, the objective criterion for estimating the visual acuity in the image space is its standard deviation (Honkavaara [2008]). A further measure of the resolving power (RP) of an optical system is the FWHM (Full Width at Half Maximum) (Beaton and Farley [1991]). Furthermore, the RP can be determined with the spatial frequency at which the MTF reaches a certain (minimum) value, often 10 % of the contrast (MTF10). For consumer digital cameras, the value MTF10 is frequently above the Nyquist frequency and thus, this value is measured with a high uncertainty. It is often the spatial frequency where the image information disappears. Therefore, a frequency at which the contrast has dropped to 50 % (MTF50) is preferably used as an indicator of image sharpness (Koren, N. [2013], Imatest LLC [2017]).

In the course of the presented research, the employed camera Sony NEX 5R with the 16 mm Sony lens were tested for image quality and resolution by taking an image of the Siemens star target in static laboratory conditions. The Siemens star of a diameter of 65 cm was placed ~ 9 m from the camera. The pixel size equals to  $4.78 \mu\text{m}$  and the nominal GSD is equivalent to 0.266 cm. The aperture was set to f/5.6.

The target is illustrated in Fig. 6.11 with a detail on the diameter (determined in pixels) in which the drop in contrast equals to 50 %, Fig. 6.12. The evaluation was carried out in a dedicated software for the PSF and MTF analysis (Becker et al. [2006]). The pertinent results from the analysis are listed in Tab. 6.6. The  $\sigma_{PSF}$  is around 0.37 pixels and the point spread function is approximately  $\pm 1$  pixel, Fig. 6.13.

By multiplying the resolution values  $RP_{MTF10}$  and  $RP_{FWHM}$  with the nominal  $GSD_{TMF10}$  or  $GSD_{FWHM10}$ , the relevant resolution in the object space can be obtained (Cramer and Leinss [2014]). The nominal GSD of 0.266 cm can be almost achieved with the employed camera system. Nevertheless, Fig. 6.14 shows a detail on one of the elements of the Siemens star. A simple visual assessment leads to the conclusion that the PSF is rather in the level of ~ 2 pix.

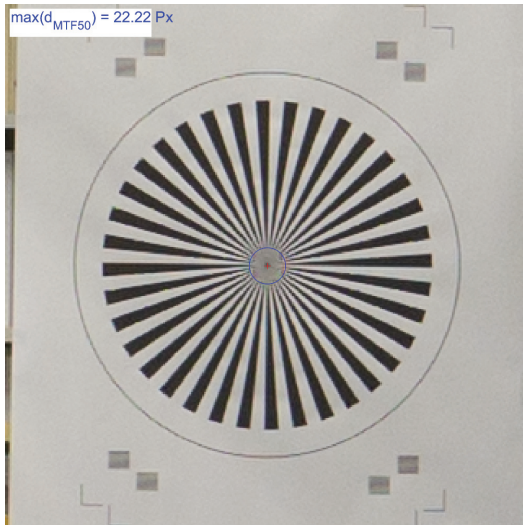


Figure 6.11 – Siemens star calibration target.

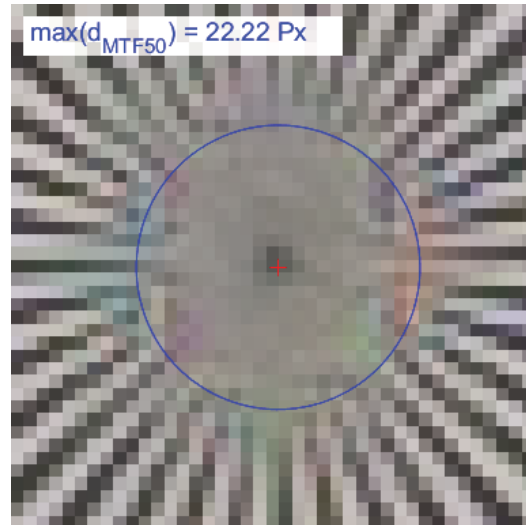


Figure 6.12 – A detail of the Siemens star target where the loss in contrast equals to 50 %.

Colour channel / parameter	Red	Green	Blue
$\sigma_{PSF}$ [pix]	0.370	0.360	0.363
MTF10 [L/pix]	0.923	0.949	0.940
MTF50 [L/pix]	0.506	0.521	0.516
$RP_{MTF10}$ [pix/L]	1.084	1.054	1.064
$RP_{FWHM}$ [pix/L]	0.872	0.848	0.855
$GSD_{MTF10}$ [cm]	0.288	0.280	0.283
$GSD_{MTF50}$ [cm]	0.232	0.225	0.227

Table 6.6 – Results of the static resolution test indicated in an image and object space.

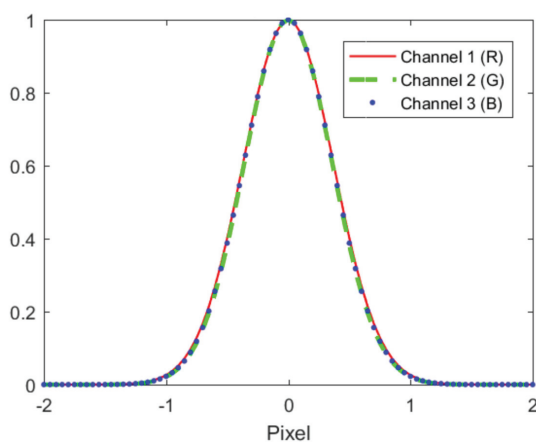


Figure 6.13 – An example of the Gaussian point spread function for different colour channels. Image courtesy of IFP, University of Stuttgart.



Figure 6.14 – A detail of the calibration target.

### Methodology

The Sony NEX 5R camera was calibrated several times, either self-calibrated during mapping projects or during dedicated flights over the close-range calibration field. The following section presents results from one of the calibration projects, namely the CR2 project from Tab. 6.1. Such a calibration flight is depicted in Fig. 6.15. The illustrated flight pattern is for one flight height only, although several flight heights were combined together.

Automatic tie-points were generated by the Pix4D Mapper and GCPs by the ARToolkitPlus library (Wagner and Schmalstieg [2007]). An image observation weighting was twofold, i.e. automatic observations were weighted to  $1\sigma \sim 1$  pixel, while those detected from coded targets to  $1\sigma \sim 0.5$  pixel. The camera positions were determined by GNSS and subsequently used as initial values in BA, but due to a large scale (GSD  $\sim 2$ -5 mm), they do not contribute to the estimation of IO parameters. Pertinent mission parameters are listed in Tab. 6.1. Camera



Figure 6.15 – Camera calibration flight over a dedicated field. The yellow line symbolises the flown trajectory, the red arrows symbolise the camera orientation during the image acquisition.

self-calibration was performed with the developed software TopoBun. A chosen Cartesian mapping frame was defined by 19 targets. The selected calibration model is according to Brown (Brown [1971]) with three radial and two tangential distortion parameters.

Several processing cases were considered each time including a new additional distortion parameter and analysing the observation residuals depicted in Fig. 6.16 and Fig. 6.17. From such a methodology it appeared that additional parameters  $K_1$  and  $K_2$  are sufficient for describing the radial lens distortion, i.e. the parameter  $K_3$  was estimated with very low accuracy that is twice the actual value of the  $K_3$ . Its omission did not modify the shape and magnitude of the residuals, and so did not the omission of  $P_1$  and  $P_2$ . The pertinent self-calibrating BA results are listed in the Tab. 6.7. It can be concluded that the RMS of the images residuals are below the size of one pixel and that IO parameters are estimated with sufficient accuracy except for  $K_3$ .

Parameter	Estimate	$\sigma$
RMS of image obs. res. $V_x$ [ $\mu m$ ]	3.74	-
RMS of image obs. res. $V_y$ [ $\mu m$ ]	3.38	-
$c$ [mm]	15.8777	0.0012
$x_0$ [mm]	-0.1694	0.0006
$y_0$ [mm]	0.1190	0.0009
$K_1$	-2.72e-04	9.92e-07
$K_2$	1.47e-06	1.41e-08
$K_3$	3.46e-11	6.04e-11
$P_1$	3.02e-05	8.85e-07
$P_2$	-3.22e-05	8.98e-07

Table 6.7 – RMS of image observation residuals and camera IO parameters from self-calibration.

Significant correlations between some of the estimated parameters are listed in Tab. 6.8. The full correlation matrix is located in Appendix in Tab. C.2. The IO and EO parameters are well-decorrelated. The inter-correlation between the additional parameters is typically high, particularly between the distortion parameters themselves, and between the principal distance and principal point coordinates. The distribution of image residuals is depicted in

Parameters	Correlation [0-100%]
$Z_0 - c$	10
$c - y_0$	75
$P_1 - y_0$	67
$P_2 - x_0$	91
$K_1 - K_2 - K_3$	>90

Table 6.8 – Significant correlations of a randomly selected image.

Fig. 6.16. It can be characterised by  $\mathcal{N}(1.2e - 05, 0.0036^2)$  [mm] with 76% values under  $1\sigma$ . Fig. 6.17 shows the image residuals with respect to the radial distance. There is no obvious trend that would indicate remaining unmodelled systematic errors.

Regarding the stability of the IO parameters over time, Sec. 7.6 provides a summary of the IO parameters that were estimated during different projects. More graphical outcomes from the calibration are in Appendix C.2.

### 6.5.2 Inertial Sensor Calibration

Due to low-cost and low-weight, MEMS IMUs have been extensively tested in the context of MAV navigation and SO (Pfeifer et al. [2012], Bäumker et al. [2013], Eling et al. [2014], Mian et al. [2015]). The predicted accuracy of these systems strongly depends on the adequate error modelling of the individual IMU sensors. The acceleration and angular speed measured by the IMUs are corrupted by relatively large errors of high complexity. These errors significantly

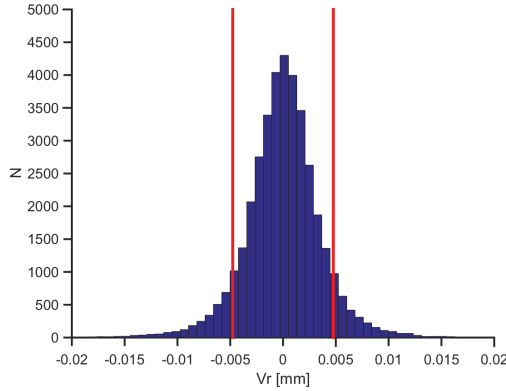


Figure 6.16 – Distribution of image residuals. The red lines represent 1 pixel size i.e.  $\sim 4.8 \mu\text{m}$ .

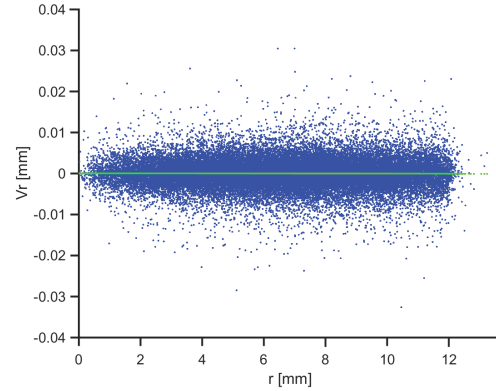


Figure 6.17 – Image residuals (blue dots) with respect to the radial distance. The green line represents a trend in residuals.

influence the final navigation solution. Thus, they need to be filtered using a plausible model. Firstly, the error characteristics of each and every sensor have to be determined (Stebler et al. [2014]). Then, the system needs to be calibrated for mean constant offsets as well as for non-orthogonality between individual sensors axis inside the IMU (Syed et al. [2007]). Finally, the inter-IMU misalignment needs to be determined for the redundant system. This misalignment constitutes a set of boresight and lever-arm parameters between the individual IMUs inside the R-IMU, where one IMU is considered the main sensor and the calibration parameters from the other sensors are estimated with respect to it. In the presented case, the boresights were calibrated by photogrammetry means, whereas the lever-arms were measured manually by a calliper. The involved distances between the IMUs are  $< 10 \text{ cm}$ .

Some types of the presented IMU errors are schematically depicted in Fig. 6.18. The process of model building is not trivial at all. The following general error model can be formulated according to Eq. 6.5 (Titterton and Weston [1997]).

$$\begin{pmatrix} \hat{l}_x \\ \hat{l}_y \\ \hat{l}_z \end{pmatrix} = \begin{bmatrix} 1 + S_x & 0 & 0 \\ -\theta_{xy} & 1 + S_y & 0 \\ \theta_{xz} & -\theta_{yz} & 1 + S_z \end{bmatrix} \cdot \begin{pmatrix} l_x \\ l_y \\ l_z \end{pmatrix} + \begin{pmatrix} b_x \\ b_y \\ b_z \end{pmatrix} \quad (6.5)$$

where

- $\hat{l}_{x, y, z}$  represents the adjusted measurements,
- $l_{x, y, z}$  are the observations,
- $S_{x, y, z}$  are the scale factors,
- $b_{x, y, z}$  are the biases,
- $\theta_{xy, xz, yz}$  is the non-orthogonality.

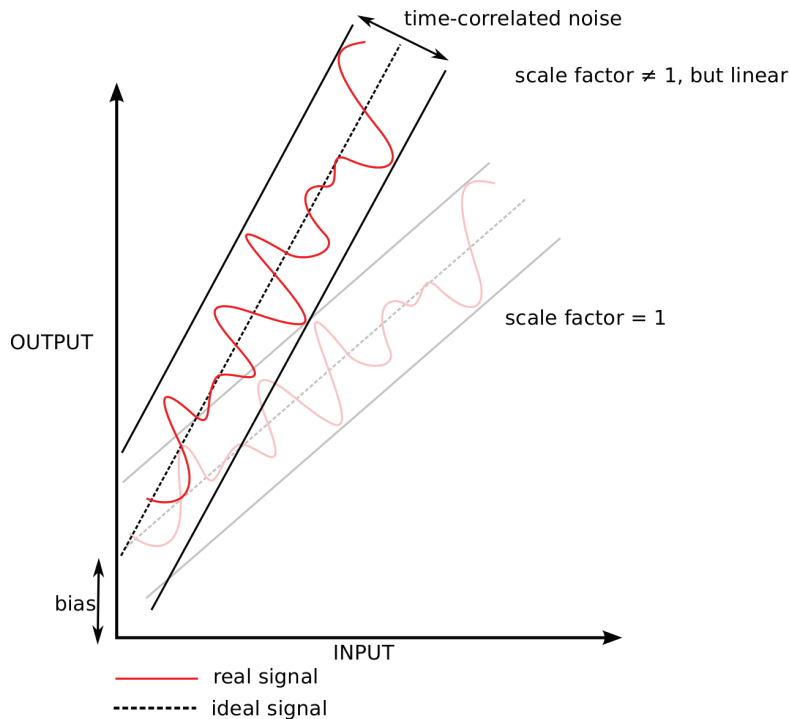


Figure 6.18 – Typical IMU errors: a bias, a scale factor, time-correlated noise. Modified after NovAtel [2014].

### Stochastic Errors

The method of the Allan variance (Hou [2004]) is often used to determine different types of random processes present in the inertial signal. The nature of the errors has to be identified by observing signal variations and decomposing the signal into different frequencies. In general, with MEMS IMUs, the Allan variance represents a mixture of several stochastic processes, such as quantisation noise (QN), white noise (WN), bias instability (B), random walk (RW), first order of Gauss-Markov (GM), and a random rate ramp (RR). The Allan variance is used to build a model type and the parameters of the model are estimated using the approach of the GMWM (Guerrier et al. [2015]). This estimation method is based on matching the empirical and model-based wavelet variances. The GMWM is able to handle complex error models for which other techniques, such as the Allan variance or expectation-maximisation algorithms fail or do not converge. The retained model consists of a mixture of several Gauss-Markov processes with white noise. The GMWM was used to estimate parameters of these processes, i.e. the variances and in the case of Gauss-Markov processes also the correlation times.

### Deterministic Errors

Three categories of deterministic errors can be distinguished: non-varying parts of biases, scale-factor errors, and misalignment (non-orthogonality) errors. Unlike stochastic errors, the



time invariant parts of deterministic errors are estimated via calibration.

The calibration procedure is based on comparing the sensor signals with nominal signals, such as gravity, Earth's rotation, or input, e.g. from a rotation table. An accelerometer error, if not removed from the measurement, is integrated twice as a part of the mechanisation process. In this case, the constant bias in acceleration becomes a linear error in velocity and a quadratic error in position (Titterton and Weston [1997]).

Regarding the employed R-IMU, a multi-position calibration was used for each IMU sensor to estimate the deterministic errors. This method uses the combined effect of the local gravity and rotation vector to build the reference signals needed for calibration (Syed et al. [2007]). The sensors do not have to be aligned to the local level frame. Nevertheless, it is necessary to have a redundant number of the IMU orientations to estimate the errors by using a least-squares adjustment knowing that constraints can be imposed for accelerometers and gyroscopes according to Eq. 6.6. The gyroscopes and accelerometers were calibrated using a custom mount that facilitates placing the R-IMU into 12 distinct positions in a static scenario for accelerometers, and dynamic scenario on a rotation table for gyroscopes (Clausen et al. [2016]).

$$f_1^2 + f_2^2 + f_3^2 - |g|^2 = 0 \tag{6.6}$$

$$\omega_1^2 + \omega_2^2 + \omega_3^2 - |\omega|^2 = 0$$

where

- $f_{1,2,3}$  are the specific forces measured along three axes (1,2,3),
- $g$  is the true local gravity,
- $\omega_{1,2,3}$  are the angular rates measured along three axes,
- $\omega$  is either the Earth's rotation rate alternatively augmented by a known value from a rotation table.

Fig. 6.19 shows the norm of the accelerometer measurements before and after calibration of one IMU. The wrong norm in different positions is caused by individual biases in each sensor axis, the scale factor, and non-orthogonality between them. The resulting biases from the calibration process are shown in Tab. 6.9. These values are significant and show that the problem of calibration cannot be ignored. As an example, the maximal value of ~ 28 mg would propagate to attitude initialisation error of ~ 2 degree according to the following equation:

$$\alpha = \arcsin\left(\frac{f_{bias}}{g}\right) \tag{6.7}$$

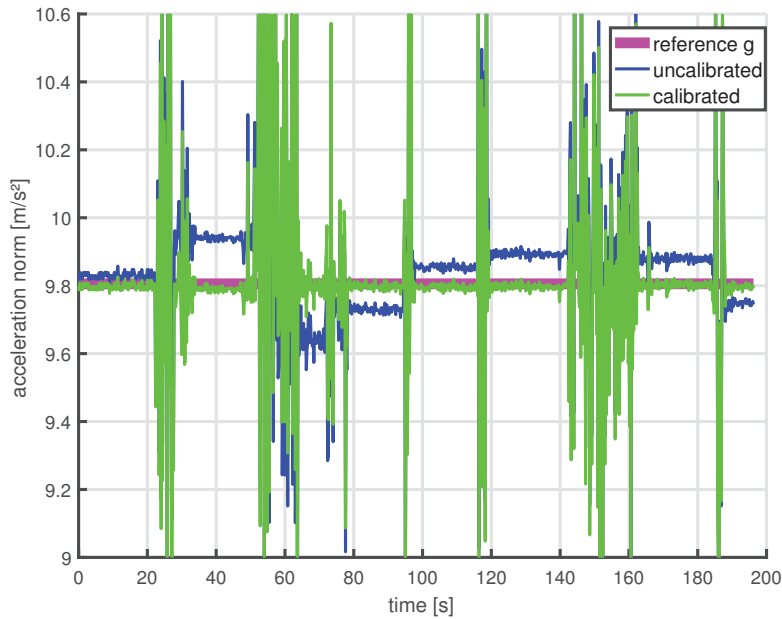


Figure 6.19 – Example data set before (blue) and after (green) calibration of an IMU showing the differences in the acceleration norm at different attitudes. The reference gravity value  $g$  is shown in a purple colour (Clausen et al. [2016]).

Property	IMU 1	IMU 2	IMU 3	IMU 4
$b_x$ [mg]	6.76	5.94	11.39	-0.99
$b_y$ [mg]	16.23	4.19	1.54	28.22
$b_z$ [mg]	-0.87	-2.52	-2.06	-5.37

Table 6.9 – Calibrated accelerometer biases of the R-IMU Clausen et al. [2016].

**Summary**

This chapter discussed the system and sensor calibration of a mapping payload on the presented MAV platforms. Firstly, calibration and testing fields were presented. A close-range calibration field features strong geometry, a high number of GCPs, and is specific to a camera calibration. The second field is located in a rural area and is dedicated to a testing of platforms under real mapping conditions. Several data sets were collected within the scope of this thesis with developed MAV platforms under different weather conditions and ground texture characteristics. Since a system and sensor calibration are essential prerequisites for DiSO and important for ISO, a significant part of this chapter was devoted to the description of the performed calibration procedures. This included a calibration of spatial offsets and sensors time synchronisation. The camera and IMU calibration procedures were presented together with the most pertinent results. The calibrated parameters from this chapter are applied throughout mapping projects presented in the following chapter.

# 7 Evaluation and Performance Assessment

*This chapter is dedicated to the analysis of the data obtained from the developed MAV systems and their adjustment. The processing chain is introduced and several projects are presented demonstrating different configurations of an integrated sensor orientation. The results are analysed and presented both graphically and numerically. The outcomes of these experiments reflect the quality of the methods and approaches described in the previous chapters. This chapter is partially adopted from the following publications: Skaloud et al. [2014], Rehak and Skaloud [2015, 2016, 2017].*

## 7.1 Introduction

In order to simplify the reader's orientation among different processing scenarios presented in this chapter, the content is organised into several thematic blocks. After a short introduction to the data processing work-flow in Sec. 7.2, the following sections deal with ISO employing different types of aerial observations.

Sec. 7.3 concentrates on absolute and relative aerial position control. Two case studies are presented. First, it is demonstrated that ISO with absolute position observations can limit or completely eliminate the number of GCPs in block configurations. Furthermore, it is shown that GNSS position bias due to an unfavourable satellite geometry can be eliminated using relative observations. The second study deals with aerial control based on a low-cost GNSS receiver. It also manifests the ability of determining the lever-arm in self-calibrating BA. The performance is evaluated by comparing the calculated trajectories from the low-cost and geodetic-grade receivers, and by their impact on mapping accuracy. Here the ground accuracy is assessed at independent ChPs.

Sec. 7.4 presents case studies that focus on aerial position and attitude control. First study concentrates on corridor mapping. It is shown that aerial attitude control has a significant impact on ground accuracy in corridors. The second study tackles a mapping project without automatic tie-points. The aim is to investigate whether aerial position and attitude observations can deliver reasonable ground accuracy without the support of hundreds of tie-points, as it is the case of AT. Then, the method of direct georeferencing is assessed. The last test from

this section briefly addresses the concept of redundant aerial observations. In Sec. 7.5, the absolute position and attitude control is extended to spatio-temporal control. Several methods of sensor time delay estimation are presented and verified on a practical example. Finally, Sec. 7.6 discusses the stability of self-calibrated IO parameters from the presented projects. The aim is to compare IO parameters estimated in the course of this research in order to investigate their stability.

## 7.2 Data Pre-processing

This section focuses on the data pre-processing that was carried out for every demonstrated project prior to BA. The presented work-flow does not follow the typical, i.e. commercial MAV photogrammetric scheme. This is due to the sensors on-board that have the ability to store raw observations. The price of having more information and control is paid by somewhat increased processing complexity. A general work-flow is illustrated in Fig. 7.1. According to the scheme, the acquired data is represented by yellow colour, the intermediate and final products by blue colour, and the green cells represent the four processing steps. These main elements are described in detail below. The grey cell representing the BA is described in Sec. 4.10.

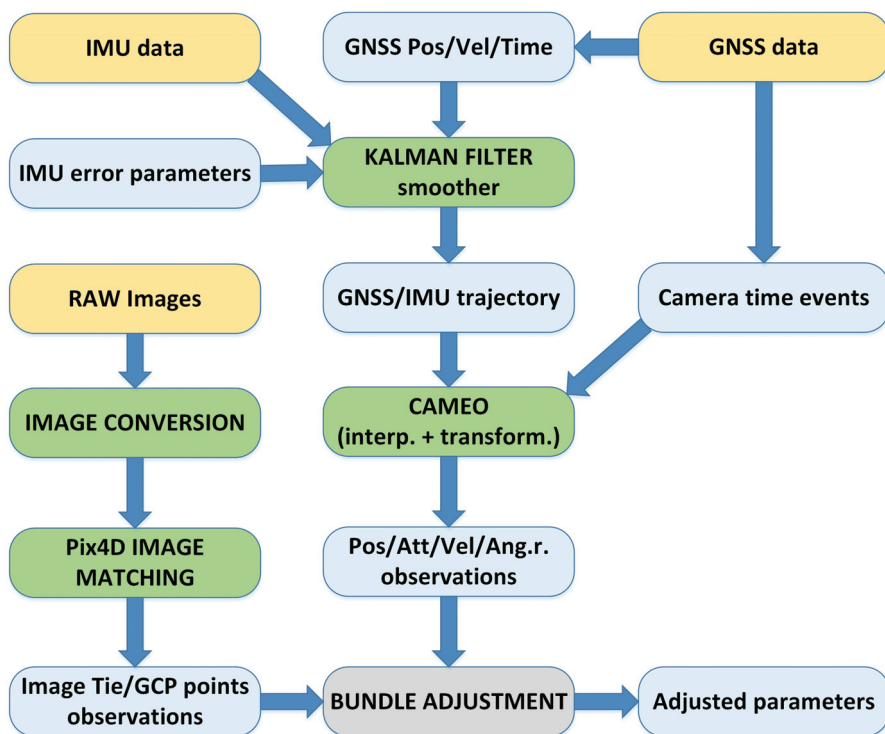


Figure 7.1 – Processing scheme; raw data inputs are in yellow, blue are the input/output products, green are the processing steps, and grey is the BA.

### 7.2.1 Image Conversion

The first step in the presented processing chain is the conversion of collected imagery from the raw format to the JPEG<sup>1</sup> format. The advantage of shooting in raw is obvious in terms of a high dynamic range as discussed in Sec. 3.3.3. The conversion is procured in a commercial photo editing suit. This step is crucial mainly for correcting the exposure in case it was wrongly set before the flight, or the light conditions changed during the acquisition phase. The contrast and white balance are among other important photo corrections. An example is given in Fig. 7.2. The left image is automatically exported from raw to JPEG using the senseFly's eMotion2 (senseFly [2015a]) data management tool, while the right image is manually corrected in a professional photo editor. It is important to note that these changes do not affect the image geometry, i.e. no lens corrections are applied. While the elimination of overexposed areas with lost texture (the road in the given image) helps the computer vision based algorithms to detect more automatic tie-points, the white balance correction improves the natural appearance of the orthophoto.



Figure 7.2 – Automatic and manual image conversion from raw to JPEG format; a) automatic conversion using the senseFly eMotion2, b) manual correction using a photo editor. The image was taken with the Canon PowerShot S110 camera having 12.1 Mpix resolution (Canon Inc. [2016]).

### 7.2.2 Image Observations

Automatic tie-point detection and manual image observations of the GCPs and ChPs was performed in the Pix4D Mapper. In the case of the close-range calibration field, the tie-points were obtained either automatically using the coded fiducial markers and customised OpenCV and computer vision libraries, or as a combination with automatic observations from the Pix4D Mapper. This way, a high number of observations was ensured while eliminating the need for manual identification of control and check points.

The quality of automatic image observations is one of the key factors determining the accuracy of mapping, particularly with limited or no aerial control. Three attributes can be

<sup>1</sup>Joint Photographic Experts Group

distinguished.

First, it is the number of tie-points. The question about the number of tie-point observations is often too simplified. For example the more observations the better results is often not valid. The reason is that not all the observations influence the results equally due to, e.g. an irregular distribution or poor quality. Second, the accuracy of detected points depends on the employed computer vision algorithms, surface texture, and/or an imaging sensor quality. The third attribute represents a tie-point observability in images. An example showing the observability of tie-points of two datasets FW1 and FW2 is shown in Fig. 7.3 in a form of a gradient map. The shades of grey represent the number of observations. The darker the grey value, the less image observations for a given area. It is clear that border areas have less observations due to the missing overlap. However, the central part of the FW2 data set has also significantly less observations despite being flown from two directions at two different heights. The presented examples demonstrate the influence of surface on the automated detection of tie-points.

The problem of surface homogeneity and the resulting quality of tie-points can be overcome by several approaches. First, the observations on automatic tie-points should be appropriately weighted, e.g. key-points detected from different scales, different surface texture etc. should have corresponding standard deviations. Second, absolute and relative aerial position and attitude control maintain network consistency in areas with a low number and/or low quality of tie-points. Third, absolute aerial position and attitude control can completely eliminate the need for automatic tie-points. In addition, different key-point extractors can provide different results over, e.g. vegetation, sand etc.

As for the accuracy of image observations, the observations derived from coded targets (used in the close-range tests) were weighted by 3/4 pix, the automatically detected tie-points by the Pix4D Mapper by 1-1.5 pix, and manually identified GCPs and ChPs by 0.5-1 pix.

### 7.2.3 GNSS/IMU Processing and Trajectory Interpolation

The airborne trajectory was estimated in a way similar to a mature mapping system using either professional or custom software packages for the GNSS/IMU integration. The GNSS data was differentially post-processed using the Waypoint GrafNav and GrafNet tools (Novatel [2016]).

As for the IMU processing, the raw observations were fused with the GNSS data into a trajectory using the Kalman filter/smoother. Two software tools were employed: First, the Postproc (Applanix Corporation [2016]) and second, an in-house developed software called Navproc (Stebler and Skaloud [2012]).

The trajectory parameters (position, velocity, attitude, and angular rates) were interpolated to image event and transformed to a mapping frame using an in-house developed software called CAMEO (Skaloud and Legat [2006]). Here the corrections of boresight and lever-arms parameters were applied (if known beforehand).

BA of the presented projects was carried out either in a local tangential plane or in the Swiss LV95 coordinate system with ellipsoidal heights (Swisstopo [2017]). In the latter case, the

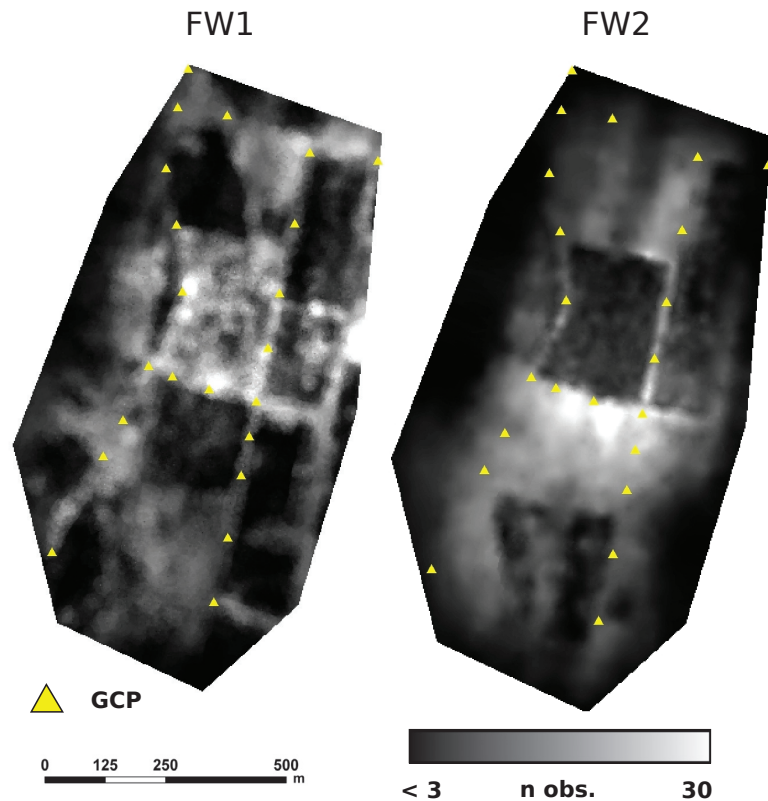


Figure 7.3 – Observability of tie-points for the datasets FW1 and FW2. The two areas were clipped in order to cover the same region.

corrections related to mapping in a national mapping frame were applied by the CAMEO as discussed in Sec. 2.6.4.

## 7.3 Aerial Position Control

This section presents several cases when employing aerial position observations in the BA. A variety of tests were carried out with both MAV platforms and GNSS receivers of different quality.

### 7.3.1 Absolute Relative Aerial Position Control in the GNSS Perturbed Environment

ISO with aerial position control was initially tested on the data set CR1 collected using the multicopter platform over a close-range calibration field equipped with coded targets as detailed in Sec. 6.1. The acquired data set whose characteristics are presented in Tab. 6.1, is highly redundant with imagery taken under a large (by airborne standards) convergence angle. The IMU observations were not used in the presented experiment. The basic IO parameters were re-estimated in all the following experiments. The adjustment was made

## Chapter 7. Evaluation and Performance Assessment

---

in the Fembun BA in a local tangential plane. The accuracy of the airborne positions was validated by comparing the GNSS-derived positions with those obtained by BA in a separate project using all the GCPs and re-estimated IO parameters. Tab. 7.1 provides a summary of the quality of image observations and GNSS data.

The image measurement precision, as gauged by the root mean square of the image point residual, is higher than might be expected when using coded targets, at about  $3\ \mu\text{m}$  ( $\sim 1/2$  of a pixel size). This can be attributed to degraded target measurement accuracy at oblique angles. The quality of the GNSS positioning was checked independently with respect to the AT-derived camera positions using all 25 GCPs. Once accounting for the camera-antenna spatial offsets, the residuals of EO positions are around 25 mm in position and height, respectively, which corresponds to the accuracy of kinematic carrier-phase differential GNSS processing.

Parameter	Value
Maximum convergence angle	$78^\circ$
Degrees of freedom	1680
RMS of image obs. res. $V_x$	$2.8\ \mu\text{m}$
RMS of image obs. res. $V_y$	$3.3\ \mu\text{m}$
RMS of aerial position residuals (X, Y, Z)	0.017, 0.025, 0.024 m

Table 7.1 – Network characteristics and accuracy of the measured tie-points and GNSS aerial positions.

### Test Setup

In order to test the influence of a possibly undetected GNSS bias on the mapping (ground) accuracy, the GNSS positioning was artificially perturbed in certain testing scenarios that are presented below for the data set CR1:

**A. Indirect SO with three GCPs placed relatively close to each other, no aerial control.**

**B. ISO with aerial position control.**

1. Absolute aerial control (all 68 obs.)
2. Absolute aerial control (6 obs.) + relative aerial control (61 obs. with  $dt_{ij} < 10\ \text{s}$ )

**C. ISO with "biased" aerial position control and one GCP.**

1. Absolute aerial control (all 68 obs. that are partially biased)
2. Absolute aerial control (6 unbiased obs.) + relative aerial control (61 obs. with  $dt_{ij} < 10\ \text{s}$ )

**D. ISO with three GCPs (as in A) and relative aerial control (61 obs. with  $dt_{ij} < 10\ \text{s}$ ).**



The results of individual test cases are represented by the overall RMS statistics of the residuals. Adjustment projects with aerial control are compared to the traditional method of indirect SO. The following testing scenarios are considered:

**Case A: Indirect SO with 3 close GCPs**

The first case is focused on the indirect sensor orientation approach, which is the dominant method of sensor orientation when mapping with MAVs. Although the power of this concept is indisputable, it might be the case that due to the inaccessibility of the mapping area, only a limited number of GCPs can be established, or their distribution does not extend over the whole field. Such extrapolation configuration will inevitably cause high distortion in object space coordinates.

In order to simulate this case, three selected GCPs were taken only from one-quarter of the mapped area as illustrated in Fig. 7.4. The outcome from the BA for this case is presented in Tab. 7.2. The close spacing in the GCPs decreased the mapping accuracy in the rest of the field and created a significant bias in the height component.

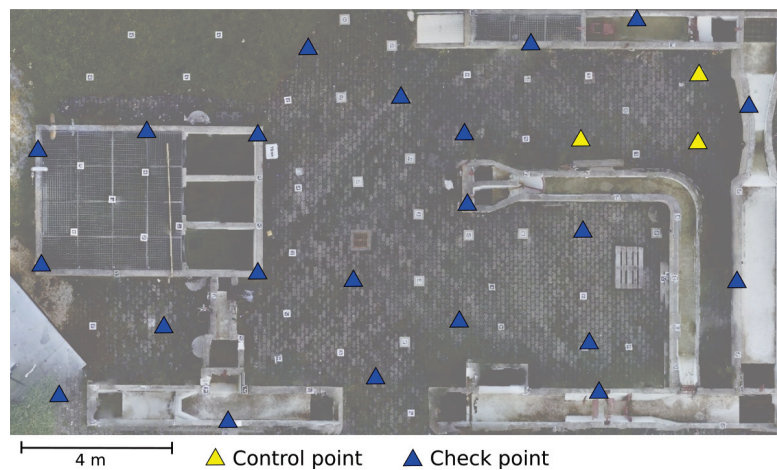


Figure 7.4 – Placement of 3 GCPs and 22 ChPs.

Position residual	X [mm]	Y [mm]	Z [mm]
Max	-72	-31	-110
Mean	-29	12	64
RMS	38	30	103

Table 7.2 – Case A: Summary of indirect SO (AT + 3 close GCPs) at 22 checkpoints.

**Case B: ISO with one GCP and absolute or relative aerial control**

The second case is focused on the contribution of the absolute and relative aerial control under optimal conditions. Although it is not essential in the absolute control, the inclusion

of one GCP improves the redundancy and contributes to better estimation of the principal distance. In the relative position control, however, at least 1 GCP, or an absolute position observation is needed for a datum definition.

The statistics of residuals presented in Tab. 7.3 confirm that under ideal circumstances, i.e. when there is indeed no bias present in the GNSS-derived absolute positions, the differences between ISO + 1 GCP + abs. GNSS and ISO + 1 GCP + abs/rel. GNSS appear negligible.

<b>B1: ISO (1 GCP + 68 abs. GNSS)</b>			
Position residual	X [mm]	Y [mm]	Z [mm]
Max	58	-40	75
Mean	11	-15	17
RMS	26	21	39
<b>B2: ISO (1 GCP + 6 abs. GNSS + 61 rel. GNSS)</b>			
Position residual	X [mm]	Y [mm]	Z [mm]
Max	59	39	79
Mean	14	-15	6
RMS	27	21	39

Table 7.3 – Case B: Summary of ISO projects without bias.

**Case C: ISO with one GCP and absolute or relative aerial control of degraded positioning quality**

Case C focuses on the scenario where the quality of the GNSS positioning is degraded in the sense that the ambiguities are not resolved, and resulting positions are biased or strongly time-correlated. In the presented case, the number of available satellites was artificially reduced to five for the first 62 exposures while maintaining all the observations for the remaining 6 exposures. This resulted in a systematic error in absolute positioning for the majority of the camera exposure stations. The predicted accuracy of the GNSS positioning is depicted in Fig. 7.5 while Fig. 7.6 and 7.7 show the differences between aerial positions interpolated from a reference and artificially perturbed trajectories. The presence of the time correlated bias is obvious in some absolute positions. Yet, this bias is eliminated by differencing in most of the following relative positions. The few remaining biases are identified as outliers and eliminated in the adjustment. Regarding the weighting, the relative observations were weighted according to Eq. 4.16. The weights were derived from the reference EO parameters. Two BA projects are considered. First, ISO configuration with absolute aerial positions and one GCP, and second, ISO configuration with 1 GCP, 6 absolute GNSS positions from the period of good GNSS reception and 61 relative observations. The results are summarised in Tab. 7.4. As expected, the bias in absolute aerial observations is reflected in degraded ground accuracy. Contrary to the first scenario, relative aerial control eliminates systematic errors in the GNSS positioning, while a few unbiased absolute positions are sufficient to ensure overall good ground accuracy. The effect of float ambiguities on aerial positions can be traditionally

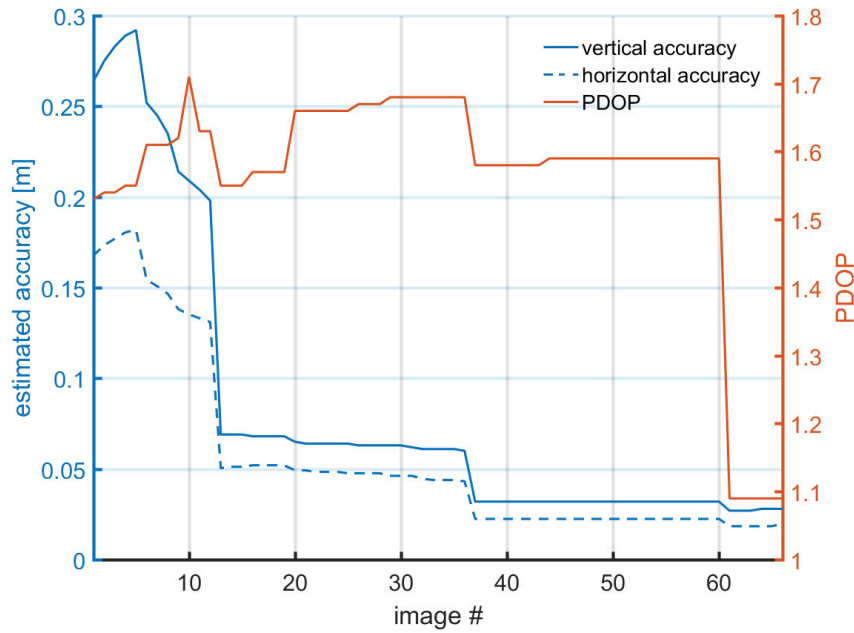


Figure 7.5 – Estimated vertical and horizontal accuracy, and position DOP values for the 68 images.

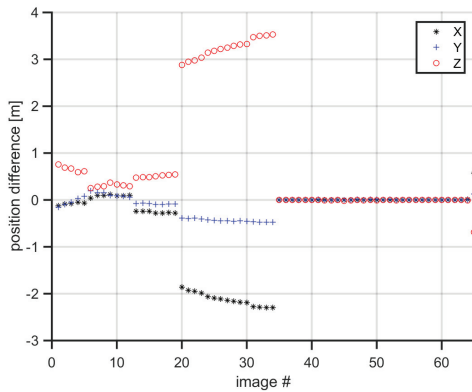


Figure 7.6 – Differences in absolute observations between reference EO parameters and those determined from a perturbed GNSS signal.

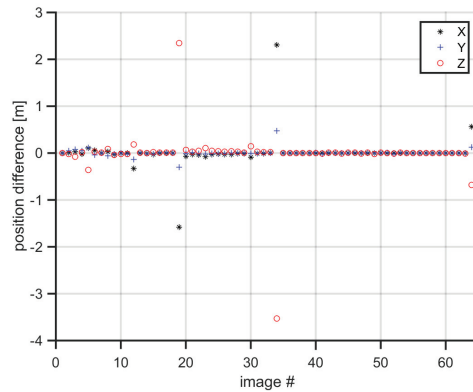


Figure 7.7 – Differences in relative observations between reference EO parameters and those determined from a perturbed GNSS signal.

mitigated by adding GNSS shift and drift parameters per strip into the adjustment. The inclusion of relative position observations raises new options when employing GNSS observations in BA. Practically, only a few good positions are needed (minimum of 1) and those can be selected from epochs where the number of tracked satellite is high and their geometry is strong. Alternatively, the minimum number of GCP, i.e. 1, can be complemented by relative GNSS observations. These are less prone to carry an undetected bias (e.g. due to

incorrect ambiguities), but enhance the strength of the whole network.

<b>C1: ISO (1 GCP + abs. GNSS with bias)</b>			
Position residual	X [mm]	Y [mm]	Z [mm]
Max	115	-79	150
Mean	32	-37	47
RMS	55	46	73
<b>C2: ISO (1 GCP + 6 abs. GNSS + 61 rel. GNSS with bias)</b>			
Position residual	X [m]	Y [m]	Z [m]
Max	63	-41	-71
Mean	15	-16	10
RMS	29	22	38

Table 7.4 – Case C: Summary of ISO on projects with GNSS positioning bias.

**Case D: ISO with three GCPs (as in A) and relative aerial control**

Case D repeats the case A to which relative aerial control of position is added. 61 derived observations were taken from the GNSS positions of a degraded quality. In comparison to the case A, the residuals at check points shown in Tab. 7.5 are 3-4 times lower in the horizontal components (< 1 cm!) and 3 times smaller in height. For a better presentation of achieved accuracy, the results from Tab. 7.2-7.5 are displayed together in Fig. 7.8.

<b>Position residual</b>	<b>X [mm]</b>	<b>Y [mm]</b>	<b>Z [mm]</b>
Max	12	20	-87
Mean	2	0	-7
RMS	5	7	36

Table 7.5 – Case D: Summary of ISO (3 close GCPs + 61 relative GNSS + GNSS bias) at 22 checkpoints.

**Summary**

This project highlighted the benefits of accurate aerial position control in the context of MAV mapping. The inclusion of aerial observations of the camera positions allowed to omit (or considerably reduce) the number of GCPs for the block of images. In the cases where the quality of GNSS positioning was not optimal, the absolute aerial observations were affected, which worsened the ground accuracy. However, Fig. 7.6 shows that the influence of wrong aerial positions was, in the presented case, mitigated by weighting as illustrated in Fig. 7.5. As a result, aerial observations did not bring significant network strengthening, because only a few unbiased and properly weighted observations were purposeful in the BA. On the contrary, the relative observation still delivered good results, as the influence of the

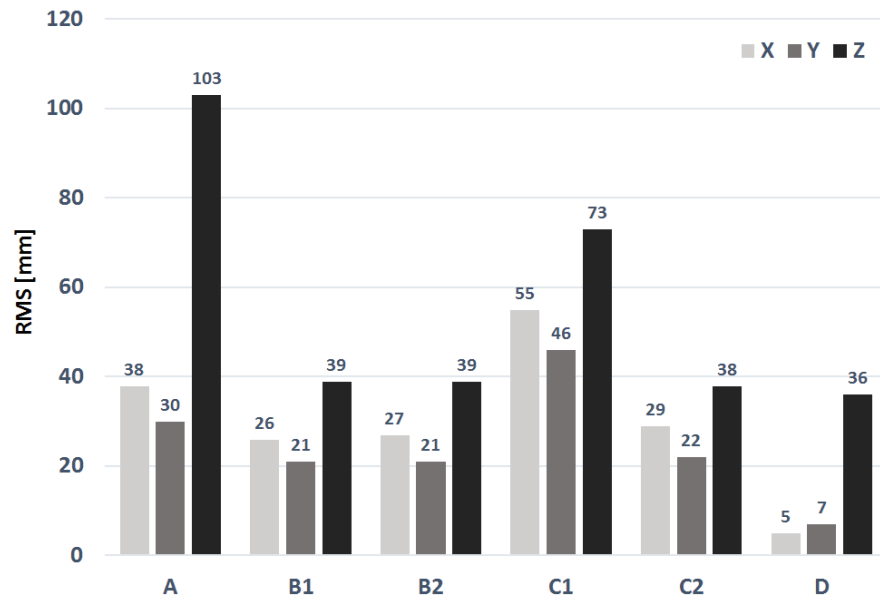


Figure 7.8 – Accuracy at ChPs from the cases A-D.

GNSS bias was mitigated. The obtained results favour the approach of ISO with a few GCPs and relative aerial position control. In the case of MAVs, the relative positioning represents additional important advantages as it allows to consider a single-frequency carrier-phase GNSS receiver which is considerably smaller and cheaper.

### 7.3.2 Aerial Position Control With a Low-cost GNSS Receiver

The following test aims at investigating whether a low-cost (<\$100) mass-market GNSS receiver U-Blox NEO-8T can provide accurate, i.e. cm-level, kinematic positioning to contribute in ISO. Additionally, the aim is to test the ability of the BA to estimate the camera-GNSS antenna lever-arm vector. The data set of this test has an acronym FWubx and is characterised in Tab. 6.1. As described in Sec. 5.4.2, the signal from the same antenna was split into the U-Blox NEO-8T and a reference receiver Javad TR-G3T using a dedicated splitter. Thus, their trajectories and resulting EO parameters can be directly compared with each other.

#### Methodology

The GNSS data was processed in the GrafNav and interpolated for each camera event. While the reference trajectory has ambiguity fixed throughout the entire flight, the U-Blox data allows only a float solution. Nevertheless, as long the float ambiguities converge to a stable value, the float solution may be exploitable as accurate enough, especially in relative aerial control. The two sets of EO position parameters derived from tested vs. reference data are compared in

## Chapter 7. Evaluation and Performance Assessment

Fig. 7.9 in an absolute, and in Fig. 7.10 in a relative way, i.e. differences between two positions of two consecutive camera stations. It can be seen that rather small (< 10 cm) differences/drift in absolute positions are practically eliminated by differencing.

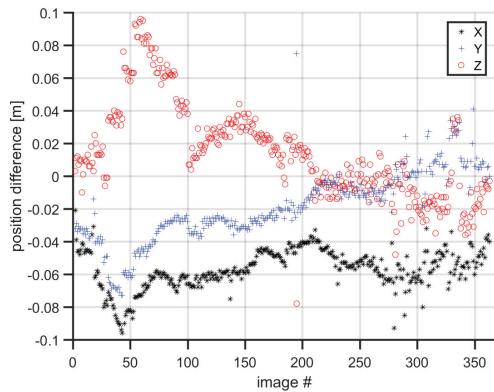


Figure 7.9 – Differences in absolute camera positions between the Javad and the U-Blox GNSS receivers.

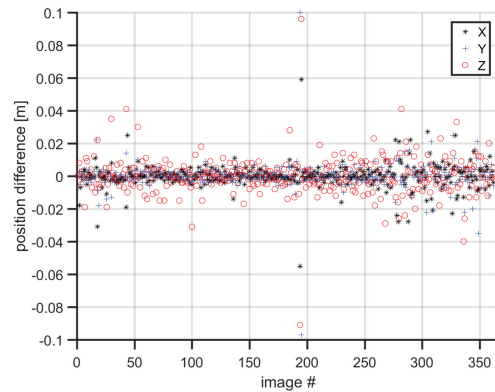


Figure 7.10 – Differences in the relative camera positions between the Javad and the U-Blox GNSS receivers.

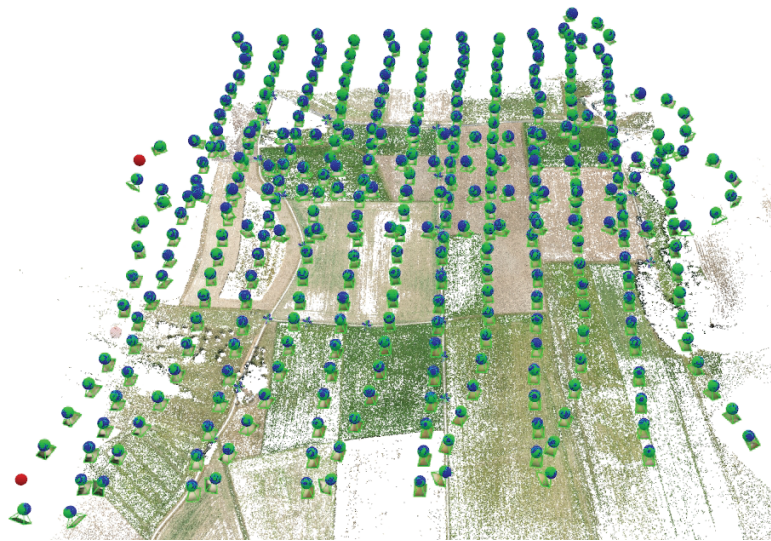


Figure 7.11 – 3D view on the scene with camera stations, GCPs and a point cloud of tie-points from the Pix4D Mapper.

### Absolute Aerial Control

As a next step, the Pix4D Mapper was used for obtaining image observations and initial attitude parameters. The reconstructed scene can be seen in Fig. 7.11. The BA was carried out in

the TopoBun and the Pix4D Mapper without GCPs and with self-calibrated IO parameters  $(c, x_0, y_0, K_1, K_2)$  in the following configurations:

- I.** Processing with a known lever-arm from the static calibration described in Sec. 6.2.2. The calibrated offset has the value of  $\mathbf{a}_{CAM-ANT}^c(a_x, a_y, a_z) = [-433, -31, 147]$  mm. This value is the calibrated lever-arm from Tab. 6.3 corrected for a spatial offset due to the mechanical mounting of the antenna splitter as depicted in Fig. 5.7 and with added ARP to the L1 phase centre offset. This lever-arm is introduced in the adjustment as a weighted observation according to Tab. 6.3.
- II.** Processing without a priori knowledge of the lever-arm, i.e. the initial offset is zero, its incertitude  $\sigma_{a_x, a_y, a_z} = (0.5, 0.5, 0.5)$  m, and is estimated in BA as an additional parameter.
- III.** The lever-arm is not considered. This processing setup is for comparing the developed TopoBun with the Pix4D Mapper which does not allow estimating the lever-arm in its current version.

The results of the cases I-III are summarised in Tab. 7.6. In general, the projects processed with EO parameters from the Javad receiver manifest overall better ground accuracy. In the case the lever-arm is known, the achieved accuracy is close to 1 pixel in position and height for the Javad and 1.5-2 pixels for the U-Blox considering the average GSD of 4 cm.

The processing II demonstrated the ability of the BA to resolve initially unknown lever-arm, but not better than 5 cm along camera's x-axis. Indeed, this could be a typical mapping scenario for consumer drones to which a GNSS receiver is added, and a lever-arm between the camera and an antenna is not known. The differences between the processing I and II are significant mainly in X and Z coordinates. This is due to the unconstrained lever-arm. The system is over-parametrised and estimated parameters are highly correlated, particularly the  $Z_0 - c - a_z$  and  $x_0 - a_x$ .

As expected, the lever-arm is highly correlated with IO parameters and camera positions, as shown in their variations in Tab. 7.6. There is a significant change of the  $x_0$  coordinate between processing I and III, i.e. with and without the lever-arm. The missing lever-arm offset is absorbed by estimated values of the principal point and camera constant, but it is not projected to the ground shift in the Z coordinate as it happened in the case II. Some pertinent correlation parameters are stated in Tab. 7.7. These are calculated during the BA project of the type I with EO parameters from the Javad receiver.

In general, the Javad receiver provided higher accuracy of absolute EO parameters. The resulting accuracy measured at independent ChPs lies in the case I in the level of  $\sim 1$  pixel in position and height, respectively. The U-Blox receiver can deliver accuracy in the level of  $\sim 2$  pixels in position and  $\sim 1.5$  pixels in height without the support of GCPs. Due to the size of the lever-arm, i.e. the  $\mathbf{a}_{CAM-ANT}^c(x)$  offset is significantly larger than  $\mathbf{a}_{CAM-ARP}^c(z)$ , the horizontal ground accuracy is more influenced than its vertical component.

## Chapter 7. Evaluation and Performance Assessment

Rx	Test		Accuracy						IO			Lever-arm		
			Mean ChP [mm]			RMS ChP [mm]			[mm]			[mm]		
			X	Y	Z	X	Y	Z	c	x <sub>0</sub>	y <sub>0</sub>	ax	ay	az
Javad	I.	TPB: known lever-arm	-1	14	31	42	27	49	15.8315	-0.0069	0.0187	-479	-19	142
	II.	TPB: unknown lever-arm	-1	14	93	41	27	100	15.8351	-0.0027	0.0181	-528	-1	59
	III.	TPB: no lever-arm Pix4D: no lever-arm	-1	15	107	46	36	115	15.8386	-0.0635	0.0167	-	-	-
U-Blox	I.	TPB: known lever-arm	46	34	-16	64	42	46	15.8376	-0.0050	0.0191	-487	-19	123
	II.	TPB: unknown lever-arm	46	34	193	63	42	188	15.8491	0.0002	0.0200	-535	-30	-174
	III.	TPB: no lever-arm Pix4D: no lever-arm	47	35	47	67	47	63	15.8440	-0.0626	0.0171	-	-	-

Table 7.6 – Mapping accuracy at 23 ChP, with an absolute aerial position control, without GCPs, and with absolute aerial positions. The acronym TPB states for the TopoBun. The average GSD of these ISO projects is 4 cm.

Parameters	Correlation [0-100%]
$X_0 - a_x$	35
$Y_0 - a_y$	36
$Z_0 - a_z$	79
$Z_0 - c$	62
$x_0 - a_x$	68
$y_0 - a_y$	84
$c - a_z$	79

Table 7.7 – Significant correlations of a randomly selected image.

### Relative Aerial Control

Relative observations were derived for both sets of EO parameters. In order to orient the network, at least one GCPs must be added. In practice, this can be, e.g. the base station point if it is visible in the imagery.

Two scenarios are considered. Relative aerial observations with one or four, well-distributed GCPs. The processing is done for the case I due to the assumption that a lever-arm can not be well-determined in relative positioning if the flight is not performed under various speed. Therefore, the camera absolute positions were first corrected for the lever-arm, and then differentiated between two consecutive epochs  $t_i$  and  $t_j$  for  $dt_{ij} < 10$  s, according to Eq. 7.1 that is a modified Eq. 4.8. The attitude was taken from the Pix4D project as the MEMS-IMU inside the autopilot cannot provide sufficient attitude accuracy for correcting this relatively long lever-arm. On the contrary, the MAV platforms with short lever-arms between a camera and a GNSS antenna, such as the eBee (senseFly [2015a]), can use attitude from the autopilot's IMU. Furthermore, the autopilot's internal clock must be time synchronised with the GNSS receiver and the camera.

$$\Delta \mathbf{X}_0^m(t_{ij}) + \mathbf{v}_{\Delta X_0}^m = \mathbf{X}^m(t_j) - \mathbf{X}^m(t_i) - (\mathbf{R}_c^m(\Gamma_{t_j}) - \mathbf{R}_c^m(\Gamma_{t_i})) \cdot \mathbf{A}^c \quad (7.1)$$



where

- $\mathbf{X}_0^m$  is the camera projection centre,
- $\mathbf{v}_{\Delta X_0}^m$  is the vector of the camera projection centre residuals,
- $\mathbf{X}^m$  is the GNSS-derived position for one epoch in a Cartesian mapping frame  $m$ ,
- $\mathbf{R}_c^m(\Gamma)$  is the estimated attitude from the Pix4D Mapper,
- $\mathbf{A}^c$  is the camera-GNSS antenna lever-arm expressed in the camera frame,
- $\mathbf{S}^m$  is the possible bias in the GNSS-derived positions.

The results from the four adjustment projects are summarised in Tab. 7.8. When the relative observations replace the absolute ones and one GCP is used, the ground accuracy lies in the level of 1.5 pixels in position and 1.5 pixels in height. After adding 3 more GCPs, the accuracy improved only in height component by  $\sim 1.5$  cm to  $\sim 1$  pixel. Such improvement is due to the additional GCPs that strengthen the absolute network orientation.

Rx	Test		Accuracy						IO		
			Mean ChP [mm]			RMS ChP [mm]			[mm]		
			X	Y	Z	X	Y	Z	c	$x_0$	$y_0$
Javad	I.	TPB: 1 GCP, known lever-arm	28	4	-26	59	28	62	15.8372	-0.0063	0.0179
	I.	TPB: 4 GCPs, known lever-arm	-25	-9	-8	51	36	49	15.8370	-0.0064	0.0180
U-Blox	I.	TPB: 1 GCP, known lever-arm	28	3	-31	59	27	64	15.8390	-0.0059	0.0182
	I.	TPB: 4 GCPs, known lever-arm	-25	-8	-6	51	35	49	15.8388	-0.0059	0.0182

Table 7.8 – Mapping accuracy at 22 ChPs, with 1 or 4 GCPs, and with relative aerial position control.

### Summary

This section demonstrated the capability of a low-cost GNSS receiver to deliver absolute and relative aerial observations, whose accuracy is in ideal conditions close to its high-end counterpart. Scenarios with and without GCPs were presented. Although mapping with just one GCP without the support of absolute aerial observations is possible, in practice it is not recommended due to low redundancy and minimum control. Despite these promising results and favourable price of the mass market L1 GNSS receiver, its hardware integration into a MAV platform is not trivial due to its sensitivity to vibrations and EMI as discussed in Sec. 5.4.2.

## 7.4 Aerial Position and Attitude Control

In this section, the effects of aerial position and attitude control on mapping accuracy are assessed. The results are compared to classical methods of indirect SO and ISO with aerial position control only. Furthermore, a newly proposed method of quasi-direct SO, so-called Fast AT (Blázquez and Colomina [2012a]), is tested in the context of MAV mapping.

### 7.4.1 Aerial Control in Corridor Mapping

The data of the following project have an acronym FW1 and are detailed in Tab. 6.1. The following test consists of two steps. First, the fixed-wing platform is calibrated for boresight and camera IO parameters, and second, mapping accuracy is assessed in a narrow corridor. Fig. 7.12 illustrates the composition of the FW1 flight and particularly its separation into the calibration and testing parts. The strips from **A** to **E** and **H** to **J** served for the system and camera self-calibration. These two perpendicular block configurations were executed in altitudes of 120 and 150 meters in order to better decorrelate IO/EO parameters. Two strips, **F** and **G**, representing the corridor, were excluded from the processing, and were exclusively used for the accuracy assessment. The length and width of the corridor were 1200 m and 180 m, respectively. The differences in terrain topology were around 30 m between the lowest and the highest points. The average GSD was 3.8 cm. In total 467 images were captured out of which 406 were used for the calibration and 61 for the corridor evaluation.

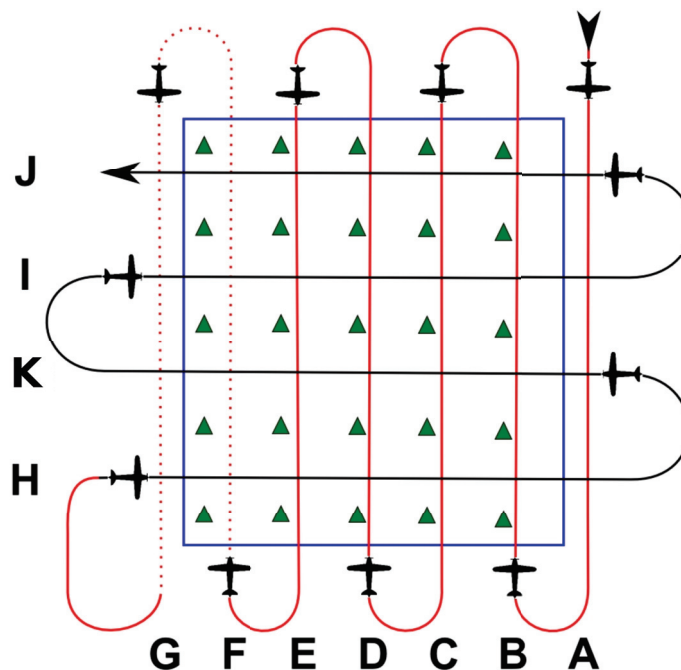


Figure 7.12 – A scheme of a strip separation of the FW1 flight. Green triangles represent the GCPs.

**Self-calibration**

The camera EO parameters with coordinates of 17 signalised GCPs were introduced as weighted observations and the IO parameters and boresight were considered as unknowns. Tab. 7.9 summarises the estimated accuracy of the IO parameters together with the boresight. They are all estimated with a reasonable precision. Tab. 7.10 highlights the quality of aerial position and attitude data, i.e. the RMS of the residuals between the observed vs. estimated parameters. The aerial position and attitude residuals fulfil the required accuracy of the GNSS/IMU system at this scale for ISO. To highlight this further, Fig. 7.13 depicts the achieved accuracy together with the propagation of attitude errors on the ground for two different flying heights above ground. The estimated accuracies of  $\omega$  a  $\varphi$  attitude angles can theoretically cause errors on the ground in 7 cm – 9 cm level, but as it will be analysed later in the corridor, their inclusion has a positive influence on the ground accuracy. In the presented example, these ground errors would represent an error of approximately 2 times the GSD. The estimated precision of object point coordinates and control points also show optimistic values below 1.5 pixel both in position and height, respectively.

Parameter	Estimate	$\sigma$
RMS of image obs. res. $V_x$ [ $\mu m$ ]	3.36	-
RMS of image obs. res. $V_y$ [ $\mu m$ ]	3.34	-
$c$ [mm]	15.8352	0.0003
$x_0$ [mm]	-0.0645	0.0004
$y_0$ [mm]	0.0609	0.0003
$K_1$	-2.62e-04	6.81e-07
$K_2$	1.42e-06	9.08e-09
$b_\omega, b_\varphi, b_\kappa$ [deg]	-0.021, 0.635, 0.942	0.001, 0.002, 0.002

Table 7.9 – RMS of image obs. residuals with the camera IO parameters and boresight from self-calibration.

Parameter	X [m]	Y [m]	Z [m]
RMS of aerial position residuals	0.014	0.013	0.026
Maximum aerial position residuals	0.053	0.049	0.127
Mean precision values on object points	0.017	0.019	0.044
Poorest precision values on object points	0.128	0.134	0.341
Mean precision values on control points	0.004	0.004	0.009
Poorest precision values on control points	0.021	0.020	0.034

Parameter	Omega [deg]	Phi [deg]	Kappa [deg]
RMS of aerial attitude residuals	0.040	0.035	0.151
Maximum aerial attitude residuals	0.164	0.216	0.445

Table 7.10 – Quality of the GNSS/IMU data and estimated precision of the object and control points.

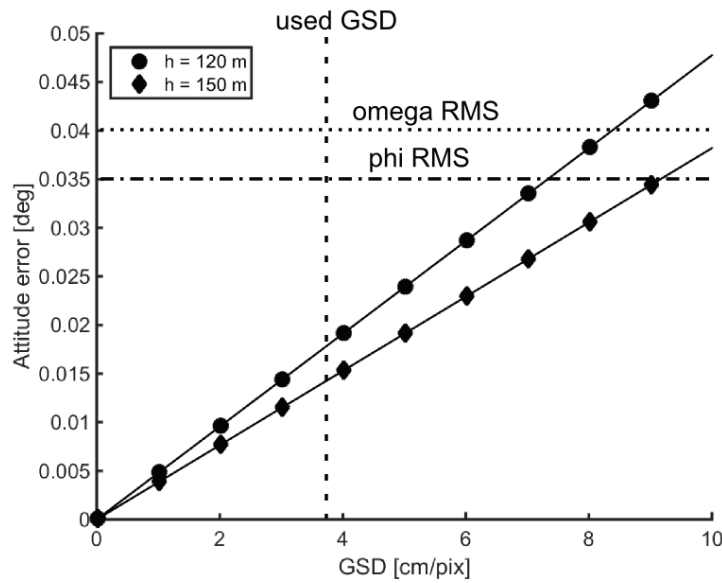


Figure 7.13 – The propagation of roll and pitch errors on the ground from two different flying heights in contrast with the estimated accuracy of measured angles.

**The Influence of Aerial Control on Mapping Accuracy**

The previously estimated boresight angles were considered when transforming GNSS/IMU-derived attitude for the two strips of the corridor. The ISO adjustment was run twice with different configurations. In both cases, the IO parameters were fixed and no GCPs coordinates entered the adjustment. In the first case I, the adjustment was done with GNSS/IMU-derived aerial positions only. In the second case II, the aerial positions and orientations were included. The results are summarised in Tab. 7.11 with respect to 9 independent check points whose distribution is depicted in Fig. 7.14.

Test	Accuracy					
	Mean ChP [mm]			RMS ChP [mm]		
	X	Y	Z	X	Y	Z
I.: ISO + abs. Pos	-44	11	-40	50	26	69
II. ISO + abs. Pos, abs. Att	-15	0	-27	26	22	67

Table 7.11 – Residuals at 9 check points, no GCPs used in the adjustment.

In the case I, the insufficient lateral overlap causes noticeable errors in the X component due to the absence of attitude control as the orientation of the corridor is approximately north-south, i.e. aligned with Y-axis of the mapping frame. The lack of GCPs degrades the accuracy of estimated image orientations that directly propagates on the ground. Systematic errors can be recognised by a larger mean value which is in this case over 3 centimetres. Additionally, the position residuals are evidently higher with respect to the case II, except in the height component that is comparable.

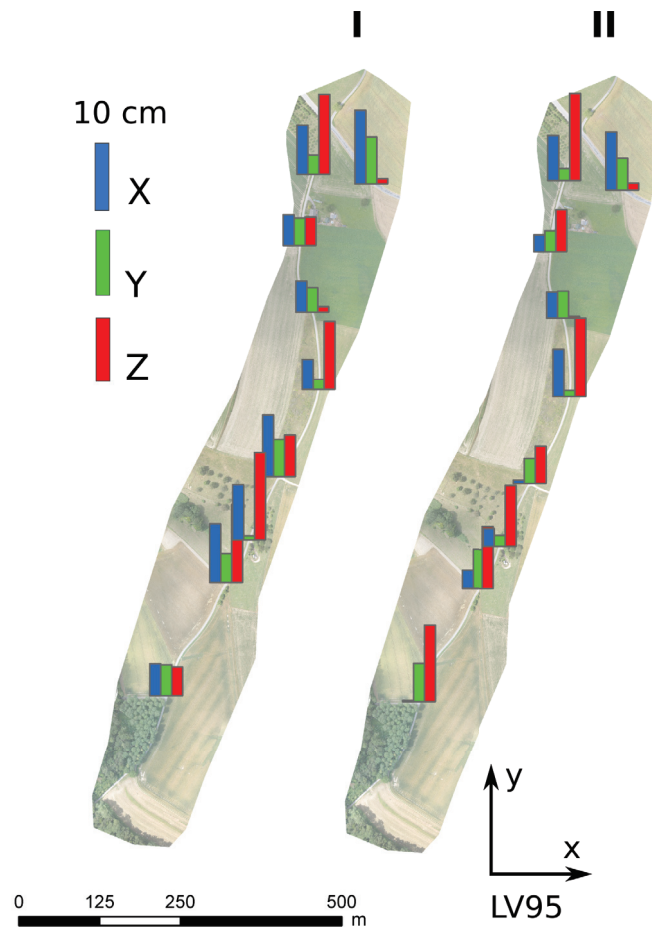


Figure 7.14 – Residuals at ChPs. ISO configuration with absolute aerial position control (I), and with position and attitude control (II). The base orthophoto was processed in the Pix4D Mapper.

In the case II, any significant mean value would indicate problems either in the estimated IO parameters, wrongly calibrated offsets, or a synchronisation issue. However, values close to zero indicate that this is not likely the case, or that the errors are absorbed by two strips flown in the opposite directions. It can be seen that in all the selected statistical indicators, the angular observations improved the results at independent check points. It can be clearly concluded that when having weak geometry of just two strips, as is often the case of UAV corridor mapping, the angular observations play an important role in the final ground accuracy.

The corridor was also processed in the Pix4D Mapper to compute the digital surface model. Its current version (3.0) allows using aerial position control, hence mapping without the GCPs is possible. The measured attitude can also be introduced, however it does not contribute to the final mapping accuracy since the inputted values serve only as initial approximations. Therefore, the full potential of aerial attitude control cannot be demonstrated by this software. Despite that, the directly estimated attitude was used to correct the lever-arm, which indirectly affects the positioning quality as well.

Fig. 7.15 shows absolute height differences of resulting digital surface models with respect to a reference model that was calculated from the entire block oriented by 25 GCPs in the Pix4D Mapper. It is obvious that the geometrical precision degrades with decreasing overlap on both sides of the corridor. There is no obvious difference between the model oriented by 9 GCPs (case A) and the one oriented from the GNSS/IMU-derived absolute position observations (case C). Nevertheless, when the distribution of GCPs is not favourable (case B), the accuracy degrades significantly in the absence of aerial control. A similar situation is depicted in Fig. 7.16 after processing in the TopoBun. The error ellipsoids are scaled 30 times to highlight the influence of GCPs distribution and aerial control on estimated precision of object coordinates of tie-points. In this figure, the differences between the cases A and C are more obvious than in Fig. 7.15, and are in favour of the case C due to the inclusion of attitude observations.

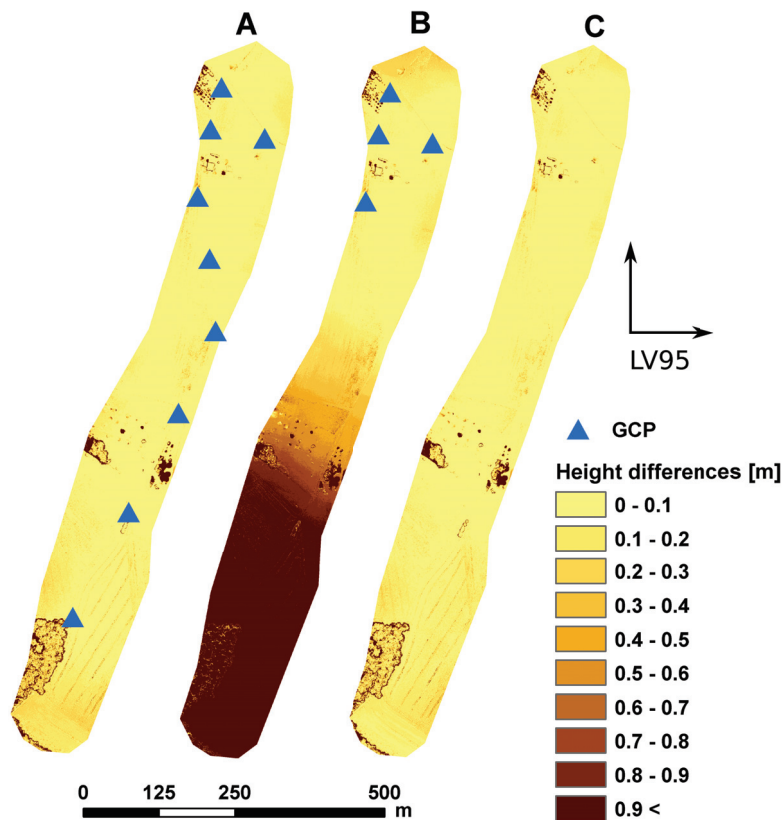


Figure 7.15 – DSM differences with respect to the reference for different types of absolute orientation; A) 9 GCPs, B) 4 GCPs, C) accurate GNSS/IMU-derived positions.

### Summary

This section presented a case study on the benefits of absolute position and attitude control in MAV mapping. First, camera IO parameters were calibrated together with a boresight misalignment of the employed IMU. A small corridor consisting of two parallel strips was selected and

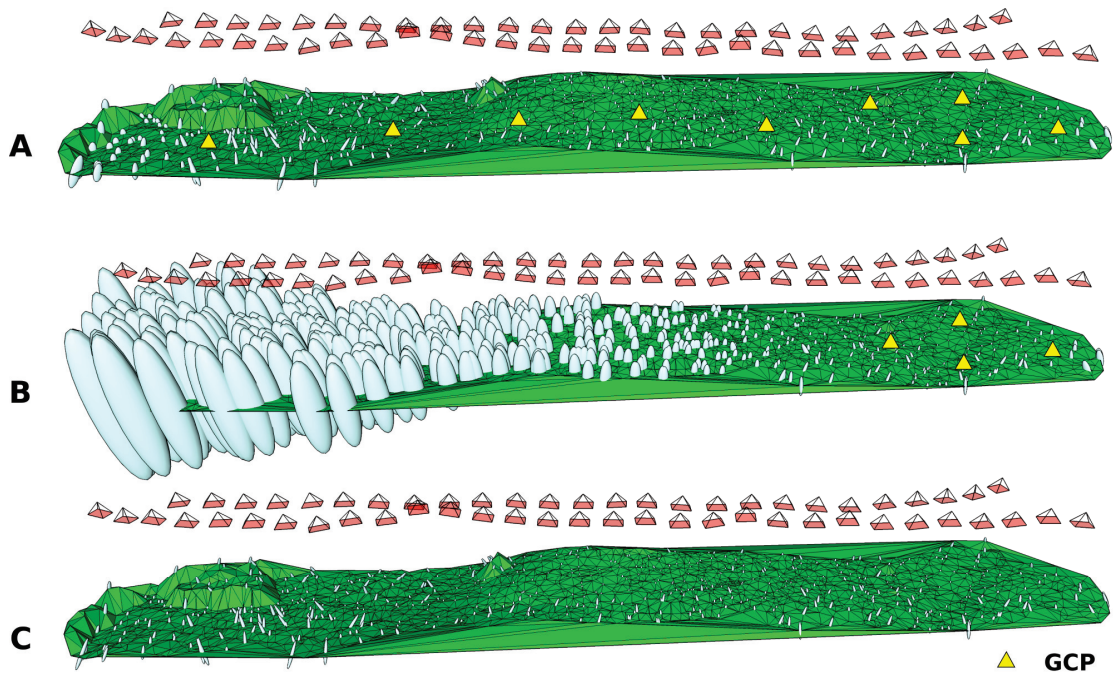


Figure 7.16 – Estimated precision of object coordinates of tie-points for different types of absolute orientation. A) 9 GCPs, B) 4 GCPs, C) accurate GNSS/IMU-derived positions and attitude.

adjusted in the developed BA, and in a commercial software tool. Several processing strategies were tested with the conclusion that directly measured exterior orientation parameters can significantly improve ground accuracy while dropping the need for ground control establishment. It was also practically demonstrated that although the observed attitude accuracy is lower than the direct orientation requirements, it considerably contributes in the field of aerial triangulation. The RMS of  $\omega$  and  $\varphi$  angles was estimated to  $\sim 0.04$  deg which is excellent for the MEMS IMU of such size.

#### 7.4.2 Sensor Orientation Without Automatic Tie-points

This section investigates a method of ISO where image observations are limited to ground control and/or check points, so called Fast AT. In the context of airborne mapping with high-end GNSS/IMU, it showed that accurate aerial control (absolute or relative) together with a few image observations can deliver results that are comparable to classical aerial triangulation with thousands of image measurements (Blázquez and Colomina [2012a]). This procedure is interesting as it reduces the demands on processing time and the requirements on the existence of a surface texture, e.g. for an orthophoto update using an existing DEM. Here, this method is investigated and compared with indirect SO, ISO, and DiSO to show its potential for rapid mapping with MAVs.

The data set FW2 was processed in the same way as demonstrated in Sec. 7.2. The IO param-

eters were used from the previous project presented in Sec. 7.4.1 and were fixed in Fast AT and DiSO, but were re-calibrated in ISO configurations. The boresight that was estimated in the previous flight FW1 could not be used as the R-IMU was replaced with another sensor board with 4 IMUs (the previous had only 2 IMUs). Although this is not an optimal solution as the boresight parameters may absorb some errors which would normally influence the ground accuracy, there was no other possibility to estimate the boresight. In an ideal case, the boresight should be calibrated independently in a different data set. Nevertheless, this inconvenience affects only those methods that rely on absolute attitude observations. Therefore, the boresight misalignment was calibrated in a dedicated ISO configuration with all GCPs, and then fixed in Fast AT and DiSO.

### Test data

The data set FW2 consists of 7 parallel stripes and 7 cross strips, flown in two separate flight heights as depicted in Fig. 7.17. The flight was performed during a crop vegetation stage and thus the surface suffers from strong homogeneity. The quality of detected key-points and tie-points, respectively, is significantly degraded in certain areas as discussed in Sec. 7.2.2 and shown in Fig. 7.3. The aim of this study is to present the novel approaches of SO on MAVs on realistic data sets. Indeed, surface homogeneity is very common in agricultural areas and, given the expansion of MAVs in precision farming, a number of applications need to deal with such surfaces on a regular basis. The distribution of object points in the adjustment scene is depicted in Fig. 7.18. While the Fast AT image observations are limited only to GCPs and ChPs, the ISO project uses thousands of automatic tie-points. Regarding the accuracy assessment, 5 points were used as GCPs and 15 as independent ChPs. The placement of GCPs was such that it emulates mapping of a badly accessible area where GCPs can be placed only in the vicinity of the launching area, Fig. 7.17. It is important to say that the very same points were used for all the testing scenarios, and in the case of DiSO, the GCPs were completely excluded.

### Processing and Evaluation

The adjustment showed an interesting fact that despite the executed boresight calibration, relatively high residuals are present in the trajectory. Fig. 7.19 depicts the residuals of attitude angles. High residuals are obviously in omega and kappa angles. Repetitive patterns are caused by correlation in attitude, e.g. due to initialisation/alignment or by a residual boresight. This somewhat less accurate attitude determination is of a minor importance in the strong block configuration as its effect is mitigated by parallel strips, especially in the case of ISO with good distribution of tie-points. However, the influence on ground accuracy is gaining importance in the scenarios with higher requirements on aerial control, e.g. Fast AT or DiSO. A solution to this problem offers relative orientation. By differentiating the attitude observations, the effects of boresight are eliminated, as proved in Sec. 4.6, and mitigate the remaining correlated part at the same time. To highlight this further, Fig. 7.20 shows the differences



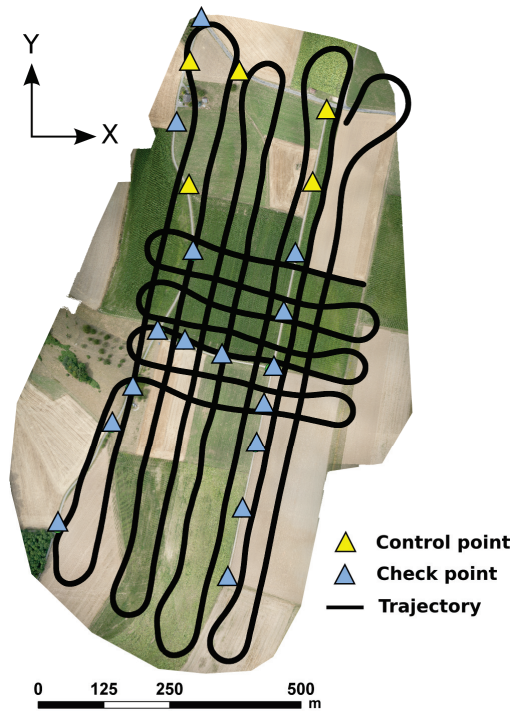


Figure 7.17 – Flown trajectory, ground control, and check points on a base orthophoto map from the Pix4D Mapper.

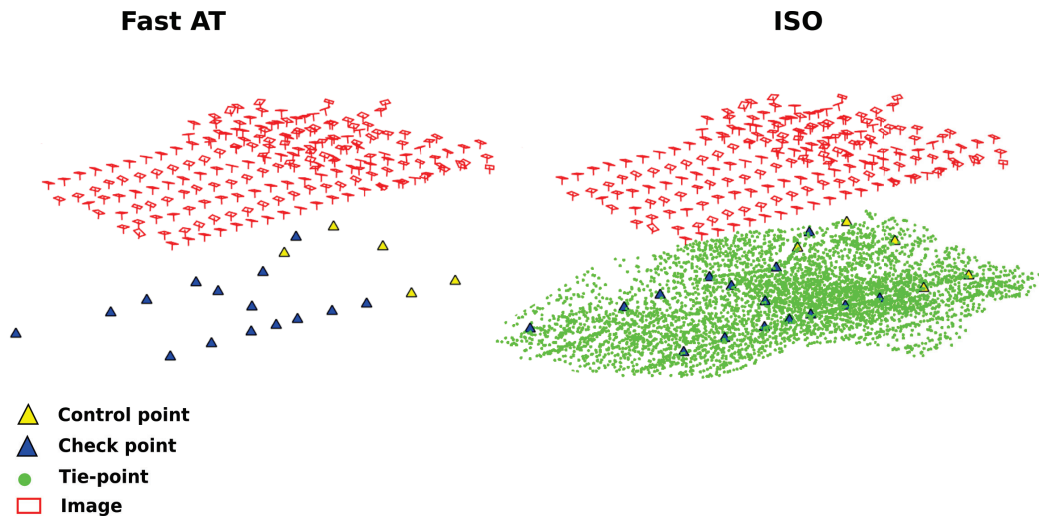


Figure 7.18 – Distribution of GCPs, ChPs, and tie-points in Fast AT and ISO.

between initial relative attitude observations and relative attitude computed from adjusted attitude parameters. It can be seen that the effects of a residual boresight have vanished, and the residuals have lower RMS. The practical evaluation was done by calculating different SO methods. The different combinations of observations are listed in Tab. 7.12, and the accuracy is evaluated at the check points.

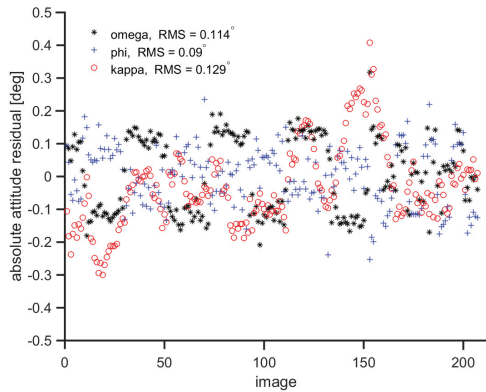


Figure 7.19 – Absolute attitude residuals; influence of an IMU residual boresight on attitude accuracy.

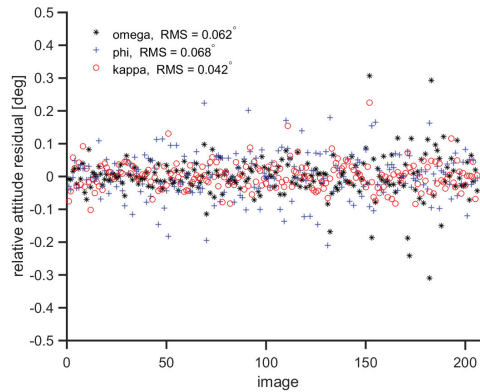


Figure 7.20 – Relative attitude residuals.

Mode	Position cont.	Attitude cont.	Camera cal.	Boresight
Indirect SO	-	-	Yes	-
ISO	Absolute	Absolute	Yes	Known
ISO	Absolute	Relative	Yes	-
ISO	Relative	Relative	Yes	-
Fast AT	Absolute	Absolute	No	Known
Fast AT	Absolute	Relative	No	-
Fast AT	Relative	Relative	No	-
DiSO	Absolute	Absolute	No	Known

Table 7.12 – Test configurations and their properties

Considering the results of the Block 2015 data set from Tab. 7.13, and given the average spatial resolution of 4.5 cm, the achieved accuracy varies significantly between different SO approaches. As expected from the nature of the data, indirect SO is far less accurate (RMS in the Z coordinate in m-level). The reduced number of automated image observations and their low quality together with weak ground control resulted in huge residuals at the check points. Next, three ISO projects were processed. Again, due to the lower quality of the image measurements and poor distribution of the GCPs, the accuracy is mainly driven by aerial control. Relative attitude control slightly outperforms absolute control by eliminating the systematic residual error, as seen in Fig. 7.19. When removing image observations of tie-points from the adjustment and using Fast AT method, similar results to that of ISO can be obtained. The usage of absolute and relative aerial control together with a few GCPs and a very limited number of image measurements is sufficient to provide an accuracy of 1.5 pixel both in position and height while being significantly faster in processing. The inclusion of relative attitude control improved the accuracy more than the absolute control. Nevertheless, relative position control weakens the geometry in Fast AT and significantly shifts the mean in the X axis. The accuracy of DiSO corresponds to less than 2 pixels in position and around 3.5

pixels in height.

The precision of object point coordinates is depicted in Fig. 7.21. The estimated 3D precision from one of the ISO projects is symbolised by white ellipsoids that are scaled in order to highlight the variances. Despite the obvious lower precision in the border areas, also the central parts exhibit rather low precision. This is expected due to the low observability of the tie-points as depicted for the used dataset FW2 in Fig. 7.3. Changes in aerial control configuration, e.g. absolute vs. relative, do not significantly influence the precision.

Test	Accuracy					
	Mean ChP [mm]			RMS ChP [mm]		
	X	Y	Z	X	Y	Z
Indirect SO	68	8	-664	16	145	1171
ISO + abs. Position + abs. Attitude	6	16	35	32	29	53
ISO + abs. Position + rel. Attitude	5	16	32	30	28	53
ISO + rel. Position + rel. Attitude	-38	39	16	52	58	42
Fast AT + abs. Position + abs. Attitude	9	-21	7	37	45	65
Fast AT + abs. Position + rel. Attitude	8	38	-22	24	47	61
Fast AT + rel. Position + rel. Attitude	-42	-2	-38	78	32	58
DiSO	-5	-13	-15	52	63	166

Table 7.13 – Accuracy assessment at independent check points; 5 GCPs and 15 ChPs, the test parameters correspond to those in Tab. 7.12. In DiSO, no GCPs were used.

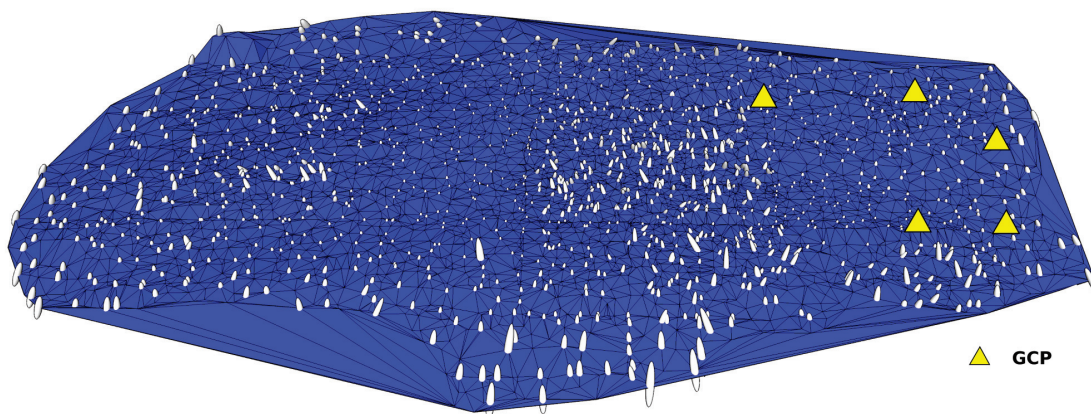


Figure 7.21 – Estimated 3D precision of object coordinates of tie-points represented by error ellipsoids (scaled 70 times). The ISO project with absolute position, absolute attitude, and 5 GCPs.

### Summary

This investigation empirically confirmed that thanks to aerial control, accurate 3D ground positions can be derived even with areas with badly distributed GCPs. The main contribution

of attitude absolute and relative control is the elimination of the need of a block structure and reduction of ground control in the mapping configurations with weak geometry. On the contrary, the contribution of attitude observation in strong AT blocks with well-distributed tie-points is rather limited. The best achieved accuracy lies in the level of approx. 1 pixel, both in position and height. This accuracy is usually hardly achievable by MAVs with conventional methods of sensor orientation, i.e. indirect SO or ISO with absolute aerial control.

For certain projects with lower demands on accuracy, DiSO represents a very convenient and rapid way of mapping. Finally, Fast AT proved to be an excellent compromise between ISO and DiSO particularly in the context of relative attitude control. This method provides accuracy close to ISO while by speed and demands on configuration, e.g. image overlaps, it is close to DiSO. Fast AT also offers considerably higher degree of robustness than DiSO, and should be considered a feasible and very practical approach to MAV mapping over surfaces with limited texture.

### 7.4.3 Redundancy in EO observations

Redundancy in IMU data can be treated in several ways. Firstly, all individual IMUs can be combined by different approaches during GNSS/IMU data filtering into one trajectory. The principal methods of combinations are discussed, for instance in Waegli et al. [2008], with practical experiments in Stebler and Skaloud [2013]. The second option is based on computing several trajectories independently and imputing them as additional observations into BA. However, this approach requires separate boresight calibration of all the IMUs as well as handling the correlations between them due to, e.g. the use of same GNSS observations, initialisation errors, and flight dynamics. Here, the employment of relative orientation is practical as the boresights are eliminated and the residual correlations become small.

In order to assess the contribution of additional EO camera observations, several BA projects were computed with the FW2 data set. The boresights were estimated in a separate ISO project because the R-IMU board changed between the data sets FW1 and FW2, as already addressed in Sec. 7.4.2. The IO parameters were used from the ISO project described in Sec. 7.4.1 and these parameters remained fixed in Fast AT and DiSO, but were re-calibrated in ISO.

Overall, four sets of EO parameters were available after processing the four individual IMUs with the common GNSS data. Six cases are considered, and the individual combinations of aerial observations are described in Tab. 7.14. The outcomes of these tests are presented in Tab. 7.15, in terms of check point residuals.

In the case of ISO, the additional attitude observations do not significantly improve the solution in comparison to the similar scenario from Tab. 7.13. With the exception of height, which experienced small improvements both in mean and RMS values. The ground accuracy lies in the level of 1 pixel both in position and height.

Regarding the Fast AT projects, an inclusion of additional sets of absolute observations (configuration Fast AT I) slightly improved the RMS in the Y axis by 1 cm when compared to Tab. 7.13. When the absolute attitude observations (Fast AT II) were replaced by the relative ones (Fast AT III), the RMS worsening in Y axis was compensated by an improvement in the Z axis.

## 7.4. Aerial Position and Attitude Control

However, the inclusion of 3 extra sets of relative position and attitude observations improved the accuracy in comparison to the case when only one set was used.

As for the DiSO, additional absolute observations significantly improved the accuracy both horizontally (from ~ 1.8 to ~ 1.2 pixels) and vertically (from ~ 3.6 to ~ 1.6 pixels).

Mode	$P_1/A_1$	$P_2/A_2$	$P_3/A_3$	$P_4/A_4$
ISO	a/r	-/r	-/r	-/r
Fast AT I	a/a	a/a	a/a	a/a
Fast AT II	a/a	-/a	-/a	-/a
Fast AT III	a/r	-/r	-/r	-/r
Fast AT IV	r/r	r/r	r/r	r/r
DiSO	a/a	a/a	a/a	a/a

Table 7.14 – Testing configurations with redundant EO parameters;  $Position_n/Attitude_n$  where  $n$  is a particular set of EO parameters (1-4); "a" and "r" stand for absolute and relative observations, respectively.

Test	Accuracy					
	Mean ChP [mm]			RMS ChP [mm]		
	X	Y	Z	X	Y	Z
ISO	17	18	24	24	38	47
Fast AT I	24	16	-18	37	36	68
Fast AT II	25	15	-17	37	35	67
Fast AT III	15	-17	22	32	47	43
Fast AT IV	-2	9	-34	58	41	54
DiSO	19	17	-31	38	36	75

Table 7.15 – Results of BA with redundant EO parameters. In ISO and Fast AT, the same 5 GCPs as depicted in Fig. 7.17 were used. In DiSO, no GCPs were used. Accuracy evaluated at 15 ChPs. One pixel = 45 mm.

### Summary

In ISO, the inclusion of additional EO parameters did not affect the ground accuracy. The Fast AT configurations are positively affected mainly through absolute position and attitude control. The most significant difference can be seen in DiSO. The achieved results demonstrate that a MEMS R-IMU can provide attitude of sufficient accuracy when certain redundancy in geometric configuration is maintained. In these cases, the images are oriented by absolute EO parameters, and the projected ground errors are averaged in the neighbouring strips.

In conclusion, redundancy in aerial control can bring a small improvement either in height component in ISO through relative attitude, or in Fast AT and DiSO, but mainly when absolute attitude is used. On the contrary, redundant observations add significant labour in post-processing, as several trajectories have to be produced, and in the case of absolute attitude,

boresights have to be determined. Nonetheless, the potential of redundant IMU observations is significant as they can be treated in several ways, e.g. inside a dynamic network BA, which allows direct usage of inertial observation and thus eliminate the need of trajectory smoothing.

### 7.5 Spatio-temporal Aerial Control

This section presents several strategies for determining the synchronisation delay as a function of available observations. As discussed in Sec. 6.4.2, errors due to synchronisation can be partially absorbed by other parameters, e.g. a GNSS shift, a lever-arm or coordinates of the principal point. Therefore, when it is needed to estimate  $\Delta t$  with a high precision, these parameters should be determined beforehand in a different project and remain fixed in BA.

#### 7.5.1 Processing Strategy

In this project, the lens radial distortion parameters were used from the camera calibration presented in Sec. 6.5.1, assuming that due to the missing optical lens stabilisation system, these parameters are temporally stable and thus applicable in different missions. The tangential distortion parameters exhibited strong correlation with the coordinates of the principal point, as shown in Tab. 6.8, and were therefore excluded from the parameter set, e.g. the principal point was re-calibrated within a mission, as explained below. The lever-arm was known from the static calibration introduced in Sec. 6.2.2, and the boresight was self-calibrated in-flight. The estimated lens radial distortion parameters were fixed during the processing of the data set FW1. This flight was split into two parts - A and B as described in Tab. 7.16 and depicted in Fig. 7.22, where a different set of parameters was calibrated in each part. In the first block (A), the camera principal point coordinates and the principal distance were estimated by the means of ISO with lower weight on aerial control to account for the possible influence of a synchronisation error. Additionally, the boresight was estimated for one of the employed IMU sensors. The most pertinent self-calibration results are summarised in Tab. 7.17. It can be stated that the parameters are estimated with a sufficient accuracy. These parameters were then fixed in the second block (B), during which the  $\Delta t$  was estimated. The main flight lines were oriented with and against wind to maximise variations in ground speed that were up to 13 m/s.

The last data set FW2 was used for independent verification and for investigations of the impact of the synchronisation error on mapping accuracy.

#### 7.5.2 Testing Methods

Four methods of delay determination are tested. The tests are based on the available observations and their usage in the adjustment. The first (I) and the most simple method is based on an analysis of residuals between the observed camera positions and those estimated by indirect SO. The second method (II) uses absolute spatio-temporal models with position

Data	FW1	
	Block A	Block B
No. of photos	204	263
No. of GCPs	18	13
No. of ChPs	0	0
Self-calibrated parameters	$c, y_0, x_0, \text{boresight}$	$\Delta t$
Fixed parameters	distortion	all IO

Table 7.16 – Data set FW1 division into two blocks and their properties.

Data set	Parameter	Value	$\sigma$
Close-range	$K_1$	-2.72e-04	9.92e-07
	$K_2$	1.47e-06	1.41e-08
Block (A)	$x_0$ [mm]	0.0023	0.0004
	$y_0$ [mm]	0.0550	0.0005
	$c$ [mm]	15.8491	0.0006

Table 7.17 – Pertinent results from the self-calibrating BA.

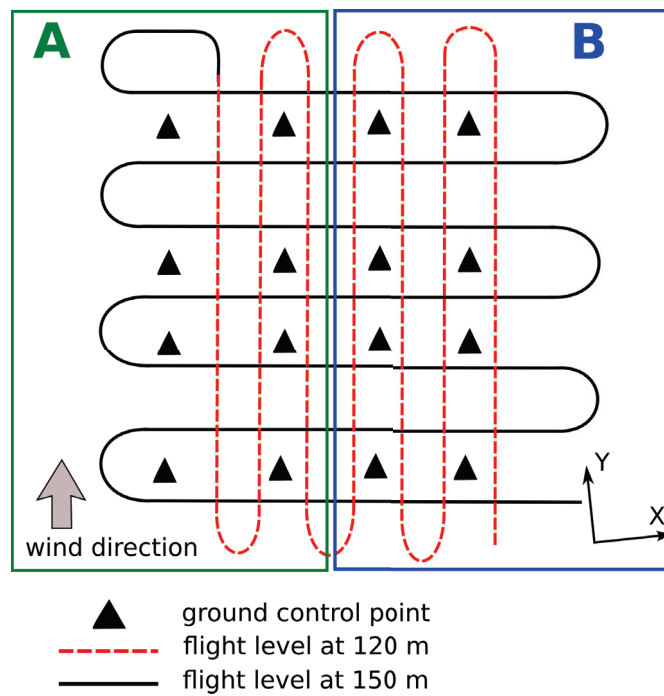


Figure 7.22 – A scheme of the calibration block FW1 and its division.

( $P$ ) and velocity ( $V$ ) observations. In the third method (III), the absolute spatio-temporal attitude model with attitude ( $A$ ) and angular rate observations ( $Ar$ ) is used together with absolute positions without the velocity observations. The last method (IV) combines absolute spatio-temporal models with position, attitude, velocity, and angular rate observations.

### 7.5.3 Processing Steps

The method of estimating the potential synchronisation errors depends on the data availability and a mapping system. In the case of commercial MAV platforms, users have generally very limited or no access to raw navigation data (senseFly [2015a], MAVinci GmbH [2015]). The GNSS solution processed as RTK is either encoded into images or saved in a log file, but the carrier-phase GNSS differential post-processing may not be possible. Also, no raw inertial observations are stored. In the presented custom GNSS/IMU/Camera payload, all raw observations are available and can be exploited in detail. The processing steps are depicted in Fig. 7.23.

In the first step, the trajectory parameters (position, velocity, attitude and angular rates) are interpolated to image events and transformed to a mapping frame as discussed in Sec. 7.2. In the next step, the set of exterior parameters together with the corresponding velocity and angular rate observations enter the BA. After the first BA iteration, the estimated delay is used for extraction of a new set of the *PVAAR* observations. This process is repeated iteratively until the correction  $\Delta t$  is negligible, and  $\delta \hat{x}$  from Eq. 4.21 meets the convergence criteria. This approach assures obtaining the *PVAAR* observations closer to the camera exposure. Indeed, as the velocities, and mainly angular rates, change rapidly, they have to be updated after each BA iteration.

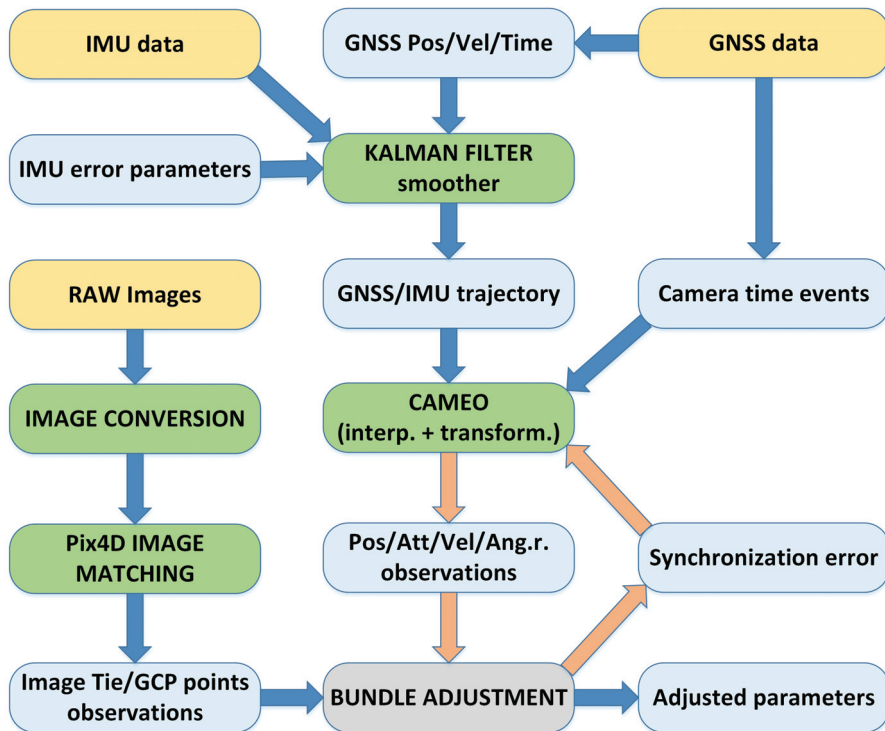


Figure 7.23 – Modified processing scheme in Fig. 7.1: raw data inputs are in yellow, blue are the input/output products, green are the processing steps, and the BA is in grey. Red arrows symbolise iterative processes.



### 7.5.4 Residual Analysis

An iterative estimation process was run in several configurations with different observations. First, the block was oriented only by all the GCPs and the aerial camera positions were compared to those estimated by the GNSS/IMU (method I). This way, the indirect SO provides the mean of  $\Delta t$  estimation. The trend of camera residuals is fitted with a polynomial of the first degree, Eq. 7.2 in a least-square manner.

$$f(x) = a_0(x) + a_1 \quad (7.2)$$

The coefficient  $a_0$  determines the trend which is  $\Delta t$ . The coefficient  $a_1$  determining the offset is not important, as the EO positions are not used as observations and the estimated EO parameters absorb other systematic errors due to high correlation with IO. This test is depicted in Fig. 7.24. The trend of residuals shows a consistent  $\Delta t = -9.2$  ms error. The sign of  $\Delta t$  can be determined when expressing the residuals in the camera frame.

Then, the GCPs were supplemented with aerial control (position and attitude) and with either velocity (method II), angular rate observations (method III), or a combination of both (method IV) as depicted in Tab. 7.18. The results for different combination of aerial control

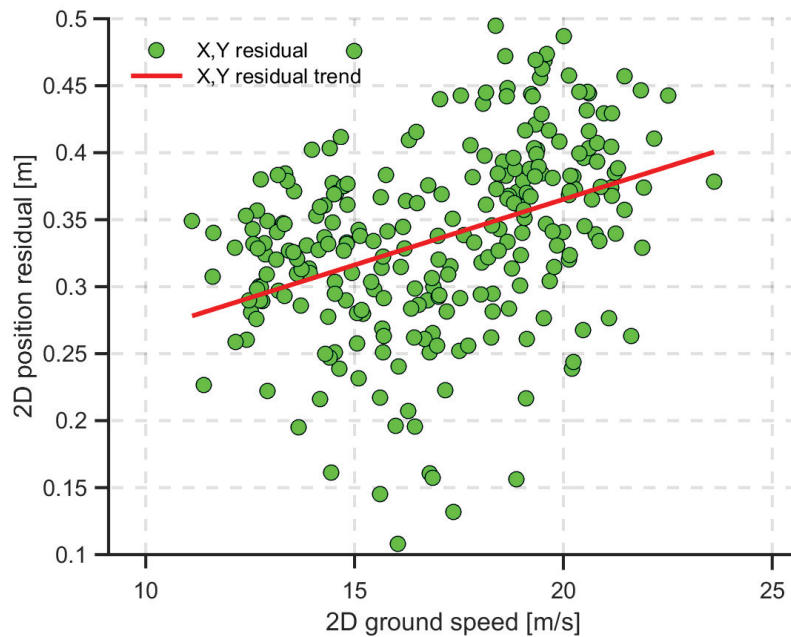


Figure 7.24 – Block B: Aerial 2D camera position residuals; low weights on aerial position observations = indirect SO (all GCPs, all IO parameters self-calibrated). The trend in residuals corresponds to  $\Delta t = -9.2$  ms.

are listed in Tab. 7.18. The estimated time delays are relatively consistent with an exception of the case III using only position, attitude, and angular rate observations. In this case, the observed angular rates are not sufficient for determining the synchronisation error, as the

flight had insufficient angular dynamics. In Fig. 7.25, the residuals depicted for the case IV

Method	Observations	Time delay [ms]	$\sigma$ [ms]
I	GCPs	-9.2	-
II	PAV + GCPs	-5.6	0.2
III	PAAr + GCPs	-1.9	0.5
IV	PVAAr + GCPs	-6.2	0.1

Table 7.18 – Estimated synchronisation errors using different observations.

are considerably smaller. Their trend is in good agreement with the directly estimated time delay parameter. Considering the combination of temporal position and attitude control, i.e. *PVAAr*, to be the most suitable method of delay estimation, the time marks of camera stations were subsequently corrected for the estimated delay of  $\Delta t = -6.2$  ms, and the iterative processing was run again, as illustrated in Fig. 7.23. The camera position residuals from this adjustment are shown in Fig. 7.26. The residual error of  $\Delta t = -0.3$  ms after such correction is caused by observation noise in measured velocities and angular rates, and lies within  $\pm 3\sigma$  of  $\Delta t$ .

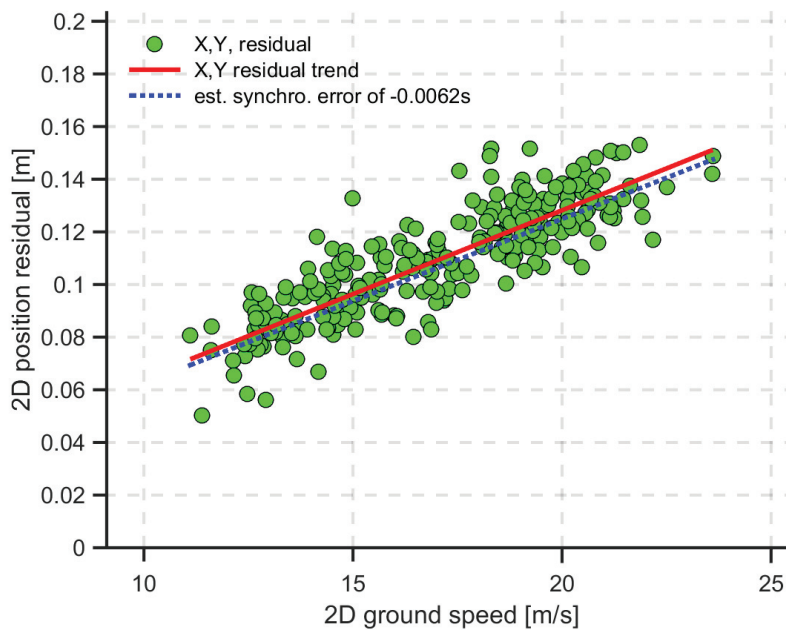


Figure 7.25 – Block B: Residuals in the horizontal camera positions and a fitted slope in comparison to the slope of the time delay of  $\Delta t = -6.2$  ms estimated in the BA using absolute spatio-temporal position and attitude observations.

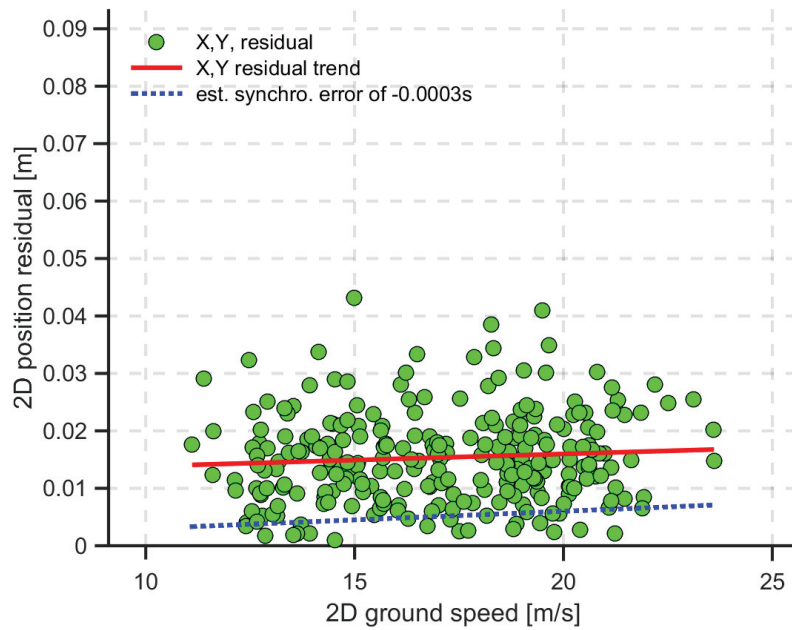


Figure 7.26 – Block B: Residuals in horizontal camera positions and fitted slope in comparison to the slope of the residual time delay of  $\Delta t = -0.3$  ms estimated in the BA using absolute spatio-temporal position and attitude observations.

### 7.5.5 Convergence and Stability

In order to test the performance of the algorithm for different synchronisation errors, the original time events were corrected for the estimated delay  $\Delta t = -6.2$  ms, and then artificially perturbed for positive and negative synchronisation errors ranging from -20 to +20 ms by a step of 5 ms. The estimated values using the BA with spatio-temporal position and attitude observations were compared to known perturbation. The good agreement between them in Fig. 7.27 shows the capability of the presented algorithm to determine synchronisation errors between the camera and the employed GNSS/IMU system over a large range. The artificial delay was correctly estimated in all cases with the accuracy around 1 ms (except for the case of 5 ms where the difference is two times larger).

### 7.5.6 On the Origin of the Camera Delay

The estimated negative delay of  $\sim 6$  ms is related to the emission of a flash pulse caused by the flash synchronisation signal. The situation is schematically depicted in Fig. 7.28. The flash pulse is sent by the camera a few milliseconds ahead of shutter opening to give the flashbulb time to reach peak brightness before exposing the camera sensor. In the case of Sony NEX-5R camera, this pulse is sent always, i.e. whether the flash is activated in the camera settings or not. Furthermore, the important aspect when using a flash is the maximum shutter speed for the flash synchronisation pulse to allow correct scene exposition, or in other words,

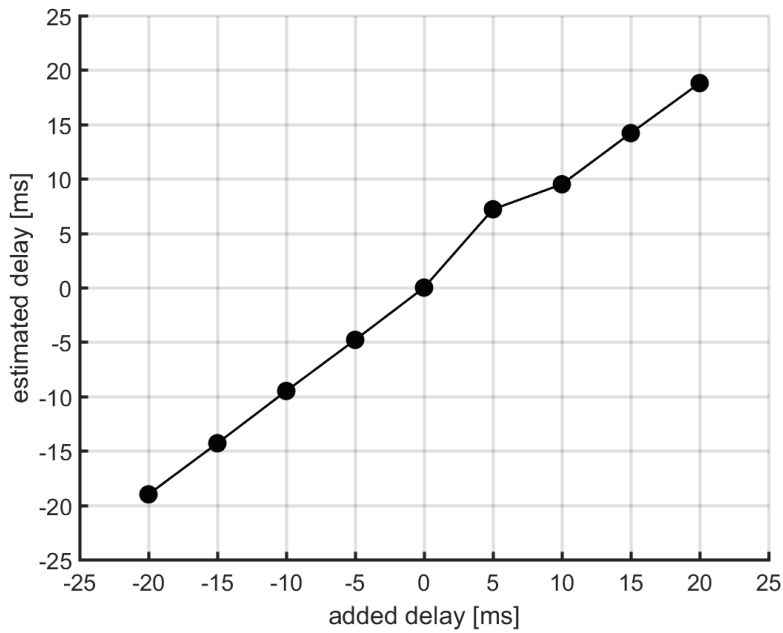


Figure 7.27 – Added vs. estimated delay after correcting the original time events for  $\Delta t = -6.2$  ms.

to match the shutter blades wide-open moment with the peak-output moment of the bulb. This is depicted in the lower part of Fig. 7.28. In this particular case, the camera might have a hard-coded "waiting interval" for the shutter to reach its mid-exposure to start the flash independently of the actual shutter speed that was in our case 1/1250 s. This was, however, not investigated during these experiments.

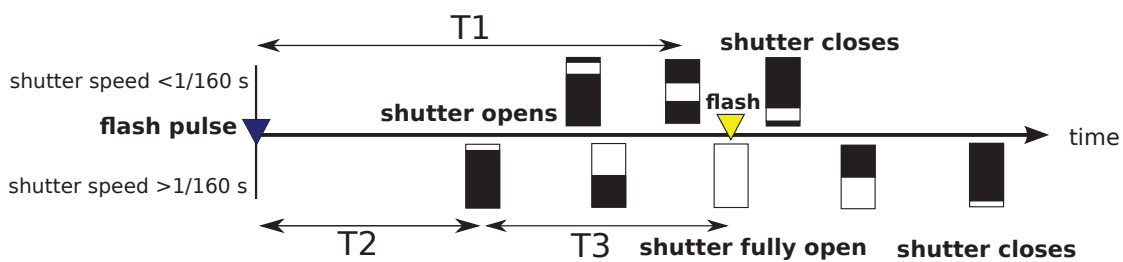


Figure 7.28 – Simplified schematics of the possible source of a synchronisation error. Time T1 is an interval between the mid-exposure and shutter opening to which the EO parameters are related. Time T2 is a delay between the flash pulse and shutter initial opening. Interval T3 is the half of the max. synchronisation shutter speed, i.e.  $\geq 1/320$ s, for Sony NEX 5R. The sum of T2 and T3 is the time needed for the flash electronics to prepare for flashing and for reaching the maximal flash intensity.

### 7.5.7 Impact on Mapping Accuracy

Knowing that a MAV photogrammetry system suffers from synchronisation errors is important especially in the scenarios with limited redundancy. The next experiment aims at investigating how the time delay of -6.2 ms influences the mapping accuracy. The 3D point accuracy is assessed within block and corridor mapping scenarios.

The data set FW2 presented in Tab. 6.1 was processed in three configurations, each time with an original and a corrected set of EO parameters. First configuration investigates whether  $\Delta t$  influences the mapping accuracy in ISO with absolute aerial position observations, without GCPs and with self-calibrated IO parameters. Indeed, this is a typical mapping scenario of platforms equipped with a RTK GNSS receiver, e.g. the eBee Plus (senseFly [2015a]) or the Sirius Pro (MAVinci GmbH [2015]). The second configuration was modified by adding four GCPs placed regularly inside the block. The third configuration was created by selecting one strip from the block. As corridor configurations have higher demands on aerial control, the adjustment was supplemented with absolute attitude control. The IO parameters were not re-estimated, but the estimated values from the second configuration with four GCPs were used.

The results are listed in Tab. 7.19. The results suggest that corrected EO parameters slightly improved the accuracy at ChPs in the Y axis in the first two configurations. This was expected as the flight direction affected by large variations in speed was approximately aligned with the Y-axis of the mapping frame. The difference is even more obvious in the single strip corridor. Both mean and RMS values are significantly smaller when the EO parameters are corrected for  $\Delta t$ . Nevertheless, the effect of  $\Delta t$  could be also partially mitigated by adding a second strip from the opposite direction.

Test	Accuracy					
	cam. EO [mm]			ChP [mm]		
	RMS			mean RMS		
	X	Y	Z	X	Y	Z
<b>O:</b> Block + abs. $P$	12	17	33	46 54	16 36	11 58
<b>C:</b> Block + abs. $P$	12	15	33	48 56	-2 26	10 54
<b>O:</b> Block + abs. $P$ + 4 GCPs	12	17	34	40 50	13 26	0 51
<b>C:</b> Block + abs. $P$ + 4 GCPs	12	15	33	39 47	-2 18	2 46
<b>O:</b> Single strip corridor + abs. $PA$	-	-	-	-15 63	-92 107	12 111
<b>C:</b> Single strip corridor + abs. $PA$	-	-	-	8 50	-30 50	12 112

Table 7.19 – Evaluation Block (E); estimated accuracy of aerial positions and ground accuracy measured at 9 independent check points in the case of block configuration and 7 check points of single strip corridor, respectively. The parameter **O** states for original, **C** states for calibrated events, i.e. the time events corrected for  $\Delta t = -6.2$  ms. The average GSD of this project is 4.5 cm.

### 7.5.8 Summary

Several methods of time delay estimation were presented with the conclusion that sufficiently varying ground speed allows correct recovery of the synchronisation delay. On the contrary, proportionally lower accuracy of measured attitude and lower variations of angular rates did not make absolute spatio-temporal attitude control sufficient for synchronisation delay estimation. Such situation is, however, specific to a test scenario of a fixed-wing MAV. The angular-rates variability is known to be high on multirotable platforms. Nevertheless, even in the tested scenarios, the inclusion of angular rates improved the observability and precision of the recovered delay.

The practical evaluation on an independent data set showed that despite the relatively large synchronisation delay of  $\Delta t = -6.2$  ms, the final impact on mapping accuracy is relatively small in block configurations. Its influence is mitigated with cross strips and self-calibrating BA. Indeed, the essence of BA is to find optimal values of all variables. The synchronisation error is then absorbed/compensated by other self-calibrated parameters, e.g. the principal point coordinates. However, in the scenarios with a lower redundancy, such as the single strip corridor, the errors in EO parameters cannot be absorbed, and therefore, the impact on ground accuracy is significant.

## 7.6 Stability of Camera IO parameters

This section provides an overview of the results from several camera calibration projects. The aim was to test the stability of IO parameters over time. Although consumer grade cameras are in a majority of photogrammetric projects self-calibrated, the ability to fix or at least set appropriate confidence levels (weights) can be of a big advantage when estimating other parameters that are correlated with them, e.g. the system parameters.

In general, the stability of IO parameters is twofold. First, the stability within a mission is essential to achieve precision in photogrammetric reconstruction. Nevertheless, thanks to the typical block configurations with a high forward and side overlap, the redundancy allows to estimate IO parameters even for every image independently, but with high correlations (Remondino and Fraser [2006]). Second, the stability of certain IO parameters can be considered sufficient across various mapping projects.

The stability of IO parameters on consumer grade cameras with a fixed focal length lens largely depends on the following elements:

- Mechanical construction of the camera body and lens. In general, the camera body/lens construction made of plastic is less rigid than when made of aluminium alloy.
- Lens mount system, e.g. bayonet mounting. This component will likely influence the camera's principal distance and coordinates of the principal point every time the lens is detached, as there is always a little play in the mechanical construction. On the contrary, a lens with a screw-threaded mount provides a more rigid connection.

- Mechanical instability of the lens elements caused by tolerances in manufacturing processes, or control rings (e.g. the focus ring is too used and evinces certain mechanical play when rotating).
- Stabilisation systems of the sensor or lens. Although the stabilisation can be switched off, a mechanically suspended mount permits the sensor or the lens' elements to move under vibrations or a sudden shock due to the UAV landing. Under such circumstances, the IO parameters will inevitably change.

The employed Sony NEX 5N (R) has no optical or sensor stabilisation, the camera body is made of solid plastic and aluminium, plus the lens bayonet mount (E-Mount) is made of steel. To be able to compare parameters from different projects, the processing was done with the same configuration:

- Complete sets of data, i.e. full blocks, no corridors,
- all available GCPs,
- absolute aerial position control without the correction of  $\Delta t$ , corrected for the lever-arm,
- Brown distortion model with  $K_1$ ,  $K_2$  additional parameters,
- the same initial values of all self-calibrated IO parameters.

The following results in Tab. 7.20 are presented only for Sony NEX 5R paired with a 16 mm lens. It has to be noted that the lens was detached a few times between the projects. Although the flight missions were carried out over the same field, the surface texture changed over time and so did the quality and distribution of the automatically observed tie-points. Also other mission parameters, such as height, overlap, speed, etc., varied across individual projects. The results show consistent values for the principal distance  $c$ . The variations are in the level of  $\pm 3 \mu m$ . This corresponds to 0.65 pixel. The coordinates of the principal point  $x_0$ ,  $y_0$  are relatively consistent between FW1 and FW2 projects and the change in  $y_0$  is likely to be correlated to  $\Delta t$ , as discussed in Sec. 7.5. On the contrary, the coordinates are different in the project FWubx due to the high correlation of  $x_0$ ,  $y_0$  with the lever-arm. The radial distortion parameters  $K_1$ ,  $K_2$  demonstrate stable values over all the projects and are estimated with good precision. Nevertheless, these parameters are well decorrelated from  $c$  only in the CR2 project. Correlations between the estimated IO and EO parameters are shown in Fig. 7.29. The CR2 project has significant correlations between EO parameters, but the IO and EO parameters are sufficiently decorrelated between themselves. The remaining correlation matrices show nearly identical results, as the data was collected under similar conditions. The EO parameters are typically correlated between  $\omega - Y$  or  $\varphi - X$ , while the principal point coordinates are medium-correlated with radial distortion parameters in all flights performed with the fixed-wing MAV. This is due to a rather low separation between two flight levels and low variations in attitude angles.

## Chapter 7. Evaluation and Performance Assessment

Data set	Year	$c \sigma$ [mm]	$x_0 \sigma$ [mm]	$y_0 \sigma$ [mm]	$K_1 \sigma$	$K_2 \sigma$
CR2	2015	-	-	-	-2.75e-04 1.0e-06	1.48e-06 1.4e-08
FW1	2014	15.8361 0.0003	-0.0351 0.0001	0.0515 0.0002	-2.62e-04 6.3e-07	1.43e-06 8.4e-09
FW2	2015	15.8393 0.0004	-0.0399 0.0001	0.0321 0.0002	-2.66e-04 8.2e-07	1.51e-06 1.1e-08
FWubx	2016	15.8331 0.0004	0.0217 0.0001	0.0073 0.0002	-2.60e-04 6.2e-07	1.38e-06 8.1e-09

Table 7.20 – Comparison of IO parameters and their precision. The data set CR2 did not use the same camera body.

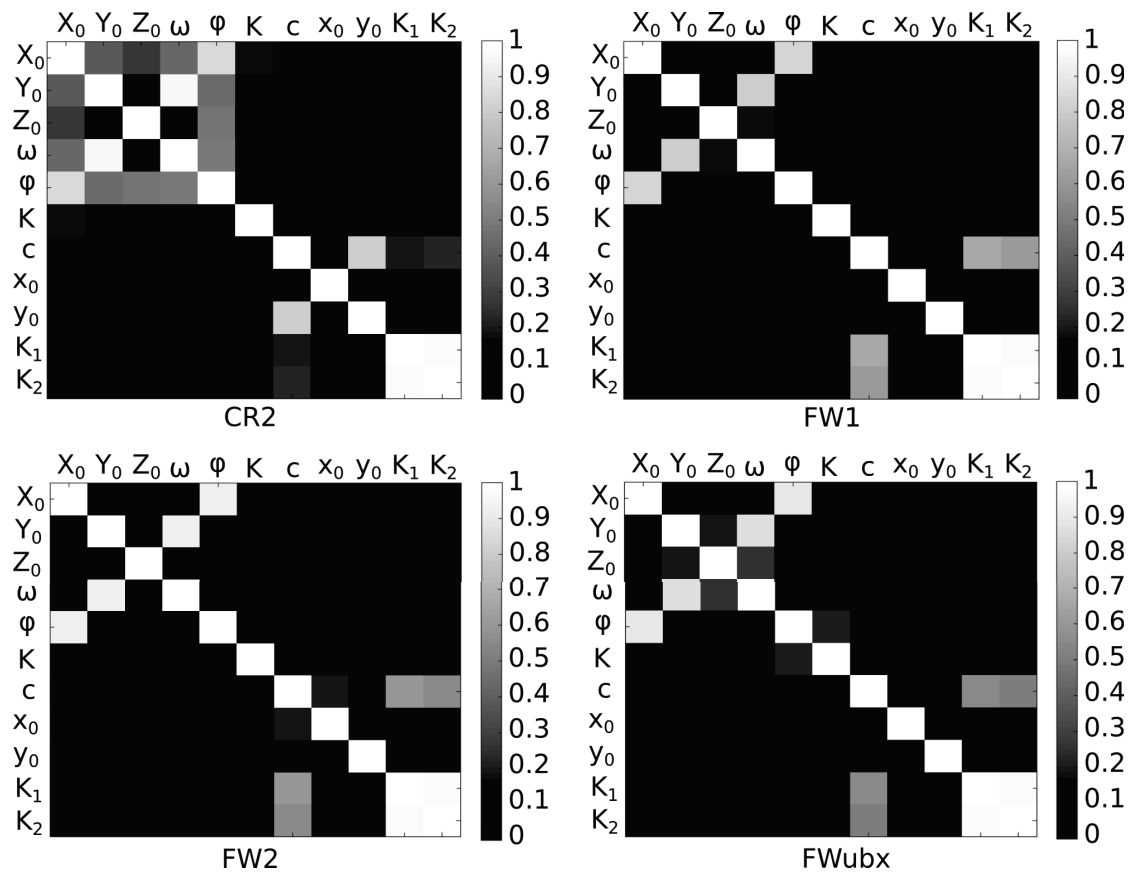


Figure 7.29 – Correlations between EO and IO parameters for randomly selected images.



### Summary

The goal of this chapter was to investigate the performance of various methods of aerial control in real mapping projects. First, a general processing procedure was disclosed. An importance of image conversion and image observations was addressed and followed by a description of the GNSS/IMU processing and interpolation. A section dealing with aerial position control presented a mapping scenario during which the GNSS signal quality is degraded. The inclusion of relative position control mitigated the GNSS position bias, and a few unbiased absolute observations ensured good ground accuracy. Next project dealt with aerial position control using a low-cost single-frequency GNSS receiver. Despite delivering only a float solution, the relative accuracy of aerial observation was close to that obtained by a geodetic-grade, multi-frequency receiver.

The next part of this chapter presented projects with aerial attitude control. The first project was focused on an in-flight system calibration and accuracy evaluation in a small corridor. Mapping without the support of automatic image observations was the subject of the following project. It was empirically confirmed that aerial control, both absolute and relative, can deliver cm-level ground accuracy in scenarios without classical aerial triangulation with thousands of tie-points. In addition, an example was given on the processing of redundant IMU observations. A significant part of this chapter was dedicated to spatio-temporal observations. A constant error in time synchronisation between the camera and GNSS/IMU was discovered and estimated/compensated by this concept.

The last part of this chapter was devoted to the stability and correlation of IO parameters among different projects. The drawn conclusion was that certain parameters, i.e. those modelling lens distortion, are sufficiently stable and as such, can be fixed if they are decorrelated from the others.



## 8 Conclusion and Perspectives

*This research aimed at developing a methodology to perform integrated sensor orientation on micro aerial vehicles for precise mapping. Theoretical concepts were introduced, followed by a description of custom software and hardware development and by performance investigations in real mapping projects. This section highlights major contributions of this thesis, and summarises the performance of the developed system and the methods used. Finally, perspectives for future developments and research activities are suggested.*

### 8.1 Summary of Contributions

The achievement of accurate ISO and data processing required the development of new methods both on a theoretical/conceptual level and on an algorithmic/engineering level. Accordingly, the main contributions of the author can be divided in these two categories:

#### 8.1.1 Theoretical/Conceptual Contributions

- **Methods of Advanced Photogrammetric Mission Planning**

The concepts of mission planning that increase the chances of collecting data of high quality were established and later implemented via MSc. projects of Florian Gandor (Gandor [2015]) and Roberta Pascale (Pascale [2016]). These concepts included, e.g. mission planning in a combination with a custom 3D model to better account for obstacles, or to improve results of functions for spatial and quality analysis. Among different functions, the most important are: GNSS signal reception prediction, estimation of overlap, and assessment of image overlap in the planned or executed flights. These features are important in the mapping of morphologically challenging areas, such as mountains or deep valleys. In addition, mission planning is performed in compliance with platforms physical limits. Considered are: platform's endurance, turning radius, or, in the case of multicopters, also camera obliquity.

The performance of this planner was analysed in the field experiments. Although not

yet fully mature (e.g. the planner does not allow a real-time connection to the platform), it proved to be stable enough to be employed for photogrammetric tasks with MAVs.

- **Sensor and System Calibration**

System and sensor parameters were calibrated using either a dedicated ground calibration field, or via in-flight self-calibration during some of the presented projects. A good estimation of the system and camera parameters is essential for obtaining cm-level accuracy in mapping a mission with a higher demand on aerial control, namely in corridor mapping, Fast AT or DiSO. Detailed methodologies were introduced, in particular focused on the lever-arm determination and camera additional parameters of lens distortion.

The methodology of time synchronisation of consumer-grade cameras was introduced. Several methods of time delay estimation were tested and practically verified.

- **Concept of Integrated Sensor Orientation on MAVs**

Although the concept of ISO is well-known in airborne photogrammetry, its application on MAVs is new and has not yet been addressed in such a detail. In general, MAVs have limited payload capacity that does not allow to carry metric cameras and large IMUs of tactical- or navigation-grade performance. Besides, the electronics of MAVs is perturbing the quality of the GNSS signal reception, particularly its carrier-phase. These drawbacks set requirements on data acquisition, proper sensor placement and system calibration, as well as on data processing. All these individual elements were both theoretically and practically assessed in this thesis.

The methods of absolute, relative, and spatio-temporal control were theoretically described, implemented, and verified in mapping missions. Furthermore, thanks to the R-IMU and its proper calibration, a set of redundant EO parameters was used in the adjustment. A thorough search of relevant literature yielded no related article dealing with the issue.

- **Utilisation of a Low-cost, Single-frequency GNSS Receiver**

A low-cost, single-frequency GNSS receiver was tested for the purpose of aerial position control. This receiver was mounted on a fixed-wing platform and its performance evaluated in a mapping project directly with a reference receiver of superior performance. The accomplishment of this experiment opens new possibilities for many MAV users for which a geodetic-grade receiver is unaffordable. However, its integration into a MAV platform is not trivial due to its sensitivity to vibrations, EMI, and limited synchronisation possibilities. These drawbacks were addressed and discussed in detail.

### 8.1.2 Engineering Contributions

- **Development of MAV Platforms**

The development and construction of working MAVs was a crucial part of this research since the commercially available platforms allow neither collecting nor accessing all

types of data that are necessary for ISO. Besides, due to the high price of commercial MAVs, such experiments would not be possible. Commercial platforms do not allow any hardware modification, nor are compatible with the developed mission planner.

The flight characteristics of the developed platforms are comparable to the state-of-the-art commercial platforms while allowing users to access raw observations. These platforms and their functionality were the central issues of this thesis.

- **Establishment of Calibration Fields**

Although this part of the project was a pure engineering work, its importance on the theoretical development was very significant. Overall, two calibration fields were constructed for both close range and large scale aerial mapping (in MAV standards). Both target fields are covered by a dense network of precisely surveyed points. Such setup allows performing various tasks while providing the necessary ground reference.

- **Data Processing Software**

Several software modules were developed in the framework of this thesis, the most important being a bundle adjustment. Although the concept of the bundle adjustment is well-established in photogrammetry and computer vision, commercially available tools are often limited in functionality as a trade-off between performance and user-friendliness. Furthermore, the majority of open-source systems are insufficiently documented or too complex for other people to contribute.

The developed processing tool allows adjusting photogrammetric networks with various types of aerial observations. It supports popular data formats and both graphically and numerically presents the results. It is designed in a way that further extension or modification should not be a problem for a user with a background in photogrammetry. The main strength of this tool is the observations that can be treated and their stochastic modelling. A user has a full control of the adjustment process which is particularly important when using accurate aerial control observations. Furthermore, thanks to the inclusion of new observation models, it is possible to estimate sensor and system parameters including a multisensory synchronisation error.

## 8.2 Conclusions

This thesis presented a detailed work-flow for integrated sensor orientation with imagery captured by MAVs. The conducted research work allows to make several conclusions.

In general, aerial control can be combined in many ways. In block configurations with highly overlapping imagery and strips, the asset of aerial position control is mainly in the elimination of GCPs. On the contrary, the contribution of attitude observation is rather limited. Nevertheless, its inclusion starts to be significant in blocks with low-quality, low-number, or poor distribution of automatic tie-points. Such situation was demonstrated in a project without automatic tie-points. The achieved ground accuracy was comparable to a ISO configuration with thousands of tie-points.

In corridors without side overlapping strips, the absolute aerial control is essential for ob-

taining undistorted results, unless a large number of GCPs is regularly distributed (at least in two strips) along the strip. Aerial attitude control improves the accuracy as the omega angle compensates the inherent orientation instability due to the absence of neighbouring strips. With a relation to MAVs, the employment of relative observations has a great practical potential since the need of boresight calibration is omitted and the process of system calibration facilitated. Moreover, relative attitude mitigates problems related to the imperfections in the IMU initialisation. Indeed, wrong initial alignment has similar impact on the attitude determination as a residual boresight. Both effects were shown in several studies.

Regarding the relative position control, substituting absolute positions with the relative ones mitigated the influence of a residual GNSS positioning bias. Such scenarios are rather frequent with the MAVs operating close to buildings, or in challenging terrain morphology. In the presented experiments, the inclusion of relative positions yielded similar results as with absolute observations when a low-cost single-frequency GNSS receiver was used. By differencing the two observations, the residual bias in aerial positions was practically eliminated. Furthermore, under certain circumstances, using relative absolute positions can limit the influence of a constants-synchronisation error, or a residual lever-arm on the positioning accuracy.

Finally, spatio-temporal control models proved to be very beneficiary for determining the synchronisation delay in a photogrammetric system. The practical evaluation using an independent data set showed that despite the relatively large synchronisation delay, the final impact on mapping accuracy is relatively small in block configurations and self-calibrating BA. However, in the scenarios with a lower redundancy, such as a single-strip operation, the errors in EO parameters cannot be absorbed. In this case, the impact on ground accuracy is significant. Although the spatio-temporal models were implemented and tested at end of the presented research, the determined delay did not significantly influence the results in the previous projects. Its influence was either absorbed in ISO configuration with self-calibrating camera IO parameters and/or mitigated in cross-strips.

The stability of IO parameters investigated over several projects proved to be sufficient for certain orientation modes, such as DiSO. It was shown that the main IO parameters ( $c$ ,  $x_0$ ,  $y_0$ ) are consistent over time but their recalibration is advised for increasing the overall accuracy, as they absorb/compensate systematic errors due to, e.g. incorrect system calibration. Regarding the additional parameters of lens distortion, these appeared to be stable throughout this research. The small variations in the presented results were mainly due to the differences in image observation quality.

### 8.3 Perspectives

In the course of the development of this thesis, new research challenges have emerged that make further investigations worthwhile.

- **Inertial Redundancy**

R-IMUs are already used in many fields (e.g. aviation, robotics, virtual reality). Their sole purpose is often to increase reliability. However, an improvement in accuracy has not yet been fully acknowledged in real-world experiments. Navigation and photogrammetry in particular could benefit from this concept, as the price-drop of system components and evolution in the field of miniaturisation made the high-quality MEMS-IMUs easily affordable. A closer investigation of the R-IMU processing and integration into processing software could be highly beneficiary. Although an example was given in this thesis, the potential of redundant IMU observations is much larger as they can be treated in several ways, e.g. creating a synthetic IMU, or inside a dynamic network adjustment. Also, the change from kinematic to platform's-dependent dynamic modelling (VDM/IMU/GNSS)<sup>1</sup> can further greatly improve the attitude estimation.

- **ISO in Close-range Mapping**

ISO as a mode of operation can deliver superior accuracy to all the other SO methods. As this is obvious from the presented research, its place is mainly in aerial photogrammetry. Nonetheless, VTOL MAV platforms equipped with accurate GNSS/IMU sensors could bring new possibilities in, e.g. inspection and documentation tasks. However, these applications bring new challenges into mission planning and execution mainly due to the possible GNSS signal unavailability, as well as due to the specific dynamics of VTOL platforms.

- **Low-cost GNSS Receivers**

Further research on utilisation of low-cost, single-frequency GNSS receivers may confirm new possibilities or limits for general MAV users.

- **Simulations of Achievable Accuracy**

One of the most prominent issues is the difficulty to predict, quantify, and ultimately guarantee the global accuracy of the resulting mapping product for a given mapping site. When operating UAVs in difficult scenarios, the operators can rely only on their experience to assess whether the desired level of accuracy could eventually be reached given the mission plan and the number of GCPs. The next generation of mission planners should incorporate accuracy emulation functionality into the planning process and set semi- or fully-automatic mission parameters based on the user's requirements and platform's physical constraints. The presented mission planner is an ideal platform for further development in this area thank to its open-source characteristic and operating system-independent platform.

- **Data Availability**

A structured summary of the research data that were used in this thesis will be available online. This will allow users without an access to the raw observations to test the presented methods and continue in the future development.

---

<sup>1</sup>Vehicle Dynamic Model (Khaghani and Skaloud [2016])





# **A Overview of Photogrammetric Platforms, Sensors, and Mission Planners**

**Appendix A. Overview of Photogrammetric Platforms, Sensors, and Mission Planners**

Name	Manufacturer	Weight [kg]	Endurance [min]	Camera Type or Payload	Other sensors
<b>Fixed-wing</b>					
Aero-M	3DRobotics	3	40	Canon SX260, 12.1 Mpix	
eBee	senseFly	0.7	40	Canon S110 (RGB, NIR, RE), 12 Mpix	Topcon RTK GNSS
eBee Plus	senseFly	1.1	59	S.O.D.A 20 Mpix, Parrot Sequoia	Topcon RTK GNSS
GeoScan 101	GeoScan	3.1	60	Sony A5000, Sony DSX-RX1	RTK GNSS
Lancaster 5	Precision Hawk	3.5	45	RGB, Multispectral, Hyperspectral, Thermal	
Smart Plane	Smart Planes	1.5	45	Ricoh GR, 16.2 Mpix	
Q-100	Quest UAV	2	60	Sony QX1, 20 Mpix	
Q-200	Quest UAV	3.3	30-90	not specified	
UX5 HP	Trimble	2.9	35	Sony Alpha 7R, 36 Mpix	Trimble RTK GNSS
Pteryx	FotoMapy	5	55 / 120	1 kg / 0.45 kg	
Sirius, Sirius Pro	MAVinci	3	50	Sony RX1RII, 42.2 Mpix	Topcon RTK GNSS
Kahu	Skycam	3.9	120	Double-head 16 Mpix RGB cameras	
DT18	Delair-Tech	2	120	not specified	Trimble RTK GNSS
Cumulus One	Little Smart Things	2.2	not specified	Sony RX-100 III / 0.6 kg	
<b>Multi-rotors</b>					
Albris	senseFly	1.8	22	RGB (38 Mpix), Thermal (80x60 pix)	
MD4-200	Microdrones	1.1	30	0.25 kg	
MD4-1000	Microdrones	3	45-90	1.2 kg	
HT-8-2000	Height-Tech	5	17	2 kg	
Aibot x6	Aibotix	2.4	30	2.5 kg	RTK GNSS
Falcon 8	Ascending technologies	1.45	25	0.75 kg	
HexaKopter	MikroKopter	1.2	25	1 kg	
Fox4	Heliceo	4	15-30	0.6 kg	
Phantom 4	DJI	1.4	28	DJI 12.4 Mpix	
<b>VTOL+Fixed-Wing</b>					
Songbird 500	Aerolution	5	60	RGB (24 Mpix), thermal, hypersp. or 0.6 kg	
WingtraOne	Wingtra	4.4	not specified	Sony QX1 / 0.8 kg	

Table A.1 – Main MAVs (<5 kg) currently available on the market that are dedicated to photogrammetry.

Name	Manufacturer	Weight [g]	Size [mm]	Shutter	Sensor Size [mm]	Resolution [Mpix]	Price [Eur]	Note
<b>RGB Cameras</b>								
NEX-5R	Sony	210	111 x 59 x 39	rolling	23.7 x 15.6	16.1	330	discontinued
QX1	Sony	216	74 x 70 x 53	not specified	23.7 x 15.6	20.1	450	
RX1-RII	Sony	507	113 x 65 x 72	rolling	36 x 24	42	3 100	
X-M1	Fuji	330	117 x 67 x 39	rolling	23.7 x 15.6	16.3	470	
S110	Canon	198	99 x 59 x 27	global	7.4 x 5.6	12.1	370	
G9X	Canon	206	98 x 58 x 31	global	13.2 x 8.8	20.2	500	
S.O.D.A	senseFly	not specified	not specified	global	12.8 x 8.5	20	1400	
GR II.	Ricoh	248	117 x 63 x 35	not specified	23.7 x 15.6	16.2	650	
<b>Multi &amp; Hyperspectral</b>								
Sequoia	Parrot	72	59 x 41 x 28	rolling/global	not specified	16/1.2	3 300	550-790 nm
ADC Lite	Tetracam	200	114 x 77 x 22	rolling	not specified	3.2	3 600	400-750 nm
Micro-MCA 6	Tetracam	530	116 x 80 x 68	rolling/global	6.7 x 5.3	1.3	12 300	450-1000 nm
Ricola	Ricola	720	not specified	snapshot	not specified	1.3	not specified	500-950 nm
RedEdge	MicaSense	150	121 x 6.6 x 4.6	not specified	not specified	1.2	5 500	450-750 nm
Nano-Hyperspec	Headwall	520	76 x 76 x 120	pushbroom	not specified	0.64	not specified	400-1000 nm
OXI 40	Gamaya	250	60 x 110 x 90	global	not specified	2	not specified	400-1000 nm
<b>Thermal</b>								
WIRIS 640	Workswell	400	139 x 84 x 69	snapshot	not specified	640 x 512	10 000	not specified
Vue	FLIR	113	57 x 44 x 44	snapshot	not specified	640 x 512	2 800	7.500 - 13.5 $\mu$ m

Table A.2 – Frequently used RGB and multi/hyperspectral/thermal cameras on MAVs.

## Appendix A. Overview of Photogrammetric Platforms, Sensors, and Mission Planners

Name	Real-time	3rd party platforms	Open source	Flight management	Multiple UAVs	Environment	Mobile version	Aerial mapping	Advanced functions
Mission Planner	+	+	+	+	-	height map	+	++	customizable, drone configuration and calibration
Mikrokopter	+	-	-	+	-	2D	-	+	drone configuration and calibration
DJI	+	-	-	++	-	3D	+	++	no-fly zones, simulations
UGCS	+	+	-	+++	+	3D	-	++	import of custom 3D objects
eMotion3	+	-	-	+++	+	3D	-	+++	connected to processing sw. custom DSM, simulations
msCockpit	+	-	-	++	-	3D	-	++	drone control over server
Mavinci	+	-	-	++	-	3D	-	+++	connection to processing sw, simulations
Pix4D Capture	+	+	-	++	-	height map	+	++	connection to cloud processing
Drone Deploy	+	+	-	++	-	height map	+	++	connection to cloud processing
TOPO MP	-	+	+	+	-	3D	-	+++	GNSS visibility, custom DSM, overlap and GSD prediction

Table A.3 – Main mission planners dedicated to MAVs; A value "-" means no functionality or very low, "+" means low, "++" means medium, "+++ means high. This categorisation is based on the author's personal opinion and does not completely reflect the true functionality as some of the mission planners were not available for testing.

## B TOPOBUN Bundle Adjustment

The partial derivatives of the image observation equations are give hereunder. The derivatives of aerial observations were derived using the Matlab symbolic toolbox The MathWorks Inc. [2016]. These are not stated here. Partial derivatives constituting the design matrix **A** are schematically depicted in Tab. B.1.

For the collinearity equation:

$$x = x_0 - c \cdot \frac{r_{11}(X - X_0) + r_{21}(Y - Y_0) + r_{31}(Z - Z_0)}{r_{13}(X - X_0) + r_{23}(Y - Y_0) + r_{33}(Z - Z_0)} + \Delta x$$

$$y = y_0 - c \cdot \frac{r_{12}(X - X_0) + r_{22}(Y - Y_0) + r_{32}(Z - Z_0)}{r_{13}(X - X_0) + r_{23}(Y - Y_0) + r_{33}(Z - Z_0)} + \Delta y$$
(B.1)

the following notations can be introduced:

$$N_x = r_{11}(X - X_0) + r_{21}(Y - Y_0) + r_{31}(Z - Z_0)$$

$$N_y = r_{12}(X - X_0) + r_{22}(Y - Y_0) + r_{32}(Z - Z_0)$$

$$N_z = r_{13}(X - X_0) + r_{23}(Y - Y_0) + r_{33}(Z - Z_0)$$
(B.2)

The rotation matrix  $R_c^m$  is:

$r_{11} = \cos(\varphi) \cos(\kappa)$	$r_{12} = -\cos(\varphi) \sin(\kappa)$	$r_{13} = \sin(\varphi)$
$r_{21} = \cos(\omega) \sin(\kappa) + \sin(\omega) \sin(\varphi) \cos(\kappa)$	$r_{22} = \cos(\omega) \cos(\kappa) - \sin(\omega) \sin(\varphi) \sin(\kappa)$	$r_{23} = -\sin(\omega) \cos(\varphi)$
$r_{31} = \sin(\omega) \sin(\kappa) - \cos(\omega) \sin(\varphi) \cos(\kappa)$	$r_{32} = \sin(\omega) \cos(\kappa) + \cos(\omega) \sin(\varphi) \sin(\kappa)$	$r_{33} = \cos(\omega) \cos(\varphi)$

## Appendix B. TOPOBUN Bundle Adjustment

---

**Partial derivatives with respect to interior orientation:  $c, x_0, y_0$**

**The x-coordinate equation**

$$\frac{\delta x}{\delta x_0} = 1 \quad \frac{\delta x}{\delta y_0} = 0 \quad \frac{\delta x}{\delta c} = -\frac{N_x}{N_z} \quad (\text{B.3})$$

**The y-coordinate equation**

$$\frac{\delta y}{\delta x_0} = 0 \quad \frac{\delta y}{\delta y_0} = 1 \quad \frac{\delta y}{\delta c} = -\frac{N_y}{N_z} \quad (\text{B.4})$$

**Partial derivatives with respect to coordinates of the camera perspective centre**

**The x-coordinate equation**

$$\frac{\delta x}{\delta X_0} = c \cdot \frac{N_z \cdot r_{11} - N_x \cdot r_{13}}{N_z^2} \quad \frac{\delta x}{\delta Y_0} = c \cdot \frac{N_z \cdot r_{21} - N_x \cdot r_{23}}{N_z^2} \quad \frac{\delta x}{\delta Z_0} = c \cdot \frac{N_z \cdot r_{31} - N_x \cdot r_{33}}{N_z^2} \quad (\text{B.5})$$

**The y-coordinate equation**

$$\frac{\delta y}{\delta X_0} = c \cdot \frac{N_z \cdot r_{12} - N_x \cdot r_{13}}{N_z^2} \quad \frac{\delta y}{\delta Y_0} = c \cdot \frac{N_z \cdot r_{22} - N_x \cdot r_{23}}{N_z^2} \quad \frac{\delta y}{\delta Z_0} = c \cdot \frac{N_z \cdot r_{32} - N_x \cdot r_{33}}{N_z^2} \quad (\text{B.6})$$

**Partial derivatives with respect to camera orientation**

**The x-coordinate equation**

$$\frac{\delta x}{\delta \omega} = -c \cdot \frac{N_x \cdot [r_{33} \cdot (X - X_0) - (Z - Z_0) \cdot r_{23}] + N_z \cdot [r_{21} \cdot (Z - Z_0) - (Y - Y_0) \cdot r_{31}]}{N_z^2}$$

$$\frac{\delta x}{\delta \varphi} = -c \cdot \frac{N_x [N_y \sin(\kappa) - N_x \cos(\kappa)] - N_z^2 \cos(\kappa)}{N_z^2} \quad (\text{B.7})$$

$$\frac{\delta x}{\delta \kappa} = -c \cdot \frac{N_y}{N_z}$$

---

### The y-coordinate equation

$$\frac{\delta y}{\delta \omega} = -c \cdot \frac{N_y \cdot [r_{33} \cdot (Y - Y_0) - (Z - Z_0) \cdot r_{23}] + N_z \cdot [r_{22} \cdot (Z - Z_0) - (Y - Y_0) \cdot r_{32}]}{N_z^2}$$
$$\frac{\delta y}{\delta \varphi} = -c \frac{N_y [N_y \sin(\kappa) - N_x \cos(\kappa)] + N_z^2 \sin(\kappa)}{N_z^2} \quad (\text{B.8})$$
$$\frac{\delta y}{\delta \kappa} = c \frac{N_x}{N_z}$$

### Partial derivatives with respect to object point coordinates

#### The x-coordinate equation

$$\frac{\delta x}{\delta X} = c \cdot \frac{r_{13} \cdot N_x - r_{11} \cdot N_z}{N_z^2}$$
$$\frac{\delta x}{\delta Y} = c \cdot \frac{r_{23} \cdot N_x - r_{21} \cdot N_z}{N_z^2} \quad (\text{B.9})$$
$$\frac{\delta x}{\delta Z} = c \cdot \frac{r_{33} \cdot N_x - r_{31} \cdot N_z}{N_z^2}$$

#### The y-coordinate equation

$$\frac{\delta y}{\delta X} = c \cdot \frac{r_{13} \cdot N_y - r_{12} \cdot N_z}{N_z^2}$$
$$\frac{\delta y}{\delta Y} = c \cdot \frac{r_{23} \cdot N_y - r_{22} \cdot N_z}{N_z^2} \quad (\text{B.10})$$
$$\frac{\delta y}{\delta Z} = c \cdot \frac{r_{33} \cdot N_y - r_{32} \cdot N_z}{N_z^2}$$

### Partial derivatives with respect to additional parameters of lens distortion

#### The x-coordinate equation

$$\frac{\delta x}{\delta K_1} = x \cdot r^2 \quad \frac{\delta x}{\delta K_2} = x \cdot r^4 \quad \frac{\delta x}{\delta K_3} = x \cdot r^6 \quad \frac{\delta x}{\delta P_1} = 2xy \quad \frac{\delta x}{\delta P_2} = 2x^2 + r^2 \quad (\text{B.11})$$

## Appendix B. TOPOBUN Bundle Adjustment

---

The y-coordinate equation

$$\frac{\delta y}{\delta K_1} = y \cdot r^2 \quad \frac{\delta y}{\delta K_2} = y \cdot r^4 \quad \frac{\delta y}{\delta K_3} = y \cdot r^6 \quad \frac{\delta y}{\delta P_1} = 2y^2 + r^2 \quad \frac{\delta y}{\delta P_2} = 2xy \quad (\text{B.12})$$



A	EO parameters										Object coordinates of tie-points								Obj. coordinates of GCPs			IO			Syn. Velocities			Ang. rates			Boresight			Lever arm					
	EO PH1			EO PH2			EO PH3			TP1	TP2	TP3	TP4	TP5	TP6	TP7	TP8	X <sub>GCP1</sub>	Y <sub>GCP1</sub>	Z <sub>GCP1</sub>	GCP2	GCP3	c	x0	y0	Dt	Vx	Vy	Vz	Arx	Ary	Arz	Bp	Bk	Bx	By	Bz		
L	X <sub>PH1</sub>	Y <sub>PH1</sub>	Z <sub>PH1</sub>	ω <sub>PH1</sub>	φ <sub>PH1</sub>	κ <sub>PH1</sub>	X <sub>TP1</sub>	Y <sub>TP1</sub>	Z <sub>TP1</sub>	X <sub>GCP1</sub>	Y <sub>GCP1</sub>	Z <sub>GCP1</sub>	GCP2	GCP3	c	x0	y0	Dt	Vx	Vy	Vz	Arx	Ary	Arz	Bp	Bk	Bx	By	Bz	Bx	By	Bz							
X <sub>PH1</sub> TP1																																							
Y <sub>PH1</sub> TP1																																							
X <sub>PH1</sub> GCP1																																							
Y <sub>PH1</sub> GCP1																																							
Z <sub>PH1</sub> GCP1																																							
XGNSSPH1																																							
YGNSSPH1																																							
ZGNSSPH1																																							
OmPH1																																							
PhiPH1																																							
KappaPH1																																							
VxPH1																																							
VyPH1																																							
VzPH1																																							
ArxPH1																																							
AryPH1																																							
ArzPH1																																							

Table B.1 – Structures of the design matrix **A** and the vector of observations **L**. In addition to the depicted observations, the following parameters can be used as weighted observations: camera IO, a boresight, a lever-arm and  $\Delta t$ .



# C System and Sensor Calibration

## C.1 Lever-Arm Calibration



Figure C.1 – The lever-arm calibration setup. The fuselage without wings and with the camera and antenna pointing towards the calibration field.

## C.2 Camera Calibration

The distribution of points in all images is illustrated in Fig. C.2. The residuals are visualised in Fig. C.3 where the image residuals are grouped in sectors according to their location in the sensor and scaled.

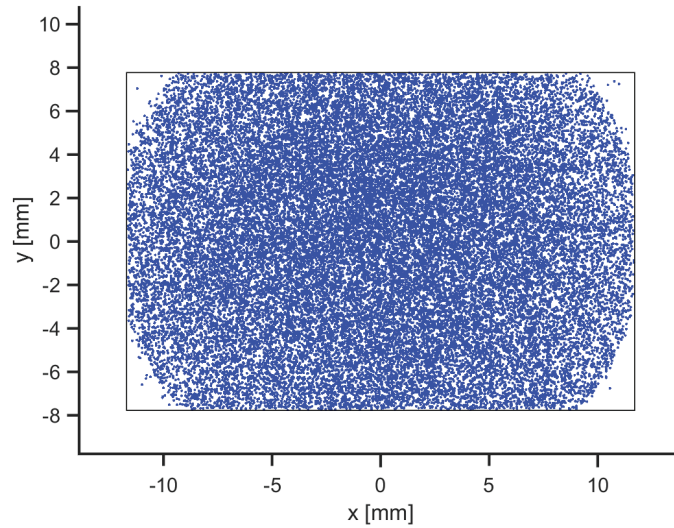


Figure C.2 – Distribution of image observations in the image plane.

	$X_0$	$Y_0$	$Z_0$	$\omega$	$\phi$	$\kappa$	$c$	$x_0$	$y_0$	$K_1$	$K_2$	$K_3$	$P_1$	$P_2$
$X_0$	1													
$Y_0$	0.27	1												
$Z_0$	0.08	0.03	1											
$\omega$	-0.33	-0.84	-0.04	1										
$\phi$	0.69	0.40	0.16	-0.48	1									
$\kappa$	-0.13	-0.05	-0.03	-0.02	-0.10	1								
$c$	-0.02	0.01	0.01	0.02	-0.01	0.01	1							
$x_0$	0.01	0	0	0	-0.06	0	0.01	1						
$y_0$	-0.01	0.01	0.09	0.04	-0.01	0.01	0.75	0.02	1					
$K_1$	0	0	0	0	0	0	-0.17	0	0.07	1				
$K_2$	0	0	0.01	0	0	0	0.21	0.01	0.02	-0.97	1			
$K_3$	0	0	0	0	0	0	-0.20	0	0	0.92	-0.99	1		
$P_1$	-0.01	0	0.06	0.04	0	0.01	0.26	0.03	0.067	0.09	-0.01	0.01	1	
$P_2$	0	0	0	0	0.06	0	0	0.91	0	0	0	0	0.03	1

Table C.1 – Parameters and their correlation for a random image from the dataset.

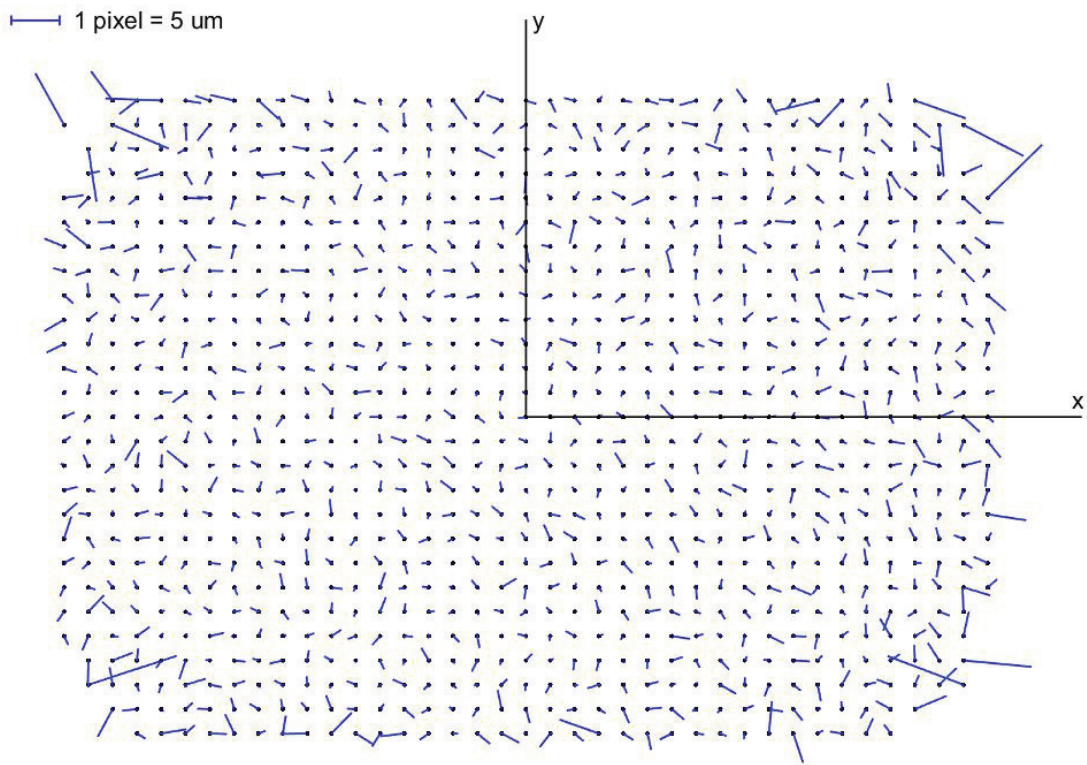


Figure C.3 – Image residuals in the camera sensor plane.



# Bibliography

- S. Abraham and T. Hau. Towards autonomous high precision calibration of digital cameras. In *SPIE 3174*, San Diego, CA, United States, 1997. doi: 10.1117/12.279802.
- F. Ackermann. On the theoretical accuracy of planimetric block triangulation. *Photogrammetria*, 21(5):145–170, 1966. URL <http://www.sciencedirect.com/science/article/pii/0031866366900093>.
- Aerolution GmbH. Songbird 1400. <http://www.aerolution-systems.com/en/products/songbird-1400-2/>, 2016. [Online; accessed 31-October-2016].
- Agisoft. Agisoft photoscan. <http://www.agisoft.com/>, 2014. [Online; accessed 12-September-2016].
- Aibotix GmbH. Aibotix X6 UAV. <https://www.aibotix.com/en/>, 2016. [Online; accessed 13-August-2016].
- Antcom Corp. GPS, GNSS, SBAS, OmniSTAR/TerraStar, CRPA Antennas. <http://www.antcom.com/products/gps-gns-sbas-crpa.php>, 2016. [Online; accessed 22-November-2016].
- Applanix Corporation. APX-15 UAV. <http://www.applanix.com/products/dms-uavs.htm>, 2015. [Online; accessed 5-August-2016].
- Applanix Corporation. Applanix PosPac, Postproc. <http://www.applanix.com/products/pospac-mms.htm>, 2016. [Online; accessed 31-October-2016].
- ArduPilot Dev Team. Ardupilot. <http://ardupilot.com/ardupilot/index.html>, 2016. [Online; accessed 19-September-2016].
- ArduPilot Dev Team and Michael Osborne. Mission Planner. <http://plane.ardupilot.org/planner/docs/mission-planner-overview.html>, 2016. [Online; accessed 19-September-2016].
- Ascending Technologies. Falcon 8. <http://www.asctec.de/en/uav-uas-drones-rpas-roav/asctec-falcon-8/>, 2016. [Online; accessed 3-November-2016].
- B & H Foto & Electronics Corp. Sony NEX 5N. [https://www.bhphotovideo.com/c/product/692505-REG/Sony\\_NEX5A\\_B\\_Alpha\\_NEX\\_5\\_Interchangeable\\_Lens.html](https://www.bhphotovideo.com/c/product/692505-REG/Sony_NEX5A_B_Alpha_NEX_5_Interchangeable_Lens.html), 2016. [Online; accessed 25-November-2016].

## Bibliography

---

- W. Baarda. Testing Procedure for Use in Geodetic Networks. *Publication on Geodesy, Netherlands Geodetic Commission*, (5), 1968. URL <http://citeseerx.ist.psu.edu/viewdoc/download?doi=10.1.1.367.8131&rep=rep1&type=pdf>.
- C. Bartone. GNSS Antennas: A Crucial Element. *Inside GNSS*, (9-10):28–29, 2013. URL <http://www.insidegnss.com/node/3685>.
- M. Bäumker and H.-J. Przybilla. Investigation on the accuracy of the navigation data of unmanned aerial vehicles using example of the system Mikrokopter. In *ISPRS - The International Archives of the Photogrammetry, Remote Sensing and Spatial Information Sciences*, pages 113–118, Zurich, Switzerland, 2011.
- M. Bäumker, H. J. Przybilla, and A. Zurhorst. Enhancements in UAV flight control and sensor orientation. In *ISPRS - The International Archives of the Photogrammetry, Remote Sensing and Spatial Information Sciences*, pages 33–38, Rostock, Germany, 2013. URL <http://www.int-arch-photogramm-remote-sens-spatial-inf-sci.net/XL-1-W2/33/2013/isprsarchives-XL-1-W2-33-2013.pdf>.
- H. Bay, T. Tuytelaars, and L. V. Gool. SURF: Speeded Up Robust Features. Graz, Austria, 2006. URL <http://www.vision.ee.ethz.ch/~surf/eccv06.pdf>.
- R. J. Beaton and W. W. Farley. Comparative study of the MTF, ICS, and SQRI image quality metrics for visual display systems. Technical report, DTIC Document, 1991. URL <http://oai.dtic.mil/oai/oai?verb=getRecord&metadataPrefix=html&identifier=ADA252116>.
- S. Becker, N. Haala, E. Honkavaara, and L. Markelin. Image restoration for resolution improvement of digital aerial images: a comparison of large format digital cameras. In *ISPRS - The International Archives of Photogrammetry, International Society*, volume 36, 2006. URL <http://www.isprs.org/proceedings/xxxvi/part1/papers/T01-03.pdf>.
- L. Benoit, O. Martin, and C. Thom. Low-cost GPS Sensors for deformation monitoring. *GIM International*, 29(4):25–27, 2015. URL <https://www.gim-international.com/magazines/gim-international-april-2015.pdf>.
- P. Blyenburgh. Unmanned Aircraft Systems The Current Situation. [http://www.easa.europa.eu/ws\\_prod/g/doc/Events/2008/February/1-Overview%20of%20the%20UAV%20Industry%20\(UVS\).pdf](http://www.easa.europa.eu/ws_prod/g/doc/Events/2008/February/1-Overview%20of%20the%20UAV%20Industry%20(UVS).pdf), 2008. [Online; accessed 10-August-2016].
- M. Bláha, H. Eisenbeiss, D. Grimm, and P. Limpach. Direct georeferencing of UAVs. In *ISPRS - The International Archives of the Photogrammetry, Remote Sensing and Spatial Information Sciences*, Zurich, Switzerland, 2011.
- M. Blázquez. A new approach to spatio-temporal calibration of multi-sensor systems. In *ISPRS-The International Archives of the Photogrammetry Remote Sensing and Spatial Information Sciences*, volume 37, pages 481–486, Beijing, China, 2008. URL [http://www.isprs.org/proceedings/xxxvii/congress/1\\_pdf/81.pdf](http://www.isprs.org/proceedings/xxxvii/congress/1_pdf/81.pdf).



- M. Blázquez and I. Colomina. On the role of self-calibration functions in integrated sensor orientation. In *ISPRS - The International Archives of the Photogrammetry, Remote Sensing and Spatial Information Sciences*, Castelldefels, Spain, 2010. URL [http://www.isprs.org/proceedings/xxxviii/eurocow2010/euroCOW2010\\_files/papers/05.pdf](http://www.isprs.org/proceedings/xxxviii/eurocow2010/euroCOW2010_files/papers/05.pdf).
- M. Blázquez and I. Colomina. Fast AT: a simple procedure for quasi direct orientation. *ISPRS Journal of Photogrammetry and Remote Sensing*, 71:1–11, 2012a.
- M. Blázquez and I. Colomina. Relative INS/GNSS aerial control in integrated sensor orientation: models and performance. *ISPRS Journal of Photogrammetry and Remote Sensing*, 67: 120–133, 2012b.
- D. C. Brown. Close-range camera calibration. *Photogrammetric Engineering*, 37(8):855–866, 1971. URL [http://www.vision.caltech.edu/bouguetj/calib\\_doc/papers/Brown71.pdf](http://www.vision.caltech.edu/bouguetj/calib_doc/papers/Brown71.pdf).
- N. Butcher, A. Stewart, and S. Biaz. Securing the MAVLink communication protocol for unmanned aircraft systems. Technical report, 2014.
- C-Astral Aerospace. Bramor. <http://www.c-astral.com/en>, 2016. [Online; accessed 3-November-2016].
- Canon Inc. PowerShot S110. <https://www.usa.canon.com/internet/portal/us/home/products/details/cameras/point-and-shoot/advanced-cameras/powershot-s110>, 2016. [Online; accessed 25-November-2016].
- T. A. Clarke and J. G. Fryer. The development of camera calibration methods and models. *The Photogrammetric Record*, 16(91):51–66, 1998. URL <http://onlinelibrary.wiley.com/doi/10.1111/0031-868X.00113/abstract>.
- P. Clausen, M. Rehak, and J. Skaloud. UAV sensor orientation with pre-calibrated redundant IMU/GNSS observations: Preliminary results. In *Publikationen der Deutschen Gesellschaft für Photogrammetrie, Fernerkundung und Geoinformation (DGPF)*, volume 25, pages 26–33, Bern, Switzerland, 2016.
- I. Colomina. GPS, INS and aerial triangulation: What is the best way for the operational determination of photogrammetric image orientation. In *ISPRS - The International Archives of the Photogrammetry, Remote Sensing and Spatial Information Sciences*, volume 32, pages 121–130, Munich, Germany, 1999.
- I. Colomina. From off-line to on-line geocoding: the evolution of sensor orientation. In Dieter Fritsch, editor, *Photogrammetric Week*, pages 173–183, Stuttgart, Germany, 2007.
- I. Colomina and M. Blázquez. On the stochastic modeling and solution of time dependent networks. Barcelona, Spain, 2005.
- I. Colomina and P. Molina. Unmanned aerial systems for photogrammetry and remote sensing: a review. *ISPRS Journal of Photogrammetry and Remote Sensing*, 92(6):79–97, 2014. URL <http://www.sciencedirect.com/science/article/pii/S0924271614000501>.

## Bibliography

---

- M. Cramer. Performance of GPS/Inertial solutions in photogrammetry. In *Photogrammetric Week*, pages 49–62, Heidelberg, Germany, 2001. URL <http://www.ifp.uni-stuttgart.de/publications/phowo01/Cramer.pdf>.
- M. Cramer. Integrated GPS/inertial and digital aerial triangulation - recent test results. In *Photogrammetric Week*, pages 161–172, Heidelberg, Germany, 2003.
- M. Cramer and B. Leinss. Welche ist am besten? – Anmerkungen zur Auswahl von Kamerasystemen in der UASLuftbildphotogrammetrie. 2014. URL [http://www.ifp.uni-stuttgart.de/publications/2016/2016-DVW\\_Schriftenreihe\\_CRAMER.pdf](http://www.ifp.uni-stuttgart.de/publications/2016/2016-DVW_Schriftenreihe_CRAMER.pdf).
- M. Cramer and D. Stallmann. System calibration for direct georeferencing. In *Photogrammetric Computer Vision, ISPRS Commission III Symposium*, Graz, Austria, 2002.
- CSG Shop. UBLOX NEO-M8T. [http://www.csgshop.com/product.php?id\\_product=205](http://www.csgshop.com/product.php?id_product=205), 2016. [Online; accessed 26-October-2016].
- Delair-Tech. Power lines inspection using MINI-UAV. [http://www.ugpti.org/smartse/research/citations/downloads/DeltairTech-Power\\_Line\\_Inspection-2014.pdf](http://www.ugpti.org/smartse/research/citations/downloads/DeltairTech-Power_Line_Inspection-2014.pdf), May 2014. [Online; accessed 6-September-2016].
- DGAC. Drones (aéronefs télépilotes). <http://www.developpement-durable.gouv.fr/Drones-civils-loisir-activite>, 2016. [Online; accessed 8-August-2016].
- W. Ding, J. Wang, Y. Li, P. Mumford, and Ch. Rizos. Time synchronization error and calibration in integrated GPS/INS systems. *ETRI journal*, 30(1):59–67, 2008. URL <http://etrij.etri.re.kr/etrijournal/article/article.do?volume=30&issue=1&page=59>.
- DIY Drones. 3DR IRIS gets approved in France by DGAC (french FAA). <http://diydrones.com/profiles/blogs/3dr-iris-gets-approved-in-france-by-dgac-french-faa>, 2014. [Online; accessed 1-November-2016].
- DJI Innovations. AGRASMG-1. <http://www.dji.com/>, 2016. [Online; accessed 12-August-2016].
- Drone Mapper. DroneMapper. <https://dronemapper.com/>, 2016. [Online; accessed 20-November-2016].
- DroneAnalytics. DroneLogbook. <https://www.dronelogbook.com/homePage/index.php>, 2016. [Online; accessed 12-November-2016].
- DroneDeploy. Dronedeploy app - Automated Mapping for Beginners and Professionals. <https://www.dronedeploy.com/>, 2016. [Online; accessed 20-September-2016].
- EASA. Unmanned Aircraft Systems (UAS) and Remotely Piloted Aircraft Systems (RPAS). <https://www.easa.europa.eu/unmanned-aircraft-systems-uas-and-remotely-piloted-aircraft-systems-rpas>, 2016. [Online; accessed 8-August-2016].

- H. Ebner. Self calibrating block adjustment. In *ISPRS - The International Archives of Photogrammetry, International Society for Photogrammetry and Remote Sensing*, Helsinki, Finland, 1996.
- H. Eisenbeiß. *UAV Photogrammetry*. PhD thesis, ETH Zurich, 2009.
- C. Eling, L. Klingbeil, M. Wieland, and H. Kuhlmann. A precise position and attitude determination system for lightweight unmanned aerial vehicle. In *ISPRS - The International Archives of the Photogrammetry, Remote Sensing and Spatial Information Sciences*, pages 113–118, Rostock, Germany, 2013. URL <http://www.int-arch-photogramm-remote-sens-spatial-inf-sci.net/XL-1-W2/113/2013/isprsarchives-XL-1-W2-113-2013.pdf>.
- C. Eling, L. Klingbeil, M. Wieland, and H. Kuhlmann. Direct georeferencing of micro-aerial vehicles - system design, system calibration and first evaluation tests. *Journal of photogrammetry, remote sensing and geoinformation processing (PFG)*, 4:227–237, 2014.
- C. Eling, M. Wieland, C. Hess, L. Klingbeil, and H. Kuhlmann. Development and evaluation of a UAV based mapping System for remote sensing and surveying applications. In *ISPRS - The International Archives of the Photogrammetry, Remote Sensing and Spatial Information Sciences*, volume XL-1/W4, pages 233–239, Toronto, Canada, August 2015. doi: 10.5194/isprsarchives-XL-1-W4-233-2015. URL <http://www.int-arch-photogramm-remote-sens-spatial-inf-sci.net/XL-1-W4/233/2015/>.
- C. Ellum and N. El-Sheimy. Inexpensive Kinematic Attitude Determination from MEMS-Based Accelerometers and GPS-Derived Accelerations. *NAVIGATION: Journal of The Institute of Navigation*, 49(3):117–126, 2002.
- SPH Engineering. Universal Ground Control Station. <https://www.ugcs.com/>, 2016. [Online; accessed 20-September-2016].
- ESA Navipedia. Receiver types. [http://www.navipedia.net/index.php/Receiver\\_Types](http://www.navipedia.net/index.php/Receiver_Types), 2014. [Online; accessed 4-September-2016].
- ESA Navipedia. Antennas. <http://www.navipedia.net/index.php/Antennas>, 2016. [Online; accessed 15-August-2016].
- Esri. Drone2Map for ArcGIS. <http://www.esri.com/products/drone2map>, 2016. [Online; accessed 20-November-2016].
- H. Eugster and S. Nebiker. UAV-based augmented monitoring-Real-time georeferencing and integration of video imagery with virtual globes. In *ISPRS - The International Archives of the Photogrammetry, Remote Sensing and Spatial Information Sciences*, volume XXXVII, pages 1229–1236, Beijing, China, 2008.
- Federal Aviation Administration. Unmanned Aircraft Systems. <https://www.faa.gov/uas/>, 2016. [Online; accessed 8-October-2016].

## Bibliography

---

- M. Fiala. Designing highly reliable fiducial markers. *IEEE Transactions on Pattern analysis and machine intelligence*, 32(7):1317–1324, 2010. URL [http://ieeexplore.ieee.org/xpls/abs\\_all.jsp?arnumber=5184844](http://ieeexplore.ieee.org/xpls/abs_all.jsp?arnumber=5184844).
- FiducialMark. Photogrammetry meets kite aerial photography. <http://fiducialmark.blogspot.ch/2009/03/photogrammetry-meets-kite-aerial.html>, 2016. [Online; accessed 20-September-2016].
- FOCA. Drones civils : loisir ? activité professionnelle ? <https://www.bazl.admin.ch/bazl/en/home/good-to-know/drones-and-aircraft-models.html>, 2017. [Online; accessed 3-February-2017].
- W. Förstner. Matching strategies for point transfer. In *Photogrammetric Week*, pages 173–183, Heidelberg, Germany, 1995. URL <http://www.ipb.uni-bonn.de/pdfs/Forstner1995Unified.pdf>.
- C.S Fraser. On the use of non-metric cameras in analytical non-metric photogrammetry. *International Archives of Photogrammetry and Remote Sensing*, 24(5):156–166, 1982.
- C.S. Fraser. Digital camera self-calibration. *ISPRS Journal of Photogrammetry and Remote Sensing*, 52(4):149–159, 1997.
- Fujifilm Corporation. Fuji X-M1. [http://www.fujifilm.com/support/digital\\_cameras/specifications/x/fujifilm\\_x\\_m1/](http://www.fujifilm.com/support/digital_cameras/specifications/x/fujifilm_x_m1/), 2017. [Online; accessed 24-January-2017].
- W. Förstner and B.P. Wrobel. *Photogrammetric Computer Vision: Geometry, Orientation and Reconstruction*. Geometry and Computing. Springer International Publishing, 2016. ISBN 978-3-319-11549-8. URL <https://books.google.ch/books?id=odbJoQEACAAJ>.
- Gamaya SA. Gamaya OXI 40. <http://gamaya.com/>, 2017. [Online; accessed 1-February-2017].
- F. Gandor. Mission planner for micro aerial vehicles. Master Thesis, The Swiss Federal Institute of Technology Lausanne (EPFL), Lausanne, Switzerland, 2015.
- F. Gandor, M. Rehak, and J. Skaloud. Planificateur de missions photogrammétriques pour drones ultra-légers (Micro Aerial Vehicle MAV). *Geomatique Suisse*, 9:371–375, 2015a.
- F. Gandor, M. Rehak, and J. Skaloud. Photogrammetric mission planner for RPAS. In *ISPRS-The International Archives of the Photogrammetry Remote Sensing and Spatial Information Sciences*, volume XL-1/W4, pages 61–65, Toronto, Canada, 2015b. doi: 10.5194/isprsarchives-XL-1-W4-61-2015. URL <http://dx.doi.org/10.5194/isprsarchives-XL-1-W4-61-2015>.
- M. Gerke. Using horizontal and vertical building structure to constrain indirect sensor orientation. *ISPRS Journal of Photogrammetry and Remote Sensing*, 66(3):307–316, May 2011. ISSN 09242716. doi: 10.1016/j.isprsjprs.2010.11.002. URL <http://linkinghub.elsevier.com/retrieve/pii/S0924271610001188>.

- M. Gerke and H.-J. Przybilla. Accuracy analysis of photogrammetric UAV image blocks: Influence of onboard RTK-GNSS and cross flight patterns. *Photogrammetrie, Fernerkundung, Geoinformation (PFG)*, 2016(1):17–30, March 2016. ISSN 14328364. doi: 10.1127/pfg/2016/0284. URL <http://openurl.ingenta.com/content/xref?genre=article&issn=1432-8364&volume=2016&issue=1&spage=17>.
- L. V. Gool, T. Moons, and D. Ungureanu. *Affine/photometric invariants for planar intensity patterns*. Cambridge, UK, 1996. doi: 10.1007/BFb0015574.
- GPS Source. Tiny Splitter. <https://www.gpssource.com/products/s12t-tiny-gps-splitter>, 2016. [Online; accessed 31-October-2016].
- A. Grün. The accuracy potential of the modern bundle block adjustment in aerial photogrammetry. *Photogrammetric Engineering and Remote Sensing*, 48:45–54, 1982.
- A Grün. Photogrammetrische punktbestimmung mit der bündelmethode. In *Mitteilungen, Vol. 40*, ETH Zürich, Switzerland, 1986.
- A. Grün. Development and status of image matching in photogrammetry: Development and status of image matching in photogrammetry. *The Photogrammetric Record*, 27(137):36–57, 2012. ISSN 0031868X. doi: 10.1111/j.1477-9730.2011.00671.x. URL <http://doi.wiley.com/10.1111/j.1477-9730.2011.00671.x>.
- GS1. Regulatory status for using RFID in the EPC Gen2 band (860 to 960 MHz) of the UHF spectrum. [http://www.gs1.org/docs/epc/UHF\\_Regulations.pdf](http://www.gs1.org/docs/epc/UHF_Regulations.pdf), 2016. [Online; accessed 4-September-2016].
- S. Guerrier, R. Molinari, and J. Skaloud. Automatic identification and calibration of stochastic parameters in inertial sensors. *NAVIGATION: Journal of the Institute of Navigation*, 62(4): 265–272, 2015. URL <http://onlinelibrary.wiley.com/doi/10.1002/navi.119/full>.
- R. Hartley and A. Zisserman. *Multiple View Geometry in Computer Vision*. Cambridge University Press, New York, USA, 2 edition, 2003. ISBN 0521540518.
- M. Hassaballah, A. A. Abdelmgeid, and H. A. Alshazly. Image features detection, description and matching. In *Image Feature Detectors and Descriptors*, pages 11–45. Springer International Publishing, 2016. ISBN 978-3-319-28852-9 978-3-319-28854-3. URL [http://link.springer.com/10.1007/978-3-319-28854-3\\_2](http://link.springer.com/10.1007/978-3-319-28854-3_2).
- Headwall. Nano-hyperspec. <http://www.headwallphotonics.com/spectral-imaging/hyperspectral/nano-hyperspec>, 2016. [Online; accessed 25-October-2016].
- C. Heipke, K. Jacobsen, and H. Wegmann. Analysis of the results of the OEEPE test "Integrated sensor orientation". *OEEPE Official Publication*, 43, 2002.
- Hexagon Geospatial. IMAGINE Photogrammetry. <http://www.hexagongeospatial.com/products/producer-suite/ imagine-photogrammetry>, 2016. [Online; accessed 20-October-2016].

## Bibliography

---

- HiSystems GmbH. MikroKopter Tool. <http://wiki.mikrokoetter.de/en/MikroKopterTool>, 2016. [Online; accessed 19-September-2016].
- Eija Honkavaara. *Calibrating digital photogrammetric airborne imaging systems using a test field*. Finnish Geodetic Institute, Kirkkonummi, 2008. ISBN 978-951-711-275-8 978-951-711-276-5. OCLC: 500545922.
- H. Hou. Modeling inertial sensors errors using Allan variance. Master Thesis, University of Calgary, Department of Geomatics Engineering, Calgary, Canada, 2004. URL [http://www.ucalgary.ca/engo\\_webdocs/NES/04.20201.HaiyingHou.pdf](http://www.ucalgary.ca/engo_webdocs/NES/04.20201.HaiyingHou.pdf).
- ICAO. The International Civil Aviation Organization. <http://www.icao.int/Pages/default.aspx>, 2016. [Online; accessed 8-August-2016].
- Icaros. OneButton. <https://www.icaros.us/onebutton/>, 2016. [Online; accessed 20-November-2016].
- IGI mbH. IGIplan - Mission Planning Software. <http://www.igi-systems.com/igiplan.html>, 2017. [Online; accessed 24-January-2017].
- IGN France. MicMac. <http://logiciels.ign.fr/?Micmac>, 2016. [L'Institut national de l'information géographique et forestière. Online; accessed 20-November-2016].
- Imatest LLC. Sharpness: What is it and how is it measured? . <http://www.imatest.com/docs/sharpness/>, 2017. [Online; accessed 7-February-2017].
- Intersense. Navchip. <http://www.intersense.com/pages/16/246/>, 2015. [Online; accessed 12-December-2015].
- A. Ip, N. El-Sheimy, and M. Mostafa. Performance analysis of integrated sensor orientation. *Photogrammetric Engineering & Remote Sensing*, 73:89–97, 2007.
- K. Jacobsen. Block adjustment. [https://www.ipi.uni-hannover.de/uploads/tx\\_tkpublikationen/block\\_adjustment.pdf](https://www.ipi.uni-hannover.de/uploads/tx_tkpublikationen/block_adjustment.pdf), 2002a.
- K. Jacobsen. Calibration aspects in direct georeferencing of frame imagery. In *ASPRS Fall Meeting (PECORA)*, pages 82–89, Denver, CO USA, 2002b. URL <http://www.isprs.org/proceedings/XXXIV/part1/paper/00013.pdf>.
- K. Jacobsen. Direct/Integrated sensor orientation - pros and cons. In *ISPRS-The International Archives of the Photogrammetry Remote Sensing and Spatial Information Sciences*, pages 829–835, Istanbul, Turkey, 2004.
- K. Jacobsen and M. Schmitz. A new approach of combined block adjustment using GPS-Satellite constellation. In *ISPRS - The International Archives of the Photogrammetry Remote Sensing and Spatial Information Sciences*, volume XXXI, pages 355–359, Vienna, Austria, 1996. URL [http://www.isprs.org/proceedings/XXXI/congress/part3/355\\_XXXI-part3.pdf](http://www.isprs.org/proceedings/XXXI/congress/part3/355_XXXI-part3.pdf).

- Javad GNSS Inc. Javad TRE-G3t. <http://www.javad.com/jgnss/products/oem/>, 2016. [Online; accessed 14-August-2016].
- J. Jon, B. Koska, and J. Pospisil. Autonomous airship equipped with multi-sensor mapping platform. In *ISPRS - The International Archives of the Photogrammetry Remote Sensing and Spatial Information Sciences*, pages 119–124, Trento, Italy, 2013. URL <http://www.int-arch-photogramm-remote-sens-spatial-inf-sci.net/XL-5-W1/119/2013/isprsarchives-XL-5-W1-119-2013.pdf>.
- A. D. Jones. *Manual of Photogrammetry*, volume 12. American Society of Photogrammetry, Falls Church, VA, USA, 1982. doi: 10.1080/00690805.1982.10438226. URL <http://dx.doi.org/10.1080/00690805.1982.10438226>.
- K. Kakaes, F. Greenwood, M. Lippincott, P. Meier, and S. Wich. *DRONES AND AERIAL OBSERVATION: New Technologies for Property Rights, Human Rights, and Global Development*. New America, 2015. URL <http://drones.newamerica.org/primer/>.
- Th. Kersten, K.R. Holm, and A. Grün. On-line point positioning with single frame camera data. Final technical report, London, England, 1992. URL [http://www.igp-data.ethz.ch/berichte/Graue\\_Berichte\\_PDF/197.pdf](http://www.igp-data.ethz.ch/berichte/Graue_Berichte_PDF/197.pdf).
- M. Khaghani and J. Skaloud. Autonomous vehicle dynamic model-based navigation for small UAVs. *NAVIGATION, Journal of The Institute of Navigation*, 63(3):345–358, 2016.
- T. Kluter. *GECKO4NAV Technical Reference Manual*. HuCE-mircroLab, Bern University of Applied Sciences, Bern, Switzerland, 1.0 edition, 2013.
- O. Kölbl. Transfer functions in image data collection. In *50th Photogrammetric Week*, Stuttgart, 2005.
- Koren, N. Introduction to resolution and MTF curves. <http://www.normankoren.com/Tutorials/MTF.html>, 2013. [Online; accessed 7-February-2017].
- T. Kraft, M. Geßner, H. Meißner, H. J. Przybilla, and M. Gerke. Introduction of a photogrammetric camera system for RPAS with highly accurate GNSS/IMU information for standardized workflows. In *ISPRS - The International Archives of the Photogrammetry, Remote Sensing and Spatial Information Sciences*, volume XL-3/W4, pages 71–75, Lausanne, Switzerland, 2016. URL <http://www.int-arch-photogramm-remote-sens-spatial-inf-sci.net/XL-3-W4/71/2016/isprs-archives-XL-3-W4-71-2016.pdf>.
- E. Kruck. Combined IMU and sensor calibration with BINGO-F. In *Integrated Sensor Orientation, Proc. of the OEEPE Workshop* ", pages 84–108, Hannover, 2001. CD-ROM.
- W. Kunysz. Effect of Antenna Performance on the GPS Signal Accuracy. In *Proceedings of the National Technical Meeting -Institute of Navigation*, pages 575–580. Institute of Navigation, 1998. URL <http://www.novatel.com/assets/Documents/Papers/effectofantenna.pdf>.

## Bibliography

---

- K. Legat. Approximate direct georeferencing in national coordinates. *ISPRS Journal of Photogrammetry & Remote Sensing*, 60:239–255, 2006.
- K. Legat, J. Skaloud, and R. Schmidt. Reliability of direct georeferencing phase 2: A case study on practical problems and solutions. In *Checking and Improving of Digital Terrain Models / Reliability of Direct Georeferencing*. EuroSDR Official Publication 51, 2006.
- Leica Geosystems. Mission Pro. <http://leica-geosystems.com/products/airborne-systems/software/leica-missionpro>, 2016. [Online; accessed 2-August-2016].
- Leica Geosystems. Leica DMC III Airborne Digital Camera. <http://leica-geosystems.com/products/airborne-systems/imaging-sensors/leica-dmciii>, 2017. [Online; accessed 24-January-2017].
- S. Leutenegger, M. Chli, and R. Y. Siegwart. BRISK: Binary robust invariant scalable keypoints. In *International Conference on Computer Vision*, pages 2548–2555, Barcelona, Spain, 2011. URL [http://ieeexplore.ieee.org/xpls/abs\\_all.jsp?arnumber=6126542](http://ieeexplore.ieee.org/xpls/abs_all.jsp?arnumber=6126542).
- K. Li and J. Stueckmann-Petring. Methods and results of combined adjustment utilizing kinematic GPS positioning and photogrammetric data. 29:213–213, 1992. URL [http://www.isprs.org/proceedings/xxix/congress/part3/213\\_XXIX-part3.pdf](http://www.isprs.org/proceedings/xxix/congress/part3/213_XXIX-part3.pdf).
- D. Lichti and M.A. Chapman. Constrained FEM self-calibration. *Photogrammetric Engineering and Remote Sensing*, 63(9):1111–1119, 1997.
- D. Lichti, J. Skaloud, and P. Schaer. On the calibration strategy of medium format cameras for direct georeferencing. In *ISPRS-The International Archives of the Photogrammetry Remote Sensing and Spatial Information Sciences*, Castelldefels, Spain, 2008.
- D. G. Lowe. Object recognition from local scale-invariant features. In *Computer vision, 1999. The proceedings of the seventh IEEE international conference on Computer Vision*, volume 2, pages 1150–1157, 1999. URL [http://ieeexplore.ieee.org/xpls/abs\\_all.jsp?arnumber=790410](http://ieeexplore.ieee.org/xpls/abs_all.jsp?arnumber=790410).
- D. G. Lowe. Distinctive image features from scale-invariant keypoints. *International journal of computer vision*, 60(2):91–110, 2004. URL <http://link.springer.com/article/10.1023/B:VISI.0000029664.99615.94>.
- R. Mabillard. Sensor Orientation with Gecko4Nav RIMU. Master Thesis, The Swiss Federal Institute of Technology Lausanne (EPFL), Lausanne, Switzerland, 2013.
- Makezine. Build a Wi-Fi drone disabler with Raspberry Pi. <http://makezine.com/projects/build-wi-fi-drone-disabler-with-raspberry-pi/>, 2016. [Online; accessed 16-November-2016].
- O. Martin, C. Meynard, M. Pierrot-Deseilligny, J. Souchon, and C. Thom. Réalisation d’une caméra photogrammétrique ultralégère et de haute résolution. [https://drone.teledetection.fr/articles/Souchon\\_CAMLIGHT\\_IGN\\_rev.pdf](https://drone.teledetection.fr/articles/Souchon_CAMLIGHT_IGN_rev.pdf), 2014.



- M. Martínez, M. Blázquez, A. Gómez, and Ismael Colomina. A new approach to the use of position and attitude control in camera orientation. In *7th International Geomatic Week*, Barcelona, Spain, 2007.
- MAVinci GmbH. Sirius Pro. <http://www.mavinci.com>, 2015. [Online; accessed 13-August-2016].
- Maxtena. Rugged L1/L2 GPS GLONASS Active Antenna. <http://www.maxtena.com/products/helicore/m1227hct-a2-sma/?v=1ee0bf89c5d1>, 2016. [Online; accessed 31-October-2016].
- L. Meier, P. Tanskanen, L. Heng, G.H. Lee, F. Fraundorfer, and M. Pollefeys. PIXHAWK: A micro aerial vehicle design for autonomous flight using onboard computer vision. *Autonomous Robots*, 33(1-2):21–39, 2012. URL <https://pixhawk.ethz.ch/>.
- O. Mian, J. Lutes, G. Lipa, J. J. Hutto, E. Gavelle, and S. Borghini. Direct georeferencing on small unmanned aerial platforms for improved reliability and accuracy of mapping without the need for ground control points. In *ISPRS - The International Archives of the Photogrammetry Remote Sensing and Spatial Information Sciences*, volume XL-1/W4, pages 397–402, Toronto, Canada, 2015. URL <http://www.int-arch-photogramm-remote-sens-spatial-inf-sci.net/XL-1-W4/397/2015/isprsarchives-XL-1-W4-397-2015.pdf>.
- Microdrones GmbH. mdCockpit. <https://www.microdrones.com/en/products/software/mdcockpit/>, 2016. [Online; accessed 19-September-2016].
- G. J. K. Moernaut and D. Orban. GNSS Antennas. *GPS World*, (2):42–48, 2009. URL <http://www2.unb.ca/gge/Resources/gpsworld.february09.pdf>.
- C. Mongredien, C. Hide, P. Faihust, and D. Ammann. Centimeter positioning for UAVs and mass-market applications. *GPS World*, 10, 2016. URL <http://gpsworld.com/centimeter-positioning-for-uavs-and-mass-market-applications/>.
- M. Mostafa. Camera/IMU boresight calibration: New advances and performance analysis. In *ASPRS Annual Meeting*, Washington, DC, USA, 2002.
- M. Mostafa, J. Hutton, and B. Reid. GPS/IMU products – the Applanix approach. In *Photogrammetric Week*, pages 63–83, Heidelberg, Germany, 2001.
- MVP. Electronic shuttering. <http://www.motionvideoproducts.com/MVP%20papers/Rolling%20vs%20Global%20Shutter.pdf>, 2009. [Online; accessed 16-November-2016].
- NASA. World Wind. <http://worldwind.arc.nasa.gov/java/>, 2016. [Online; accessed 10-November-2016].
- NASA Earth data. Remote Sensors. <https://earthdata.nasa.gov/user-resources/remote-sensors>, 2016. [Online; accessed 15-October-2016].

## Bibliography

---

- S. Nassar and N. El-Sheimy. Sensor integration and image georeferencing for airborne 3D mapping applications. [http://www.isprs.org/proceedings/2005/banff2005/presentations/WG%201-2\\_20.pdf](http://www.isprs.org/proceedings/2005/banff2005/presentations/WG%201-2_20.pdf), 2005.
- NovAtel. IMU Errors and Their Effects. <http://www.novatel.com/assets/Documents/Bulletins/APN064.pdf>, 2014. [Online; accessed 9-September-2016].
- Novatel. Waypoint Software. <http://www.novatel.com/products/software/>, 2016. [Online; accessed 31-October-2016].
- OSSIM. Orthorectification. <https://trac.osgeo.org/ossim/wiki/orthorectification>, 2016. [Online; accessed 25-October-2016].
- Parrot. Sequoia. <https://www.parrot.com/us/Business-solutions/parrot-sequoia#parrot-sequoia->, 2016. [Online; accessed 25-October-2016].
- R. Pascale. Quality management in flight planning - An advanced mission planner for uav. Master Thesis, The Swiss Federal Institute of Technology Lausanne (EPFL), EPFL, Switzerland, 2016.
- J. H. Perry and J. Childs. Timing on the fly: Synchronization for direct georeferencing on small UAVs. *Inside GNSS*, 11/12:34–40, 2009. URL <http://www.insidegnss.com/node/1715>.
- J.H. Perry. A synthesized directly georeferenced remote sensing technique for small unmanned aerial vehicles. Master Thesis, University of Florida, Gainesville, FL, USA, 2009. URL [http://etd.fcla.edu/UF/UFE0025070/perry\\_j.pdf](http://etd.fcla.edu/UF/UFE0025070/perry_j.pdf).
- N. Pfeifer, P. Glira, and C. Briese. Direct georeferencing with on board navigation components of light weight UAV platforms. In *ISPRS-The International Archives of the Photogrammetry Remote Sensing and Spatial Information Sciences*, volume XXXIX-B7, pages 487–492, Melbourne, Australia, 2012.
- Phase One. iXU Aerial Camera System. [http://industrial.phaseone.com/iXU\\_camera\\_system.aspx](http://industrial.phaseone.com/iXU_camera_system.aspx), 2016. [Online; accessed 3-August-2016].
- PhotographyLife. Understanding ISO, shutter speed and aperture. <https://photographylife.com/iso-shutter-speed-and-aperture-for-beginners>, 2016. [Online; accessed 27-October-2016].
- Pix4D SA. Pix4D Mapper 3.0. <http://pix4d.com/>, 2016. [Online; accessed 15-November-2016].
- A. Pothou, Ch. Stamatiou, and A. Georgopoulos. Performance evaluation of multiple scale automatic aerial triangulation. In *ISPRS-The International Archives of the Photogrammetry Remote Sensing and Spatial Information Sciences*, volume XXXV, pages 595–600, Istanbul, Turkey, 2004.
- QGC Dev Team. Qgroundcontrol. <http://qgroundcontrol.com/>, 2016. [Online; accessed 19-September-2016].

- B. Reese and Ch. Heipke. Towards a closer combination of direct and indirect sensor orientation of frame cameras. Castelldefels, Spain, 2006. URL [http://www.isprs.org/proceedings/2006/eurocow06/eurocow06\\_files/papers/EuroCOW\\_ReeseHeipke.pdf](http://www.isprs.org/proceedings/2006/eurocow06/eurocow06_files/papers/EuroCOW_ReeseHeipke.pdf).
- M. Rehak and J. Skaloud. Fixed-wing micro aerial vehicle for accurate corridor mapping. In *ISPRS Annals of the Photogrammetry, Remote Sensing and Spatial Information Sciences*, volume II-1/W4, pages 23–31, Toronto, Canada, 2015. doi: 10.5194/isprsannals-II-1-W1-23-2015. URL <http://dx.doi.org/10.5194/isprsannals-II-1-W1-23-2015>.
- M. Rehak and J. Skaloud. Applicability of new approaches of sensor orientation to micro aerial vehicles. In *ISPRS - Annals of the Photogrammetry, Remote Sensing and Spatial Information Sciences*, volume III-3, pages 441–447, Prague, Czech Republic, 2016. doi: 10.5194/isprsannals-III-3-441-2016. URL <http://www.isprs-ann-photogramm-remote-sens-spatial-inf-sci.net/III-3/441/2016/>.
- M. Rehak and J. Skaloud. Time synchronisation of consumer cameras on Micro Aerial Vehicles. *ISPRS Journal of Photogrammetry and Remote Sensing*, 123(1):114–123, 2017. URL <http://www.sciencedirect.com/science/article/pii/S0924271616303823>.
- F. Remondino. Heritage Recording and 3d Modeling with Photogrammetry and 3d Scanning. *Remote Sensing*, 3(12):1104–1138, May 2011. ISSN 2072-4292. doi: 10.3390/rs3061104. URL <http://www.mdpi.com/2072-4292/3/6/1104/>.
- F. Remondino. Automated Tie point extraction - Latest developments. EuroCOW. Lausanne, Switzerland, February 2016.
- F. Remondino and C. Fraser. Digital camera calibration methods: considerations and comparisons. In *ISPRS-The International Archives of the Photogrammetry Remote Sensing and Spatial Information Sciences*, volume 36, pages 266–272, Dresden, Germany, 2006. URL <http://masters.dgtu.donetsk.ua/2007/ggeo/sagaidak/library/book2.htm>.
- C. Ressel. The impact of conformal map projections on direct georeferencing. In *Photogrammetric Computer Vision*, Symposium, Vienna, 2002.
- M. Rieke, T. Foerster, J. Geipel, and T. Prinz. High-precision positioning and real-time data processing of UAV-system. In *ISPRS-The International Archives of the Photogrammetry Remote Sensing and Spatial Information Sciences*, volume XXXVIII-1/C22, Zurich, Switzerland, 2011.
- N. Rodday. Hacking a professional drone. [https://www.rsaconference.com/writable/presentations/file\\_upload/ht-w03-hacking\\_a\\_professional\\_police\\_drone.pdf](https://www.rsaconference.com/writable/presentations/file_upload/ht-w03-hacking_a_professional_police_drone.pdf), 2016. [Online; accessed 16-November-2016].
- D. Rouzaud and J. Skaloud. Rigorous integration of inertial navigation with optical sensors by dynamic networks. *NAVIGATION, Journal of The Institute of Navigation*, 58(2):141–152, 2011.

## Bibliography

---

- SBG Systems. SBG Ekinox Series. <https://www.sbg-systems.com/products/high-end-inertial-systems-overview>, 2016. [Online; accessed 13-August-2016].
- P. Schaer. *In-flight quality assessment and data processing for airborne laser scanning*. PhD Thesis, The Swiss Federal Institute of Technology Lausanne (EPFL), EPFL, Switzerland, 2009.
- P. Schaer, J. Skaloud, S. Landtwig, and K. Legat. Accuracy estimation for laser point cloud including scanning geometry. In *ISPRS-The International Archives of the Photogrammetry Remote Sensing and Spatial Information Sciences*, volume 36, Part 5-W8, 2007.
- F. Schaffalitzky and A. Zisserman. Multi-view matching for unordered image sets. In *Seventh European conference on computer vision*, pages 414–431, Copenhagen, Denmark, 2002. URL [http://link.springer.com/chapter/10.1007/3-540-47969-4\\_28](http://link.springer.com/chapter/10.1007/3-540-47969-4_28).
- K. P. Schwarz, M.A. Chapman, M.E. Cannon, and P. Gong. An integrated INS/GPS approach to the georeferencing of remotely sensed data. *Photogrammetric Engineering and Remote Sensing*, 59(11):1167–1674, 1993.
- senseFly. senseFly drones and cameras. <http://www.sensefly.com>, 2015a. [Online; accessed 13-August-2016].
- senseFly. Drones vs traditional instruments: corridor mapping in Turkey. <https://www.sensefly.com/fileadmin/user-cases/2015/senseFly-Case-Study-Corridor-Mapping-Turkey.pdf>, 2015b. [Online; accessed 6-September-2016].
- T. Sieberth, R. Wackrow, and J.H. Chandler. Automatic isolation of blurred images from UAV image sequences. In *ISPRS-The International Archives of the Photogrammetry Remote Sensing and Spatial Information Sciences*, Rostock, Germany, 2013. URL <https://dspace.lboro.ac.uk/dspace-jspui/handle/2134/16129>.
- T. Sieberth, R. Wackrow, and J. H. Chandler. UAV Image Blur - Its influence and ways to correct it. In *ISPRS-The International Archives of the Photogrammetry Remote Sensing and Spatial Information Sciences*, volume XL-1/W4, pages 33–39, Toronto, Canada, August 2015. doi: 10.5194/isprsarchives-XL-1-W4-33-2015. URL <http://www.int-arch-photogramm-remote-sens-spatial-inf-sci.net/XL-1-W4/33/2015/>.
- SimActive. Correlator3D. <http://www.simactive.com/en>, 2016. [Online; accessed 20-November-2016].
- J. Skaloud. *Optimizing georeferencing of airborne survey systems by INS/DGPS*. PhD Thesis, University of Calgary, Calgary, Canada, 1999.
- J. Skaloud. Reliability of direct georeferencing phase 1: An overview of the current approaches and possibilities. In *Checking and Improving of Digital Terrain Models / Reliability of Direct Georeferencing*. EuroSDR Official Publication 51, 2006.

- J. Skaloud and K. Legat. Cameo - camera exterior orientation by direct deoreferencing, 2006.
- J. Skaloud and K. Legat. Theory and reality of direct georeferencing in national coordinates. *ISPRS Journal of Photogrammetry & Remote Sensing*, 63:272–282, 2008.
- J. Skaloud and K. Legat. *Navigation techniques*. Lecture notes, EPFL TOPO, Lausanne, Switzerland, 2010.
- J. Skaloud and P. Schaer. Towards a more rigorous boresight calibration. In *ISPRS International Workshop on Theory Technology and Realities of Inertial/GPS/Sensor Orientation*, Castelldefels, Spain, 2003.
- J. Skaloud and P. Schaer. Optimizing computational performance for real-time mapping with airborne laser scanning. In *ISPRS-The International Archives of the Photogrammetry Remote Sensing and Spatial Information Sciences*, volume 38, page 9, 2010.
- J. Skaloud, M. Cramer, and K. P. Schwarz. Exterior orientation by direct measurements of camera position and attitude. In *ISPRS-The International Archives of the Photogrammetry Remote Sensing and Spatial Information Sciences*, volume 31, pages 125–130, 1996.
- J. Skaloud, M. Rehak, and D. Lichti. Mapping with MAV: Experimental study on the contribution of absolute and relative position control. In *ISPRS-The International Archives of the Photogrammetry Remote Sensing and Spatial Information Sciences*, volume 40-3/W1, pages 123–129, Castelldefels, Spain, 2014. doi: 10.5194/isprsarchives-XL-3-W1-123-2014.
- Skyward. Cloud-based operations management that scales from startup to enterprise. <https://skyward.io/>, 2016. [Online; accessed 12-November-2016].
- N. Snavely, S.M. Seitz, and R. Szeliski. Modeling the world from internet photo collections. *International Journal of Computer Vision*, 80(2):189–210, November 2008. ISSN 0920-5691, 1573-1405. doi: 10.1007/s11263-007-0107-3. URL <http://link.springer.com/10.1007/s11263-007-0107-3>.
- Sony. Sony NEX-5R. <http://www.sony.co.uk/support/en/product/nex-5r>, 2016. [Online; accessed 14-August-2016].
- Y. Stebler and J. Skaloud. NAVPROC - Inertial navigation processing software, 2012.
- Y. Stebler and J. Skaloud. *Modeling and Processing Approaches for Integrated Inertial Navigation*. PhD Thesis, The Swiss Federal Institute of Technology Lausanne (EPFL), Lausanne, Switzerland, 2013.
- Y. Stebler, S. Guerrier, J. Skaloud, and M-P. Victoria-Feser. The generalized method of wavelet moments for inertial navigation filter design. *IEEE Transactions on Aerospace and Electronic Systems*, 50(3):2269–2283, July 2014.

## Bibliography

---

- W. Stempfhuber and M. Buchholz. A precise, low-cost RTK GNSS system for UAV applications. In *ISPRS - The International Archives of the Photogrammetry, Remote Sensing and Spatial Information Sciences*, pages 289–293, Zurich, Switzerland, 2011. URL <http://www.int-arch-photogramm-remote-sens-spatial-inf-sci.net/XXXVIII-1-C22/289/2011/isprsarchives-XXXVIII-1-C22-289-2011.pdf>.
- C. Strecha, A. Bronstein, M. Bronstein, and P. Fua. LDAHash: Improved matching with smaller descriptors. *IEEE Transactions on Pattern Analysis and Machine Intelligence*, 34(1):66–78, 2012. URL [http://ieeexplore.ieee.org/xpls/abs\\_all.jsp?arnumber=5770264](http://ieeexplore.ieee.org/xpls/abs_all.jsp?arnumber=5770264).
- Survey Group. Taming a monster – large-scale RTK corridor mapping in remotest Australia. [https://www.sensefly.com/fileadmin/user\\_upload/sensefly/images/web2014/applications/senseFly-Case-Study-eBee-RTK-Talawana.pdf](https://www.sensefly.com/fileadmin/user_upload/sensefly/images/web2014/applications/senseFly-Case-Study-eBee-RTK-Talawana.pdf), 2015. [Online; accessed 12-September-2016].
- Swisstopo. New National Survey LV95. <https://www.swisstopo.admin.ch/en/knowledge-facts/surveying-geodesy/reference-frames/local/lv95.html>, 2017. [Online; accessed 12-February-2017].
- Z.F. Syed, P. Aggarwal, C. Goodall, X. Niu, and N. El-Sheimy. A new multi-position calibration method for MEMS inertial navigation systems. *Measurement Science and Technology*, 18(7):1897–1907, 2007.
- Tallysman Wireless. Selecting Antennas for GPS/GNSS. <http://www.tallysman.com/wp-content/uploads/2014/Resources/White-Paper-on-GNSS-Antennas.pdf>, 2014. [Online; accessed 16-August-2016].
- P.J.G. Teunissen. *Adjustment Theory: An Introduction*. Series on mathematical geodesy and positioning. Delft University Press, 2000. ISBN 978-90-407-1974-5.
- The MathWorks Inc. Matlab v. 8.40. [http://uk.mathworks.com/index.html?s\\_tid=gn\\_loc\\_drop](http://uk.mathworks.com/index.html?s_tid=gn_loc_drop), 2016. [Online; accessed 2-November-2016].
- D.H. Titterton and J.L. Weston. *Strapdown inertial navigation technology*. Stevenage, U.K., 1997.
- C. Toth, S.W. Shin, D.A. Grejner-Brzezinska, and J.H. Kwon. On accurate time synchronization of multi-sensor mobile mapping systems. *Journal of Applied Geodesy*, 2(3), 2008. URL <http://www.degruyter.com/view/j/jag.2008.2.issue-3/jag.2008.018/jag.2008.018.xml>.
- B. Triggs, P.L. McLauchlan, R.I. Hartley, and A.W. Fitzgibbon. *Vision algorithms: theory and practice*, chapter Bundle adjustment – a modern synthesis, pages 298–372. Springer, 2000.
- Trimble. Trimble Inpho - Precision Photogrammetry & Digital Modeling. <http://www.trimble.com/imaging/inpho.aspx>, 2016. [Online; accessed 20-October-2016].
- Trimble Inc. Sketchup. <http://www.sketchup.com/>, 2016. [Online; accessed 26-October-2016].

- U-Blox. NEO/LEA-8T. <https://www.u-blox.com/en/product/neolea-m8t>, 2016. [Online; accessed 4-September-2016].
- UniFly. UnifyUTMS. <http://unify.aero/>, 2016. [Online; accessed 12-November-2016].
- Unmanned Aerial Vehicle Systems Association. UAV or UAS? . [https://www.uavs.org/index.php?page=what\\_is](https://www.uavs.org/index.php?page=what_is), 2016. [Online; accessed 25-October-2016].
- J. Vautherin, S. Rutishauser, K. Schneider-Zapp, H. Fai Choi, V. Chovancova, A. Glass, and C. Strecha. Photogrammetric accuracy and modeling of rolling shutter cameras. *ISPRS Annals of Photogrammetry, Remote Sensing and Spatial Information Sciences*, III-3:139–146, June 2016. ISSN 2194-9050. doi: 10.5194/isprsannals-III-3-139-2016. URL <http://www.isprs-ann-photogramm-remote-sens-spatial-inf-sci.net/III-3/139/2016/isprs-annals-III-3-139-2016.pdf>.
- Velodyne LiDAR. Vpl-16. <http://velodynelidar.com/vlp-16.html>, 2016. [Online; accessed 25-October-2016].
- A. Waegli, S. Guerrier, and J. Skaloud. Redundant MEMS-IMU integrated with GPS for performance assessment in motorsports. In *PLANS 2008 - Joined Symposium of IEEE and ION on Position Location and Navigation*, 2008.
- D. Wagner and D. Schmalstieg. ARToolKitPlus for pose tracking on mobile devices. In *12th. Computer Vision Winter Workshop (CVWW'07)*, Sankt Lambrecht, Austria, 2007.
- C.S. Yoo and I.K. Ahn. Low cost GPS/INS sensor fusion system for UAV navigation. volume 2, pages 8–A, Indianapolis, IN, USA, 2003. IEEE. URL [http://ieeexplore.ieee.org/xpls/abs\\_all.jsp?arnumber=5731136](http://ieeexplore.ieee.org/xpls/abs_all.jsp?arnumber=5731136).

# Curriculum Vitae

First name: **Martin**  
Family name: **Rehak**  
Date of birth: 14.12.1986  
Citizenship: Czech Republic  
e-mail: rehi.martin@gmail.com

## Professional Experience

---

2011 – 2012 Part-time: UAV operator in Control System CA, Canada.  
3D modelling of open pit mines using UAVs and LiDAR.  
2011 – 2012 Self-intern: Aerial Photographer and UAVs builder.  
Providing services and consultation.  
2010 – 2012 Research Assistant at the Czech Technical University in Prague.  
Working on GIS research projects, Land use analysis.  
06-09/2011 T-Cart: GIS technician, Prague, Czech Republic  
Summer internship, working on a new GIS database for city of Prague.  
2007 – 2010 Self-intern: Construction and maintenance of computer networks.  
Installation of computers, LAN and end-devices.

## Education

---

9/2012-1/2017 **PhD** in Environmental and Civil Engineering at École Polytechnique Fédérale de Lausanne, Switzerland  
Thesis title: **Integrated Sensor Orientation on Micro Aerial Vehicles**  
2010 – 2012 **M.Sc.** in Geomatic Engineering, Czech Technical University in Prague, Czech Republic  
Thesis title: **UAV Photogrammetry**  
2006 – 2010 **B.Sc.** in Geomatic Engineering and Land Surveying, Czech Technical University in Prague, Czech Republic  
Thesis title: **Land use and land cover evolution in Melnik village during 40 year time period using remote sensing techniques**

## Honours

---

2015 "Hansa-Luftbild Preis 2015" for co-authoring the best publication of the year 2014 in the PFG journal entitled: A Micro Aerial Vehicle with Precise Position and Attitude Sensors.  
2014 "A best doctoral poster award" - 1st prize during ENAC Research Day, EPFL, 2014.  
2013 "A best paper award" attributed to young researchers at the 2nd edition of the conference focusing on Unmanned Airborne Vehicles in Geomatics (UAV-g), held in Rostock, Germany, Sep. 4-6, 2013" for the paper entitled: "A Micro-UAV with the Capability of Direct Georeferencing".

## Teaching

---

2013-2016 Sensor Orientation, master course, EPFL.  
2013 Introduction to Statistics, bachelor course, EPFL.  
2014-2015 Advanced Satellite Navigation, master course, EPFL.  
2016 2 weeks intensive course: Hands on UAV mapping, master and PhD course, UofC.  
2012-2016 Co-supervisor of 3 master and 3 semester projects, EPFL.



## Language Skills

---

Czech (native language)  
English (fluently written and spoken)  
French (intermediate)  
German (beginner)

## Computer Skills

---

- Programming languages: Matlab, Java (basics), C/C++ (basics)
- Software: Adobe Lightroom, ArcGIS, Agisoft Photoscan, Bingo adjustment, Pix4D, Inkscape, Solidworks, MS Office

## Other Skills

---

- Cisco network academy - Network fundamentals
- Athens internship course at UTM Madrid - An Overview of Hyperspectral and Time Series Data in Remote Sensing Applied to Environmental Studies.
- CAD design, CNC machining, HW integration and soldering.
- Land surveying, GNSS data processing.
- Driving license: A, B.

## Personal interests and hobbies

---

- UAVs and RC models
- Ice hockey, hiking
- Photography, travelling

## Publications

---

### JOURNALS

- **M. Rehak** and J. Skaloud. Time synchronization of consumer cameras on Micro Aerial Vehicles, in ISPRS Journal of Photogrammetry and Remote Sensing, vol. 1/2017, p. 114-123, 2017.
- E Gandor, **M. Rehak** and J. Skaloud. Planificateur de missions photogrammétriques pour drones ultra-légers (Micro Aerial Vehicle MAV), in Géomatique Suisse, vol. 9/2015, p. 371-375, 2015.
- Y. Akhtman, D. Constantin, **M. Rehak**, V. M. Nouchi and G. Shinkareva et al. Télédétection multi-échelle des lacs depuis un aéronef ultraléger motorisé, in Géomatique Suisse, vol. 9, num. 395-398, 2014.
- J. Skaloud, **M. Rehak** and P. Clausen. Ein Mikroflugzeug zur genauen Kartierung ohne Passpunkte am Boden, in Géomatique Suisse, vol. 9, p. 376-380, 2014.
- **M. Rehak**, R. Mabillard and J. Skaloud. A Micro Aerial Vehicle with Precise Position and Attitude Sensors, in Photogrammetrie, Fernerkundung, Geoinformation (PFG), vol. 4, p. 0239-0251, 2014

### CONFERENCE PROCEEDINGS

#### Peer-reviewed

- **M. Rehak** and J. Skaloud. Applicability of new approaches of sensor orientation to Micro Aerial Vehicles. ISPRS Annals. XXIII ISPRS Congress, Prague, Czech Republic, 2016.

- F. Gandor, **M. Rehak** and J. Skaloud. Photogrammetric mission planner for RPAS. ISPRS Archives. UAV-g, Toronto, Canada, 2015.
- **M. Rehak** and J. Skaloud. Fixed-wing Micro Aerial Vehicle for accurate corridor mapping. ISPRS Annals. UAV-g, Toronto, Canada, 2015.
- J. Skaloud, **M. Rehak** and D. Lichti. Mapping with MAV: Experimental study on the contribution of absolute and relative aerial position control. ISPRS Archives. European Calibration and Orientation Workshop, Castelldefels, Spain, 2014.
- **M. Rehak**, R. Mabillard and J. Skaloud. A micro-UAV with the capability of direct georeferencing. ISPRS Archives. UAV-g, Rostock, Germany, 2013.

## Other

- P. Clausen, **M. Rehak** and J. Skaloud. UAV Sensor orientation with pre-calibrated redundant IMU/GNSS observations: Preliminary results. 36te Dreiländertagung Photogrammetrie and Fernerkundung der SGPF, DGPF und OVG, Bern, Switzerland, 2016.
- P. Clausen, **M. Rehak** and J. Skaloud. Drohne für ein hoch genaues Korridor-Mapping. AHORN 2015 – der Alpenraum und seine Herausforderungen im Bereich Orientierung, Navigation und Informationsaustausch, Wildhaus, 2015.
- D. Constantin, **M. Rehak**, Y. Akhtman and F. Liebisch. Detection of crop properties by means of hyperspectral remote sensing from a micro UAV. 20. und 21. Workshop Computer-Bildanalyse in der Landwirtschaft - 3. Workshop Unbemannte autonom fliegende Systeme (UAS) in der Landwirtschaft, Braunschweig, Germany, 2015.
- M. Tarasov, G. Shinkareva, O. Tutubalina, M. Lychagin, D. Constantin, **M. Rehak** et al. Investigation of heavy metals distribution in suspended matter and macrophytes of the Selenga river delta using airborne hyperspectral remote sensing. 9th EARSeL SIG Imaging Spectroscopy workshop, LIST, Luxembourg, 2015.
- H. G. E. J. Clenet, D. Constantin, **M. Rehak**, Y. Akhtman and T. Bajjouk et al. UAV based multispectral imaging over a lagoon with corals in Reunion Island. 9th EARSeL SIG Imaging Spectroscopy workshop, LIST, Luxembourg, 2015.
- D. Constantin, **M. Rehak**, Y. Akhtman and F. Liebisch. Hyperspectral remote sensing of crop properties with Unmanned Aerial Vehicles. 9th EARSeL SIG Imaging Spectroscopy workshop, LIST, Luxembourg, 2015.
- **M. Rehak**, J. Skaloud and Y. Akhtman. High-Precision Geomonitoring using Micro Aerial Vehicles. Deltas: Genesis, dynamics, modelling and sustainable development, Istomino, Republic of Buryatia. Russian Federation, 2014.
- Y. Akhtman, D. Constantin, **M. Rehak**, V. M. Nouchi and D. Bouffard et al. Leman-Baikal: Remote sensing of lakes using an ultralight plane. 6th Workshop on Hyperspectral Image and Signal Processing, Lausanne, Switzerland, 2014.

## INVITED TALKS

- **M. Rehak** and J. Skaloud. Sensor Orientation on Micro Aerial Vehicles. Swiss GEOSummit meeting, Workshop "Facts and Trends: Nutzung von Drohnen in der Schweiz, Bern, Switzerland, 2014.
- **M. Rehak**. Accurate mapping with RPAS - sensor orientation methods. Annual student conference on remote sensing and GIS, Telc, Czech Republic, 2014.
- **M. Rehak**. A micro-UAV with the capability of direct georeferencing. Fall Meeting of The Swiss Society of Photogrammetry and Remote Sensing (SSPT), EPFL, Lausanne, Switzerland, 2013.

